University of Alberta

Syntheses and Optical Properties of Silicon Based Nanomaterials

by

Mita Dasog

A thesis submitted to the Faculty of Graduate Studies and Research
in partial fulfillment of the requirements for the degree of

Doctor of Philosophy

Department of Chemistry

© Mita Dasog

Spring 2014
Edmonton, Alberta

Permission is hereby granted to the University of Alberta Libraries to reproduce single copies of this thesis and to lend or sell such copies for private, scholarly or scientific research purposes only. Where the thesis is converted to, or otherwise made available in digital form, the University of Alberta will advise potential users of the thesis of these terms.

The author reserves all other publication and other rights in association with the copyright in the thesis and, except as herein before provided, neither the thesis nor any substantial portion thereof may be printed or otherwise reproduced in any material form whatsoever without the author's prior written permission.

Dedicated to my family.

"न चोरहार्यं न च राजहार्यं न भ्रातृभ्राज्यं न च भारकारि।

व्यये कृते वर्धत एव नित्यं विद्याधनं सर्वधनप्रधानम्॥"

- Vedas

Abstract

Silicon (Si) based nanomaterials have the potential to revolutionize the microelectronics industry by introducing desirable nanoscale properties into electronic components without compromising the material composition. They have also been proposed as a greener alternative for many Group III-V and II-VI semiconductors. However, the high temperature and costly infrastructure required for the large scale synthesis and characterization of Si based materials still poses a challenge that impedes their widespread application. This thesis describes the synthesis of silicon (Si), silicon carbide (SiC), silicon nitride (Si_3N_4), and silica (SiO_2) nano- and micromaterials from compositionally tuned sol-gel polymers. Si based materials were prepared either *via* disproportionation of $(RSiO_{1.5})_n$ sol-gel polymers or by a magnesiothermic reduction method. Magnesiothermic reduction was carried out at the lowest temperature reported in the literature to date (500 - 600 ^oC) to make Si, Si_3N_4, and SiC materials with various morphologies.

Detailed chemical investigations were carried out to understand the origin of blue luminescence in Si nanocrystals (NCs). It was determined that the presence of nitrogen, oxygen, and chlorine based impurities in trace amounts can lead to blue emission *via* a charge transfer process. Si-NCs with various surface protecting groups were synthesized in order to tune their luminescence across the visible spectrum. The luminescence is believed to originate from surface defects, and the excited state lifetimes of such emissions are short lived (a few nanoseconds). This is the first example to demonstrate emission across the visible spectrum by tuning the surface protecting groups.

The materials and methodologies summarized in this thesis open up new avenues in the pursuit of Si nanomaterial based photovoltaics, sensors, biological applications, redox reactions, greenhouse gas sequestration, and many more.

Acknowledgements

As I conclude my graduate studies, I am grateful to those who have contributed to my educational and professional development.

Foremost, I offer my sincere gratitude to my supervisor, Dr. Jonathan Veinot for supporting me throughout my doctoral program. You have challenged me and given me the utmost freedom in regards to my projects. You are not only a great mentor but also a good colleague and friend.

I would like to thank all my undergraduate supervisors, especially Dr. Robert Scott, who has taught me to be an independent and creative scientist. Thanks to my committee members, Drs. Eric Rivard, Arthur Mar, Mark McDermott, and Greg Goss for your valuable input over the years and always entertaining my "drop-by" questions. I would like to thank Dr. Byron Gates for serving as an external and for his valuable input. I am also grateful to Professor Rieger and his group for hosting me at the Technical University of Munich and introducing me to the Bavarian culture.

This work would not have been possible without the technical expertise of Wayne Moffat (Analytical Services), Kai Cui (TEM), Dmitri Karpuzov (XPS), Tate Hauger, Sharon Saunders, George Braybook (SEM), and Peter Gigler (BET) - you are all thanked for your help. Every materials chemist needs a physicist even though we never speak the same scientific language. Glenda De les Royes, Dr. Frank Hegmann, and Omri Wolf are thanked for shedding light on silicon nanocrystals, sometimes literally.

I have had the opportunity to work with some really great people in the Veinot group who have made this journey a little easier and a lot more fun. I would especially like to thank Kevin Yang, Leah Coumont, Lydia Glover, Dr. Brenna Brown, Christina Gonzales, Yi Zhai, Regina Sinelnikov, Larissa Smith, and Alex Smith, it was great discussing science and working with you all on various projects. You have all taught me to live life and play a little harder.

Thanks also to the Lowary group for adopting me as your honorary member. Melanie Lui and Sweeney, your energy is so contagious and you guys never fail to bring a smile on my face. Paul Lummis, you are always there to listen or grab a drink when I have had "one of those days." Alena, my late night buddy, you made it possible to carry out numerous HF etches at odd times and I will miss our hallway chats. Thank you all! Thanks to Drs. Andrew Grosvenor, Jens Müller, Alex Bartole-Scott, Princy Joseph and Pia Wennek for the moral support over the years.

I would like to thank the amazing department staff members - Anita Weiler, Bonnie Gover, Ryan Lewis, Bernie Hippel and Lynne Lechelt for all their help from day one. Thanks to NSERC, Alberta Innovates, Killam Trusts, German Federal Ministry, and University of Alberta for the financial support.

I would like to thank my family for their endless love and support. Words cannot come close to expressing my gratitude for everything you have done for me. Last but not least, I would like to thank Ryan Snitynsky. You have put up with me through numerous ups and downs. You have my eternal gratitude and I would have never come this far without you beside me.

Table of Contents

Chapter 1: Introduction 1

1.1 Inorganic semiconductor nanocrystals 2

1.2 Silicon nanocrystals 3

1.3 Synthetic methods for preparing Si-NCs 6

1.4 Sol-gel reactions 17

1.5 Si-NC optical properties 20

1.6 Thesis Outline 28

1.7 References 30

Chapter 2: Attempts to lower the solid-state syntheses temperature to make Si-NCs 38

2.1 Silicon nanomaterials derived from $(RSiO_{1.5})_n$ sol-gel polymers 39

2.1.1 Introduction 39

2.1.2 Experimental 41

2.1.3 Results and discussion 45

2.1.4 Conclusions 58

2.2 Influence of the matrix on the formation of Si-NCs 60

2.2.1 Introduction 60

2.2.2 Experimental 61

2.2.3 Results and discussion 63

2.2.4 Conclusions 71

2.3 References 73

Chapter 3: Synthesis of silicon nano/micro materials *via* magnesiothermic reduction 75

3.1 Synthesis of silicon materials via magnesiothermic reduction 76

3.1.2 Introduction 76

3.1.2 Experimental 77

3.1.3 Results and discussion 82

3.1.4 Conclusions 91

3.2 Mechanistic insight into magnesothermic reduction 93

3.2.1 Introduction 93

3.2.2 Experimental 95

3.2.3 Results and discussion 97

3.2.4 Conclusions 108

3.3 References 110

Chapter 4: Low temperature synthesis of silicon nitride and silicon carbide nanomaterials *via* magnesiothermic reduction method..... 113

4.1 Solid-state synthesis of silicon nitride nanocrystals 114

4.1.2 Introduction 114

4.1.2 Experimental 115

4.1.3 Results and discussion 119

4.1.4 Conclusions 126

4.2 Solid-state synthesis of silicon carbide nanomaterials..... 127

4.2.1 Introduction 127

4.2.2 Experimental 128

4.2.3 Results and discussion 131

4.2.4 Conclusions 137

4.3 References 138

Chapter 5: Chemical insight into the origin of red and blue photoluminescence arising from freestanding silicon nanocrystals 141

5.1 Introduction 142

5.2 Experimental 145

5.3 Results and discussion 154

5.4 Conclusions 178

5.5 References 180

Chapter 6: Tunable photoluminescence from silicon nanocrystals 184

6.1 Introduction 185

6.2 Experimental 186

6.3 Results and discussion 194

6.4 Conclusions 223

6.5 References 225

Chapter 7: Conclusions and Future Directions 229

7.1 Conclusions 230

7.2 Future directions 233

7.3 References 239

Appendices **240**

Appendix A 241

Appendix B 243

List of Tables

Table 2-1: The excitation wavelength, slit widths and reference for the etched samples.....45

Table 2-2: Condensation copolymers and their decomposition temperatures.....47

Table 2-3: Thermally processed composites, processing conditions and the products obtained.....49

Table 2-4: HF etched samples and their luminescent properties.....54

Table 2-5: Reagent amounts for various reactions.....63

Table 2-6: Thermally processed composites and processing conditions 67

Table 2-7: Thermally processed composites and processing conditions 70

Table 3-1: Varying Stöber silica particle sizes with the reaction time and respective reaction yields. The particle size was determined from electron microscopy images.....78

Table 3-2: Silica and Si-NCs sizes obtained from electron microscopy.....86

Table 5-1: A summary of the titration procedure used to monitor the influence of nitrogen containing reagent on Si NC photoluminescence 148

List of Figures

Figure 1-1: Schematic band structure showing a direct and indirect band gap.....4

Figure 1-2: Schematic representation of wave function broadening in Si-NCs.....6

Figure 1-3: Scanning electron micrograph (SEM) image of *p*-Si.....7

Figure 1-4: Schematic representation of size separation of Si-NCs prepared *via* SiH_4 decomposition. (**A**) Size separation of particles due to difference in velocities and (**B**) particles of different sizes are deposited at different places on the substrate after passing through a rotating chopper slit.....8

Figure 1-5: Photograph of Si-NCs of varying sizes under UV-illumination prepared from pyrolysis of silane gas using plasma.....9

Figure 1-6: (**A**) Bright field TEM image and (**B**) PL spectra of alkyl terminated Si-NCs synthesized by decomposition of Zintl phases.....10

Figure 1-7: (**A**) Bright field TEM image and (**B**) PL spectra of octyl terminated Si-NCs synthesized from reduction of $SiCl_4$.....12

Figure 1-8: (**A**) Bright field TEM image and (**B**) excitation wavelength dependent PL spectra of hexyl terminated Si-NCs prepared *via* reduction $SiCl_4$ using a hydride source.....13

Figure 1-9: Bright field TEM images of (**A**) 3 nm, (**B**) 6 nm and (**C**) 9 nm Si-NCs obtained from thermal decomposition of HSQ at 1100, 1200 and 1300 ^{o}C, respectively.....16

Figure 1-10: PL spectra of hydride terminated Si-NCs obtained from thermal decomposition of HSQ. Inset: photograph of Si-NCs under UV-illumination.....16

Figure 1-11: Schematic representation of Stöber silica particle formation and growth.....19

Figure 1-12: SEM images for Stöber silica particles sonicated with diamond powder.....19

Figure 1-13: Schematic representation of change in DOS and bandgap of Si with changing crystal size.....21

Figure 1-14: Calculated relationship between the band gap of Si-NC and the NC size based upon EMA and tight binding model predictions.....22

Figure 1-15: Simulated structures of various Si clusters.....23

Figure 1-16: Band gap and Si=O trapped state energy in Si-NCs as a function of NC size.....25

Figure 1-17: Radiative transitions according to surface state model..... 26

Figure 1-18: Calculated radiative centers in SiO_2-like encapsulated Si-NCs. (**A**) Excitation and relaxation at non-bridging oxygen trap state, (**B**) excitation into O_3^+ shallow state followed by its relaxation to (**C**) Si_3^0 trap state and its radiative relaxation, and (**D**) emission from relaxation to SiO_3^+ trap state.....27

Figure 1-19: Emission peak maximum vs. Si-NC size for various literature reported alkyl passivated Si-NCs.....27

Figure 2-1: FT-IR spectra of sol-gel derivatized copolymers.....47

Figure 2-2: XRD patterns of the copolymers processed at 1400 ^oC for two hours under Ar atmosphere.....51

Figure 2-3: HR XP spectra of the Si 2p region of the composites processed at 1400 ^oC. For the clarity of the figure only Si $2p_{3/2}$ spin-orbit lines are shown. The full-width half maxima of the Si $2p_{3/2}$ spin-orbit lines were constrained below 1.2 eV. (Color code: Black - data obtained, red - fitted line, yellow - Si(I), pink - Si (II), green - Si(III) and blue - Si(IV)).....52

Figure 2-4: HR XP spectra of the Si 2p region of the samples **A4 – C4.** For the clarity of the figure only Si $2p_{3/2}$ spin-orbit lines are shown. The full-width half maxima of the Si $2p_{3/2}$ spin-orbit

lines were constrained below 1.2 eV. (Color code: Black - data obtained, red - fitted line and blue - Si(IV)).....53

Figure 2-5: HR XP spectra of the Si 2p region of the HF etched samples. For the clarity of the figure only Si $2p_{3/2}$ spin-orbit lines are shown. (Color code: Black - data obtained, red - fitted line, yellow - Si(I), pink - Si (II), green - Si(III) and blue - Si(IV)).....55

Figure 2-6: HR XP spectra of the C 1s region of the HF etched samples.....56

Figure 2-7: FTIR spectra of the HF etched samples.....57

Figure 2-8: Photograph of toluene dispersions of **A5**, **B5** and **C5** samples under UV illumination.....57

Figure 2-9: FTIR spectra of $(HSiO_{1.5})_n$ condensation polymer.....64

Figure 2-10: FTIR spectra of $(HSiO_{1.5})_n$ condensation polymer made in presence of 1 mmol $AlCl_3$ salt.....65

Figure 2-11: FTIR spectra of alumina-$(HSiO_{1.5})_n$ hetero sol-gel polymers with varying amounts of alumina.....66

Figure 2-12 XRD pattern of various composites and the relationship of Si-NC size vs. varying amount of $AlCl_3$ added.....68

Figure 2-13: HR XP spectra of O 1s region of the samples **M2**, **G2** and **H2**.....69

Figure 2-14: XRD pattern of composites **N1**, **O1**, **P1**, **Q1**, **R1** and **M2**.....71

Figure 3-1: Evolution of Stöber silica particle size as a function of reaction time.....82

Figure 3-2: Scanning electron micrograph (SEM) images of Stöber silica particles of average sizes *ca*. (**A**) 15 nm (**B**) 40 nm (**C**) 75 nm (**D**) 95 nm (**E**) 145 nm, and (**F**) 200 nm. The scale bar represents 200 nm.....83

Figure 3-3: FTIR spectrum of 200 nm Stöber silica particles.....83

Figure 3-4: Powder X-Ray diffraction patterns of (**A**) 4 nm (**B**) 9 nm (**C**) 20 nm (**D**) 32 nm (**E**) 45 nm, and (**F**) 70 nm Si-NCs, respectively.....84

Figure 3-5: TEM images of *ca*. (**A**) 4 nm (**B**) 23 nm (**C**) 75 nm (**D**) 110 nm (**E**) 177 nm, Si-NCs. (**F**) SAED pattern for the 110 nm Si-NCs. The d-spacing for (111), (220) and (311) Miller indices are 3.24 Å, 1.93 Å and 1.69 Å respectively. (**G**) EDX spectrum of 110 nm Si-NC sample. EDX analyses of all the Si-NCs showed very similar spectra.....85

Figure 3-6: (**A**) Thickness (SEM) of Si layer formed as a function of initial Mg thickness. The values were obtained from SEM analysis. (**B**) SEM image of a cross-section of Si thin film on quartz.....87

Figure 3-7: (**A**) Absorbance spectra of Si thin films of varying thickness on quartz. (**B**) Photograph of Si thin films on quartz with varying thickness.....88

Figure 3-8: Transparency of Si thin films of various thickness at 700, 550, and 400 nm.....89

Figure 3-9: Device structure of OLED with Si thin film and ITO as transparent conducting layer.....90

Figure 3-10: . Typical I-V curves obtained from testing OLEDs with (A) 135 nm thick Si film, (B) 170 nm thick Si film, and (C) ITO as the transparent conducting layer.....91

Figure 3-11: Electron microscopy images of silicon based nano/micromaterials in the shape of (**A**) fibers, (**B**) rods, (**C**) cubes, and (**D**) freestanding film.....92

Figure 3-12: The growth of publications in the area of magnesiothermic reduction to form silicon micro/nanomaterials since 2008.....93

Figure 3-13: SEM secondary electron images of thin-film cross-sections of (**A**) Mg deposition on glass, (**B**) after heating the Mg substrate, and (**C**) after exposure to aqueous HCl. Elemental composition (determined using XPS) at different depths for thin films (**D**) after Mg deposition on glass, (**E**) after heating the Mg substrate, and (**F**) after HCl washing.....99

Figure 3-14: Pore size distribution (BJH) plots of Stöber silica particles with average particle size of (**A**) 90 nm and (**B**) 140 nm.....100

Figure 3-15: (**A**) N_2 sorption isotherm and (**B**) pore size distribution (BJH plot) for Si-NCs.....101

Figure 3-16: Stober silica particles with average diameter of (**A**) 125 nm, (**B**) 255 nm, (**C**) 600 nm and (**D**) Commercial sand particles of about 2 µm.....102

Figure 3-17: XRD patterns of the composites obtained from magnesiothermic reduction of various silica precursors.....103

Figure 3-18: (**A**) SEM image of the cross-section of the borosilicate glass after heating it with 2.5 µm Mg on it. (**B**) Elemental composition at different depths for film shown in (**A**).....104

Figure 3-19: Secondary electron SEM images of Si-NCs formed at (**A**) 500 ^{o}C, (**B**) 600 ^{o}C, (**C**) 700 ^{o}C, and (**D**) 800 ^{o}C. The scale bar is 1 µm.....105

Figure 3-20: Secondary electron SEM images of silica aerogel (**A**) before reduction and (**B**) after reduction. Bright field TEM images of commercial MCM-41 (**C**) before reduction and (**D**) after reduction.....106

Figure 3-21: TEM images of Si products after etching and originally obtained by reducing (**A**) Stöber silica particles, (**B**) MCM-41, and (**C**) silica aerogel.....107

Figure 3-22: Si-NCs functionalized with dodecylamine (blue), TOPO (yellow) and dodecyl (red), under UV-illumination.....108

Figure 4-1: SEM images of TEOS derived Stöber silica particles.....119

Figure 4-2: (**A**) XRD pattern and (**B**) appearance under ambient (left) and UV (right) illumination of the crude reaction product after HCl extraction.....120

Figure 4-3: XRD patterns of reaction product mixtures obtained by thermally processing SiO_2, Mg and urea mixture at the indicated temperatures.....121

Figure 4-4: Thermogravimetric analysis (TGA) of crude Si_3N_4 NCs in air at a heating rate of 18 ^{o}C/min.....122

Figure 4-5: (**A**) HRTEM and (**B**) inverse Fourier transformed HRTEM image of freestanding β-Si_3N_4 NCs.....123

Figure 4-6: FTIR spectrum of freestanding β-Si_3N_4 NCs obtained by drop casting toluene suspension of the NCs on silicon wafer.....124

Figure 4-7: HR XP spectra of Si 2p and N 1s region of β-Si_3N_4 NCs. For clarity only $2p_{3/2}$ peaks are shown (Red - fitted line).....125

Figure 4-8: (**A**) Absorbance and (**B**) PL spectra of freestanding β-Si_3N_4 NCs.....126

Figure 4-9: Bright-field transmission electron microscopy (TEM) images of (**A**) 30.6 ± 2.2 nm (**B**) 66.8 ± 5.7 nm and (**C**) 213.8 ± 5.4 nm silica nanoparticles.....131

Figure 4-10: Scanning electron microscopy (SEM) images of β-SiC NCs with diameters of (**A**) 51.3 ± 5.5 nm, (**B**) 92.8 ± 6.6 nm, (**C**) 278.3 ± 8.2 nm, (**D**) High resolution transmission electron micrograph (HRTEM) image of β-SiC NC, (**E**) Fourier transformed image of (D) showing lattice spacing, and (**F**) Selected area electron diffraction (SAED) pattern of β-SiC NCs.....132

Figure 4-11: Representative high-resolution X-Ray photoelectron spectra of (**A**) Si 2p and (**B**) C 1s regions of *β*-SiC particles. (**C**) FTIR spectrum of *β*-SiC particles obtained from preparing KBr pellet.....133

Figure 4-12: SEM images of silica (**A**) rods and (**B**) fibers.....134

Figure 4-13: SEM images of SiC (**A**) Rods (length = 1.5 ± 0.2 µm, diameter = 0.20 ± 0.05 µm), (**B**) Fibers (length > 10 µm, diameter = 0.18 ± 0.04 µm) and (**C**) Fibers (length > 25 µm, diameter = 0.050 ± 0.001 µm).....135

Figure 4-14: XRD pattern of various different *β*-SiC morphologies.....135

Figure 4-15: XRD pattern of the reaction product obtained from SiO_2, Mg and C mixture at various temperatures XRD pattern of the reaction product obtained from SiO_2, Mg and C mixture at various temperatures.....136

Figure 5-1: X-ray powder diffraction pattern of Si NCs embedded in silica.....155

Figure 5-2: FT-IR spectrum of hydride terminated Si NCs obtained by drop coating on Si wafer from a toluene suspension.....156

Figure 5-3: (A) PL spectrum of H-Si NCs (excitation λ = 300 nm). Inset Photograph of toluene suspension of H-Si NCs. (B) Excited state lifetimes.....157

Figure 5-4: Bright field TEM image of H-Si NCs.....157

Figure 5-5: FT-IR spectrum of Si NC-A drop-coated from a toluene solution.....158

Figure 5-6: X-ray photoelectron spectra (XPS) of dodecyl surface functionalized Si NCs (Si NC-A). (**A**) Survey spectrum showing emissions arising from Si, C and O. (**B**) High resolution XP analysis of the silicon 2p spectral region. For clarity, only Si $2p_{3/2}$ emissions are shown.....159

Figure 5-7: (**A**) PL spectra of Si NC-A excited at indicated wavelengths. (**B**) Excited state lifetimes. (**C**) Toluene dispersions of dodecyl terminated Si NCs under ambient (left) and UV irradiation (right).....160

Figure 5-8: (**A**) Bright field TEM image of Si NC-A. (**B**) High-resolution transmission electron micrograph showing fringes of 0.33 nm characteristic of the Si {111} lattice spacing. (**C**) The inverse Fourier transform of the HRTEM image in **B**.....160

Figure 5-9: FTIR spectrum of Si NC-B.....161

Figure 5-10: (**A**) Bright-field TEM image of Si NC-B. (**B**) HRTEM image showing lattice spacings of 0.32 nm characteristic of the {111} plane of Si.....162

Figure 5-11: Excitation wavelength dependant PL spectra of Si NC-B in toluene.....162

Figure 5-12: High-resolution X-ray photoelectron spectra (XPS) of the (**A**) N 1s and (**B**) Si 2p spectral regions of Si NC-B. Only Si $2p_{2/3}$ fitting peaks are shown. Si $2p_{1/2}$ components have been omitted for clarity.....163

Figure 5-13: FT-IR spectrum of Si NC-C.....164

Figure 5-14: Excitation wavelength dependent PL spectra of Si NC-C obtained in toluene.....165

Figure 5-15: (**A**) Bright-field TEM image of Si NC-C. (**B**) HRTEM image showing fringes of 0.192 nm characteristic of the Si {220} lattice spacing.....165

Figure 5-16: High resolution XP spectra of the (**A**) N 1s and (**B**) Si 2p spectral regions of Si NC-C.....166

Figure 5-17: HR XP spectrum of (**A**) N 1s region and (**B**) Si 2p region of H-Si NCs reacted with TOAB. For clarity only Si $2p_{3/2}$ peaks are shown.....169

Figure 5-18: (**A**) Excitation wavelength dependent PL spectra, (**B**) Excited state lifetimes of H-Si NCs reacted with TOAB.....169

Figure 5-19: Bright field TEM image of H-Si NCs reacted with TOAB. The average particle size = 3.6 ± 0.8 nm.....170

Figure 5-20: Photograph of H-Si NCs under UV illumination that have been reacted with increasing amount of TOAB.....171

Figure 5-21: (**A**) Excitation wavelength dependent PL spectra, (**B**) Excited state lifetimes of H-Si NCs reacted with NH_4Br.....171

Figure 5-22: Bright field TEM image of H-Si NCs reacted with NH_4Br.....172

Figure 5-23: Photograph of H-Si NCs under UV illumination that have been reacted with increasing amount of NH_4Br.....172

Figure 5-24: HR XP spectrum of (A) N1s region and (B) Si 2p region of H-Si NCs reacted with NH_4Br. Only Si $2p_{3/2}$ peaks are shown for clarity.....173

Figure 5-25: PL intensity at 420 nm vs. nitrogen concentration for H-Si NCs reacted with (A) TOAB and (B) NH_4Br.....174

Figure 5-26: PL maximum vs. solvent polarity for different Si NCs. P = pentane, CH = cyclohexane, T = toluene, B = benzene and C = chloroform. The Si NC concentration was 1 mg/mL and the excitation wavelength was 300 nm.....176

Figure 5-27: Effect of ligand-induced surface doping on Si-NCs. Two tunneling spectra measured on (A) NH_4Br capped 3 nm Si NCs presented in the inset and (B) allylamine functionalized Si NCs shown in the inset.....178

Figure 6-1: FT-IR spectrum of dodecyl functionalized Si-NCs under inert atmosphere.....195

Figure 6-2: (**A**) Bright field TEM image of dodecyl Si-NCs functionalized under inert atmosphere. (**B**) Particle size distribution.....196

Figure 6-3: PL spectrum of dodecyl Si-NCs functionalized under inert atmosphere (λ_{ex} = 350 nm).....197

Figure 6-4: FT-IR spectrum of dodecyl Si-NCs functionalized in air.....198

Figure 6-5: High resolution XP spectrum of Si 2p region for dodecyl Si-NCs functionalized in air. For clarity only Si $2p_{3/2}$ peaks are shown.....199

Figure 6-6: (**A**) Bright field TEM image of dodecyl Si-NCs functionalized in air. (**B**) Particle size distribution.....199

Figure 6-7: (**A**) PL spectrum of dodecyl Si-NCs functionalized in air (λ_{ex} = 350 nm). (**B**) Long-lived excited state lifetime of dodecyl Si-NCs with τ = 40 μs. (**C**) Short-lived excited state lifetimes of dodecyl Si-NCs with τ = 5 ns. Red line corresponds to the fitted data.....200

Figure 6-8: FT-IR spectra of neat TOPO and hydride terminated Si-NCs reacted with TOPO.....203

Figure 6-9: High resolution XP spectrum of Si 2p region of TOPO Si-NCs. For clarity only Si $2p_{3/2}$ peaks are shown.....203

Figure 6-10: (**A**) Bright field TEM image of TOPO Si-NCs. (**B**) Particle size distribution.....204

Figure 6-11: (**A**) PL spectrum of TOPO Si-NCs (λ_{ex} = 350 nm). (**B**) Excited state lifetime of TOPO Si-NCs.....205

Figure 6-12: Tunneling spectra measured for ~ 3 nm dodecyl and TOPO Si-NCs.....206

Figure 6-13: Tunneling spectra for 3 nm, 6 nm, and 9 nm TOPO Si-NCs.....206

Figure 6-14: Evolution of the PL spectra of 3 nm TOPO Si-NCs over one year (λ_{ex} = 350 nm). The spectra were collected for a freshly prepared sample, and then after 2, 4, 6, 8, 10 and 12 months.....207

Figure 6-15: High resolution XP spectra of Si 2p region for TOPO Si-NCs at various intervals over a year.....208

Figure 6-16: FT-IR spectra of (**A**) neat dodecylamine and (**B**) dodecylamine functionalized Si-NCs.....210

Figure 6-17: High resolution XP spectrum of (**A**) Si 2p region and (**B**) N 1s region for dodecylamine functionalized Si-NCs.....210

Figure 6-18: (**A**) Bright field TEM image of dodecylamine Si-NCs. (**B**) Particle size distribution.....211

Figure 6-19: (**A**) PL spectrum of dodecylamine Si-NCs (λ_{ex} = 350 nm). (**B**) Excited state lifetimes of dodecylamine Si-NCs with τ = 6.46 ns.....212

Figure 6-20: PL maxima of dodecylamine Si-NCs *vs.* solvent polarity index. The Si-NC concentration was 0.5 mg/mL and the excitation wavelength was 350 nm.....212

Figure 6-21: FT-IR spectra of (**A**) neat diphenylamine and (**B**) diphenylamine functionalized Si-NCs.....214

Figure 6-22: High resolution XP spectra of (A) Si 2p and (B) N 1s region of diphenylamine functionalized Si-NCs.....215

Figure 6-23: (**A**) Bright field TEM image of diphenylamine Si-NCs. (**B**) Particle size distribution.....215

Figure 6-24: PL spectrum of diphenylamine Si-NCs (λ_{ex} = 350 nm).....216

Figure 6-25: FT-IR spectra of (**A**) hydride terminated Si-NCs, (**B**) hydride Si-NCs after reacting with CO_2 for 3 hours, and (**C**) hydride Si-NCs after reacting with CO_2 for 12 hours.....218

Figure 6-26: (**A**) Bright field TEM image of acetal Si-NCs. (**B**) Particle size distribution.....218

Figure 6-27: High resolution XP spectrum of Si 2p region for acetal Si-NCs. For clarity only $2p_{3/2}$ peaks are shown.....219

Figure 6-28: (**A**) PL spectrum of acetal Si-NCs (λ_{ex} = 350 nm). (**B**) Excited state lifetimes of acetal Si-NCs.....220

Figure 6-29: PL maxima of acetal Si-NCs *vs.* solvent polarity index. The Si-NC concentration was 0.4 mg/mL and the excitation wavelength was 350 nm.....220

Figure 6-30: PL spectrum of oxide coated Si-NCs obtained from reacting hydride terminated Si-NCs with CO_2 for 12 hours.....221

Figure 6-31: SEM image of the precipitate obtained from reacting hydride terminated Si-NCs with CO_2 for 12 hours.....222

Figure 6-32: Photograph of ~ 3 nm Si-NCs functionalized with various surface groups, under UV illumination.....223

Figure 7-1: Fluorescent microscopy image of MCF-7 cells incubated with mannose functionalized Si-NCs.....235

Figure 7-2: Images of dodecyl functionalized Si-NC coated filter paper under a handheld UV-lamp without the presence of nitrocompound and in the presence of solutions of TNT, PETN, and RDX, respectively.....236

List of Schemes

Scheme 1-1: Schematic representation of solution-phase syntheses of alkyl terminated Si-NCs from the decomposition of Zintl phases.....10

Scheme 1-2: Schematic representation of solution phase synthesis of alkyl terminated Si-NCs *via* reduction of $SiCl_4$ using sodium naphthalide.....11

Scheme 1-3: Surface derivatization of chloride terminated Si-NCs.....12

Scheme 1-4: Schematic representation of synthesis of alkyl terminated Si-NCs *via* reduction of $SiCl_4$ using hydride source.....13

Scheme 1-5: Schematic representation of synthesis of oxide embedded Si-NCs from pyrolysis of $(HSiO_{1.5})_n$ sol-gel polymer.....14

Scheme 1-6: Schematic representation of synthesis of oxide embedded Si-NCs from thermal decomposition of HSQ.....15

Scheme 1-7: Hydrolysis and condensation of silicon chloride and silicon alkoxide precursors.....18

Scheme 2-1: A summary of the influence of 'R' size on the density of the sol-gel network and requisite processing requirements to obtain Si-NCs.....40

Scheme 2-2: Acid catalyzed polymerization of $RSiCl_3$ to form an extended $RSiO_{1.5}$ network.....46

Scheme 3-1: Schematic representation of formation of various compounds during magnesiothermic reduction.....104

Scheme 4-1: Synthetic approach to freestanding β- Si_3N_4 NCs.....115

Scheme 5-1: Schematic representation of the experimental approach to forming blue-emitting Si NCs from exposure of H-Si NCs to common nitrogen sources (RNH_2, NH_4Br and tetraoctylammonium bromide (TOAB)).....167

Scheme 6-1: Schematic representation of synthesis of alkyl functionalized Si-NCs in inert atmosphere.....195

Scheme 6-2: Schematic representation of alkyl functionalization of Si-NC surface in air.....197

Scheme 6-3: Reactivity of hydride terminated Si-NCs with excess TOPO.....201

Scheme 6-4: Schematic representation of reactivity of Si hydride surface with TOPO.....202

Scheme 6-5: Schematic representation of synthesis of dodecylamine functionalized Si-NCs.....209

Scheme 6-6: Schematic representation of synthesis of diphenylamine functionalized Si-NCs.....213

Scheme 6-7: Reaction of hydride terminated Si-NCs with CO_2.....217

Scheme 7-1: Schematic representation of surface functionalization of Si-NC with mannose and amino acid groups.....235

Scheme 7-2: Various blue-emitting Si-NCs derived from chloride terminated Si-NCs.....238

List of Symbols, Nomenclature, and Abbreviations.

ħ:	Reduced Planck constant ($h/2\pi$)
λ:	Wavelength
^{o}C:	Degrees Celsius
Å:	Angstrom (10^{-10} m)
ACSES:	Alberta Centre for Surface Science and Engineering
AFM:	Atomic force microscopy
AlGaN:	Aluminum gallium nitride
au:	Arbitrary units
BE:	Binding energy
CB:	Conduction band
CCD:	Charge-coupled device
CdS:	Cadmium sulfide
CdSe:	Cadmium selenide
CdTe:	Cadmium telluride
CRSM:	Carbon-rich silica matrix
$CuInGaSe_2$:	Copper indium gallium selenide

Cu_2O:	Copper oxide
CVD:	Chemical vapor deposition
DI:	Deionized
DOS:	Density of states
e:	Charge of an electron (1.602×10^{-19} C)
e^-:	Electron
EDX:	Energy dispersive X-ray spectroscopy
E_g:	Band gap energy
FFT:	Fast Fourier transform
FOx:	Flowable oxide
FTIR:	Fourier transform infrared spectroscopy
FWHM:	Full-width at half maximum
g:	Gram
GaAs:	Gallium arsenide
h^+:	Hole
hr(s):	Hour(s)
HR-TEM:	High-resolution transmission electron microscopy

HSQ:	Hydrogen silsesquioxane
InAs:	Indium arsenide
InP:	Indium phosphide
IR:	Infrared
K:	Degrees Kelvin
K:	Shape factor
LED:	Light-emitting diode
MBE:	Molecular beam epitaxy
MIBK:	Methyl isobutyl ketone
min(s):	Minute(s)
MO:	Molecular orbital
n:	Number
NC:	Nanocrystal
nm:	Nanometer
PbS:	Lead sulfide
PbSe:	Lead selenide
PL:	Photoluminescence

p-Si:	Porous silicon
QD:	Quantum dot
QY:	Quantum yield
SAED:	Selected-area electron diffraction
SEM:	Scanning electron microscopy
SiC-NCs:	Silicon carbide nanocrystals
Si-NCs:	Silicon nanocrystals
SnO_2:	Tin oxide
SnS:	Tin sulfide
SnSe:	Tin selenide
SRO:	Silicon-rich oxide
STM:	Scanning tunnelling microscopy
T:	Temperature
TEM:	Transmission electron microscopy
TGA:	Thermogravimetric analysis
TiO_2:	Titanium oxide
TOPO:	Tri-*n*-octyl phosphine oxide

UV:	Ultraviolet
UV-vis:	Ultraviolet-visible (spectroscopy)
VB:	Valence band
XP:	X-ray photoelectron
XPS:	X-ray photoelectron spectroscopy
XRD:	X-ray diffraction
ZnS:	Zinc sulfide
ZnSe:	Zinc selenide

Chapter 1:

Introduction

1.1 Inorganic Semiconductor Nanocrystals – Quantum Dots

Nanomaterials have gained tremendous attention since the revolutionary discovery of fullerenes[1] and colloidal nanoparticles.[2-9] Their discovery has led to a major paradigm shift and made many in the scientific community rethink material classification solely based upon properties observed in bulk systems. The dimensions (i.e., size and shape) of materials are crucial in determining their properties, and today nanotechnology has become one of the fastest growing scientific and investment sectors.[10]

Health Canada defines nanomaterials as - "*any manufactured substance or product and any component material, ingredient, device or structure that is: (a) within the nanoscale (1-100nm) in at least one external dimension or has internal or surface structure at nanoscale; or (b) it is smaller or larger than the nanoscale in all dimensions and exhibits one or more nanoscale properties/phenomena*."[11] Some of the most widely explored material geometries include: zero- (*e.g.* nanoparticles), one- (*e.g.* nanowires), and two- (*e.g.* nanosheets) dimensional configurations.[12] Many interesting size and shape dependent electrical,[13-16] optical,[17-19] thermal,[20-23] magnetic,[24-26] and mechanical[27] properties emerge when materials are prepared in the nanoscale regime. The discovery of semiconductor colloidal quantum dots by Louis Brus[28,29] and his team at Bell Laboratories in the 1980s led to an exponential growth in both experimental and theoretical sciences to understand the structure and properties of these materials.

Quantum dots, well-known for their exquisitely tunable optical properties, are zero-dimensional semiconductor nanomaterials where the size of the particle is on the order of or smaller than the Bohr exciton (electron-hole pair) radius.[30] The most well known quantum dots are composed of group III-V (*e.g.*, GaAs, InAs, InP, *etc*.)[31] and II-VI (*e.g.*, CdSe, CdTe, CdS, ZnSe, ZnS, *etc*.)[32-36] elements. Today, group IV (*e.g.*, Si, Ge, SiC, *etc*.),[37-39] group IV-VI (*e.g.*, SnS, PbTe, PbS, *etc*.),[40-43] doped oxide (*e.g.*, TiO_2, Cu_2O, SnO_2, *etc*.),[44-47] and alloy (*e.g.*, AlGaN, $CuInGaSe_2$, *etc*.)[48-52] based quantum dots are also being investigated.

Potential quantum dot applications are vast and encompass photovoltaics,[53] sensors,[54,55] bioimaging,[56,57] drug delivery,[58,59] and lasers,[60] among others.[61] However, in light of the toxicity of many elements used in QDs (*e.g.*, cadmium, lead, selenium, and mercury)[62,63] as well as depleting concentrations of indium and gallium,[64] there has been a concerted effort to develop alternative quantum dot materials among the scientific community.

1.2 Silicon Nanocrystals (Si-NCs).

Silicon (Si) has many advantages over other semiconductor materials, including low cost, bio-compatibility, abundance, and compatibility with the existing electronics industry.[38] Indeed, many technological advances over the last few decades have been made possible by Si. While bulk Si has dominated the microelectronics industry for over a century, it does not exhibit photoluminescence (PL) and hence has few optical applications. It was only twenty years ago, with the

discovery of porous Si (*p*-Si) by Canham,[65] that its application was extended to opto-electronic devices.[64] The excitement generated by the possibility of using nanostructured Si as an optical material is reflected in over 6000 publications (found by Scifinder) mentioning "silicon nanocrystals" in the article title as of December 2013. Today both *p*-Si and free standing Si-NCs are being investigated for bioimaging, in photovoltaic devices, Li-ion batteries, photoelectrodes, sensors, *etc*.[66-73] Si-NCs show great promise to be a viable replacement for traditional binary compound quantum dots.

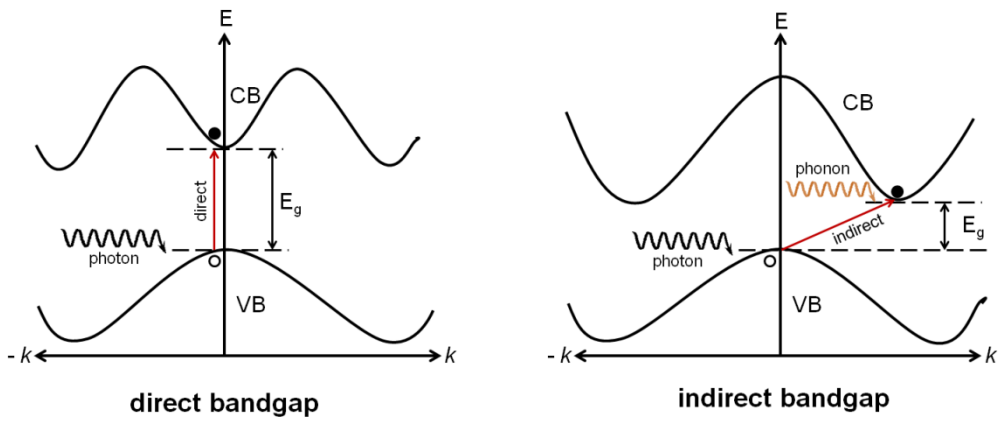

Figure 1-1. Schematic band structure showing a direct and indirect band gap.[75]

In a silicon crystal, continuous conduction (CB) and valence bands (VB) form that are separated by forbidden energy levels that are termed the band gap (E_g). For bulk Si, the energy difference between the highest point in the VB and the lowest point in the CB (i.e., band gap) is 1.13 eV at 300 K and 1.17 eV at 0 K.[74]

The density of states (DOS) is not uniform along the width of the band and is most dense at the center. Si has an indirect band gap because the maximum of the valence band and the minimum of the conduction band are not located at the same position in *k*-space (**Figure 1-1**).[75] As a result, vertical promotion/relaxation of electrons across the band gap is symmetry disallowed. A transition is only feasible when the momentum of the electron being promoted can be changed – this is made possible through lattice vibrations (*i.e.*, phonon). The probability of a so-called phonon-assisted transition is low and therefore the PL yield of bulk Si is near zero at room temperature.

When the size of a Si crystal decreases to the order of (or smaller than) the Bohr exciton radius (in Si ca. 4.5 nm), quantum confinement effects play an important role and influence material properties. Under these conditions the excitons become spatially localized within the volume of the nanocrystal. When the excitons are confined in real space, it follows from Heisenberg's uncertainty principle that their position in *k*-space is blurred. This results in broadening of the exciton wave function, which can now partially overlap even in an indirect band gap material (**Figure 1-2**).[76] These factors lead to an increase in the probability of a radiative recombination of the exciton, thus rendering nanostructured Si luminescent. While this discussion provides an explanation for the unexpected photoluminescent properties of nano-Si, its origin is complicated and remains the subject of intense investigation (*vide infra*).

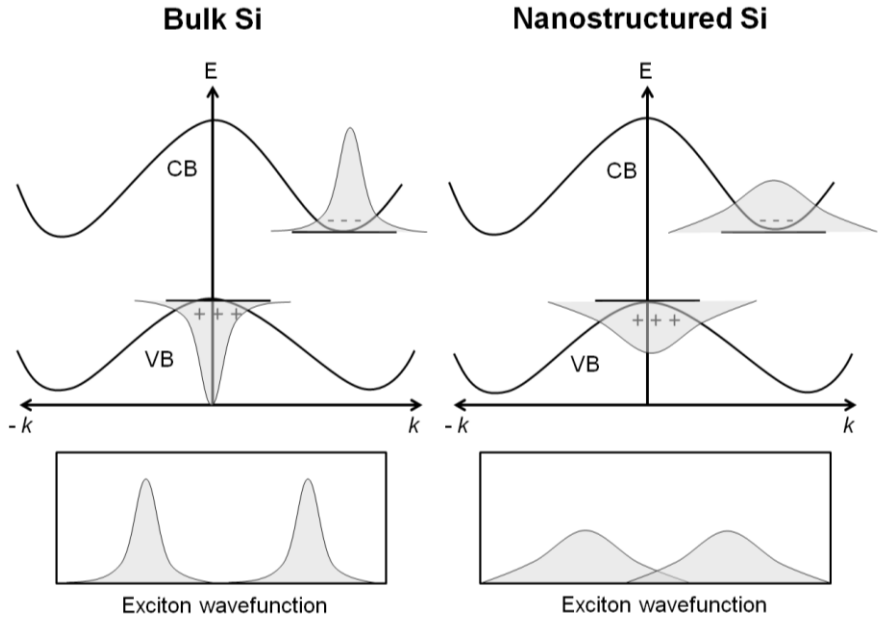

Figure 1-2. Schematic representation of wave function broadening in Si-NCs.[76]

1.3 Synthetic Methods for Preparing Si-NCs.

The story of Si-NCs began with the accidental discovery of *p*-Si in 1956 by Arthur Uhlir and Ingeborg Uhlir.[77] However, it was not until the 1990s that Leigh Canham popularized *p*-Si by effectively demonstrating its luminescent properties.[78] *p*-Si is typically prepared by anodic etching of single crystal Si wafers in hydrofluoric (HF) acid solution.[79] This etching results in a sponge-like structure where the hydride terminated Si-NCs (4 - 8 nm) are interconnected with each other (**Figure 1-3**). Free-standing Si-NCs can be obtained from *p*-Si by subjecting the wafer to ultrasonication; however, Si-NCs are prone to severe oxidation.[80-82]

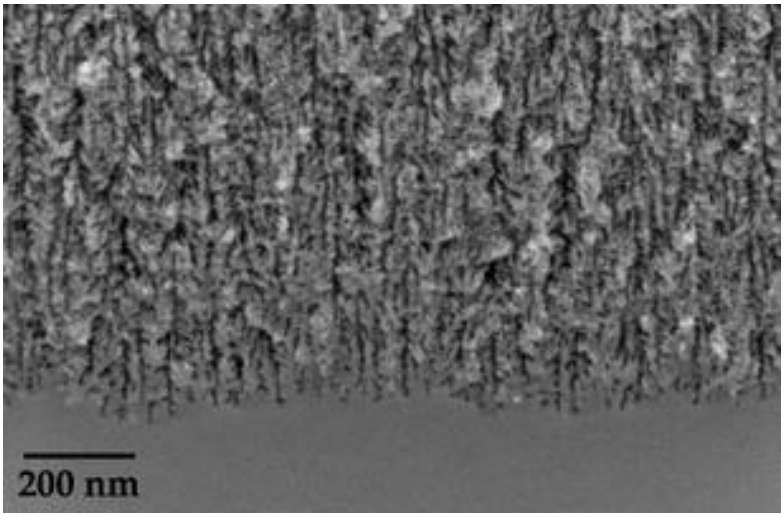

Figure 1-3. Scanning electron micrograph (SEM) image of *p*-Si. (Image taken from *Lab Chip*, 2009, **9**, 456. Reproduced by the permission of The Royal Society of Chemistry).

Since the synthesis of *p*-Si, oxide embedded Si-NCs have been prepared by precipitation of excess Si from non-stoichiometric $SiO_{x<2}$ films *via* sputtering.[83,84] Other physical methods such as ion implantation,[85-88] vapor deposition,[89,90] and laser ablation[90,91] have been used to synthesize Si-NCs as well. In the interest of work presented in this thesis, key gas-, solution-, and solid-phase methods are discussed in further detail below.

1.3.1 Gas-phase methods.

Synthesis of Si-NCs using gas phase methods frequently involves pyrolysis of silane (SiH_4) gas using a LASER or cold plasma.[92-95] Pyrolysis of silane gas affords gram-scale quantities of high purity loosely agglomerated Si nanoparticles

of varying sizes at a rate of 20 - 200 mg/h. The NCs are size separated and collected on a substrate as shown in **Figure 1-4**.

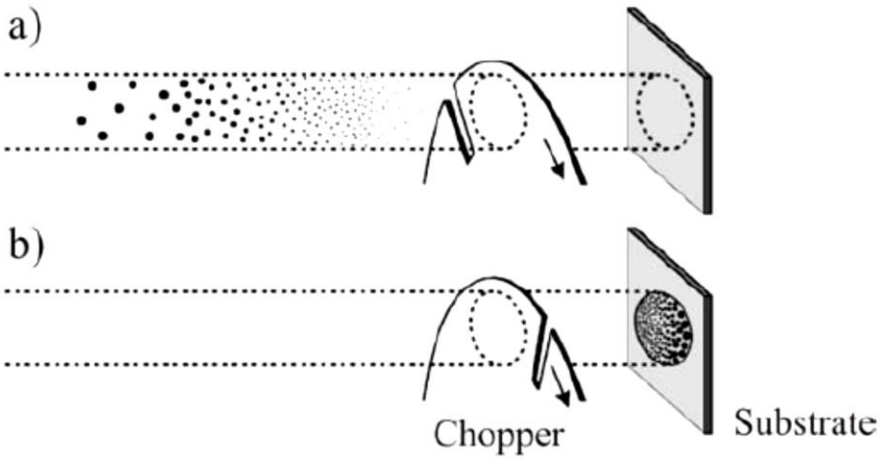

Figure 1-4. Schematic representation of size separation of Si-NCs prepared *via* SiH_4 decomposition. (**A**) Particles of different sizes move at different velocities, and can be (**B**) separated and deposited at different places on a substrate after passing through a rotating chopper slit. (Reprinted with the permission from *Appl. Phys. Lett*. 2002, **80**, 4834. Copyright 2002, AIP Publishing LLC).

After the synthesis, the particles are commonly subjected to solution phase surface functionalization *via* hydrosilylation. Freestanding NCs are obtained by etching the Si powder with a nitric acid and hydrofluoric acid (HNO_3/HF) mixture. This procedure affords control over the NC size and provides hydride terminated Si-NCs that can be further hydrosilylated with alkenes or alkynes. Complete visible

spectrum emission has been reported for Si-NCs made *via* pyrolysis of silane (**Figure 1-5**).

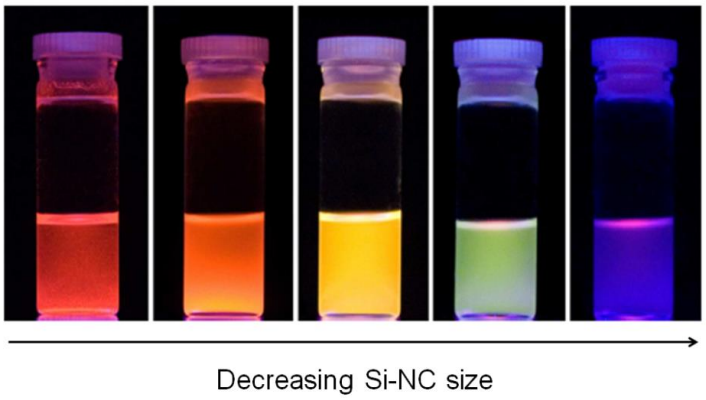

Figure 1-5. Photograph of Si-NCs of varying sizes under UV-illumination prepared from pyrolysis of silane gas using plasma. (Image from *Nanotech.*, 2008, **19**, 245603. Copyright IOP Publishing).

1.3.2 Solution-phase methods.

Solution phase syntheses offer a low-temperature route toward synthesizing Si-NCs. NCs can be prepared *via* oxidative and reductive methods. The most commonly used oxidative method involves reaction of Zintl salts such as magnesium or sodium silicide with ammonium bromide to yield hydride terminated Si-NCs (**Scheme 1-1**).[97-99] These NCs are further functionalized with alkyl protecting groups to prevent oxidation. Zintl salts can also be reacted with other oxidizing agents such as $SiCl_4$ and Br_2 to yield halide terminated Si-NCs.[100]

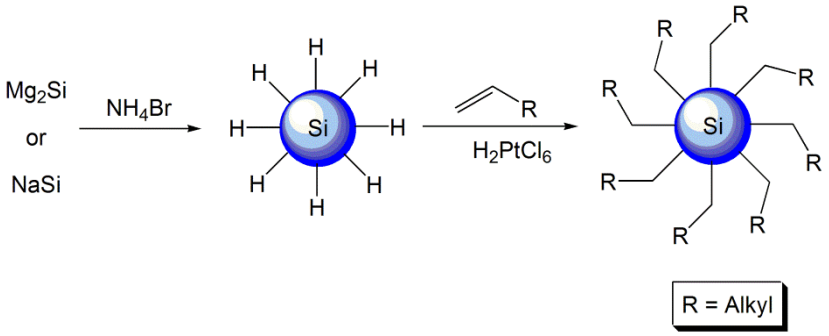

Scheme 1-1. Schematic representation of solution-phase syntheses of alkyl terminated Si-NCs from the decomposition of Zintl phases.

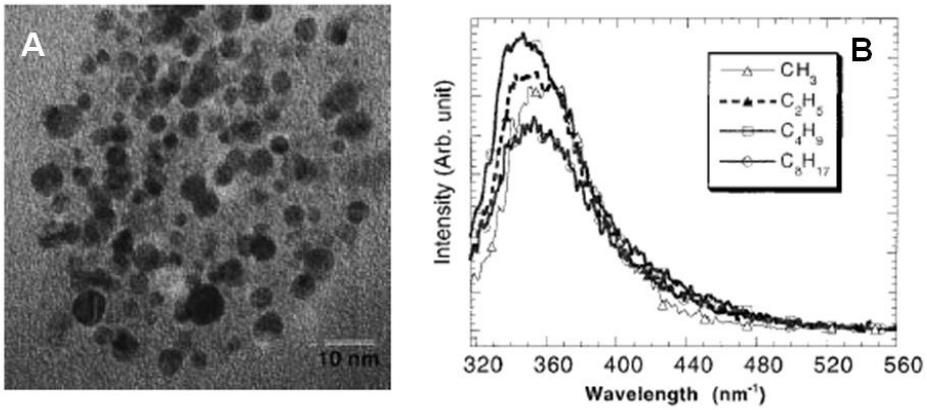

Figure 1-6. (**A**) Bright field TEM image and (**B**) PL spectra of alkyl terminated Si-NCs synthesized by decomposition of Zintl phases. (Reprinted with the permission from *J. Am. Chem. Soc*. 1999, **121**, 5191. Copyright 1999 American Chemical Society).

Si-NCs obtained using this method are typically polydisperse with sizes ranging from 2 - 10 nm. They also exhibit blue PL with short-lived excited states (ca. 5 ns) that are independent of the particle size (**Figure 1-6**).

The most common solution phase reductive methods involve reaction of silicon tetrachloride ($SiCl_4$) with either sodium metal or sodium naphthalide to yield chloride terminated Si-NCs.[101-104] These NCs are further functionalized *in situ* by reacting the particles with alkyl lithium or Grignard reagents (**Scheme 1-2**).

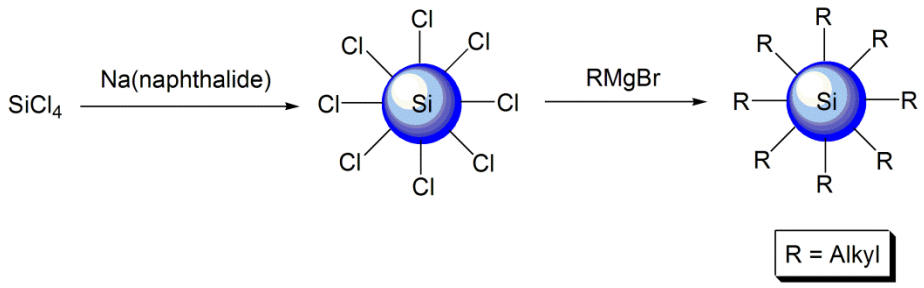

Scheme 1-2. Schematic representation of solution phase synthesis of alkyl terminated Si-NCs *via* reduction of $SiCl_4$ using sodium naphthalide.

The Si-NCs prepared using these methods exhibit diameters in the range of 2 - 5 nm and emit blue light (**Figure 1-7**). The intermediate chloride terminated Si-NCs have also been functionalized with alkoxy, siloxane, hydroxyl, and hydride functional groups (**Scheme 1-3**).[102] All chloride derived Si-NCs emit in the blue spectral region irrespective of particle size or the protecting group.

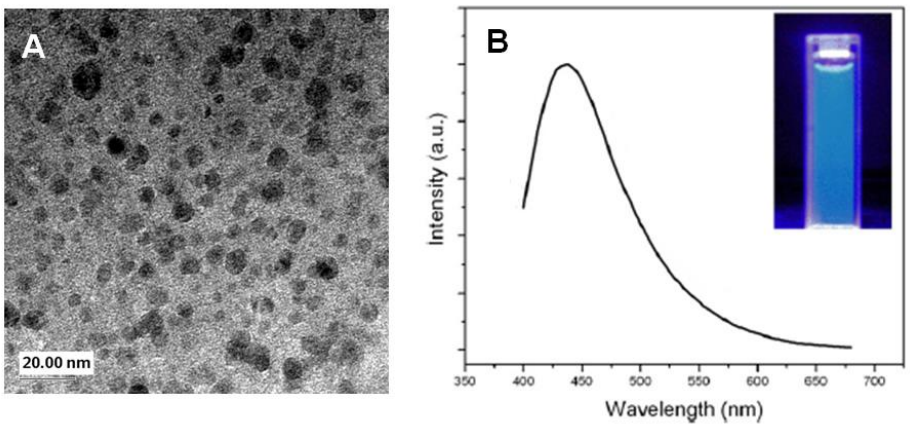

Figure 1-7. (**A**) Bright field TEM image and (**B**) PL spectra of octyl terminated Si-NCs synthesized from reduction of $SiCl_4$. (Image from *Chem. Commun*., 2002, 1822. Reproduced by the permission of The Royal Society of Chemistry).

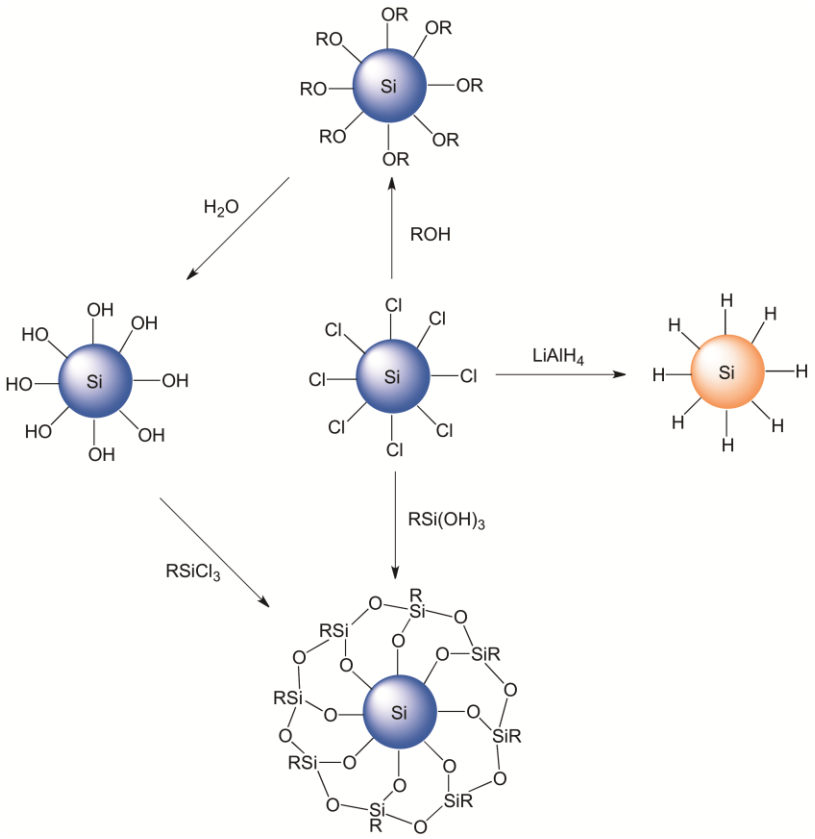

Scheme 1-3. Surface derivatization of chloride terminated Si-NCs.

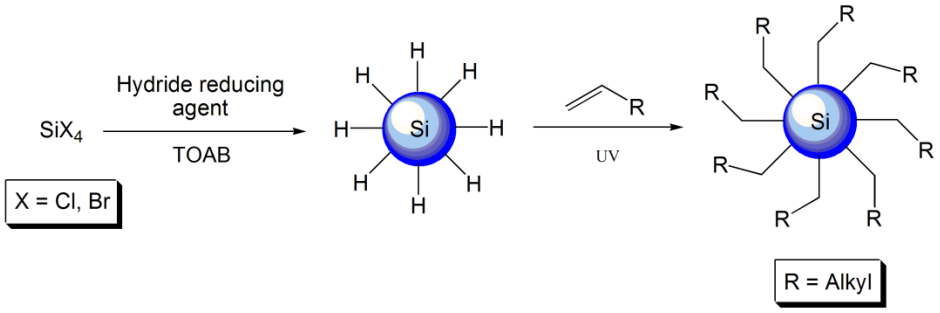

Scheme 1-4. Schematic representation of the synthesis of alkyl terminated Si-NCs *via* reduction of $SiCl_4$ using a hydride source.

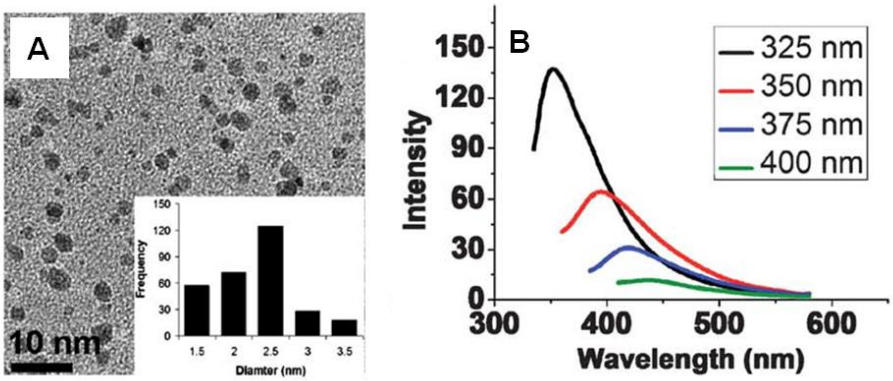

Figure 1-8. (**A**) Bright field TEM image and (**B**) excitation wavelength dependent PL spectra of hexyl terminated Si-NCs prepared *via* reduction of $SiCl_4$ using a hydride source. (Image from *Nanoscale*, 2011, **3**, 3364. Reproduced with the permission of The Royal Society of Chemistry).

Alternatively, silicon halides can be reduced with a hydride reducing agent such as lithium borohydride, super hydride, and lithium aluminum hydride to yield hydride terminated Si-NCs.[105,106] These NCs are functionalized *in situ* with alkyl

protecting groups *via* photochemical hydrosilylation (**Scheme 1-4**). The particles are 2 - 3 nm in size and emit blue with short-lived (~ 3 - 4 ns) excited states regardless of particle size (**Figure 1-8**).

1.3.3 Solid-state methods.

One of the most common solid-state methods of preparing Si-NCs is *via* pyrolysis of Si-rich sol-gel derived polymers. $(HSiO_{1.5})_n$ sol-gel polymers are prepared from hydrolysis and condensation of silane precursors such as $HSiCl_3$ or $HSi(OEt)_3$.[107,108] Subsequently, these polymers are thermally processed at high temperatures (>1000 ^oC) under inert or reducing conditions to yield Si-NCs embedded in an oxide matrix (**Scheme 1-5**). The mechanism of Si-NC formation in these systems has been studied in detail.[109] At temperatures between 400 - 500 ^oC the Si-rich oxide disproportionates to form Si(0) and SiO_2. Higher temperatures are required to promote diffusion of Si atoms through the silica matrix to form Si-NCs.

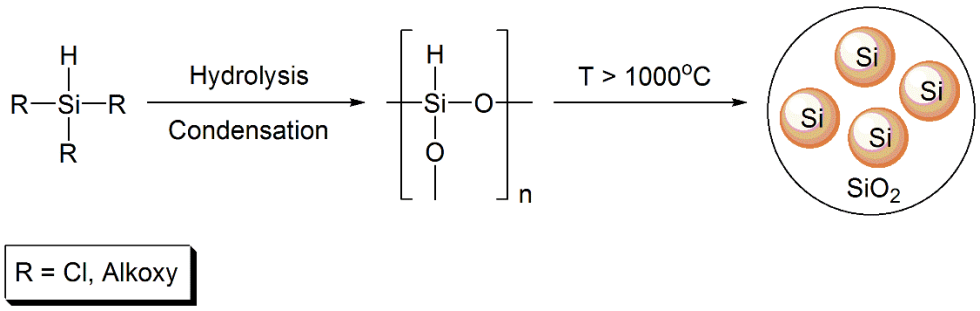

Scheme 1-5. Schematic representation of the synthesis of oxide embedded Si-NCs from pyrolysis of $(HSiO_{1.5})_n$ sol-gel polymers.

The Veinot group has developed a procedure for making size and shape controlled Si-NCs *via* disproportionation of commercially available hydrogen silsesquioxane (HSQ).[110] Similar to the sol-gel polymers, HSQ ($H_8Si_8O_{12}$) yields oxide embedded Si-NCs (ca. 3 nm in size) when heated at 1100 ^oC for an hour (**Scheme 1-6**).

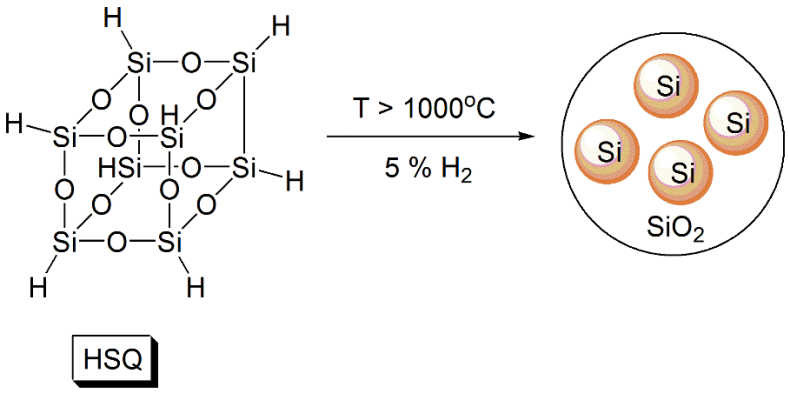

Scheme 1-6. Schematic representation of the synthesis of oxide embedded Si-NCs from thermal decomposition of HSQ.

The average Si-NC size increases to ca. 6 and ca. 9 nm when processing temperatures are increased to 1200 and 1300 ^oC, respectively (**Figure 1-9**).[111] This method allows the preparation of size mono-disperse Si-NCs on a gram-scale.

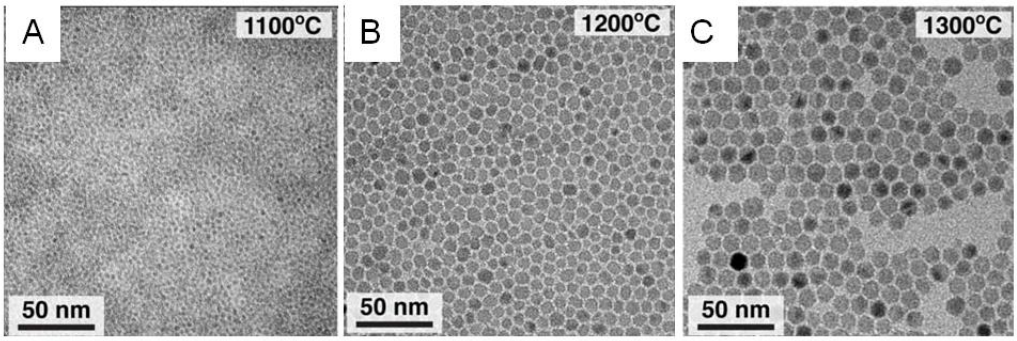

Figure 1-9. Bright field TEM images of (**A**) 3 nm, (**B**) 6 nm and (**C**) 9 nm Si-NCs obtained from thermal decomposition of HSQ at 1100, 1200, and 1300 ºC, respectively. (Reprinted with permission from *Chem. Mater*. 2011, **24**, 393. Copyrigt 2011 American Chemical Society).

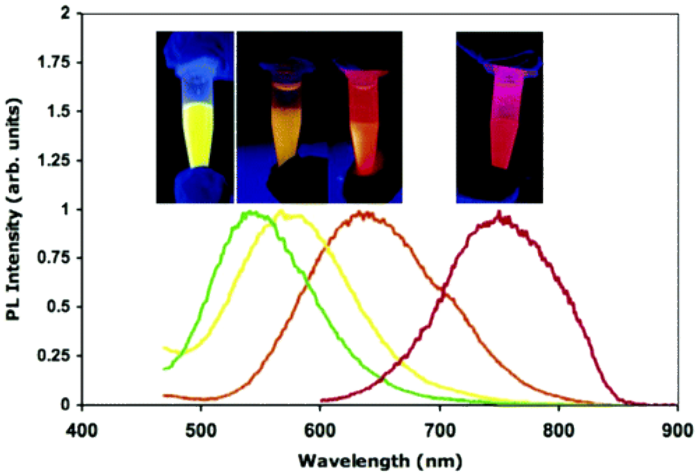

Figure 1-10. PL spectra of hydride terminated Si-NCs obtained from thermal decomposition of HSQ. Inset: Photograph of Si-NCs under UV-illumination. (Reprinted with permission from *Chem. Mater*. 2006, **18**, 6139. Copyrigt 2006 American Chemical Society).

Freestanding hydride terminated Si-NCs can be obtained by treating the oxide embedded particles with HF solutions (See Equations [**1**] and [**2**]).[110]

$$SiO_2 + 4\ HF \longrightarrow SiF_4 + 2\ H_2O \qquad [\mathbf{1}]$$

$$SiF_4 + 2\ HF \longrightarrow H_2SiF_6 \qquad [\mathbf{2}]$$

The photoluminescence from the hydride terminated Si-NCs is size dependent (**Figure 1-10**) and the particle size is controlled by the length of etching time.

Sandhage's group demonstrated the solid-state synthesis of Si microstructures *via* the magnesiothermic reduction of silica diatom frustules.[112] This method was used to make Si-NCs by reducing Stöber silica particles with Mg powder. The details of this experiment are discussed in Chapter 3 and the synthesis of Stöber silica particles is discussed in Section 1.4 (*vide infra*).

1.4 Sol-gel reactions.

Sol-gel reactions offer a versatile method of preparing a vast array of silica structures (*e.g*. films, nanostructures, polymers, *etc*.). This is possible through the rational tailoring of numerous experimental parameters such as water content, temperature, solvent, catalyst, reaction time, drying conditions, and precursor.[113] The sol-gel method can be described as the formation of an oxide network by polycondensation of molecular precursors. A sol is a stable colloidal particle and the gel is a three dimensional structure formed by agglomeration of sol.

Formation of silicates is one of the most well studied sol-gel reactions to date. They are often prepared by controlled hydrolysis and condensation of silicon halides or silicon alkoxide precursors. The chemical reaction of silica formation *via* a sol-gel process is generally catalyzed by an acid or a base. The first step of a sol-gel reaction is hydrolysis of the silicon precursor. This is followed by condensation either forming water or an alcohol (**Scheme 1-7**). Acid catalyzed reactions yield a linear polymer while a base catalyzed reaction results in a more branched final structure.[114]

At high pH (>12) conditions the condensation process occurs quickly without gelation, thus leading to the formation of stable particles. This process was discovered by Werner Stöber and today monodispersed silica particles (also known as Stöber silica) are prepared by hydrolysis and condensation of tetraethoxysilane using an ammonium hydroxide catalyst.[115]

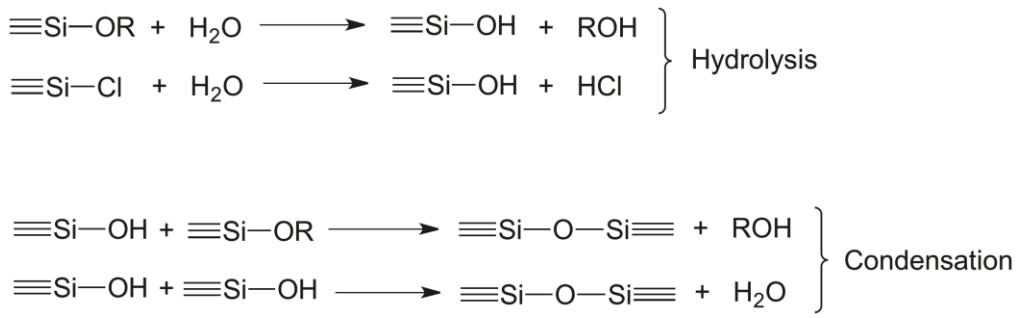

Scheme 1-7. Hydrolysis and condensation of silicon chloride and silicon alkoxide precursors.

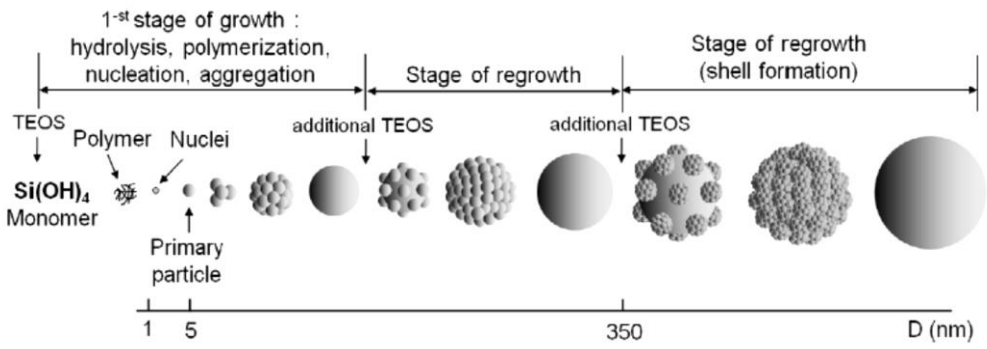

Figure 1-11. Schematic representation of Stöber silica particle formation and growth. (Image from *Nanotech*., 2011, **22**, 275718. Copyright IOP Publishing).

The mechanism for the formation of Stöber silica particles was studied by Masalov *et al*.[116] The authors propose that during the Stöber process, primary SiO_2 particles of 5 - 10 nm diameter are initially formed. These primary particles aggregate to form larger SiO_2 particles (**Figure 1-11**).

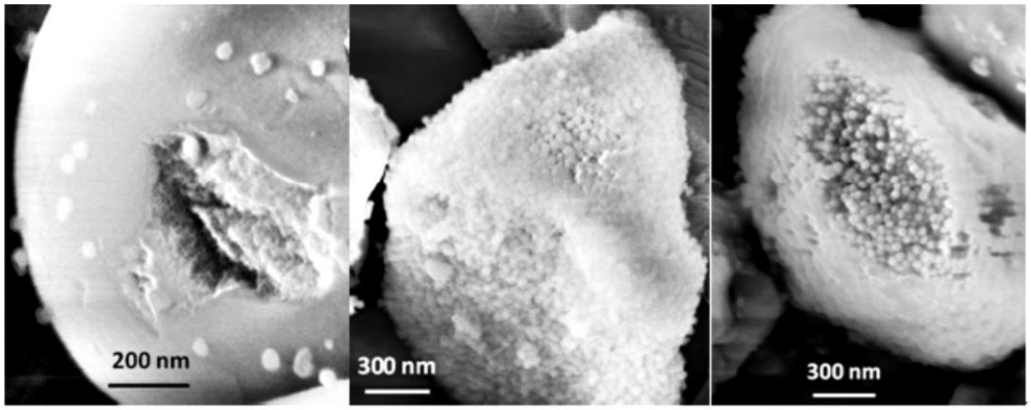

Figure 1-12. SEM images of Stöber silica particles sonicated with diamond powder (Image from *Nanotech*., 2011, **22**, 275718. Copyright IOP Publishing).

Figure 1-12 shows SEM images of diamond cut SiO_2 particles. The exterior of the particles is covered by a dense thin layer of SiO_2 and the interior is composed of smaller SiO_2 particles. The smaller particles are not densely packed and lead to meso- as well as macropore formation in Stöber particles.

1.5 Si-NC Optical Properties.

To realize the full potential of Si-NCs opto-electronic applications it is important to gain a thorough understanding of the origin of the PL in these systems. Various models have been proposed to explain its origin; however, they can be broadly classified as either quantum confined emission or defect-based emission. These models are discussed in further detail in the following sections.

1.5.1 Band gap emission (quantum confinement).

This model was originally proposed by Canham in 1990 to explain the PL originating from *p*-Si and was later extended to freestanding Si-NCs.[65] As the size of the Si crystal decreases from bulk to nanoscale, the energy levels start to become more discrete. The number of orbitals participating in band formation also decreases, leading to a "thinning" of the DOS. As the DOS is sparsest at the band-edges, the decrease in crystal size leads to the removal of energy levels from the band-edges.[17] As a result, the band gap of Si increases with decreasing crystal size (**Figure 1-13**).

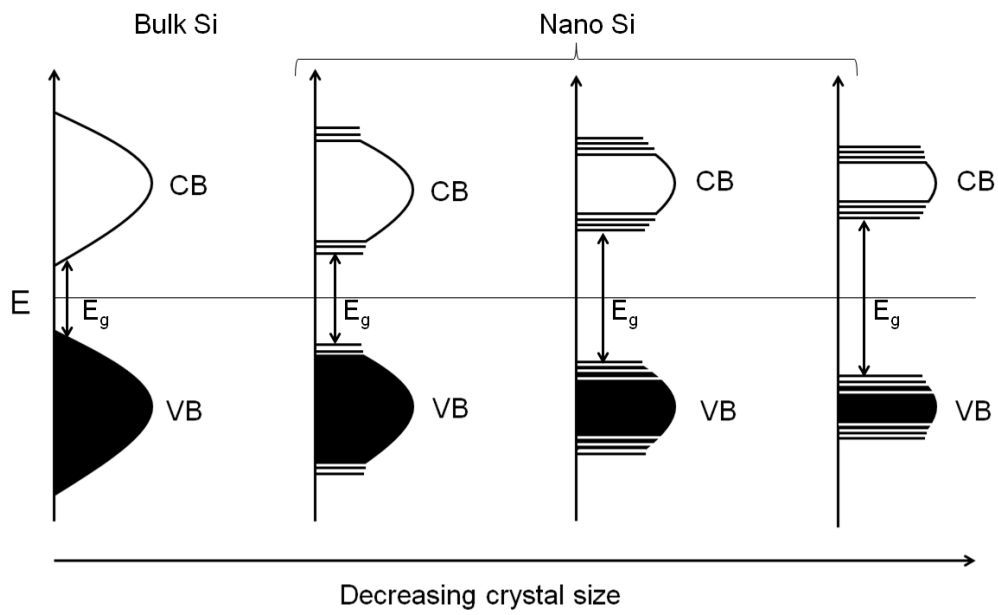

Figure 1-13. Schematic representation of change in the DOS and bandgap of Si with changing crystal size.

In the simplest, most widely employed model (also termed the effective mass approximation (EMA) model), a quantum dot is treated as a spherical quantum well. The size dependent band gap of the quantum dot is expressed according to equation [**1**],

$$E(d) = E_g + \frac{\hbar^2\pi^2}{2d^2}\left(\frac{1}{m_e^*} + \frac{1}{m_h^*}\right) - \frac{1.8\,e^2}{\varepsilon_i d} \qquad [\mathbf{1}]$$

where d is the diameter of the nanocrystal, m_e^* and m_h^* are the bulk effective masses of electron and hole, respectively, e is the charge of the electron, E_g is the bulk bandgap of Si, and ε_i is the electric permittivity of Si. The band gap is inversely proportional to the square of the diameter of the quantum dot. Band gap estimations

as a function of particle size obtained using **Equation 1** are plotted in **Figure 1-14** (solid line). Based upon the EMA model, visible PL can be expected from Si-NCs with dimensions below ca. 3 nm. This PL would result from excitation and relaxation of the electrons across the band gap of the NC.

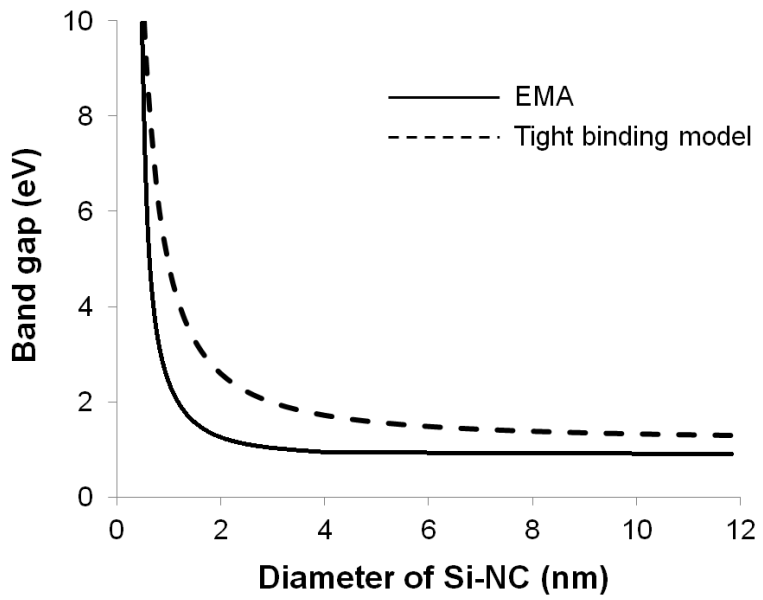

Figure 1-14. Calculated relationship between the band gap of Si-NC and the NC size based upon EMA and tight binding model predictions.

Unfortunately, the EMA does not predict experimental observations perfectly. Surface dangling bonds are often passivated with hydrogen or alkyl groups, leading to shifts in the observed PL maximum.[117-120] To account for these shifts, Delerue *et al*. proposed an inverse power law (Equation **2**) relationship between PL maximum and quantum dot diameter for surface passivated Si-NCs

based on a tight binding model (**Figure 1-5**).[121] The experimental PL maxima are in better agreement with the tight binding model than the EMA predictions.[122,123]

$$E_{PL} = E_g + 3.73\, d^{-1.39} \qquad [\mathbf{2}]$$

In both the EMA and tight binding models, Si still possesses an indirect band gap and phonon assistance is needed for a radiative transition. The excited state lifetimes of the PL resulting from transitions across the band gap are on the order of millisecond (ms) to microsecond (μs).[124]

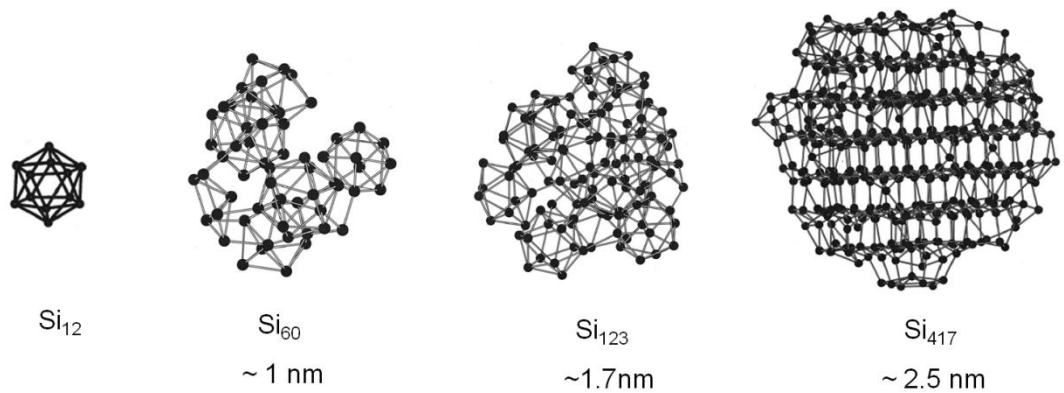

Figure 1-15. Simulated structures of various Si clusters. (Reprinted with the permission from *Phys. Rev. B* 2002, **65**, 245417. Copyright 2002 American Physical Society).

The bulk approximations cannot be applied to very small Si-NCs (ca. 2 nm) due to lack of periodicity in the Si structure lattice. Based upon theoretical

calculations (tight binding model) performed by Yu *et al*., complete symmetry breaking appears for Si-NCs between 1-2 nm (**Figure 1-15**).[125] Under these conditions there is a strong overlap of the electron and hole wave functions that leads to quasi-direct transitions with short-lived (ca. ns) excited states that approximate the properties of direct band gap materials.[126]

1.5.2 Oxide defect emission.

The impact of oxidation on Si-NC optical properties has been the subject of substantial debate for a very long time.[127-140] One of the most notable (and controversial) studies reported by Wolkin *et al*. invokes an Si=O to explain Si-NC luminescence.[141] The authors proposed that in oxidized Si-NCs, the PL properties change as a function of size and the presence of the Si=O defect state (**Figure 1-16**). For NCs larger than ca. 3 nm, the PL mechanism is dominated by the exciton recombination across the band gap (Zone I in Figure 1-17). When the NC size is between 1.5 - 3 nm, carrier recombination involves a trapped electron state and a free hole (Zone II in Figure 1-17). While there is a blue-shift in PL maximum with decreasing NC size in this region, the magnitude of the shift does not correlate with EMA predictions. For NCs with dimensions smaller than ca. 1.5 nm, the PL response is independent of particle size and is solely dominated by trapped states (Zone III in Figure 1-17). Unfortunately, the existence of Si=O bonds in Si-NCs has not been proven to date with concrete characterization details. They are proposed to exist as a stabilizing unit between an Si/SiO_2 interface. However, molecular analogues of silanones (Si=O) have been reported in the literature.[142-146]

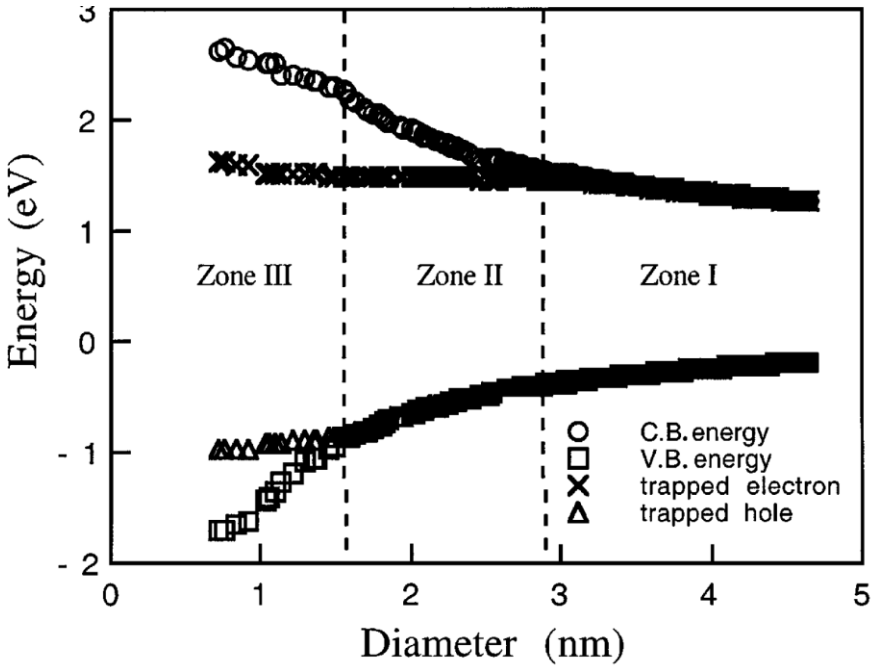

Figure 1-16. Band gap and Si=O trapped state energy in Si-NCs as a function of NC size. (Reprinted with the permission from *Phys. Rev. Lett.* 1999, **82**, 197. Copyright 2002 American Physical Society).

A surface state model has been proposed by Kanemitsu *et al*. to explain red PL (ca.1.7 eV) originating from oxidized Si-NCs or oxide-embedded Si-NCs.[147] According to this model, photon absorption occurs at the Si-NC core and the generated exciton migrates to the NC surface, where it recombines radiatively at a surface suboxide ($SiO_{x<2}$) defect. The energy of this suboxide defect state is estimated to be 1.65 eV and PL is independent of Si-NC size. However, Koch *et al*. proposed the origin of red PL is slightly more complex.[148] According to their model, quantum confinement and surface defects co-exist in a Si-NC/SiO_2 system. The photon absorption occurs in the NC core, and three different relaxation pathways

are possible (**Figure 1-17**): (1) slow transition across the band gap (E_0), (2) fast transition from NC CB band to surface state (E_1), and (3) slow surface-to-surface state transition (E_2). Smaller Si-NCs are believed to favor E_1 and E_2 transitions.

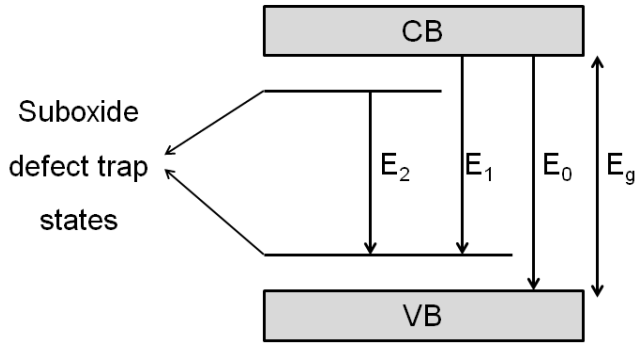

Figure 1-17. Radiative transitions according to a surface state model.[148]

The other commonly observed oxide-based emission in Si-NC/SiO_2 systems is made up of two components centered around 2.8 and 1.9 eV.[149-153] The higher energy emission is often short-lived and the orange emission has longer excited state lifetimes. It is proposed that the PL around 1.9 eV results from an isolated non-bridging oxygen atom (**Figure 1-18A**) that acts as a hole-trap center. The high energy ca. 2.7 eV PL is calculated to originate from oxygen vacant defect sites (SiO_3^+). O'Reiily and Robertson have proposed various radiative SiO_2-like defect sites that are summarized in **Figure 1-18**.[149]

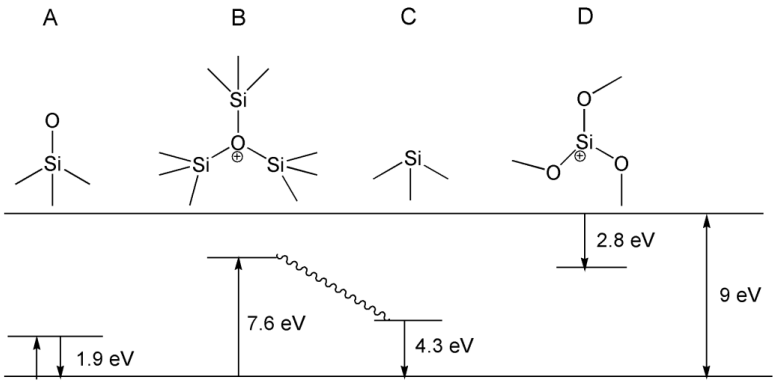

Figure 1-18. Calculated radiative centers in SiO_2-like encapsulated Si-NCs. (**A**) Excitation and relaxation at a non-bridging oxygen trap state; (**B**) excitation into an Si_3O^+ shallow state followed by its relaxation to (**C**) an Si_3^0 trap state and its radiative relaxation; and (**D**) emission from relaxation to an SiO_3^+ trap state.[149]

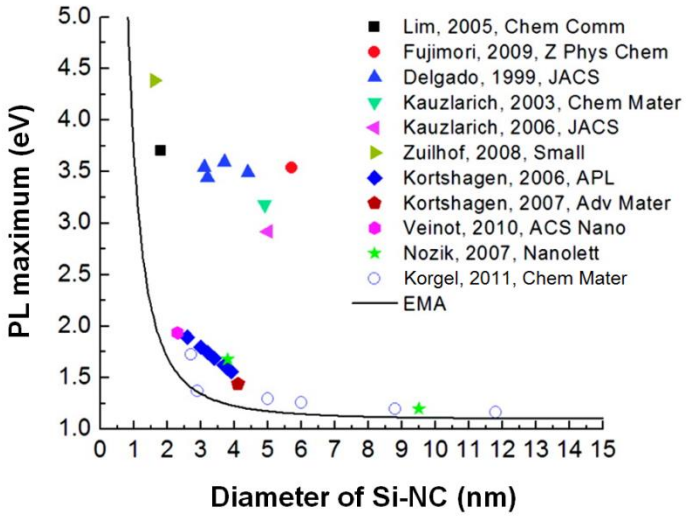

Figure 1-19. Emission peak maximum vs. Si-NC size for various literature reported alkyl passivated Si-NCs. (Reprinted with permission from *Chem. Mater*. 2011, **24**, 393. Copyrigt 2011 American Chemical Society).

Si-NCs prepared *via* solution phase methods (discussed in detail in Section 1.3.2) commonly exhibit blue luminescence irrespective of particle size, thus defying EMA approximations (**Figure 1-19**). While some authors have proposed that this PL originates from an oxide related defect, the exact chemical or physical nature of the blue emission remains unknown and is the subject of much study.

1.6 Thesis Outline.

The present thesis focuses on the syntheses and optical properties of silicon based nanomaterials. Chapter 2 concentrates on the attempts made to lower the solid-state synthesis temperature of Si-NCs prepared *via* disportionation of various $(RSiO_{1.5})_n$ sol-gel polymers. Various homo- and copolymers where R = H, C_2H_5, C_4H_9, C_6H_{13}, C_8H_{17}, $C_{10}H_{21}$, $CF_3(CH_2)_2$, $CCl_3(CH_2)_2$, and $CN(CH_2)_2$ were synthesized and their thermal decomposition was studied. Also, the influence of inorganic salts such as Na_2O, MgO, CaO, $AlCl_3$, and $MgCl_2$ on the thermal decomposition of $(HSiO_{1.5})_n$ sol-gel polymer was investigated.

Chapter 3 shifts to alternative methods for lowering processing temperatures and highlights the magnesiothermic reduction of various types of silica to form Si nano- and microstructures. Si thin films prepared *via* magnesiothermic reduction were also fabricated and evaluated as potential transparent electrodes for organic light-emitting diodes. Mechanistic studies on the Mg reduction process, the influence of reaction temperature, and precursor size and morphology are also discussed. The magnesiothermic reduction process was

extended to the preparation of silicon nitride (Si_3N_4) and silicon carbide (SiC) nano/micro structures as outlined in Chapter 4.

Chapters 5 and 6 focus on the optical properties of Si-NCs. The origin of size-independent blue luminescence in Si-NCs is investigated in Chapter 5. Chapter 6 highlights Si-NC surface modification with various surface groups to tune the PL maximum across the visible spectrum.

Finally, Chapter 7 summarizes the findings made in Chapters 2-6 and provides a brief outlook for the future application of the methodologies and materials synthesized in this thesis.

1.7 References.

1. H. W. Kroto, J. R. Heath, S. C. Obrien, R. F. Curl and R. E. Smalley, *Nature*, 1985, **318**, 162.
2. G. Frenz, *Nature Phys. Sci*., 1973, **241**, 20.
3. M. C. Daniel and D. Astruc, *Chem. Rev*., 2004, **104**, 293.
4. B. L. Cushing, V. L. Kolesnichenko and C. J. O'Connor, *Chem. Rev*., 2004, **104**, 3893.
5. Z. Lu and Y. Yin, *Chem. Soc. Rev*., 2012, **41**, 6874.
6. C. N. R. Rao, G. U. Kulakrni, P. J. Thomas and P. P. Edwards, *Chem. Soc. Rev*., 2000, **29**, 27.
7. M. A. Hayat, *Colloidal Gold: Principles, Methods and Applications, Academic Press*, 1991.
8. G. Schmid, *Chem. Rev*., 1992, **92**, 1409
9. G. Schmid, *Clusters and Colloids*, VCH, Weinheim, Germany, 1994.
10. www.nano.gov
11. www.hc-sc.gc.ca/sr-sr/pubs/nano/pol-eng.php
12. G. Cao, *Nanostructures and Nanomaterials*, Imperial College Press, London, UK, 2004.
13. A. Henglein, *J. Phys. Chem*., 1979, **83**, 2209.
14. J. Kiwi and M. Grätzel, *J. Am. Chem. Soc*., 1979, **101**, 7214.
15. A. Henglein, *Chem. Rev*., 1989, **89**, 1861.
16. A. Henglein, *Top. Curr. Chem*., 1988, **143**, 113.
17. A. P. Alivisatos, *J. Phys. Chem*., 1996, **100**, 13226.
18. K. L. Kelly, E. Coronado, L. L. Zhao and G. C. Schatz, *J. Phys. Chem*., 2003, **107**, 668.
19. S. Eustis and M. A. El-Sayed, *Chem. Soc. Rev*., 2006, **35**, 209.
20. G. Zhang and B. Li, *Nanoscale*, 2010, **2**, 1058.
21. K. Yang, S. Zhang, G. Zhang, X. Sun, S. T. Lee and Z. Liu, *Nano Lett*., 2010, **10**, 3318.
22. H. K. Moon, S. H. Lee and H. C. Choi, *ACS Nano*, 2009, **3**, 3707.

23. N. M. Iverson, P. W. Barone, M. Shandell, L. J. Trudel, S. Sen, F. Sen, V. Ivanov, E. Atolia, E. Farias, T. P. McNicholas, N. Reuel, N. M. A. Parry, G. N. Wogan and M. S. Strano, *Nat. Nanotechol*., 2013, **8**, 873.

24. S. P. Gubin, Y. A. Koksharov, G. B. Khomutov and G. Y. Yurkov, Russ. *Chem Rev*., 2005, **74**, 489.

25. A. Akbarzadeh, M. Samiei and S. Davaran, *Nano. Res. Lett*., 2012, **7**, 144.

26. A. H. Lu, E. L. Salabas and F. Schuth, *Angew. Chem. Ind. Ed*., 2007, **46**, 1222.

27. M. A. Meyers, A. Mishra and D. J. Benson, *Prog. Mater. Sci*., 2006, **51**, 427.

28. L. E. Brus, *J. Chem. Phys*., 1983, **79**, 5566.

29. L. E. Brus, *J. Chem. Phys*., 1984, **80**, 4403.

30. M. A. Reed, J. N. Rendall, R. J. Aggarwal, R. J. Matyi, T. M. Moore and A. E. Wetsel, *Phys. Rev. Lett*., 1988, **60**, 535.

31. D. K. Harris and M. G. Bawendi, *J. Am. Chem. Soc*., 2012, **134**, 20211.

32. C. B. Murray, D. J. Norris and M. G. Bawendi, *J. Am. Chem. Soc*., 1993, **115**, 8706.

33. A. P. Alivisatos, *Science*, 1996, **271**,933.

34. Z. A. Peng and X. Peng, *J. Am. Chem. Soc*., 2001, **123**, 183.

35. Y. A. Yang, H. Wu, K. R. Williams and Y. C. Cao, *Angew. Chem. Ind. Ed*., 2005, **44**, 6712.

36. N. Pradhan, D. Reifsnyder, R. Xie, J. Aldana and X. Peng, *J. Am. Chem. Soc*., 2007, **129**, 9500.

37. M. W. Dashiell, U. Denker, C. Müller, G. Costantini, C. Manzano, K. Kern and O. G. Schmidt, *Appl. Phys. Lett*., 2002, **80**, 1279.

38. J. G. C. Veinot, *Chem. Commun*., 2006, 4160.

39. J. A. Kelly, E. J. Henderson and J. G. C. Veinot, *Chem. Commun*., 2010, **46**, 8704.

40. W. K. Bae, J. Joo, L. A. Padilha, J. Won, D. C. Lee, Q. Lin, W. K. Koh, H. Luo, V. I. Klimov and J. M. Pietryga, *J. Am. Chem. Soc*., 2012, **134**, 20160.

41. Y. Xu, N. Al-Sahim, C. W. Bumby and R. D. Tilley, *J. Am. Chem. Soc*., 2009, **131**, 15990.

42. I. Moreels, K. Lambert, D. Smeets, D. D. Muynck, T. Nollet, J. C. Martins, F. Vanhaecke, A. Vantomme, C. Delerue, G. Allan and Z. Hens, *ACS Nano*, 2009, **3**, 3023.

43. M. A. Franzman, C. W. Schlenker, M. E. Thompson and R. L. Brutchey, *J. Am. Chem. Soc*., 2010, **132**, 4060.

44. L. Pan, S. Wang, J. J. Zou, Z. F. Huang, L. Wang and X. Zhang, *Chem. Commun*., 2013, DOI: 10.1039/C3CC47752E.

45. E. Knozinger, A. Kellersohn, W. Langel and M. Giersig, *Adv. Mater*., 1995, **7**, 652.

46. D. Dutta and D. Bahadur, *J. Mater. Chem*., 2012, **22**, 24545.

47. H. X. Deng, S. S. Li and J. Li, *J. Phys. Chem. C*, 2010, **114**, 4841.

48. Q. Guo, H. W. Hillhouse and R. Agrawal, *J. Am. Chem. Soc*., 2009, **131**, 11672.

49. A. J. Wooten, D. J. Werder, D. J. Williams, J. L. Casson and J. A. Hollingworth, *J. Am. Chem. Soc*., 2009, **131**, 16177.

50. M. G. Panthani, V. Akhavan, B. Goodfellow, J. P. Schmidtke, L. Dunn, A. Dodabalapur, P. F. Barbara and B. A. Korgel, *J. Am. Chem. Soc*., 2008, **130**, 16770.

51. C. Steinhagen, M. G. Panthani, V. Akhavan, B. Goodfellow, B. Koo and B. A. Korgel, *J. Am. Chem. Soc*., 2009, **131**, 12554.

52. M. Benaissa, L. Gu, M. Korytov, T. Huault, P. A. van Aken, J. Brault and P. Vennegues, *Appl. Phys. Lett*., 2009, **95**, 141901.

53. S. E. Habas, H. A. S. Platt, M. F. A. M. van Hest and D. S. Ginley, *Chem. Rev*., 2010, **110**, 6671.

54. R. Freeman and I. Willner, *Chem. Rev. Soc*., 2012, **41**, 4067.

55. M. F. Frasco and N. Chaniotakis, *Sensors*, 2009, **9**, 7266.

56. B. A. Kairdolf, A. M. Smith, T. H. Stokes, M. D. Wang, A. N. Young and S. Nie, *Annu. Rev. Anal. Chem*., 2013, **6**, 143.

57. I. L. Medintz, H. T. Uyeda, E. R. Goldman and H. Mattoussi, *Nat. Mater*., 2005, **4**, 435.

58. C. E. Probst, P. Zrazhevskiy, V. Bagalkot and X. Gao, *Adv. Drug Deliver. Rev*., 2013, **65**, 703.

59. L. Qi and X. Gao, *Expert Opin. Drug Del*., 2008, **5**, 263.

60. N. N. Ledenstov, V. M. Ustinov, V. A. Shchukin, P. S. Kopev , Z. I. Alferov and D. Bimberg, *Semiconduc*., 1998, **32**, 343.

61. D. Bera, L. Qian, T. K. Tseng and P. H. Holloway, *Materials*, 2010, **3**, 2260.

62. K. A. Graeme and C. V. Pollack Jr., *J. Emerg. Med*., 1998, **16**, 45.

63. M. C. Houston, *Altern. Ther. Health Med*., 2007, **13**, 128.

64. R. B. Gordon, M. Bertram and T. E. Graedel, *Proc. Natl. Acad. Sci.*, 2006, **103**, 1209.

65. L. T. Canham, *Appl. Phys. Lett*., 1990, **57**, 1046.

66. L. Pavesi and R. Turan, *Silicon Nanocrystals: Fundamentals, Synthesis and Applications*, Wiley-VCH, Weinheim, Germany, 2010.

67. E. Borsella, R. D'Amato, M. Falconieri, E. Trave, A. Panariti and I. Rivolta, *J. Mater. Res*., 2013, **2**, 193.

68. C. Y. Liu and U. R. Kortshagen, *Nano. Res. Lett.*, 2010, **5**, 1253.

69. D. Timmerman, I. Izeddin, P. Stallinga, I. N. Yassievich and T. Gregorkiewicz, *Nat. Photonics*, 2008, **2**, 105.

70. J. Cho, *J. Mater. Chem*., 2010, **20**, 4009.

71. H. Wu, G. Ya, L. Pan, N. Liu, M. T. McDowell, Z. Bao and Y. Cui, *Nat. Commun*., 2013, **4**, 1943.

72. W. J. Chiang, C. Y. Chen, C. J. Lin, Y. C. King, A. T. Cho, C. T. Peng, C. W. Chao, K. C. Lin and F. Y. Gan, *Appl. Phys. Lett*., 2007, **91**, 051120.

73. J. M. Buriak, *Chem. Rev*., 2002, **102**, 1271.

74. E. O. Kane, *Phys. Rev*., 1966, **146**, 558.

75. R. M. Martin, *Electronic Structure: Basic Theory and Practical Methods*, Cambridge Press, Cambridge, UK, 2004.

76. M. S. Hybersten, *Phys. Rev. Lett*., 1994, **72**, 1514.

77. V. Parkhutik, *J. Porous Mat*., 2000, **7**, 363.

78. L. T. Canham, A. G. Cullis, C. Pickering, O. D. Dosser, T. I. Cox and T. P. Lynch, *Nature*, 1994, **368**, 6467.

79. V. V. Doan and M. J. Sailor, *Science*, 1992, **256**, 1791.

80. A. Ayari-Kanoun, D. Drouin, J. Beauvais, V. Lysenko, T. Nychyporuk and A. Souifi, *Appl. Phys. Lett*., 2009, **95**, 153105.

81. T. Nychyporuk, V. Lysenko, B. Gautier and D. Barbier, *Appl. Phys. Lett*., 2005, **86**, 213107.

82. R. M. Tiggelaar, V. Verdoold, H. Eghbali, G. Desmet and J. G. E. Gardeniers, *Lab Chip*, 2009, **9**, 456.

83. H. Seifarth, R. Grotzschel, A. Markwitz, W. Matz, P. Nitzsche and L. Rebohle, *Thin Film Sol*., 1998, **330**, 202.

84. I. Izeddin, D. Timmerman and T. Gregorkiewicz, *Phys. Rev. B*, 2008, **78**, 035327.

85. A. K. Singh, K. G. Gryczynski, S. Y. Park, M. Kim and A. Neogi, *Solid State Commun*., 2011, **151**, 1405.

86. Y. Nakama, S. Nagamachi, J. Ohta and M. Nunoshita, *Appl. Phys. Exp*., 2008, **1**, 3.

87. R. Espiau, R. E. de Lamaestre and H. Bernas, *Phys. Rev. B*, 2006, **73**, 9.

88. T. Mohanty, A. Pradhan, S. Gupta and D. Kanjilal, *Nanotech*., 2004, **15**, 1620.

89. N. M. Park, T. S. Kim and S. J. Park, *Appl. Phys. Lett*., 2001, **78**, 2575.

90. L. Pavesi, L. Dal Negro, C. Mazzoleni, G. Franzo and F. Priolo, *Nature*, 2000, **408**, 440.

91. T. Baron, F. Mazen, C. Busseret, A. Souifi, P. Mur, F. Fournel, M. N. Semeria, H. Moriceau, B. Aspard, P. Gentile and N. Magnea, *Microelectron. Eng*., 2002, **61**, 511.

92. X. D. Pi, R. W. Liptak, J. D. Nowak, N. P. Wells, C. B. Carter, S. A. Campbell and U. Kortshagen, *Nanotech*., 2008, **19**, 245603.

93. X. D. Pi, R. W. Liptak, S. A. Campbell and U. Kortshagen, *Appl. Phys. Lett*., 2007, **91**, 083112.

94. L. Mangolini, E. Thimsen and U. Kortshagen, *Nano Lett*., 2005, **5**, 655.

95. X. G. Li, Y. Q. He, S. S. Taludkar and M. T. Swihart, *Langmuir*, 2003, **19**, 8490.

96. G. Ledoux, J. Gong, F. Huisken, O. Guillois and C. Reynaud, *Appl. Phys. Lett*., 2002, **80**, 4834.

97. C. S. Yang, R. A. Bley, S. M. Kauzlarich, H. W. H. Lee and G. R. Delgado, *J. Am. Chem. Soc*., 1999, **121**, 5191.

98. K. A. Pettigrew, Q. Liu, P. P. Power and S. M. Kauzlarich, *Chem. Mater*., 2003, **15**, 4005.

99. X. Zhang, D. Neiner, S. Wang, A. Y. Louie and S. M. Kauzlarich, *Nanotech*., 2007, **18**, 095601.

100. K. Dohnalova, A. Fucikova, C. P. Umesh, J. Humpolickova, J. M. J. Paulusse, J. Valenta, H. Zuilhof, M. Hof and T. Gregorkiewicz, *Small*, 2012, **8**, 3198.

101. R. K. Baldwin, K. A. Pettigrew, E. Ratai, M. P. Augustine and S. M. Kauzlarich, *Chem. Commun*., 2002, 1822.

102. J. Zou, R. K. Baldwin, K. A. Pettigrew and S. M. Kauzlarich, *Nano Lett*., 2004, **4**, 1181.

103. J. R. Heath, *Science*, 1992, **258**, 1131.

104. A. Kornowski, M. Giersig, R. Vogel, A. Chemseddine and H. Weller, *Adv. Mater*., 1993, **5**, 634.

105. J. H. Warner, A. Hoshino, K. Yamamoto and R. D. Tilley, *Angew. Chem. Int. Ed*., 2005, **44**, 4550.

106. A. Shiohara, S. Prabhaker, A. Faramus, C. Y. Hsu, P. S. Lai, P. T. Northcote and R. D. Tilley, *Nanoscale*, 2011, **3**, 3364.

107. E. J. Henderson, J. A. Kelly and J. G. C. Veinot, *Chem. Mater*., 2009, **21**, 5426.

108. M. Pauthe, E. Bernstein, J. Dumas, L. Saviot, A. Pradel and M. Ribes, *J. Mater. Chem*., 1999, **9**, 187.

109. C. M. Hessel, E. J. Henderson and J. G. C. Veinot, *J. Phys. Chem. C*, 2007, **111**, 6956.

110. C. M. Hessel, E. J. Henderson and J. G. C. Veinot, *Chem. Mater*., 2006, **18**, 6139.

111. C. M. Hessel, D. Reid, M. G. Panthani, M. R. Rasch, B. W. Goodfellow, J. Wei, H. Fujii, V. Akhavan and B. A. Korgel, *Chem. Mater*., 2011, **24**, 393.

112. Z. Bao, M. R. Weatherspoon, S. Shian, Y. Cai, P. D. Graham, S. M. Allan, G. Ahamd, M. B. Dickerson, B. C. Church, Z. Kang, H. W. Abernathy III, C. J. Summers, M. Liu and K. H. Sandhage, *Nature*, 2007, **446**, 172.

113. R. Ciriminna, A. Fidalgo, V. Pandarus, F. Beland, L. M. Ilharco and M. Pagliaro, *Chem. Rev*., 2013, **113**, 6592.

114. L. L. Hench and J. K. West, *Chem. Rev*., 1990, **90**, 33.

115. W. Stober, A. Fink and E. Bohn, *J. Colloid. Interf. Sci*., 1968, **26**, 62.

116. V. M. Masalov, N. S. Sukhinina, E. A. Kudrenko and G. A. Emelchenko, *Nanotech*., 2011, **22**, 275718.

117. N. A. Hill and K. B. Whaley, *Phys. Rev. Lett*., 1995, **75**, 1130.

118. N. A. Hill and K. B. Whaley, *Phys. Rev. Lett*., 1996, **76**, 3039.

119. M. Nishida, *Semicond. Sci. Tech*., 2006, **21**, 443.

120. L. W. Wang and A. Zunger, *J. Phys. Chem*., 1994, **98**, 2158.

121. C. Delerue, G. Allan and M. Lannoo, *Phys. Rev. B*, 1993, **48**, 11024.

122. T. Y. Kim, N. M. Park, K. H. Kim, G. Y. Sunga, Y. W. Ok, T. Y. Seong and C. J. Choi, *Appl. Phys. Lett*., 2004, **85**, 5355.

123. J. Valenta, R. Juhasz and J. Linnros, *Appl. Phys. Lett*., 2002, **80**, 1070.

124. L. E. Brus, P. F. Szajowski, W. L. Wilson, T. D. Harris, S. Schuppler and P. H. Citrin, *J. Am. Chem. Soc*., 1995, **117**, 2915.

125. D. K. Lu, R. Q. Zhang and S. T. Lee, *Phys. Rev. B*, 2002, **65**, 245417.

126. D. Kovalev, H. Heckler, M. Ben-Chorin, G. Polisski, M. Schwartzkopff and F. Koch, *Phys. Rev*., 1998, **81**, 2803.

127. S. Godefroo, M. Hayne, M. Jivanescu, A. Stesmans, M. Zacharias, O. I. Lebedev, G. Van Tendeloo and V. V. Moshchalkov, *Nat. Nanotechol*., 2008, **3**, 174.

128. T. S. Iwayama, D. E. Hole and I. W. Boyd, *J. Phys. Condens. Matter*, 1999, **11**, 6595.

129. J. S. Biteen, N. S. Lewis and H. A. Atwater, *Appl. Phys. Lett*., 2004, **84**, 5389.

130. M. Fujii, D. Kovalev, B. Goller, S. Minobe, S. Hayashi and V. Y. Timoshenko, *Phys. Rev. B*, 2005, **72**, 165321.

131. L. Ferraioli, M. Wang, G. Pucker, D. Navarro-Urrios, N. Daldosso, C. Kompocholis and L. Pavesi, *J. Nanomater*., 2007, **2007**, 43491.

132. Z. Zhou, L. Brus and R. Friesner, *Nano Lett*., 2003, **3**, 163.

133. S. W. Lin and D. H. Chen, *Small*, 2009, **5**, 72.

134. N. Mansour, A. Momeni, R. Karimzadeh and M. Amini, *Opt. Mater. Exp*., 2012, **2**, 740.

135. U. Gosele, *Nat. Nanotechol*., 2008, **3**, 134.

136. D. Kovalev, *Nat. Nanotechol*., 2010, **5**, 827.

137. M. Aceves-Mijares, A. A. Gonzalez-Fernandez, R. Lopez-Estopier, A. Luna-Lopez, D. berman-Mendoza, A. Morales, C. Falcony, C. Dominguez and R. Murphy-Arteaga, *J. Nanomater*., 2012, **2012**, 890701.

138. A. Romanyuk, V. Melnik, Y. Olikh, J. Biskupek, U. Kaiser, M. Feneberg, K. Thonke and P. Oelhafen, *J. Lumin*., 2010, **130**, 87.

139. R. N. Pereira, D. J. Rowe, R. J. Anthony and U. Kortshagen, *Phys. Rev. B*, 2011, **83**, 155327.

140. M. Zhu, G. Chen and P. Chen, *Appl. Phys. A*, 1997, **65**, 195.

141. M. V. Wolkin, J. Jones, P. M. Fauchet, G. Allan and C. Delerue, *Phys. Rev. Lett*., 1999, **82**, 198.

142. A. C. Filippou, B. Baars, O. Chernov, Y. N. Lebedev and G. Schnakenburg, *Angew. Chem. Int. Ed*., 2013, DOI: 10.1002/anie.201308433.

143. Y. Xiong, S. Yao and M. Driess, *J. Am. Chem. Soc*., 2009, **131**, 7562.

144. Y. Xiong, S. Yao, R. Muller, M. Kaupp and M. Driess, *Nat. Chem*., 2010, **2**, 577.

145. R. Rodriguez, D. Gau, T. Troadec, N. Saffon-Merceron, V. Branchadell, A. Baceiredo and T. Kato, *Angew. Chem. Int. Ed*., 2013, **125**, 9150.

146. T. Muraoka, K. Abe, Y. Haga, T. Nakamura and K. Ueno, *J. Am. Chem. Soc*., 2011, **133**, 15365.

147. Y. Kanemitsu, *Phys. Rev. B*, 1993, **48**, 4883.

148. F. Koch, V. Petrova-Koch and T. Muschik, *J. Lumin*., 1993, **57**, 271.

149. E. P. O'Reiily and J. Robertson, *Phys. Rev. B*, 1983, **27**, 3780.

150. R. Tohmon, Y. Shimogaichi, H. Mizuno and Y. Okhi, *Phys. Rev. B*, 1989, **62**, 1388.

151. L. Rebohle, J. von Borany, H. Frob and W. Skorupa, *Appl. Phys. B*, 2000, **71**, 131.

152. S. Munekumi, T. Yamanaka, Y. Shimogaichi, K. Nagasawa and Y. Yama, *J. Appl. Phys*., 1990, **68**, 1212.

153. S. M. Prokes and W. E. Carlos, *J. Appl. Phys*., 1995, **78**, 2671.

Chapter 2:

Attempts to Lower the Solid-State Syntheses Temperature to Make Silicon Nanocrystals*

*Portion of this chapter has been published:

- M. Dasog, C. Rachinsky and J. G. C. Veinot, *J. Mater. Chem.*, 2011, **21**, 12422 - 12427. (Reproduced by permission of The Royal Society of Chemistry)

2.1 Silicon Nanomaterials Derived from $(RSiO_{1.5})_n$ Sol-Gel Polymers

2.1.1 Introduction

Silicon (Si) is widely known for its applications in the electronics industry. Recent studies indicate silicon nanocrystals (Si-NCs) exhibit fascinating new properties, including size-dependent photoluminescence (PL) equivalent to that exhibited by other semiconductors NCs (*e.g.*, CdSe) without the established cytotoxicity associated with heavy metals.[1-3] The unique properties of Si-NCs have stimulated vast scientific curiosity and opened the door to many new potential applications while also prompting scientists to further investigate Si-based nanomaterials (*e.g.*, silicon carbide (SiC),[4] silicon oxycarbide (SiOC),[5] silicon nitride (Si_3N_4)[6]). Solid state synthesis offers a straightforward, cost-effective and scalable method to make Si based nanomaterials. For such syntheses sol-gel derived polymers are among the most versatile material precursors known; they allow for fabrication of fibers, oxide and non-oxide ceramics, thin films, and powders.[7-10] The exquisite tunability of the polymer structure and composition, low cost and compatibility with various processing techniques (*e.g.*, spin coating,[11] dip coating,[12] and doctor-blading[13]) make these materials extremely useful and fundamentally interesting.

Si-rich oxide sol-gel polymers such as $(SiO_{1.5})_n$ have been used as precursors in the preparation of Si-NCs.[14-17] Our group has demonstrated thermal processing of $(HSiO_{1.5})_n$ sol-gel polymers in reducing atmospheres yields Si-NCs embedded in SiO_2-like matricies.[17] The thermal processing causes redistribution to

form thermodynamically stable SiO_2, and the remaining Si atoms are then able to diffuse through the polymer structure and crystallize to form Si-NCs. Unfortunately these high processing temperatures are often incompatible with the fabrication of electronic devices. However, further research demonstrated that larger Si-NCs can be obtained from $(CH_3SiO_{1.5})_n(HSiO_{1.5})_m$ copolymer where the particle size grew with increasing $-CH_3$ content of the copolymer.[17] We attributed this later observation to an oxide network modification that resulted from the inclusion of the methyl group. This "opening" of the oxide network would favour diffusion of Si atoms during the annealing process as shown in the **Scheme 2-1**.

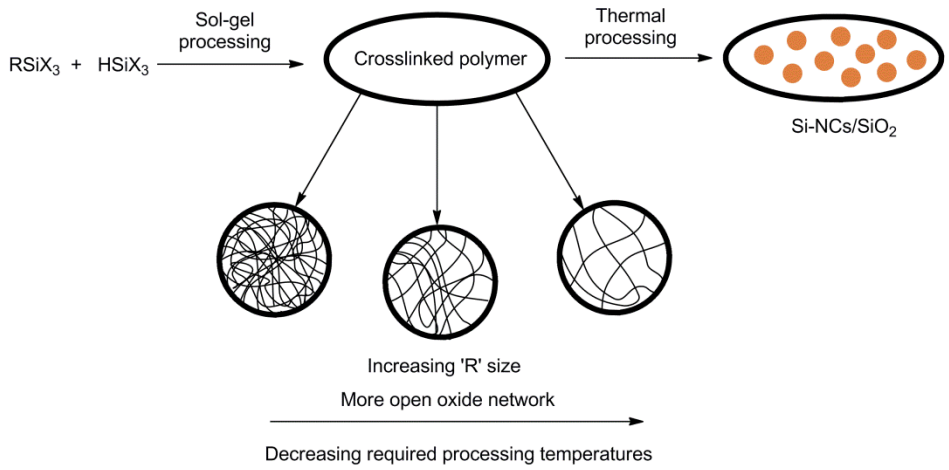

Scheme 2-1. A summary of the influence of 'R' size on the density of the sol-gel network and requisite processing requirements to obtain Si-NCs.

These observations raised the following questions: How does the nature of the 'R' group (*e.g.*, "size") influence Si-NC formation? Can larger Si-NCs

nanocrystals be formed at lower temperatures by increasing the bulk of the 'R' group? In this chapter, we report how a series of “R” moieties incorporated into $(HSiO_{1.5})_{0.95}(RSiO_{1.5})_{0.05}$ copolymers influence the material obtained upon thermal processing at temperatures up to 1400 ^{o}C. While we could not reduce the processing temperatures to make Si-NCs, we were able to synthesize interesting new nanomaterials. We have found by using a systematic synthetic approach and a wide complement of characterization methods that when R = C_2H_5, C_4H_9, and C_6H_{13} a highly luminescent (blue) amorphous mixture of silica and carbon is obtained. In contrast, oxide-embedded SiC-NCs are formed when R = C_8H_{17} and $C_{10}H_{21}$. Etching the resulting composite materials with hydrofluoric (HF) acid yielded new freestanding carbon-coated SiO_2 nanostructures and SiC-NCs, respectively.

2.1.2 Experimental

2.1.2.1 Materials.

Trichlorosilane ($HSiCl_3$, 99%), ethyl trichlorosilane ($C_2H_5SiCl_3$, 99%), butyltrichlorosilane ($C_4H_9SiCl_3$, 99%), hexyltrichlorosilane ($C_6H_{13}SiCl_3$, 97%), octyltrichlorosilane ($C_8H_{17}SiCl_3$, 97%), and ethanol (95%) were all purchased from Sigma-Aldrich. Decyl trichlorosilane ($C_{10}H_{21}SiCl_3$, 98%) was purchased from Chemos GmbH. Anhydrous ethyl ether (ACS grade) and toluene (ACS grade) were purchased from Caledon and hydrofluoric acid (49% solution) from J. T. Baker. All the reagents were used as received without further purification.

2.1.2.2 Synthesis of $[(HSiO_{1.5})_{0.95}(RSiO_{1.5})_{0.05}]_n$ condensation copolymers A1-E1.

Copolymers were synthesized according to the procedure reported by Henderson *et al.* [17] Predefined quantities of $HSiCl_3$ and $RSiCl_3$ were added to a 3-neck round bottom flask and stirred under argon while cooling in a water/ice bath (0 ^oC) using standard Schlenk techniques. The mole percent of $RSiCl_3$ (R = C_2H_5, C_4H_9, C_6H_{13}, C_8H_{17}, $C_{10}H_{21}$) relative to $HSiCl_3$ was set to 5%. Deionzied water (the volume of water was modified to maintain a H_2O : silane ratio of 2 : 1) was rapidly added to the flask with vigorous stirring into the cooled silane mixture through a septum. The reaction flask was connected to an exhaust vent to release $HCl_{(g)}$ produced upon addition of water. Hydrolysis of the precursor was confirmed by monitoring the reaction mixture pH (pH < 1). The precipitate remained immersed in the acidic aqueous reaction mixture for 30 – 120 min to ensure complete hydrolysis and condensation. The product was subsequently dried *in vacuo* for ca. 8 hours to yield a white dry solid that was maintained in inert atmosphere until subsequent thermal processing. Polymer compositions and thermal decomposition properties are summarized in **Table 2-2**.

2.1.2.3 Thermal Processing copolymers.

Condensation copolymers **A1 - E1** were transferred to quartz boats and thermally processed under slightly reducing conditions (5% H_2/95% Ar) at 1100 ^oC for one hour. The resulting products **A2 - E2** (details summarized in **Table 2-3**) were transferred to a high temperature furnace and further processed at 1400 ^oC for 2 h under Ar atmosphere to yield **A3 - E3**. Finally, composites **A3 – E3** were heated in

air at 650 ^{o}C for 30 min to remove excess residual carbon to yield **A4 - E4** (Note: Following cooling to room temperature after each thermal processing step, samples were mechanically ground to fine powders).

2.1.2.4 Hydrofluoric acid etching.

A4 – **E4** were treated with hydrofluoric acid to remove the protective SiO_2 matrix. In a typical etching procedure, 100 mg of the sample was transferred to a Teflon test tube and 1:1:1 solution of 49% $HF_{(aq)}$: H_2O : ethanol (10 mL) was added. The mixture was stirred for 60 min followed by extraction into 10 mL toluene. To obtain solid product, toluene was removed *in vacuo* yielding a cloudy viscous oil and anhydrous diethyl ether was added dropwise resulting in a white solid. The white solid was collected by vacuum filtration and washed with ice cold diethyl ether (3 x 10 mL).

2.1.2.5 Fourier Transform Infrared Spectroscopy (FTIR)

FTIR was performed on powder samples using a Nicolet Magna 750 IR spectrometer.

2.1.2.6 X-ray Powder Diffraction (XRD)

XRD was performed using an INEL XRG 3000 X-ray diffractometer equipped with a Cu K_α radiation source (λ = 1.54 Å). Bulk crystallinity for all samples was evaluated on finely ground samples mounted on a low-intensity background silicon (100) sample holder.

2.1.2.7 Thermogravimetric Analysis (TGA)

TGA was performed on PerkinElmer Pyris 1 using a platinum sample pan at a heating rate of 18 ^{o}C/min in a 5%H_2/95%Ar atmosphere.

2.1.2.8 X-Ray Photoelectron Spectroscopy (XPS)

XPS analysis was performed using a Kratos Axis Ultra instrument operating in energy spectrum mode at 210 W. The base pressure and operating chamber pressure were maintained at 10^{-7} Pa. A monochromatic Al K_{α} source (λ = 8.34 Å) was used to irradiate the samples, and the spectra were obtained with an electron takeoff angle of 90°. To minimize sample charging, the charge neutralizer filament was used when required. Survey spectra were collected using an elliptical spot with major and minor axis lengths of 2 and 1 mm, respectively, and 160 eV pass energy with a step of 0.33 eV. CasaXPS software (Vamas) was used to interpret high-resolution (HR) spectra. All of the spectra were internally calibrated to the O 1s emission (532.9 eV).[22] After calibration, the background was subtracted using a Shirley-type background to remove most of the extrinsic loss structure.

2.1.2.9 Absorbance (UV-Vis) Spectroscopy

UV-Visible spectra were recorded on Cary 400 UV-Vis Spectrometer.

2.1.2.10 Photoluminescence (PL) Spectroscopy

PL spectra for the solution phase samples were acquired in a quartz cuvette using a Varian Cary Eclipse Fluorescence Spectrometer. The solid composites were drop-coated onto optical-grade quartz (1 cm x 1 cm) and the photoluminescence (PL) spectra were obtained using the 325 nm line of a He-Cd laser excitation source at

room temperature. PL emission was detected with a fiber optic digital charge-coupled device (CCD) spectrometer whose spectral response was normalized using a standard blackbody radiator.

2.1.2.11 Photoluminescence Quantum Yield Measurement

Photoluminescence quantum yields were determined using methods adapted from the work of Williams *et al*. and discussed in detail in **Appendix A**. [18] The etched samples (**A5**, **B5** and **C5**) were dissolved in toluene. The excitation wavelength, slit widths and reference for the etched samples are summarized in **Table 2-1**.

Table 2-1: The excitation wavelength, slit widths and reference for the etched samples.

Sample	Excitation wavelength	Slit width	Reference
A5	350 nm	5 nm	Coumarin 1
B5	350 nm	5 nm	Coumarin 1
C5	350 nm	10 nm	Napthalene

2.1.3 Results and Discussion

2.1.3.1 $(HSiO_{1.5})_{0.95}(RSiO_{1.5})_{0.05}$ condensation copolymers A1-E1.

Copolymers **A1 - E1** (See **Table 2-2**) were prepared *via* sol-gel method. Polymerization was performed with 5 molar percent of Si-R (R = C_2H_5, C_4H_9, C_6H_{13}, C_8H_{17}, $C_{10}H_{21}$) and the balance of monomer being $(HSiO_{1.5})_n$ using acid catalyzed sol-gel reaction conditions arising from the formation of HCl *in situ* upon

hydrolysis of the $HSiCl_3$ and $RSiCl_3$ precursors. Under these conditions hydrolysis and condensation proceed and an extended sol-gel network results as shown in **Scheme 2-2**.[19]

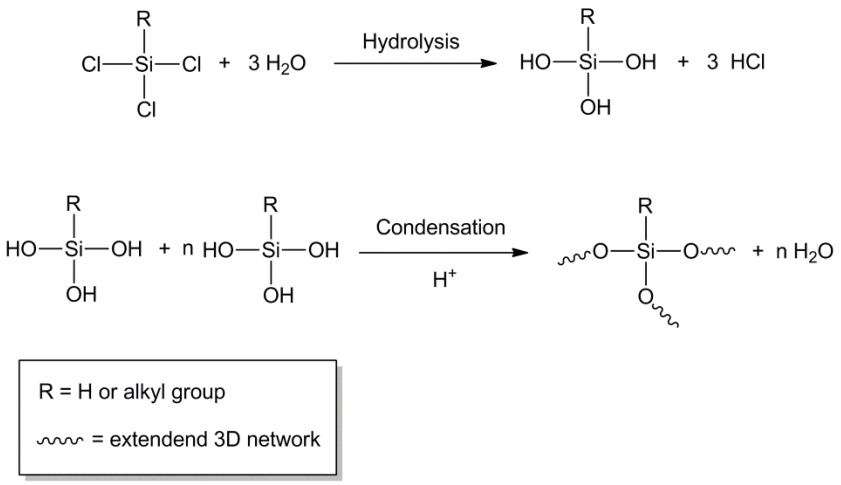

Scheme 2-2. Acid catalyzed polymerization of $RSiCl_3$ to form an extended $RSiO_{1.5}$ network.

While phase separation is known to occur because of differential reactivities of substituted silanes, it is reasonable that at the presented concentrations a near random co-polymer results.[20] **A1 - E1** copolymers were characterized using FTIR (**Figure 2-1**) and vibrational modes typical of $(HSiO_{1.5})_n(RSiO_{1.5})_m$ networks were observed.

Table 2-2. Condensation copolymers and their decomposition temperatures.

Sample	Composition	R group decomposition temperature*
A1	$(HSiO_{1.5})_{0.95}(C_2H_5SiO_{1.5})_{0.05}$	172ºC
B1	$(HSiO_{1.5})_{0.95}(C_4H_9SiO_{1.5})_{0.05}$	245ºC
C1	$(HSiO_{1.5})_{0.95}(C_6H_{13}SiO_{1.5})_{0.05}$	346ºC
D1	$(HSiO_{1.5})_{0.95}(C_8H_{17}SiO_{1.5})_{0.05}$	498ºC
E1	$(HSiO_{1.5})_{0.95}(C_{10}H_{21}SiO_{1.5})_{0.05}$	550ºC

*Determined from Thermogravimetric analysis and the processing conditions were 18ºC/min heating rate under 5% H_2/95% Ar atmosphere.

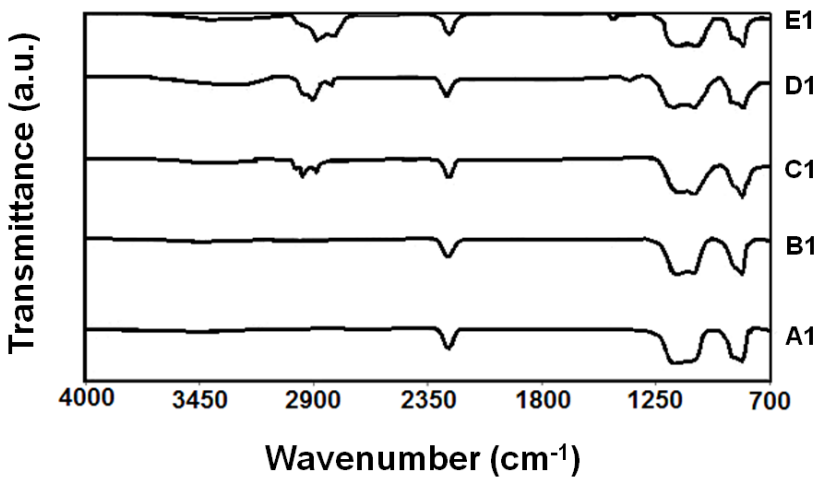

Figure 2-1. FT-IR spectra of sol-gel derivatized copolymers.

The Si–H stretching vibration at ca. 2255 cm^{-1} was observed for all copolymers indicating this moiety was not compromised during preparation. The Si–O–Si (ca. 1000 – 1200 cm^{-1}) and H–Si–O (ca. 800 – 900 cm^{-1}) vibrations and

the relative intensities of the two components associated with both bands are consistent with the formation of an extended network structures.[21] As expected, the intensities of the $–CH_3$ bending (ca. 1200 – 1250 cm^{-1}) and C–H stretching modes (ca. 2900 – 3000 cm^{-1}) increase with the alkyl chain length.[17] It should be noted some overlap of the Si–O–Si and $-CH_3$ vibration bands lead to some broadening of the feature at ca. 1000 – 1250 cm^{-1}. A weak –OH stretching band (ca. 3300 – 3400 cm^{-1}) was observed for **D1** and **E1** even after aging these polymers for 2 days. It is reasonable this feature results from incomplete condensation resulting from the influence of the steric bulk of pendent groups limiting the formation of large extended networks.[22]

2.1.3.2 Thermally processed copolymers.

Table 2-3: Thermally processed composites, processing conditions and the products obtained.

Sample	Processing conditions	Remarks
A2	A1, 1100°C, 1 h, 5% H_2/95% Ar	CRSM*
B2	B1, 1100°C, 1 h, 5% H_2/95% Ar	CRSM
C2	C1, 1100°C, 1 h, 5% H_2/95% Ar	CRSM
D2	D1, 1100°C, 1 h, 5% H_2/95% Ar	ASOM$^{\$}$
E2	E1, 1100°C, 1 h, 5% H_2/95% Ar	ASOM
A3	A2, 1400°C, 2 h, Ar	CRSM
B3	B2, 1400°C, 2 h, Ar	CRSM
C3	C2, 1400°C, 2 h, Ar	CRSM
D3	D2, 1400°C, 2 h, Ar	SiC NCs
E3	E2, 1400°C, 2 h, Ar	SiC NCs
A4	A3, 650°C, 30 min, Air	SiO_2
B4	B3, 650°C, 30 min, Air	SiO_2
C4	C3, 650°C, 30 min, Air	SiO_2
D4	D3, 650°C, 30 min, Air	SiC NCs
E4	E3, 650°C, 30 min, Air	SiC NCs

*CRSM = Carbon rich silica matrix, $^{\$}$ASOM = Amorphous silicon oxycarbide matrix.

All copolymers (i.e., **A1 - E1**) were initially thermally processed at 1100°C under a slightly reducing atmosphere to yield **A2 - E2**. The $(HSiO_{1.5})_n$ condensation homopolymer disproportionates to yield Si NCs in an SiO_2 matrix.[17] This is not the

case for **A1 - E1**. Incorporating 'R' groups into the copolymer produces carbon impurities upon thermal decomposition; these impurities prevent formation of Si NCs.[23] Thermogravimetric analysis of polymers **A1 - E1** under slightly reducing atmospheres provides insight into the decomposition behaviour of the 'R' groups. **Table 2-2** shows the decomposition temperature of the polymers depends on the 'R' group and the temperature increases with increased steric bulk (i.e., **A1**<**B1**<**C1**<**D1**<**E1**). Based upon residual masses remaining after heating, we conclude the quantity of carbon impurities incorporated increases with 'R' group size.

Samples processed at 1100°C (i.e., **A2 - E2**) were further heated at 1400°C in Ar for two hours to yield **A3 - E3.** X-ray powder diffraction was performed to probe the presence of any nanocrystalline materials (**Figure 2-2**). **A3**, **B3** and **C3** show a broad reflection at ca. 20° previously attributed to an amorphous matrix (*e.g.*, SiO_2);[24] somewhat surprisingly no reflections attributable to Si or SiC NCs were observed. **D3** and **E3** (i.e., copolymers containing octyl and decyl moieties) show broad reflections centered at 35, 60 and 72° that are readily indexed to the (111), (220), and (311) crystal planes of β-SiC indicating formation of carbon rich silica matrix (CRSM) embedded - SiC NCs.[25] Scherrer analysis (details in **Appendix B**) was performed to obtain approximate particle sizes of the SiC NCs; diameters were found to be ca. 4 and 6 nm for **D3** and **E3**, respectively. XRD analysis of **A4 - E4** yielded identical patterns (not shown) to those observed for **A3 - E4** indicating processing at 650°C did not alter the crystalline structure of these composites at the sensitivity of the XRD technique.

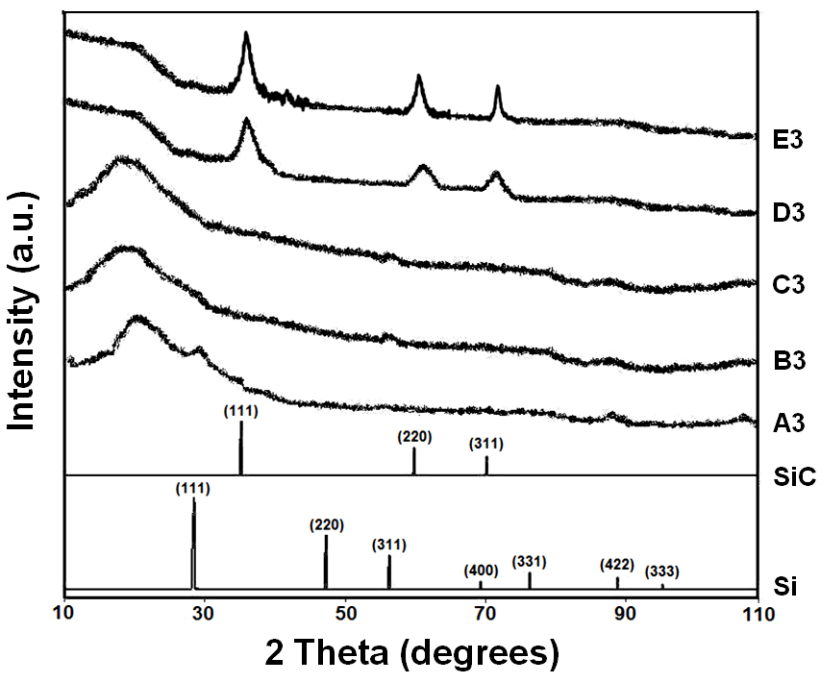

Figure 2-2. XRD patterns of the copolymers processed at 1400ºC for two hours under Ar atmosphere.

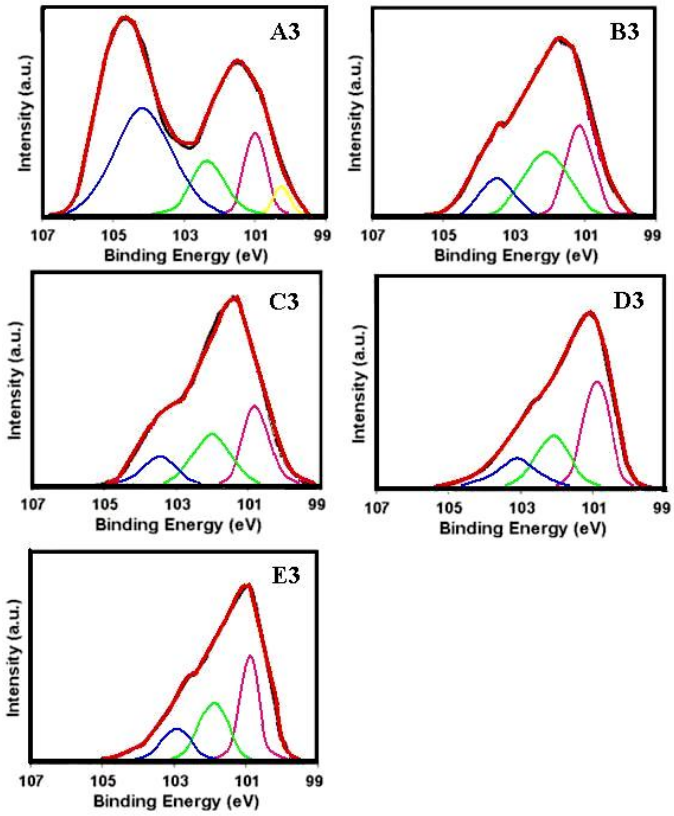

Figure 2-3. HR XP spectra of the Si 2p region of the composites processed at 1400°C. For the clarity of the figure only Si $2p_{3/2}$ spin-orbit lines are shown. The full-width half maxima of the Si $2p_{3/2}$ spin-orbit lines were constrained below 1.2 eV. (Color code: Black - data obtained, red - fitted line, yellow - Si(I), pink - Si (II), green - Si(III) and blue - Si(IV)).

X-ray photoelectron spectroscopy (XPS) studies were performed to aid in further elucidation of the identity of **A3** - **E3**. **Figure 2-3** shows the Si 2p region of **A3** - **E3** (i.e., samples annealed at 1400°C). These spectra reveal that Si is present in low oxidation states (i.e., Si (I-III)) consistent with partially oxidized Si and/or Si–C bonds being present in **A3** - **E3**, regardless of the alkyl chain length.[26]

Consistent with XRD analysis of **D3** and **E3** (*vide supra*), both materials show a $2p_{3/2}$ line centered at 100.8 eV characteristic of SiC, as well as emissions arising from $SiO_{1.5}$ and SiO_2 species.[27] It is reasonable that the low binding energy emission at ca. 101 eV in **A3**, **B3** and **C3** could arise from SiO or SiC species. From the present analysis it is difficult to definitively indentify the material composition of **A3**, **B3** and **C3**; data is consistent with both silicon oxycarbide or carbon phases in a SiO_2 matrix with interfaces consisting of C–O, Si–C, C–C, and Si–O linkages. [27]

Further annealing of **A3 - D3** in air at 650°C to remove amorphous carbon yields **A4 - D4.** **A4 - C4** were confirmed to be pure silica from XPS analysis (**Figure 2-4**). In light of the established stability of silicon oxycarbides to heating in air to 1500°C and our observations, we propose **A3 - C3** contain amorphous carbon phases dispersed within the silica matrix.[28-30] XRD and XPS analyses confirm **D4** and **E4** to be SiC NCs in a SiO_2 matrix.

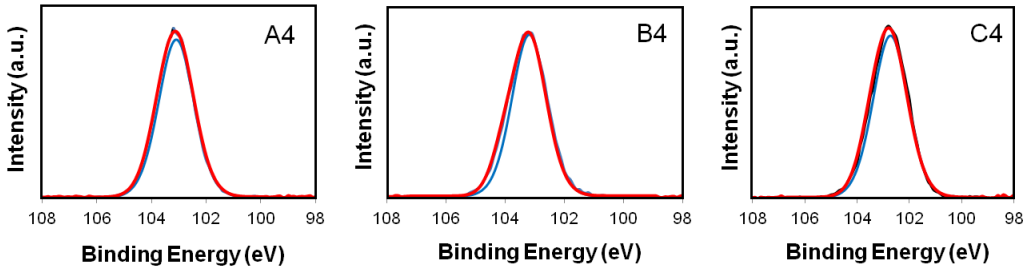

Figure 2-4. HR XP spectra of the Si 2p region of the samples **A4 – C4.** For the clarity of the figure only Si $2p_{3/2}$ spin-orbit lines are shown. The full-width half maxima of the Si $2p_{3/2}$ spin-orbit lines were constrained below 1.2 eV. (Color code: Black - data obtained, red - fitted line and blue - Si(IV)).

2.1.3.3 Liberation of nanoparticles.

Liberation of matrix encapsulated nanomaterials provides a more direct evaluation of the nanodomains obtained. In this regard, the SiO_2 matrix was etched away from **A3 - C3**, **D4**, **E4** using HF acid to liberate the carbon phase or SiC NCs.[31] Composite samples were etched using an established procedure employing a 1:1:1 mixture of 49% HF : EtOH : H_2O. Composites **A3 - C3**, **D4** and **E4** were finely ground and exposed to the etching solution for one hour. The remaining material (**A5**, **B5**, **C5, D6, E6**) was extracted with toluene and characterized using XPS, FTIR and PL spectroscopy.

Table 2-4: HF etched samples and their luminescent properties.

Sample	Processing conditions	Emission max.	Quantum yields
A5	A3, HF etch, 1h	470 nm	3.7 %
B5	B3, HF etch, 1 h	470 nm	3.6 %
C5	C3, HF etch, 1 h	422 nm	1.2 %
A6	A4, HF etch, 1 h	No emission	NA
B6	B4, HF etch, 1 h	No emission	NA
C6	C4, HF etch, 1 h	No emission	NA
D6	D4, HF etch, 1 h	No emission	NA
E6	E4, HF etch, 1 h	No emission	NA

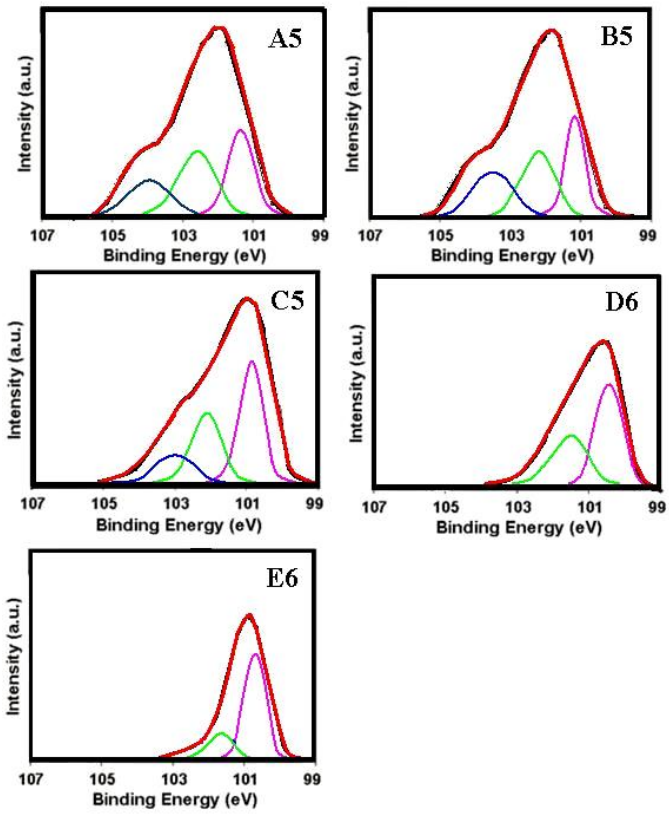

Figure 2-5. HR XP spectra of the Si 2p region of the HF etched samples. For the clarity of the figure only Si $2p_{3/2}$ spin-orbit lines are shown. (Color code: Black - data obtained, red - fitted line, yellow - Si(I), pink - Si (II), green - Si(III) and blue - Si(IV)).

XPS analyses of **A5**, **B5**, and **C5** samples indicate that they contain suboxides of Si (**Figure 2-5**). This observation is consistent with carbon phases encapsulating silicon oxide materials that would shield them from HF exposure. It is also reasonable the silicon suboxide component may arise from interfacial species bridging the carbon and silica domains. The presence of the interface is further confirmed by the investigating C 1s region in the XPS data showing the

presence of O–C–O, O-C-R and C-Si species (**Figure 2-6**).[32] XPS analyses of **D6** and **E6** show an emission peak centered at 100.8 eV consistent with SiC and they also exhibit higher oxidation state Si which maybe result of post-etching oxidation or mixed surface species (**Figure 2-5**).[21]

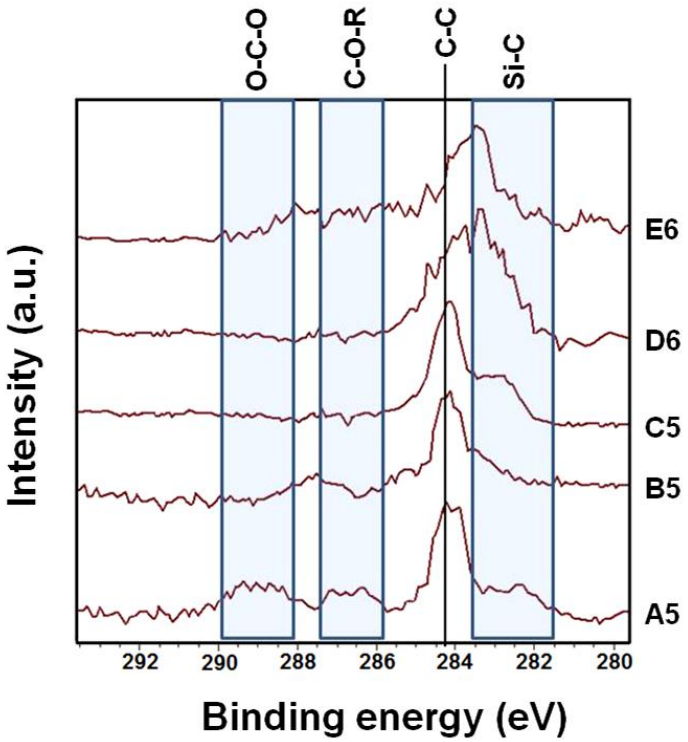

Figure 2-6. HR XP spectra of the C 1s region of the HF etched samples

The FTIR studies performed on the liberated samples show the SiC vibration between 830 – 845 cm^{-1}, O–H stretch at ca. 3500 cm^{-1}, the bands between 1000 – 1200 cm^{-1} can be attributed to Si–O, C–C and C–O–R stretches (**Figure 2-7**).[26]

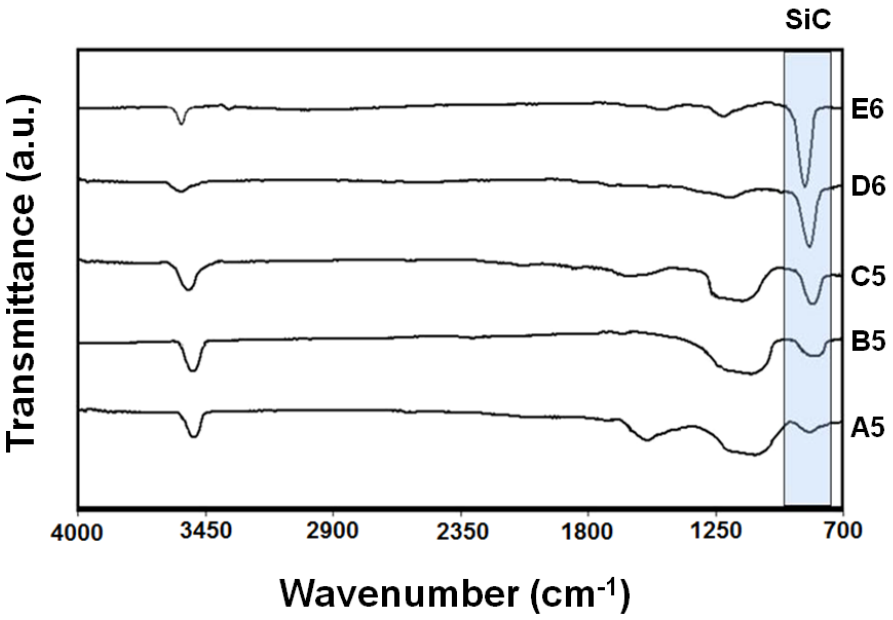

Figure 2-7. FTIR spectra of the HF etched samples

Interestingly, **A5**, **B5** and **C5** exhibit blue emission (**Figure 2-8**) with photoluminescence quantum yields of 3.7%, 3.6% and 1.2%, respectively. Previously blue luminescence has been reported for silicon-carboxy materials and is proposed to arise from a charge transfer species and it is reasonable we observe similar PL response. [33]

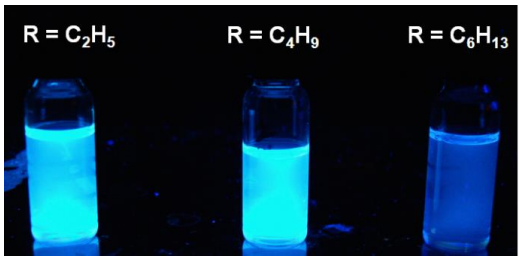

Figure 2-8. Photograph of toluene dispersions of **A5**, **B5** and **C5** samples under UV illumination.

2.1.3.4 Si nanomaterials from $[(HSiO_{1.5})_{0.95}(RSiO_{1.5})_{0.05}]_n$ copolymers where R = $CF_3(CH_2)_2$, $CCl_3(CH_2)_2$ and $CN(CH_2)_2$

In an attempt to lower the decomposition temperature of the pendant group, 'R' group containing electron withdrawing functionalities such as cyano (-CN), fluoro ($-CF_3$), chloro ($-CCl_3$) were used to weaken the Si-C bond. Unfortunately, no Si or SiC formation was observed upon thermal processing of $[(HSiO_{1.5})_{0.95}(CN(CH_2)_2SiO_{1.5})_{0.05}]$ and $[HSiO_{1.5})_{0.95}(CCl_3(CH_2)_2SiO_{1.5})_{0.05}]$ copolymers. $[HSiO_{1.5})_{0.95}(CF_3(CH_2)_2SiO_{1.5})_{0.05}]$ contained the 'R' group with lowest decomposition temperature (i.e., 102 ^oC, as measured from TGA). Thermal processing of the fluoro copolymer at 1100^oC led to formation of 5 nm Si-NCs as determined from XRD and Scherrer ananlysis. Increasing the ratio of $-(CH_2)_2CF_3$ to -H in the copolymer led to phase segregation and incomplete polymerization. Attempts to synthesize $[(CF_3(CH_2)_2SiO_{1.5})_{0.05}]_n$ were unsuccessful as only oligomers were obtained from hydrolysis and condensation of $CF_3(CH_2)_2SiCl_3$.

2.1.4 Conclusions

By preparing and thermally processing sol-gel derived polymers $[(HSiO_{1.5})_{0.95}(RSiO_{1.5})_{0.05}]_n$ we have established that Si NCs are not formed when large quantities of C are incorporated. These new precursor systems afford SiC nanocrystals or new amorphous carbon encapsulated silica nanomaterials upon thermal processing of these polymers. This previously unknown encapsulated nanomaterial shows characteristic blue photoluminesence when illuminated with

UV light. In light of the established need for efficient blue emitters, these materials are the subject of ongoing investigations in our laboratory. $[HSiO_{1.5})_{0.95}(CF_3(CH_2)_2SiO_{1.5})_{0.05}]$ was the only copolymer to successfully yield Si-NCs upon thermal processing.

2.2 Influence of the Matrix on the Formation of Si-NCs

2.2.1 Introduction

The attempts to lower the Si-NC synthesis temperature *via* matrix structure modification was unsuccessful as discussed in **Section 2.1** of this chapter. Therefore we began to investigate the influence of the chemical composition of the matrix on the formation of Si-NCs. Previously, it has been shown that upon annealing $(HSiO_{1.5})_n$ polymer at high temperatures (>1300°C), the SiO_2 matrix softens and leads to formation of large Si structures. If the melting point of the matrix can be lowered, one would be able to synthesize Si-NCs at desired temperatures.

Silica begins to soften at temperatures near 1300 - 1700°C (depending on the crystal structure).[34] Around 5000 B.C. Egyptians discovered that addition of salt impurities to silica lowered its softening temperatures.[35] The salts commonly (which are now termed as "flux") used for such procedures are soda ash (Na_2O), lime (CaO), magnesia (MgO) and alumina (Al_2O_3).[36-40] We took a similar approach and studied the influence of various salts on the matrix softening and in turn formation of Si-NCs from $(HSiO_{1.5})_n$ sol-gel polymer.

Initially, we mechanically formed mixtures of the $(HSiO_{1.5})_n$ sol-gel polymer and the a metal oxide (Na_2O, CaO or Al_2O_3). Upon thermal treatment of these mixtures at 1100°C in 5% H_2 atmosphere, no significantly different results were obtained compared to the thermal processing of $(HSiO_{1.5})_n$ sol-gel polymer on its own. To obtain better homogeneity, the salts were added during the sol-gel

syntheses but the metal oxides form alkaline solution in aqueous environment which led to oxidation of $HSiO_{1.5}$ suboxide to SiO_2. Therefore we switched the salts used from metal oxides to metal halide such as sodium chloride (NaCl), magnesium chloride ($MgCl_2$) and aluminum chloride ($AlCl_3$). Unfortunately NaCl and $MgCl_2$ salts did not make a significant difference in formation of Si-NCs.

$AlCl_3$ salt altered the matrix chemical composition to form either mixture of aluminasilicate and γ-Al_2O_3 or mullite ($Al_6Si_2O_{13}$) depending on the alumina content. The former matrix softens at lower temperatures (~800°C) and led to formation of larger Si-NCs. Mullite did not alter the size of Si-NCs, however the Si-NCs embedded in SiO_2/mullite matrix emit red color under UV-illumination. We have studied the effect of $AlCl_3$ concentration and annealing temperatures on the formation of Si-NCs. The experimental and characterization details for this study are discussed in the following section.

2.2.2 Experimental

2.2.2.1 Materials.

Trichlorosilane ($HSiCl_3$, 99 %) and anhydrous aluminum trichloride ($AlCl_3$, 98 %) were purchased from Sigma-Aldrich. Sodium hydroxide (NaOH, 97 %) was purchased from Caledon chemicals. All the reagents were used as received.

2.2.2.2 Synthesis of the $(HSiO_{1.5})_n$ condensation polymer.

The $(HSiO_{1.5})_n$ polymer was synthesized according to the previous procedure reported by Henderson *et al*.[17] $HSiCl_3$ (4.5 mL, 45 mmol) was added to a three neck flask and cooled to 0°C using a ice bath, under N_2 atmosphere. Deionized (DI) water (1.59 mL, 90mmol) was added to $HSiCl_3$ and the reaction mixture was stirred together for an hour at room temperature. The resulting white product was isolated and dried *in vacuo*. The polymer was kept under inert atmosphere to prevent oxidation.

2.2.2.3 Synthesis of the $(HSiO_{1.5})_n$ condensation polymers in presence of $AlCl_3$.

In a typical synthesis, $HSiCl_3$ (12 mmol, 1.2 mL) was added to a round bottom flask and was cooled in a salt ice bath (ca. -10°C) for 10 minutes under inert N_2 atmosphere. $AlCl_3$ salt (required amount, **Table 2-5**) dissolved in DI water (24 mmol, 0.45 mL) was added to the $HSiCl_3$ solution. The reaction mixture was stirred until complete condensation occurred and the solid was dried *in vacuo*. The resulting white amorphous powder was stored under N_2 atmosphere until further use.

Table 2-5: Reagent amounts for various reactions.

Sample	$AlCl_3$	$HSiCl_3$	DI-Water
G1	2 mmol, 0.26 g	12 mmol, 1.2 mL	24 mmol, 0.45 mL
H1	4 mmol, 0.52 g	12 mmol, 1.2 mL	24 mmol, 0.45 mL
I1	6 mmol, 0.78 g	12 mmol, 1.2 mL	24 mmol, 0.45 mL
J1	8 mmol, 1.04 g	12 mmol, 1.2 mL	24 mmol, 0.45 mL
K1	10 mmol, 1.30 g	12 mmol, 1.2 mL	24 mmol, 0.45 mL
L1	12 mmol, 1.56 g	12 mmol, 1.2 mL	24 mmol, 0.45 mL

2.2.2.4 Thermal processing of the sol-gel polymers.

The polymers were transferred to a quartz boat and thermally processed at various temperatures for one hour under reducing conditions (5% H_2/95% Ar). The samples were cooled to room temperature after thermal processing and ground into a fine powder. The processing details for various composites are tabulated in **Table 2-6** and **2-7**.

2.2.3 Results and Discussion

2.2.3.1 $(HSiO_{1.5})_n$ and hetero sol-gel polymers

$(HSiO_{1.5})_n$ sol-gel polymers were synthesized by hydrolysis of $HSiCl_3$ to form silanol (Si–OH) groups, which further condenses to make Si–O–Si linkages. The reaction was carried out at lower temperature to reduce the rate of hydrolysis. Water molecules attack the electron deficient Si centers and release HCl as a

byproduct which catalyzes the condensation reaction. The pH of the reaction mixture at this point is lower than 1. Thus, formed silanol groups undergo polycondensation to form a three dimensional $(HSiO_{1.5})_n$ sol-gel network in which the Si:O ratio was maintained at 1:1.5. The sol-gel polymer was characterized using FTIR spectroscopy (**Figure 2-9**). Characteristic vibrations i.e., Si–H stretch at ca. 2255 cm^{-1}, Si–O–Si stretch at ca. 1160 and 1075 cm^{-1} and H–Si–O vibrations at 875 and 830 cm^{-1} were observed.[17]

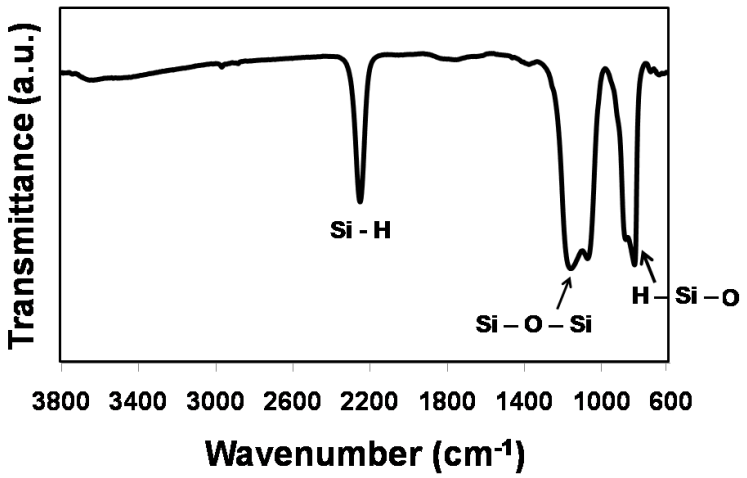

Figure 2-9. FTIR spectra of $(HSiO_{1.5})_n$ condensation polymer.

To investigate the effect of $AlCl_3$ salt on the formation of Si NCs, the salt was added during the sol-gel polymer synthesis to achieve maximum homogeneity. The salt was dissolved in the water prior to its addition to the $HSiCl_3$ solution. $AlCl_3$ is well-known to undergo hydrolysis to form $[Al(H_2O)_6]^{3+}$ cation in water. This

complex can further undergo condensation with silanol groups to form alumino-silicate heteropolymers.[41] **Figure 2-10** shows typical vibrations present in thus formed heteropolymer. Similar to the parent $(HSiO_{1.5})_n$ polymer we observe Si–H stretch at ca. 2190 cm^{-1}, Si–O–Si vibrations at ca. 1110 - 1050 cm^{-1} and H–Si–O vibrations at ca. 870 - 830 cm^{-1} . In addition to these vibrations we observe Al–O stretch at ca. 630 cm^{-1}.[42] As seen in the FTIR spectrum of the parent $(HSiO_{1.5})_n$ polymer we observe two separate components in Si–O–Si and H–Si–O stretches. However in the heteropolymer additional feature appears owing to the Si–O–Al stretch (ca. 1060 cm^{-1}).[43] FTIR spectra of sol-gel polymers with varying amounts of $AlCl_3$ is shown in **Figure 2-11**. Detailed inspection reveals that with increasing concentrations of $AlCl_3$ salt, the intensity of the following stretches also increases: Si–O–Al (ca. 1170 - 1050 cm^{-1}), Al–OH (ca. 925 - 915 cm^{-1}), tetrahedral Al–O–Al (ca. 780 - 730 cm^{-1}) and octahedral Al–O–Al (ca. 650 - 610 cm^{-1}).[42]

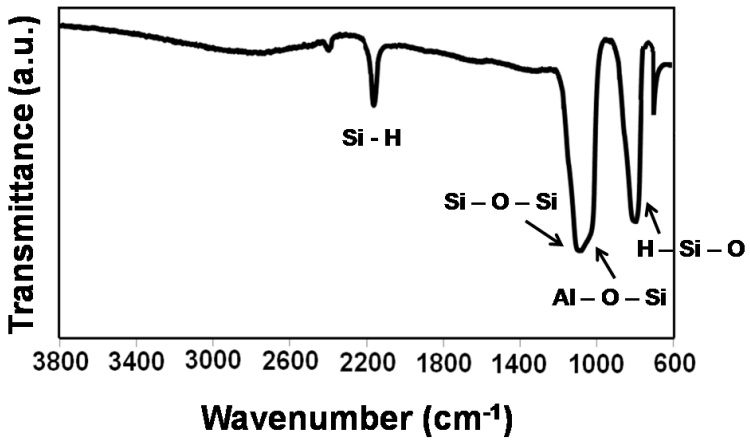

Figure 2-10. FTIR spectra of $(HSiO_{1.5})_n$ condensation polymer made in presence of 1 mmol $AlCl_3$ salt.

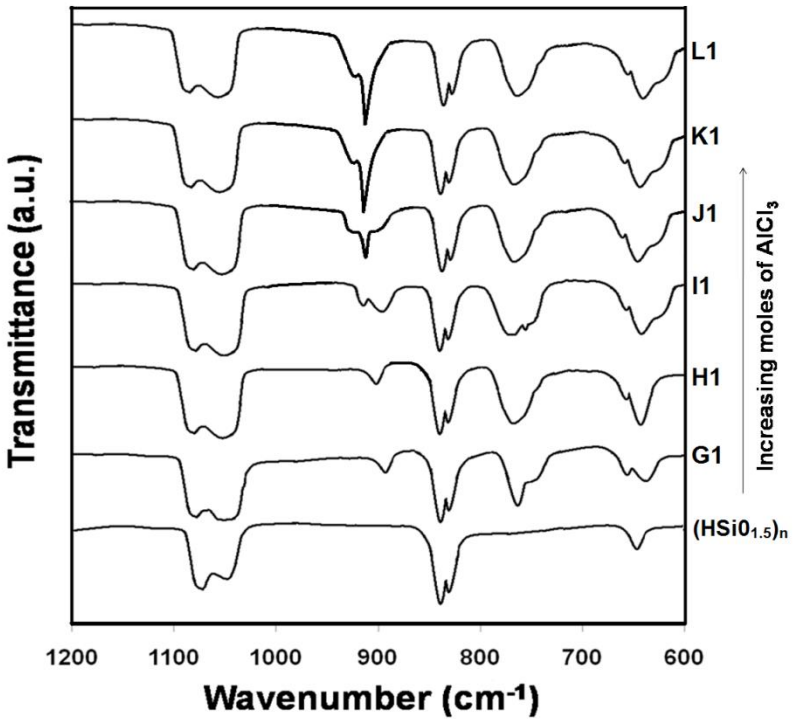

Figure 2-11. FTIR spectra of alumina-$(HSiO_{1.5})_n$ hetero sol-gel polymers with varying amounts of alumina.

2.2.3.2 Thermally processed hetero sol-gel polymers (influence of $AlCl_3$ concentration)

The hetero sol-gel polymers with varying amounts of alumina (i.e., **G1**, **H1**, **I1**, **J1**, **K1** and **L1**) were heated at 1100°C for an hour. The resulting composites were analyzed using XRD and XPS techniques.

Table 2-6: Thermally processed composites and processing conditions.

Sample	Processing conditions
G2	**G1**, 1100°C, 1 h, 5% H_2/95% Ar
H2	**H1**, 1100°C, 1 h, 5% H_2/95% Ar
I2	**I1**, 1100°C, 1 h, 5% H_2/95% Ar
J2	**J1**, 1100°C, 1 h, 5% H_2/95% Ar
K2	**K1**, 1100°C, 1 h, 5% H_2/95% Ar
L2	**L1**, 1100°C, 1 h, 5% H_2/95% Ar
M2	$(HSiO_{1.5})_n$, 1100°C, 1 h, 5% H_2/95% Ar

The composites **G2** and **H2** contained Si-NCs embedded in amorphous silica/aluminosilicate matrix, whereas composites **I2** and **J2** had Si-NCs within a complex matrix containing silica, aluminosilicate and γ-Al_2O_3 (whose corresponding diffraction peaks where observed in the XRD pattern, **Figure 2-12**).[43] At higher aluminum concentrations Si-NCs embedded in a silica and mullite matrix were obtained (**K2** and **L2**).[44]

The particle size (calculated *via* Scherrer analysis) increased from 5.9 to 10.4 nm going from composite **G2** to **H2** (**Figure 2-12**). This observation is attributed to the increasing content of aluminosilicate which softens at lower temperature (~800°C) and allows for the better mobility of Si atoms. The particle size does not vary significantly going from composite **H2** to **J2** (**H2** = 10.4 nm, **I2** = 11.3 nm and **J2** = 10 nm). At higher concentrations of $AlCl_3$ (i.e. composites **K2** and **L2**) the particle size decreased to 9.1 and 6.4 nm respectively, owing to the

increase in softening temperature of the matrix containing mullite. Si-NC size was calculated to be 3.4 nm for composite **M2** which did not contain any aluminum salt in its synthesis.

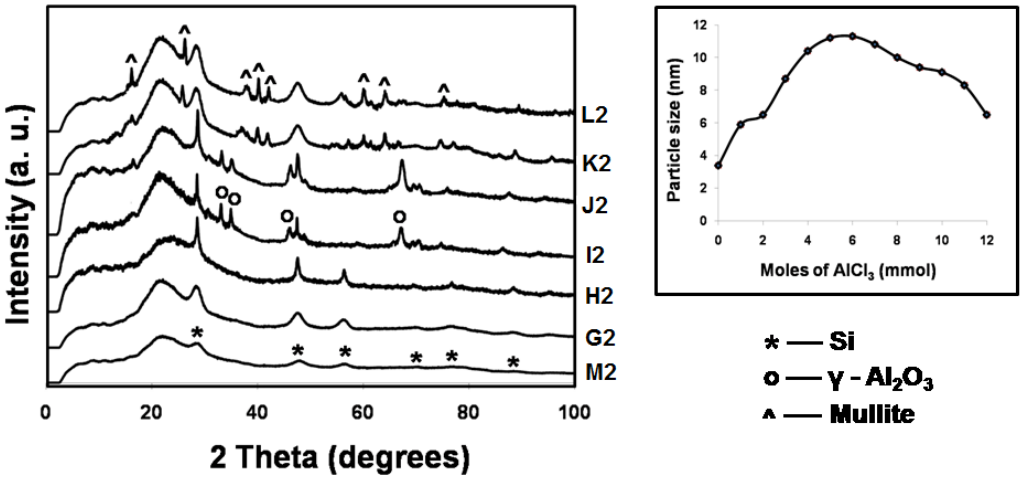

Figure 2-12. XRD pattern of various composites and the relationship of Si-NC size vs. varying amount of $AlCl_3$ added.

Since the matrix composition of samples **G2** and **H2** were not evident from XRD analysis due to their amorphous nature, their chemical composition was analyzed using O 1s XP spectra (**Figure 2-13**). Distinctive binding energies exist for O atoms bridging between Si, Al or combination of Si and Al atoms. The matrix in composite **M2** was primarily constituted of silica with peak centered at 533 eV. Composite **G2** contained silica and Si-O-Al bonds with binding energies centered at 533.4 and 531.7 eV, respectively. Composite **H2** contained combination of silica,

aluminosilicate and alumina with binding energies of the component peaks centered at 533.5, 532.1, and 530.9 eV respectively.[45]

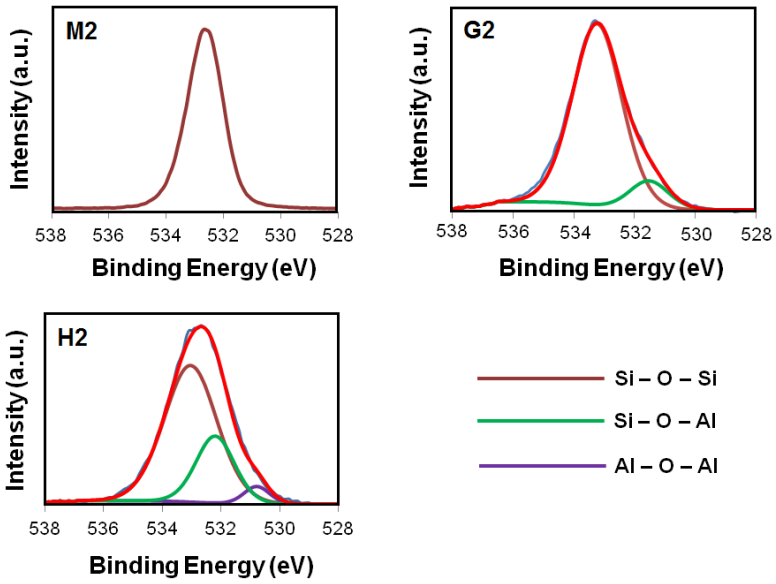

Figure 2-13. HR XP spectra of O 1s region of the samples **M2**, **G2** and **H2**.

2.2.3.3 Thermally processed hetero sol-gel polymers (influence of processing temperature)

Heteropolymer **H1** was processed at different temperatures ranging from 700 - 1100°C as summarized below.

Table 2-7: Thermally processed composites and processing conditions.

Sample	Processing conditions
N1	**H1**, 700°C, 1 h, 5% H_2/95% Ar
O1	**H1**, 800°C, 1 h, 5% H_2/95% Ar
P1	**H1**, 900°C, 1 h, 5% H_2/95% Ar
Q1	**H1**, 1000°C, 1 h, 5% H_2/95% Ar
R1	**H1**, 1100°C, 1 h, 5% H_2/95% Ar

The particle size increased with increasing temperatures as analyzed using XRD technique (**Figure 2-14**). The NC size was calculated to be 3.5, 4.8, 6.2, 8.4, and 10 nm for composites **N1**, **O1**, **P1**, **Q1** and **R1**, respectively.

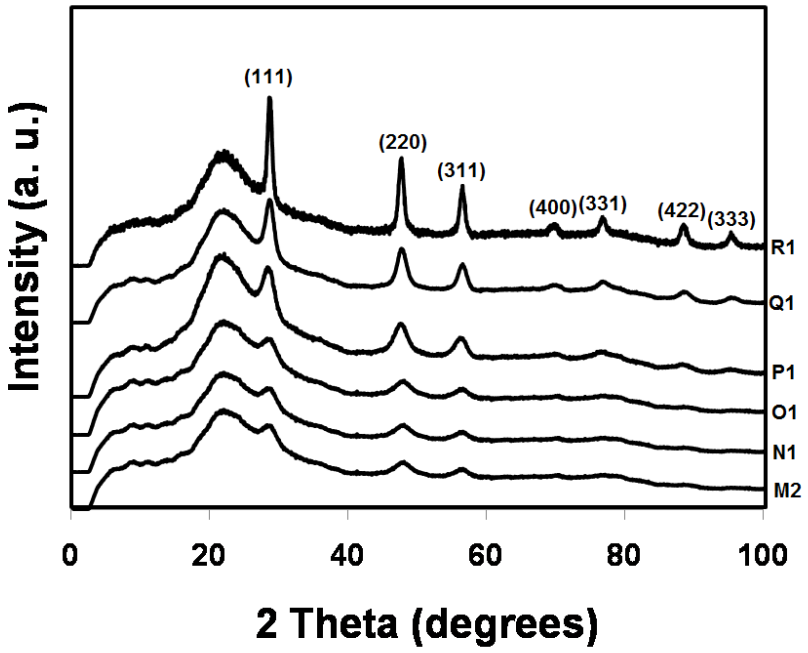

Figure 2-14. XRD pattern of composites **N1**, **O1**, **P1**, **Q1**, **R1** and **M2**.

Attempts were made to extract the Si-NCs from the matrix *via* HF etching. Except for the composite **M2** we were not able to completely etch away the matrix and isolate free-standing Si-NCs. Etching with caustic solutions such as NaOH and KOH was also attempted. However the etching rate could not be controlled and the Si-NCs were completely oxidized.

2.2.4 Conclusions

In conclusion, effects of various salts such as Na_2O, CaO, Al_2O_3, NaCl, $MgCl_2$ and $AlCl_3$ was studied on the softening of matrix. Promising results were

obtained with $AlCl_3$, where the salt hydrolyzed and polymerized with $HSi(OH)_3$ to yield hetero-copolymer. Upon thermal processing these sol-gel polymers yielded Si-NCs embedded within combination of silica, aluminosilicate, γ-alumina and mullite matrix depending on the $AlCl_3$ concentration. The resulting NCs were larger than those obtained from $(HSiO_{1.5})_n$ polymer alone. However we were not able to isolate free-standing Si-NCs as proper etching medium could not be determined.

2.3 References.

1. X. Chen, S. Shen, L. Guo and S. S. Mao, *Chem. Rev*., 2010, **110**, 6503.
2. M. Wang and W. Wang, *Environ. Sci. Technol*., 2008, **42**, 940.
3. F. Erogbogbo, K. T. Yong, I. Roy, G. X. Xu, P. N. Prasad and M. T. Swihart, *ACS Nano*, 2008, **2**, 873.
4. J. Y. Fan, X. L. Wu and P. K. Chu, *Prog. Mater. Sci*., 2006, **51**, 983.
5. H. Brequel, J. Parmentier, S. Walter, R. Badheka, S. Trimmel, S. Masse, J. Latournerie, P. Dempsey, C. Turquat, A. Desmartin-Chomal, L. Le Neindre-Prum, U. A. Jayasooriya, D. Hourlier, H. –J. Kleebe, G. D. Soraru, S. Enzo and F. Babonneau, *Chem. Mater*., 2004, **16**, 2585.
6. H. Wang, W. Yang, Z. Xie, Y. Wang, F. Xing and L. An, *J. Phys. Chem. C*, 2009, **113**, 5902.
7. R. Raj, R. Riedel and G. D. Soraru, *J. Am. Ceram. Soc*., 2001, **84**, 2158.
8. R. P. Alonso and G. D. Soraru, *J. Sol-Gel Sci. Technol*., 2007, **43**, 313.
9. P. H. Mutin, *J. Sol-Gel Sci. Technol*., 1999, **14**, 27.
10. Y. W. Kim, S. H. Kim, H. D. Kim and C. B. Park, *J. Mater. Sci*., 2004, **39**, 5647.
11. R. Ciriminna, M. Sciortino, G. Alonzo, A. De Schrijver and M. Pagliaro, *Chem. Rev*., 2011, **111**, 765.
12. S. E. Habas, H. A. S. Platt, M. F. A. M. van Hest and G. S. Ginley, *Chem. Rev*. 2010, **110**, 6571.
13. O. Kulikovska, L. M. Goldenberg, L. Kulikovsky and J. Stumpe, *Chem. Mater*., 2008, **20**, 3528.
14. C. M. Hessel, E. J. Henderson and J. G. C. Veinot, *Chem. Mater*., 2006, **18**, 6139.
15. C. M. Hessel, D. Reid, M. G. Panthani, M. R. Rasch, B. R. Goodfellow, J. Wei, H. Fujii, V. Akhavan and B. A. Korgal, *Chem. Mater*., 2012, **24**, 393.
16. M. Jimenez De Castro and J. C. Pivin, *J. Sol-Gel Sci. Tech*., 2003, **28**, 37.
17. E. J. Henderson, J. A. Kelly and J. G. C. Veinot, *Chem. Mater*., 2009, **21**, 5426.
18. A. T. R. Williams, S. A. Winfield and J. N. Miller, *Analyst*, 1983, **108**, 1067.
19. H. Nam, B. Boury and S. Y. Park, *Chem. Mater*., 2006, **18**, 5716.
20. V. Raman, O. P. Bahl and N. K. Jha, *J. Mater. Sci. Lett*., 1993, **12**, 1188.
21. C. C. Yang and W. C. Chen, *J. Mater. Chem*., 2002, **12**, 1138.
22. A. Chemtob, D. –L. Versace, C. C. Barghorn and S. Rigolet, *Macromolecules*, 2008, **41**, 7390.

23. C. Turquat, H. J. Kleebe, G. Gregori, S. Walter and G. D. Soraru, *J. Am. Ceram. Soc*., 2001, **84**, 2189.

24. D. Moore, J. R. Morber, R. L. Snyder and Z. L. Wang, *J. Phys. Chem. C*, 2008, **112**, 2895.

25. W. Yang, H. Miao, A. Xie, L. Zhang and L. An, *Chem. Phys. Lett*. 2004, **383**, 441.

26. A. Santoni, R. Frycek, P. Castrucci, M. Scarselli and M. D. Crescenzi, *Surf. Sci*., 2005, **582**, 125.

27. A. Avila, I. Montero, L. Galan, J. M. Ripalda and R. Levy, *J. Appl. Phys*. 2001, **89**, 212.

28. G. M. Renlund, S. Prochazka and R. H. Doremus, *J. Mater. Res*., 1991, **6**, 2723.

29. Y. Shi, Y. Wan, Y. Zhai, R. Liu, Y. Meng, B. Tu and D. Zhao, *Chem. Mater*., 2007, **19**, 1761.

30. M. Birot, J. –P. Pillot and J. Dunogues, *Chem. Rev*., 1995, **95**, 1443.

31. E. J. Henderson and J. G. C. Veinot, *J. Am. Chem. Soc*., 2009, **131**, 809.

32. S. S. Jedlicka, J. L. Rickus and D. Y. Zemlyanov, *J. Phys. Chem. B*, 2007, **111**, 11850.

33. W. H. Green, K. P. Le, J. Grey, T. T. Au and M. J. Sailor, *Science*, 1997, **276**, 1826.

34. E. W. Washburn, *J. Ind. Eng. Chem*., 1921, **13**, 477.

35. C. J. Phillips, *J. Chem. Educ*., 1942, **19**, 398.

36. M. M. Smedskjaer, J. C. Mauro, R. E. Youngman, C. L. Hogue, M. Potuzak and Y. Yue, *J. Phys. Chem. B*, 2011, **115**, 12930.

37. A. Tilocca and N. H. de Leeuw, *J. Mater. Chem*., 2006, **16**, 1950.

38. H. J. Clueley, *Analyst*, 1954, **79**, 567.

39. H. D. Richmond, *Analyst*, 1923, **48**, 260.

40. J. C. Hamilton, *Ind. Eng. Chem*., 1970, **62**, 16.

41. U. Schubert and N. Husing, *Synthesis of Inorganic Materials*, Wiley, Weinheim, 1st edn., 2000, ch. 4, pp. 215-220.

42. J. Roy, N. Bandyopadhya, S. Das and S. Maitra, *Ceramica*, 2010, **56**, 273.

43. Y. Liu, D. Ma, X. Han, X. Bao, W. Frandsen, D. Wang and D. Su, *Mater. Lett*., 2008, **62**, 1297.

44. M. A. Sainz, F. J. Serrano, J. M. Amigo, J. Bastida and A. Caballero, J. *Eur. Ceram. Soc*., 2000, **20**, 403.

45. M. Todea, E. Vanea, S. Bran, P. Berce and S. Simon, *Appl. Surf. Sci*., 2013, **270**, 777.

Chapter 3:

Synthesis of Silicon Nano/Micro Materials *via* Magnesiothermic Reduction*

* Portions of this chapter has been published

- M. Dasog, Z. Yang and J. G. C. Veinot, *CrystEngComm*., 2012, **14**, 7576 - 7578.

(Reproduced by permission of The Royal Society of Chemistry)

3.1 Synthesis of Silicon Materials *via* Magnesiothermic Reduction.

3.1.1 Introduction

Silicon nanocrystals (Si-NCs) have become a material of significant interest due to their unique optoelectronic properties,[1] biocompatibility,[2] and abundance. Si-NCs may be prepared using physical methods such as, ion implantation,[3] vacuum evaporation,[4] and sputtering.[5] These methods often require costly infrastructure and are impractical for making large quantities of material. Si-NCs can also be prepared chemically *via* solution phase methods, however these syntheses often employ somewhat specialized and/or harmful precursors.[6-8] In addition, Si-NCs obtained from these procedures are often size polydisperse, amorphous, and can require high temperature annealing to induce crystallinity. Solid-state synthesis of Si-NCs from silicon rich oxide (SRO) precursors has gained substantial attention due to the ease and scalability as discussed in the Chapter 2.[9-11] These syntheses use high temperatures (*i.e.*, T>1000ºC) to yield silicon oxide embedded Si-NCs. Unfortunately, the atom economy of these procedures is poor and only approximately one quarter of the available silicon in the precursor is converted into elemental silicon (*i.e.*, $4SiO_{1.5} \rightarrow 3SiO_2 + Si$). In addition, disproportionation of SROs allows preparation of Si-NCs only in the size regime of 3 – 15 nm and as particle dimension increases so does the size polydispersity.[12] To date, no reports describing the syntheses of large Si-NCs (diameter > 20 nm) with narrow size distribution have appeared.

Magnesiothermic reduction offers a straightforward way to convert silica (inexpensive and the most stable source of Si) into elemental silicon while retaining silica particle morphology.[13] In this section of this Chapter, the syntheses of Si particles and thin films by direct reduction of silica precursors using magnesium (Mg) is described. The optical properties of the Si thin films obtained *via* Mg reduction is also summarized. Simple organic light emitting diodes (OLEDs) were fabricated with Si thin film as transparent conductor and the device performance is briefly discussed.

3.1.2 Experimental

3.1.2.1 Materials.

Tetraethoxysilane (TEOS, 99%, Sigma-Aldrich), ammonium hydroxide (NH_4OH, 42%, Caledon), magnesium powder (Mg, 99%, BDH), toluene (ACS grade, BDH), ethanol (ACS grade, Sigma-Aldrich), hexanes (ACS grade, BDH), FOx® 16 - a methyl isobutyl ketone (MIBK) solution of hydrogen silsesquioxane (HSQ, Dow Corning), poly(3,4-ethylenedioxythiophene)-poly(styrenesulfonate) 1.3 wt% solution in water (PEDOT:PSS, Sigma-Aldrich), poly[2-methoxy-5-(2-ethylhexyloxy)-1,4-phenylenevinylene] (MEH-PVV, Sigma-Aldrich) were used as received. The quartz and indium tin oxide (ITO) coated glass were purchased from Esco products.

3.1.2.2 Synthesis of Stöber silica particles.

Stöber silica particles were synthesized *via* base catalyzed sol-gel method. Briefly, TEOS (10 mL, 45 mmol) was stirred with ethanol (10 mL), deionized water (20 mL) and NH_4OH solution (42 %, 5 mL) for varying times (tabulated below) to yield different size particles. The white precipitate was collected by vacuum filtration and washed with deionized water multiple times (4 × 25 mL). The solid was transferred to an oven and kept there for 24 hours at 100 ^{o}C to drive off any residual water and ethanol.

Table 3-1. Varying Stöber silica particle sizes with the reaction time and respective reaction yields. The particle size was determined from electron microscopy images.

Reaction time (hour)	Particle size (nm)	Reaction yield (%)
0.5	6.0 ± 2	52
1	15 ± 4	59
2	25 ± 6	63
5	40 ± 8	66
10	52 ± 8	74
24	75 ± 8	85
36	83 ± 10	82
48	95 ± 8	85
60	120 ± 10	88
72	145 ± 8	94
84	170 ± 10	90
100	200 ± 18	92

3.1.2.3 Synthesis of silicon particles.

Silica particles (1.00 g, 17 mmol) and magnesium powder (0.87 g, 36 mmol) were mixed together manually and thermally processed at 500°C for 15 hours under argon atmosphere (*Caution: Magnesium silicide might be formed as a byproduct, which can lead to formation of pyrophoric silane gas during HCl reaction*). The resulting grey/brown powder was treated with 5 M hydrochloric acid (15 mL) for an hour to remove magnesium oxide (MgO). The brown precipitate was obtained by vacuum filtration and was washed with deionized water until the washings had a neutral pH (ca. 7) as examined using pH paper. The solid was further washed with ethanol (20 mL) and acetone (3 × 20 mL) and was air dried to yield oxide coated Si-NCs.

3.1.2.4 Formation of Si thin films on quartz.

Quartz substrates were sonicated in hexanes (20 mL) to remove any organic surface residues for 15 min and dried in a jet of N_2. A pre-determined thickness of Mg was vapor deposited at a base pressure of 5×10^{-6} mbar, starting at the initial temperature of 24.7 ^{o}C. The material was laid down at 2.0 Å/s with the final temperature of the evaporation peaking at 45.7^{o}C. After deposition the substrates were transferred to a tube furnace and annealed for 8 hours at 700 ^{o}C. After cooling down to the room temperature, the substrates were immersed in 5 M HCl solution (20 mL) for an hour. The substrates were then washed using acetone and stored in vacuum oven until further use.

3.1.2.5 Fabrication of organic light-emitting diodes (OLEDs). *Note: Device fabrication was performed by Larissa Smith*.

OLEDs were fabricated by spincoating a hole transport layer, PEDOT:PSS (0.5 mL) on the silicon thin film (that were made using the procedure outlined in section 3.1.2.4) at 4000 rpm. The hole transport layer was annealed for 2 hours at 150°C in air. Then the emissive layer, MEH-PPV (10 mg/mL, in chlorobenzene) was spun coat at 3000 rpm and annealed at 70 °C for two hours in air. Finally, 80 nm of Al was deposited (*via* thermal evaporation) to act as a cathode at a rate of 1Å/s for the first 5nm, 1.5Å/s for the next 5nm and 2Å/s for the remainder of the deposition at a base pressure of $5x10^{-6}$ mTorr.

A control ITO-based device was prepared in parallel to the Si thin film (STF) devices. The ITO film was cleaned prior to use through plasma etching on a Reactive Ion Etch with 80% O_2 pressure at 150 mTorr with 235 watts of RF for 1 minute. It was then transported in a vacuum chamber and the hole transport layer was deposited *via* spincoating within thirty minutes of etching. The remaining layers were deposited in parallel when silicon thin film device was prepared.

These prototype OLEDs were tested by a Keithley 2400 multimeter with in-house software.

3.1.2.6 Fourier Transform Infrared Spectroscopy (FTIR)

FTIR spectroscopy was performed on powder samples using a Nicolet Magna 750 IR spectrometer.

3.1.2.7 X-ray Powder Diffraction (XRD)

XRD was performed using an INEL XRG 3000 X-ray diffractometer equipped with a Cu K_α radiation source (λ = 1.54 Å). Bulk crystallinity for all samples was evaluated on finely ground samples mounted on a low-intensity background silicon (100) sample holder.

3.1.2.8 Absorbance (UV-Vis) Spectroscopy

UV-Visible spectra were recorded on Cary 400 UV-Vis Spectrometer. A clean quartz substrate was used as the background.

3.1.2.9 Transmission Electron Microscopy (TEM) and Energy Dispersive X-Ray Spectroscopy (EDX)

TEM and EDX analyses were performed using a JOEL-2010 (LaB_6 filament) with an accelerating voltage of 200 kV. TEM samples of Si-NCs were drop-cast onto a holey carbon coated copper grid and allowing the solvent to evaporate under vacuum. The particle sizes were measured using Image J software.[17]

3.1.2.10 Scanning Electron Microscopy (SEM)

SEM analysis was performed on JSM- 6010LA In TouchScope instrument with an accelerating voltage of 10 kV. The powder sample was mounted on carbon tape for imaging.

3.1.3 Results and Discussion

3.1.3.1 Synthesis of Stöber silica particles.

Stöber silica particles were prepared *via* base catalysed sol-gel reactions of tetraethoxysilane (TEOS).[14] The silica particle size was tailored by controlling the reaction time as shown in **Figure 3-1**.

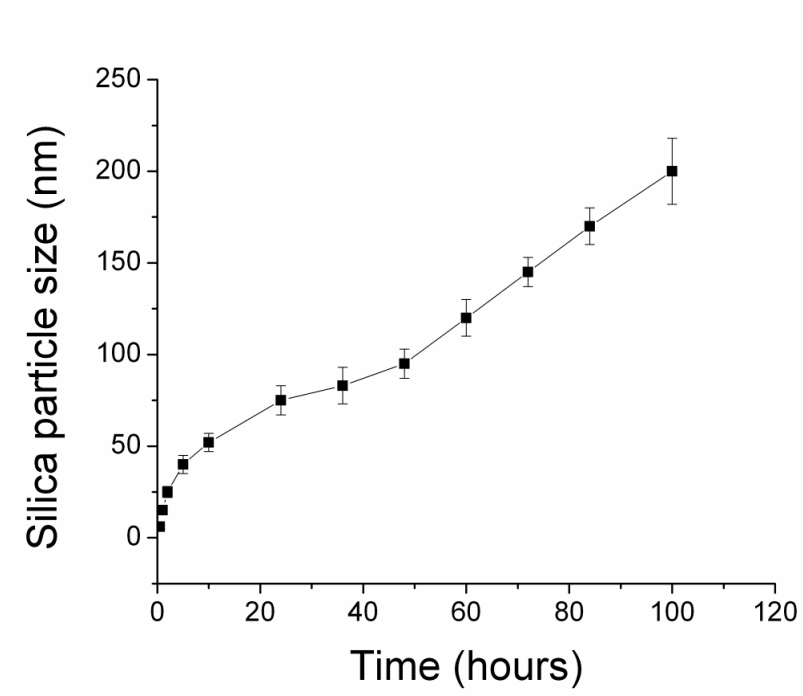

Figure 3-1. Evolution of Stöber silica particle size as a function of reaction time.

Scanning electron micrograph (SEM) images of representative silica particles are shown in **Figure 3-2**. The FTIR spectrum of representative silica particles shows characteristic Si-O-Si stretching at ca. 1100 cm^{-1} (**Figure 3-3**).[15]

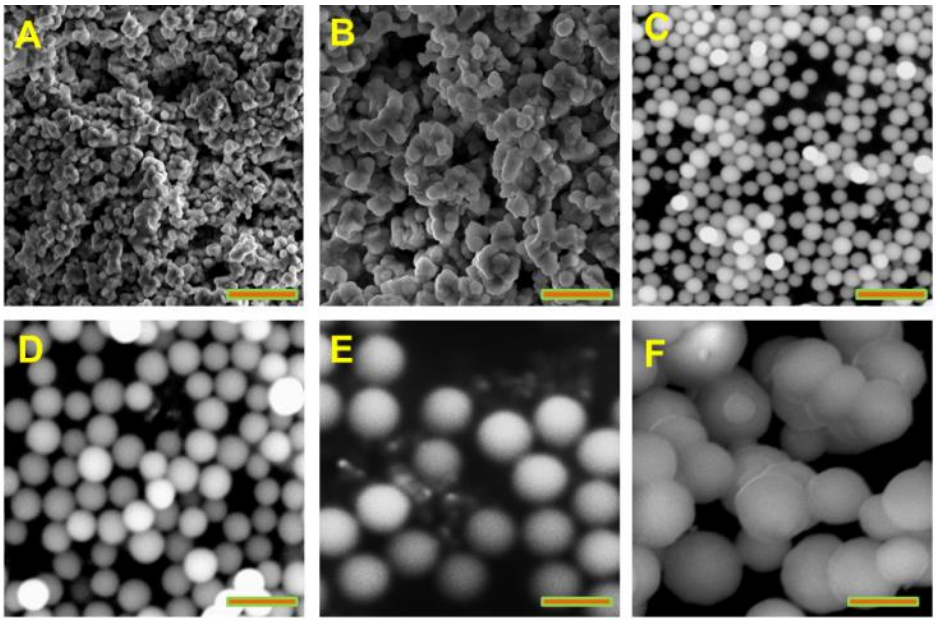

Figure 3-2. Scanning electron micrograph (SEM) images of Stöber silica particles of average sizes ca. (**A**) 15 nm (**B**) 40 nm (**C**) 75 nm (**D**) 95 nm (**E**) 145 nm, and (**F**) 200 nm. The scale bar represents 200 nm.

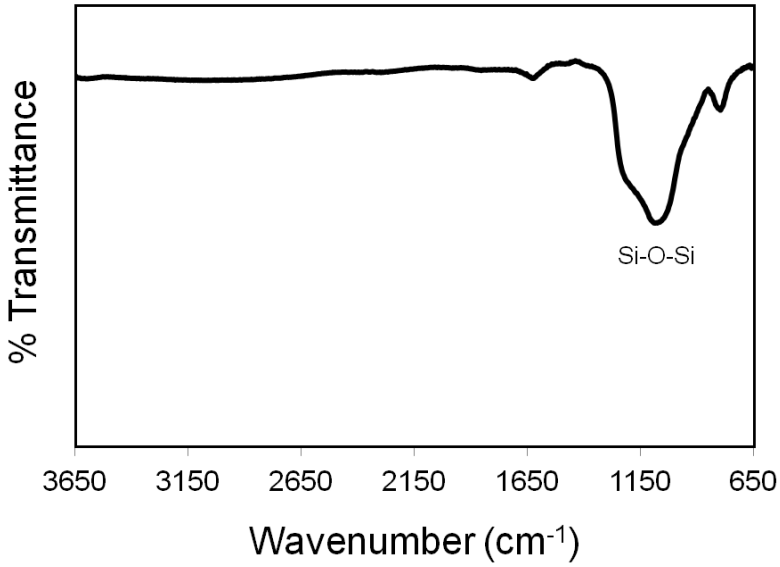

Figure 3-3. FTIR spectrum of 200 nm Stöber silica particles.

3.1.3.2 Synthesis of silicon particles *via* magnesiothermic reduction.

The silica particles were mechanically mixed with stoichiometric amounts of magnesium powder and the mixture was annealed at 500 ^{o}C in a flowing Ar atmosphere. The resulting mixture was treated with hydrochloric acid to remove magnesium oxide and unreacted Mg powder. The formation of crystalline Si was confirmed using powder X-Ray diffraction which showed characteristic peaks for diamond structure of Si (**Figure 3-4**).[9]

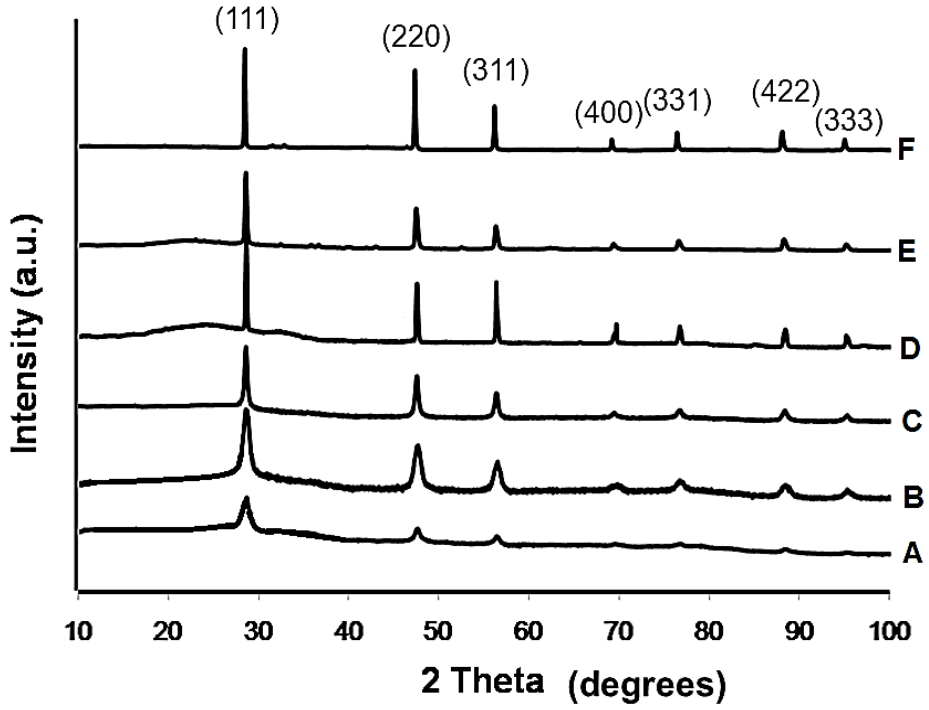

Figure 3-4. Powder X-Ray diffraction patterns of (**A**) 4 nm (**B**) 9 nm (**C**) 20 nm (**D**) 32 nm (**E**) 45 nm, and (**F**) 70 nm Si-NCs, respectively.

The transmission electron microscopy (TEM) images, representative selected area electron diffraction (SAED) and energy dispersive X-Ray (EDX) spectra of the Si-NCs are shown in **Figure 3-5**. Absence of any substantial silicon oxygen signal in EDX confirms complete reduction of silica. Of important note, no magnesium was detected at the sensitivity of the EDX method consistent with complete removal of any byproducts or unreacted Mg metal.

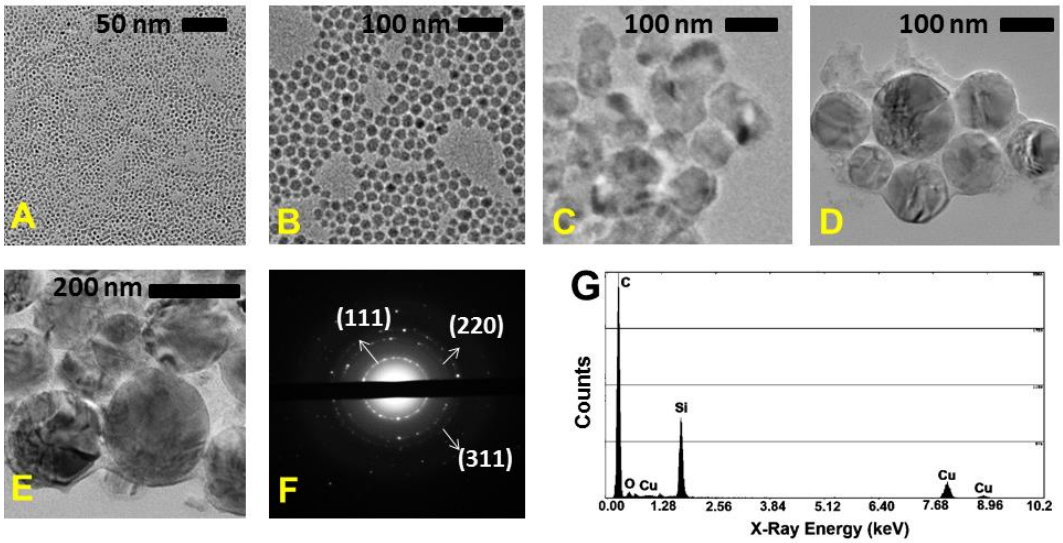

Figure 3-5. TEM images of ca. (**A**) 4 nm (**B**) 23 nm (**C**) 75 nm (**D**) 110 nm (**E**) 177 nm, Si-NCs. (**F**) SAED pattern for the 110 nm Si-NCs. The d-spacing for (111), (220) and (311) Miller indices are 3.24 Å, 1.93 Å and 1.69 Å respectively. (**G**) EDX spectrum of 110 nm Si-NC sample. EDX analyses of all the Si-NCs showed very similar spectra.

The sizes of Si-NCs prepared *via* Mg reduction are tabulated in **Table 3-2**. The particles obtained *via* Mg reduction are porous and the formation of pores are discussed in Section 3.2 of this Chapter.

Table 3-2. Silica and Si-NCs sizes obtained from electron microscopy.

Silica particles	**Si-NCs**
6.0 ± 2 nm	4 ± 1 nm
15 ± 4 nm	12 ± 3 nm
25 ± 6 nm	23 ± 2 nm
40 ± 8 nm	35 ± 5 nm
52 ± 8 nm	45 ± 6 nm
75 ± 8 nm	67 ± 8 nm
83 ± 10 nm	75 ± 7 nm
95 ± 8 nm	88 ± 8 nm
120 ± 10 nm	110 ± 15 nm
145 ± 8 nm	132 ± 12 nm
170 ± 10 nm	150 ± 20 nm
200 ± 18 nm	177 ± 20 nm

3.1.3.2 Silicon thin films.

With the depleting supply of indium,[16] a replacement for indium tin oxide (ITO) which is the most commonly used as a transparent conductor in various

electronic devices must be found.[17-20] Si thin films were explored as a potential replacement. Si films of various thicknesses were made directly on the quartz by depositing predetermined amounts of Mg and heating the substrates at 700 ^{o}C for 8 hours. The byproduct MgO was removed by immersing the substrates in HCl solution for an hour. The relationship between Mg thickness and the resulting Si film thickness is shown in the **Figure 3-6A**. A representative SEM image of the thin film is shown in **Figure 3-6B** and the film is porous in nature.

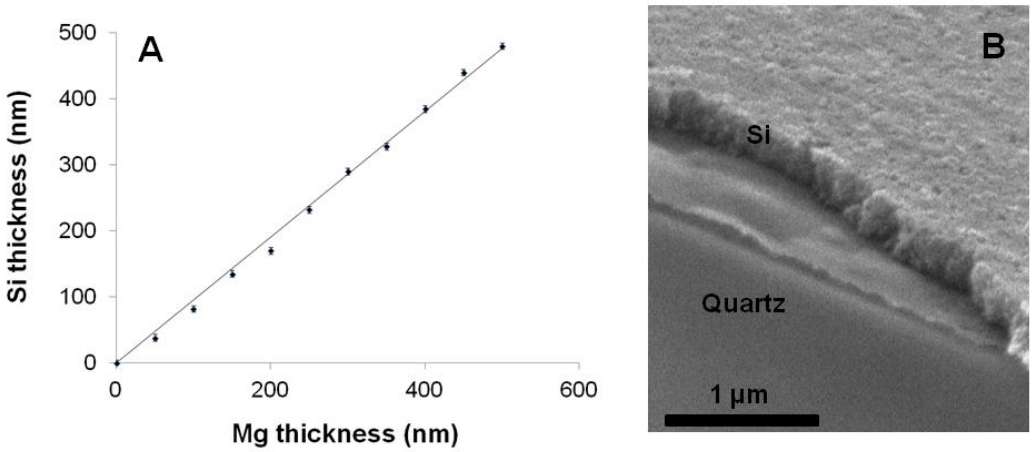

Figure 3-6. (**A**) Thickness (SEM) of Si layer formed as a function of initial Mg thickness. The values were obtained from SEM analysis. (**B**) SEM image of a cross-section of Si thin film on quartz.

The optical properties of Si thin films of various thicknesses were investigated using UV-Vis absorbance measurements (**Figure 3-7A**). The substrates become opaque at ~ 300 nm thick Si film (**Figure 3-7B**).

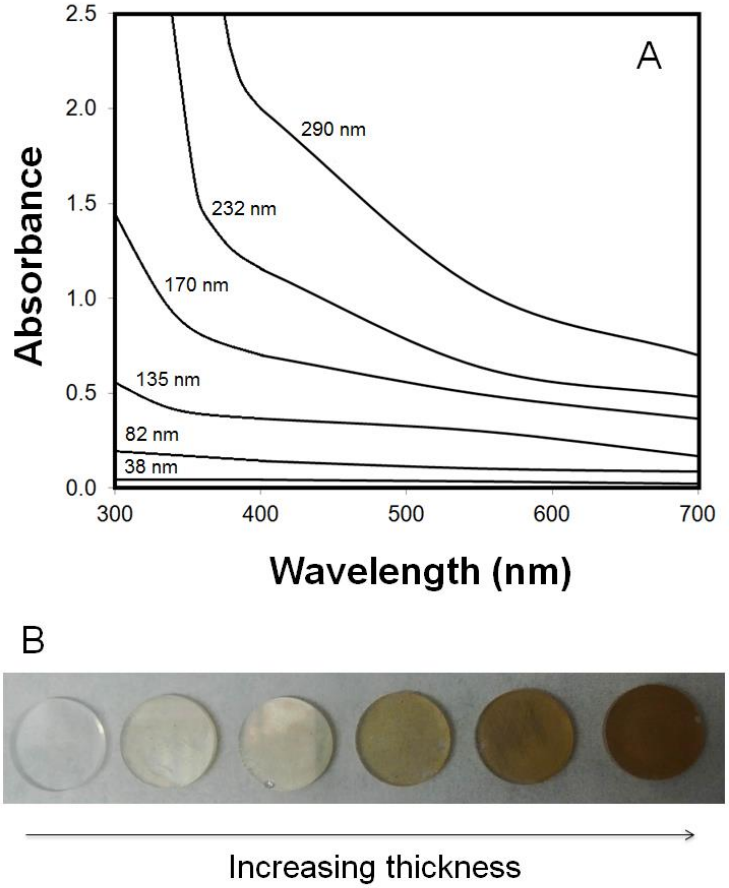

Figure 3-7. (**A**) Absorbance spectra of Si thin films of varying thickness on quartz. (**B**) Photograph of Si thin films on quartz with varying thickness.

The transmittance of Si films at three different wavelengths, *i.e.*, 700, 550, and 400 nm are shown in **Figure 3-8**. The transparency decreases rapidly with increasing Si film thickness.

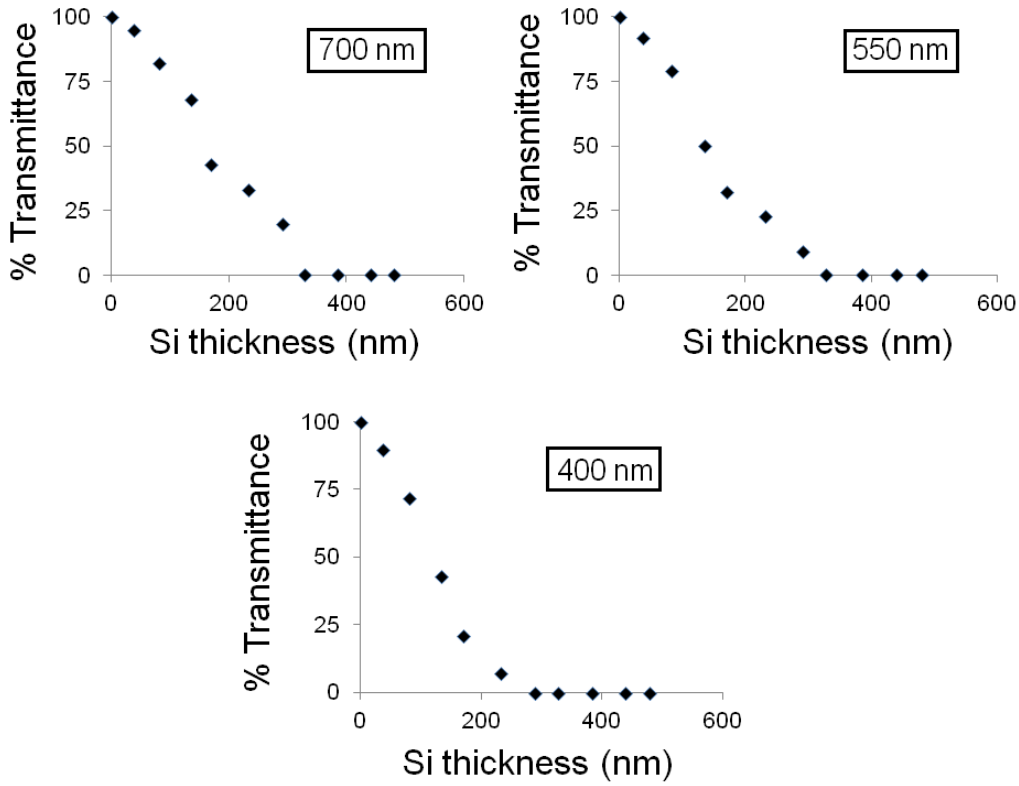

Figure 3-8. Transparency of Si thin films of various thickness at 700, 550, and 400 nm.

3.1.3.3 Si thin film based OLEDs.

The typical OLED device structure used in current study is shown in **Figure 3-9**. The ITO standards were tested alongside the Si thin film devices. They were tested within 12 hours of depositing the Al cathode to ensure that oxidation did not affect the results. The devices were tested with a Keithley 2400 sourcemeter and custom software (*device testing was performed by Tate Hauger at NINT*).[21]

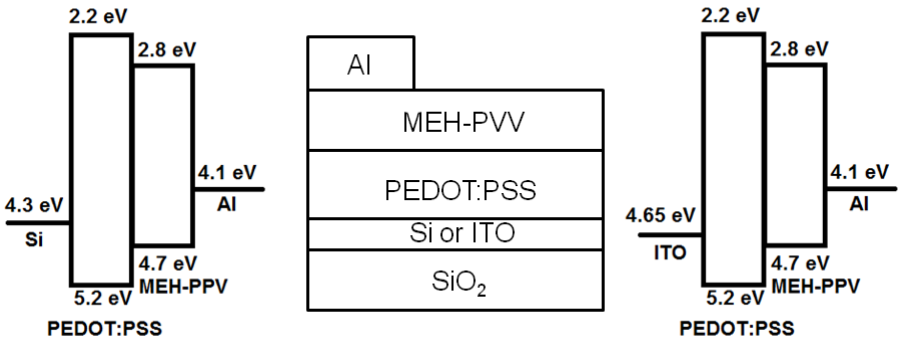

Figure 3-9. Device structure of OLED with Si thin film and ITO as transparent conducting layer.

Figure 3-10 shows the typical current-voltage (i.e., I-V) curves obtained for OLED devices. The ITO devices showed a turn-on voltages of ~ 4 V, while the Si thin film (with thickness of 135 and 170 nm) based devices had lower turn-on voltage of ~ 1.5 V. However, the Si thin film based devices shorted after 5 - 6 cycles. Also the luminance output of a Si thin film device was lower than the ITO device (examined qualitatively). The devices employing Si films with thicknesses less than 135 nm exhibited I-V curves characteristic of a resistor instead of a diode. While these preliminary results are promising, further study needs to be done with different emitting materials and a doped Si thin film to obtain devices with optimized performance.

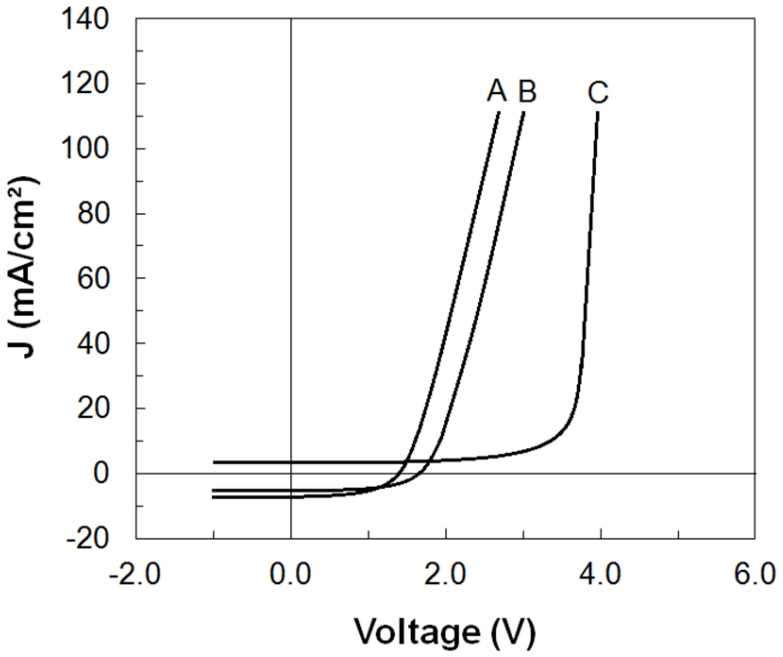

Figure 3-10. Typical I-V curves obtained from testing OLEDs with (A) 135 nm thick Si film, (B) 170 nm thick Si film, and (C) ITO as the transparent conducting layer.

3.1.4 Conclusions

Magnesiothermic reduction offers a versatile and scalable method to prepare porous Si materials. Apart from the Si-NCs and Si thin film discussed here, Si materials of different morphologies are shown in **Figure 3-11**. Si thin films were tested as a potential transparent conductor in OLEDs and requires further optimization to obtain functional devices. The Si-NCs are being investigated for Li ion battery applications.

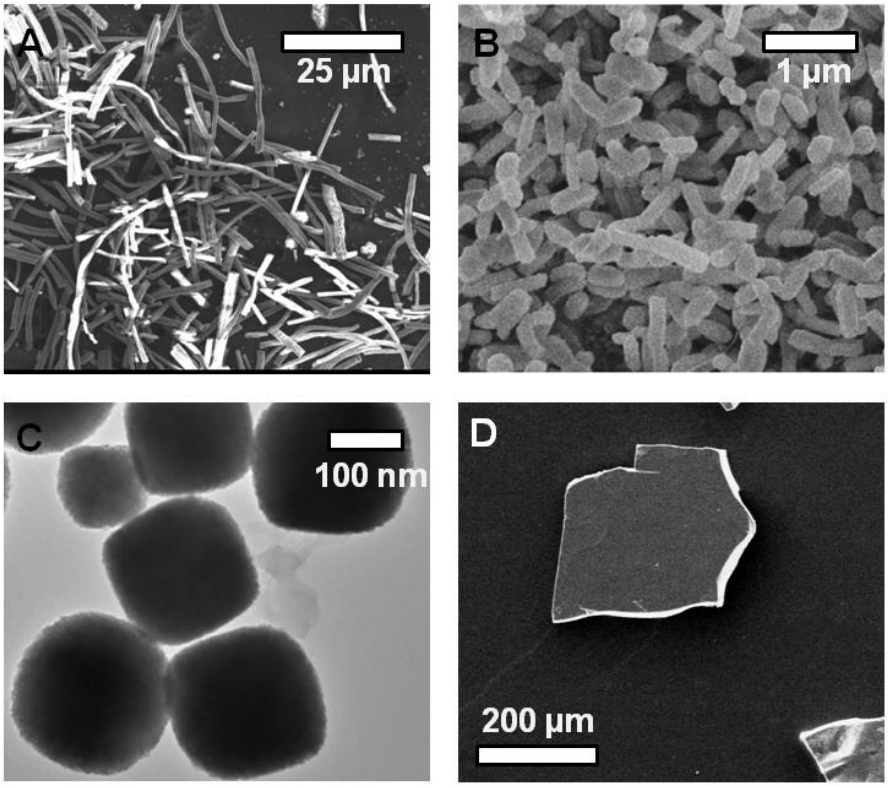

Figure 3-11. Electron microscopy images of silicon based nano/micromaterials in the shape of (**A**) fibers, (**B**) rods, (**C**) cubes, and (**D**) freestanding film.

3.2 Mechanistic Insight into Magnesiothermic Reduction.

3.2.1 Introduction

Scalable fabrication protocols for synthesizing micro- and nano-materials with complex morphologies will have a significant impact on current and potential applications of these materials in various fields including sensing, photovoltaics, portable electronics, light weight materials, *etc*.[1-7] Magnesiothermic reduction is one such method that can be employed to make materials such as aluminum (Al),[22] silicon (Si),[13] germanium (Ge),[23] their alloys,[24,25] among others[26-29] starting with their oxide precursors. This approach has been rapidly gaining attention in the scientific community, particularly from those working in silicon micro/nanomaterial syntheses; this attention is evidenced by the increase in the trend in related peer reviewed publications related to this topic over the last five years (**Figure 3-12**).[30-52]

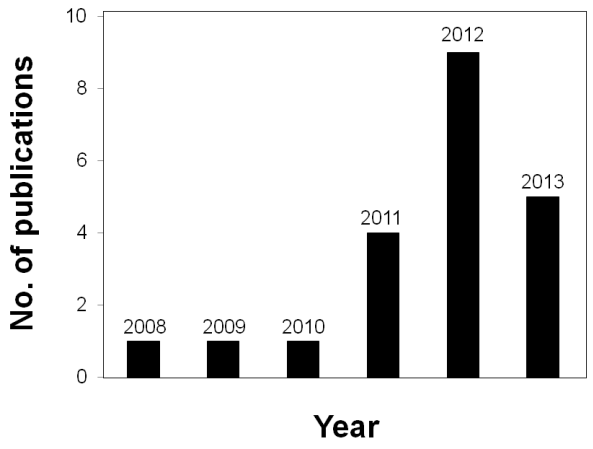

Figure 3-12. The growth of publications in the area of magnesiothermic reduction to form silicon micro/nanomaterials since 2008.[53]

Magnesiothermic reduction allows fabrication of porous Si materials starting from inexpensive silica precursors such as, glass, sand, sol-gel polymers, *etc*.[40-50] The reaction products are thermodynamically favored because of the formation of magnesium oxide (MgO) [**1**], however the reaction can proceed further to form magnesium silicide (Mg_2Si) as shown in the reaction scheme below [**2**].[54] Mg_2Si is an undesirable byproduct because pyrophoric silane gas is formed during the removal of MgO using hydrochloric acid (HCl) [**3**]. This often limits the scalability and widespread use of magnesiothermic reduction.

$$2\ Mg + SiO_2 \longrightarrow 2MgO + Si \qquad [\mathbf{1}]$$

$$2\ Mg + Si \longrightarrow Mg_2Si \qquad [\mathbf{2}]$$

$$Mg_2Si + 4\ HCl \longrightarrow SiH_4 + 2\ MgCl_2 \qquad [\mathbf{3}]$$

While reaction stoichiometry plays a crucial role, formation of Mg_2Si has been observed in the systems where Mg is the limiting reagent.[39] To date, no clear explanation has been offered for this observation. In addition, detailed analyses of reaction parameters such as effect of reaction temperature, precursor morphology, size, *etc*. on the progress of magnesiothermic reduction has not been reported to date. If use of Mg reduction is to become more widespread and its full potential realized, a detailed understanding of the contributing processes is of paramount importance.

In the following section of this Chapter, the influence of various reaction conditions (*i.e*., temperature, reactant concentrations), precursor size, shape, and porosity is discussed and a full complement of state-of-the-art characterization

techniques including, electron microscopy, XPS, XRD, and porosity measurements (BET analysis) have been used to provide this insight.

3.2.2 Experimental

3.2.2.1 Materials.

MCM-41 (99%, Sigma-Aldrich), silica aerogel (provided by Wacker Chemie, Munich, Germany), acid purified sand (50-70 mesh particles, Sigma-Aldrich), borosilicate glass (Esco products), hydrofluoric acid (HF, 49%, J. T. Baker), dichloromethane (ACS grade, BDH) were all used without further purification.

3.2.2.2 Formation of Si thin films on borosilicate glass.

Borosilicate glass was immersed in dichloromethane (10 mL) and sonicated for 15 minutes and was dried in flowing N_2. Required thickness of Mg was vapor deposited at a base pressure of $5x10^{-6}$ mbar, starting at the initial temperature of 24.7 ^{o}C. The material was laid down at 2.0 A/s with the final temperature of the evaporation peaking at 45.7 ^{o}C. After the deposition the substrates were transferred to a tube furnace and annealed at 500 ^{o}C for 12 hours. After cooling down to the room temperature, the substrates were immersed in 5 M HCl solution (20 mL) for an hour. The substrates were then washed in acetone and stored in vacuum oven until further use.

3.2.2.3 Magnesiothermic reduction of silica precursors.

The silica precursor (0.50 g, 8.33 mmol) was manually mixed with Mg powder (0.44 g, 18.33 mmol) using a spatula and transferred to an alumina boat. The reaction mixture was heated at the required temperature (between 500 – 700 ^{o}C) in a tube furnace under an argon atmosphere. After cooling to room temperature the reaction mixture was treated with 5 M HCl solution (20 mL) for an hour to remove the byproducts (*i.e.*, MgO, unreacted Mg, Mg_2Si). The Si product was collected by vacuum filtration and washed multiple times with deionized water until the washings were pH 7. The powder was dried in a vacuum over overnight at 100 ^{o}C.

3.2.2.4 Hydrofluoric (HF) acid etching.

0.25 g of the silicon material obtained from the Mg reduction was reacted with 1 mL EtOH, 0.5 g deionized water and 0.5 mL 49% HF solution for 15 minutes. The hydride terminated Si was extracted into toluene (25 mL) and was washed twice with toluene *via* centrifugation at 7000 rpm.

3.2.2.5 Depth profiling using X-ray photoelectron spectroscopy (XPS).

XPS analysis was performed using a Kratos Axis Ultra instrument operating in energy spectrum mode at 210 W. The base pressure and operating chamber pressure were maintained at 10^{-7} Pa. A monochromatic Al K_{α} source (λ = 8.34 Å) was used to irradiate the samples, and the spectra were obtained with an electron take-off angle of 90°. To minimize sample charging, the charge neutralizer filament was used when required. Survey spectra were collected using an elliptical spot with major and minor axis lengths of 2 and 1 mm, respectively, and 160 eV pass energy

with a step of 0.33 eV. CasaXPS software (VAMAS) was used to interpret high-resolution (HR) spectra. All of the spectra were internally calibrated to the C 1s emission (284.8 eV). After calibration, the background was subtracted using a Shirley-type background to remove most of the extrinsic loss structure.

The high-resolution chemical composition information was obtained as a function of depth (depth-profiling) by interleaving XPS analysis and Argon ion sputtering. Argon ion beam with an energy of 4 keV was used. The beam was rastered 1.5 X 1.5 mm2 and photoelectron signal was measured from the center of the etched crater. As usual the pass energy was 0.4 for the survey spectra and 0.1 eV for the high resolution spectra.

3.2.2.6 Porosity measurements. *Note: Measurements were performed by researchers at Wacker Chemie, Germany*.

The N_2 absorption/desorption isotherms were measured at 77 K using Sorptomatic 1990 instrument. The pore size distribution were calculated using the BJH model.[55] The surface area was calculated by the BET method.[56]

3.2.3 Results and Discussion.

3.2.3.1 Reduction mechanism.

It is commonly believed that the reduction of silica occurs *via* diffusion of Mg atoms into SiO_2 structure.[13,38-44] Bao *et al*. propose that at 650 ^{o}C gaseous Mg is formed which can diffuse through the structure and reduce silica.[13] They further

propose the MgO phase is present intertwined in the Si product and its removal yields porous Si structure. However, we have observed that the reduction can occur at much lower temperatures (~450°C) where gaseous Mg is not likely to be present. In order to understand the mobility of various ions throughout the reaction progress, SiO_2/Mg interfaces were assembled as thin films and studied to investigate the formation of Si. Evaluation of cross-sections of these controlled film geometries provided opportunity to monitor of the materials formed in the reaction zone as the reaction proceeded. A 200 nm thick Mg film was vapor deposited onto borosilicate glass and the substrates were heated for 12 hours at 500 ^{o}C in an Ar atmosphere. The films were evaluated using SEM and XPS before and after annealing (**Figure 3-13**). After heating, the Mg/SiO_2 substrates showed three distinctive layers: SiO_2, Si and MgO. Removal of the MgO layer was achieved upon exposure to dilute HCl and confirmed using SEM (see **Figure 3-13C**).

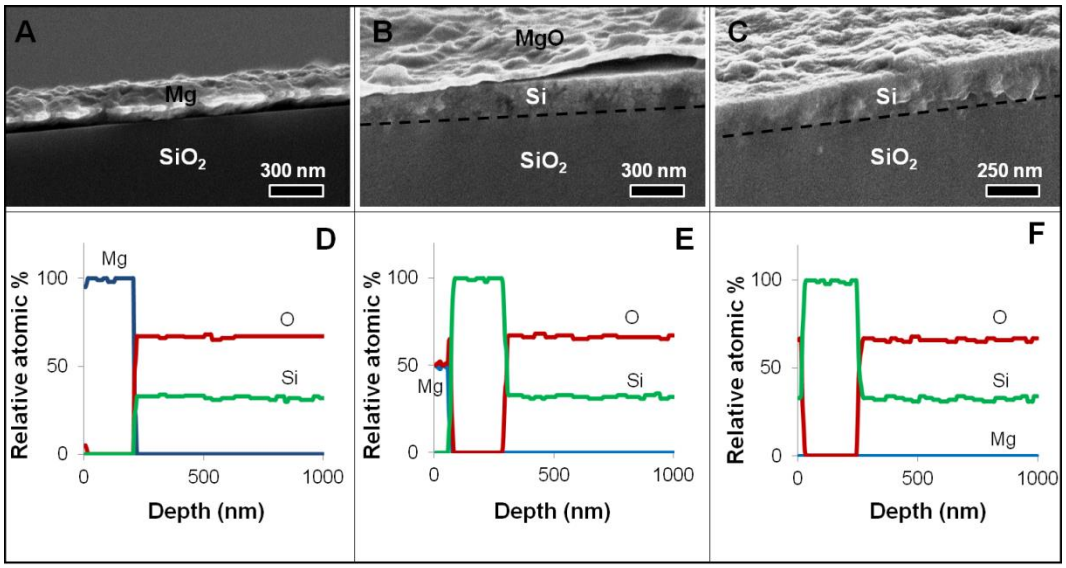

Figure 3-13. SEM secondary electron images of thin-film cross-sections of (**A**) Mg deposition on glass, (**B**) after heating the Mg substrate, and (**C**) after exposure to aqueous HCl. Elemental composition (determined using XPS) at different depths for thin films (**D**) after Mg deposition on glass, (**E**) after heating the Mg substrate, and (**F**) after HCl washing.

High-resolution elemental analysis depth profiling was performed using XPS and Ar sputtering. Contrary to previous reports, no Mg was detected within the Si layer at the sensitivity of the XPS method (ca. 3 atomic %) before or after exposure to aqueous HCl. In addition, no Si was detected in the MgO phase. These observations are consistent with oxygen (O) ions migrating during the reaction process.

Brunauer-Emmett-Teller (BET) analysis of Si obtained from magnesiothermic reduction of SiO_2 indicated the product was porous with surface

areas of ca. 150 - 170 m^2/g for particles obtained from reduction of Stöber silica. A more detailed examination of the gas adsorption isotherms indicated pores with average diameter of 30 nm for Stöber silica particles (**Figure 3-14**) and two pore types existed in the Si structures: mesopores of d = 2 - 4 nm and 25 - 50 nm (**Figure 3-15**). The 2 - 4 nm pores might be arising from removal of O atoms and shrinkage in the Si crystal structure.

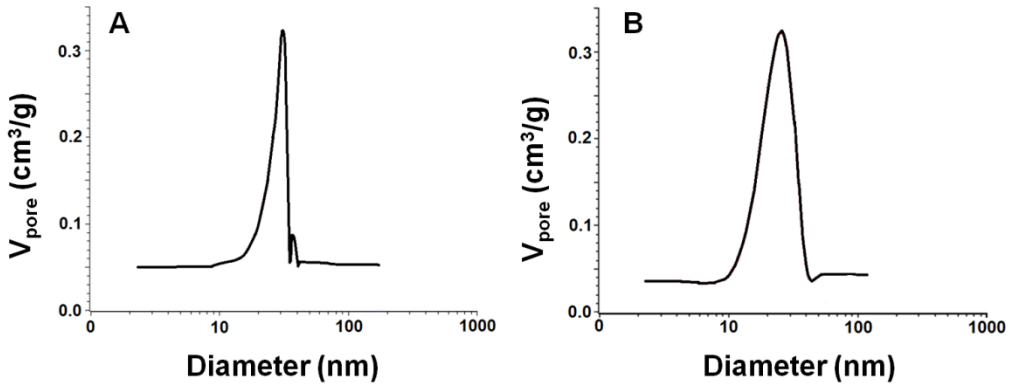

Figure 3-14. Pore size distribution (BJH) plots of Stöber silica particles with average particle size of (**A**) 90 nm and (**B**) 140 nm.

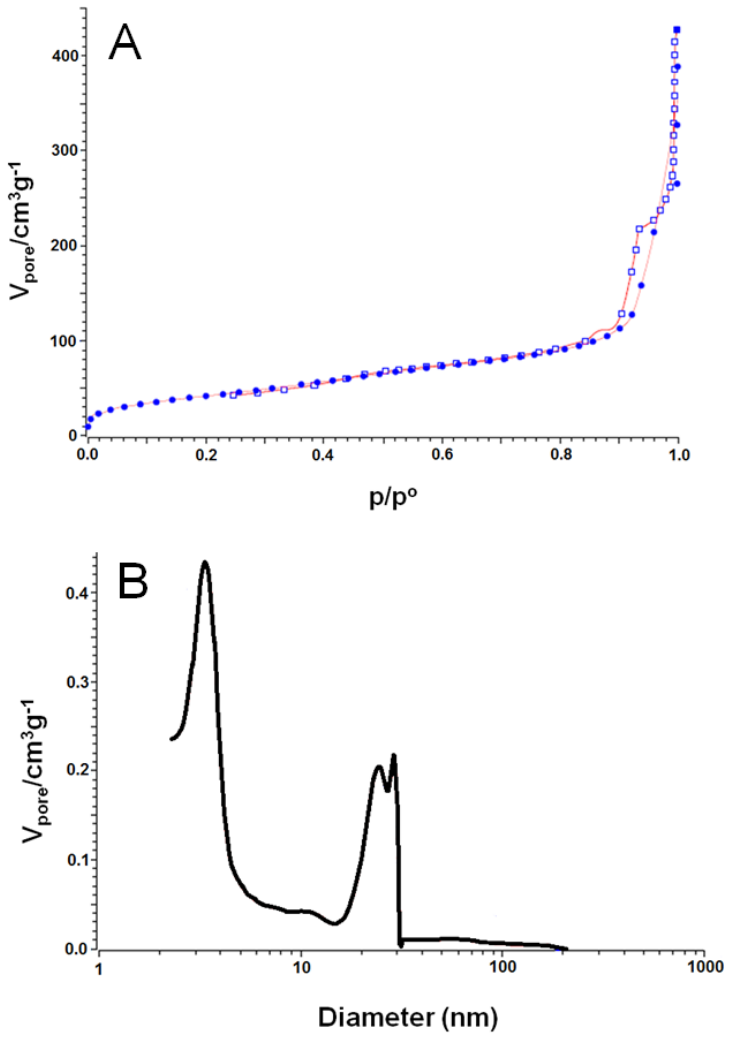

Figure 3-15. (**A**) N_2 sorption isotherm and (**B**) pore size distribution (BJH plot) for Si-NCs.

3.2.3.2 Effect of path length.

The size of the silica precursor influences the material obtained from the reaction between SiO_2 and Mg. Reduction of larger silica precursor structures (> 500 nm) provided more Mg_2Si than equivalent reactions (600°C, 12 hours) with

small silica precursors (< 500 nm) . **Figure 3-16** shows silica precursors with average diameters of 125 nm, 255 nm, 600 nm and 2 µm.

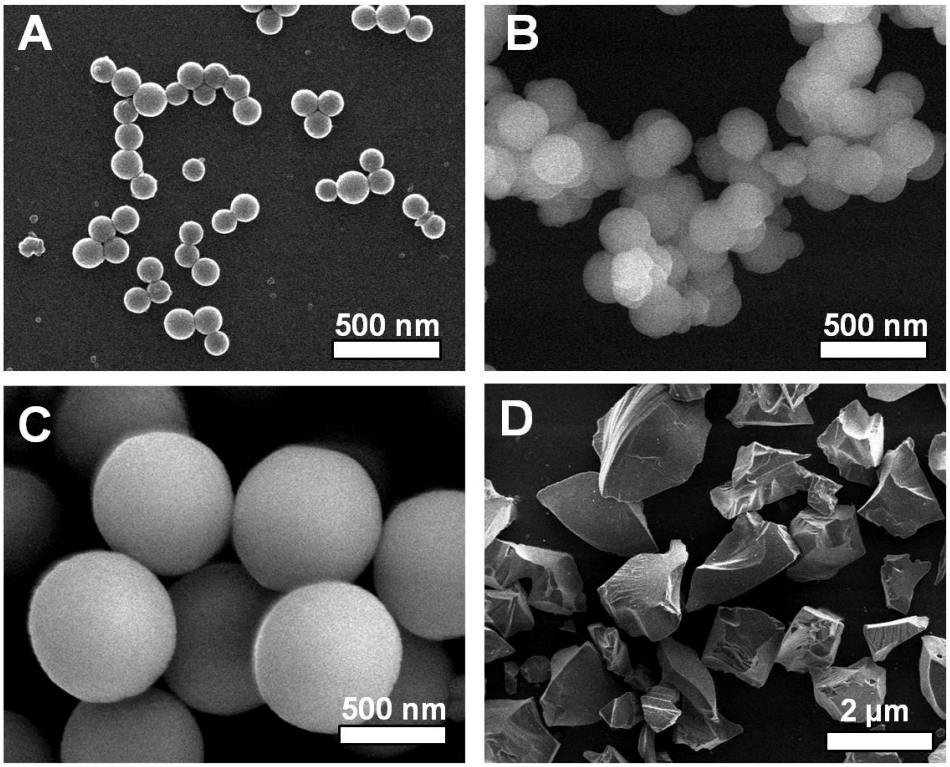

Figure 3-16. Stober silica particles with average diameter of (**A**) 125 nm, (**B**) 255 nm, (**C**) 600 nm and (**D**) Commercial sand particles of about 2 µm.

After reduction, powder XRD patterns were collected from the products before treating them with HCl solution. It was observed that the intensity of the Mg_2Si increases with increasing precursor size (**Figure 3-17**).

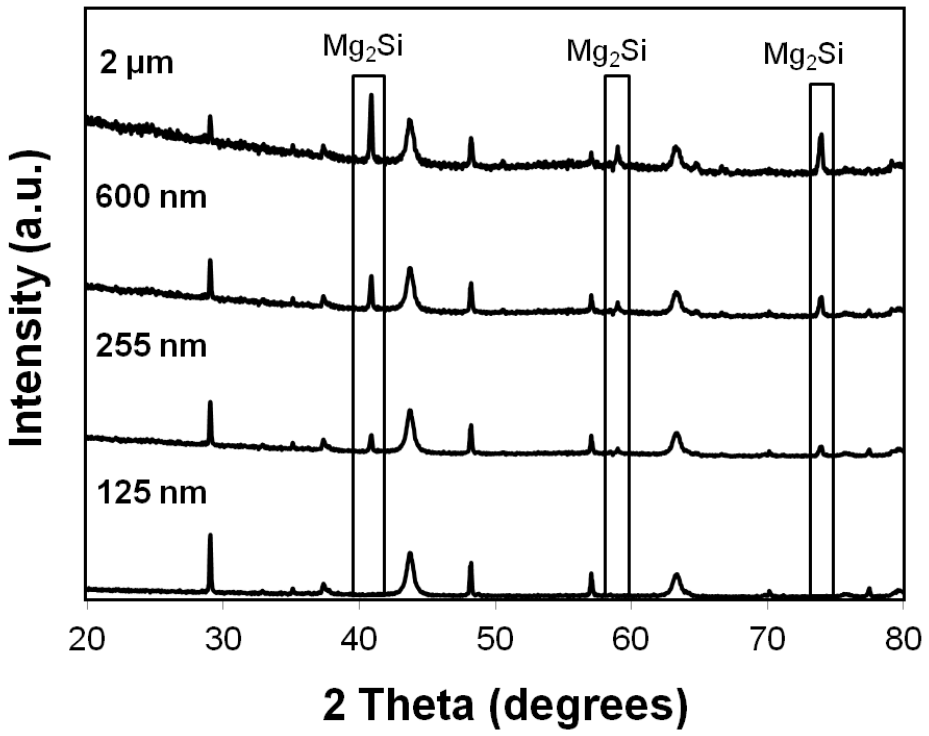

Figure 3-17. XRD patterns of the composites obtained from magnesiothermic reduction of various silica precursors.

When reactions involving thicker Mg films (i.e., 2.5 µm) were examined it was discovered that Mg_2Si, MgO and Si layers are formed on top of SiO_2 (See **Figure 3-18**). It is reasonable that after given thicknesses of Si and MgO are formed, O can no longer diffuse to the metallic Mg fast enough to compete with the reaction of Mg with Si. Under these conditions, formation of silicide is favored and the Si atoms migrate to the elemental Mg layer to form Mg_2Si (**Scheme 3-1**).

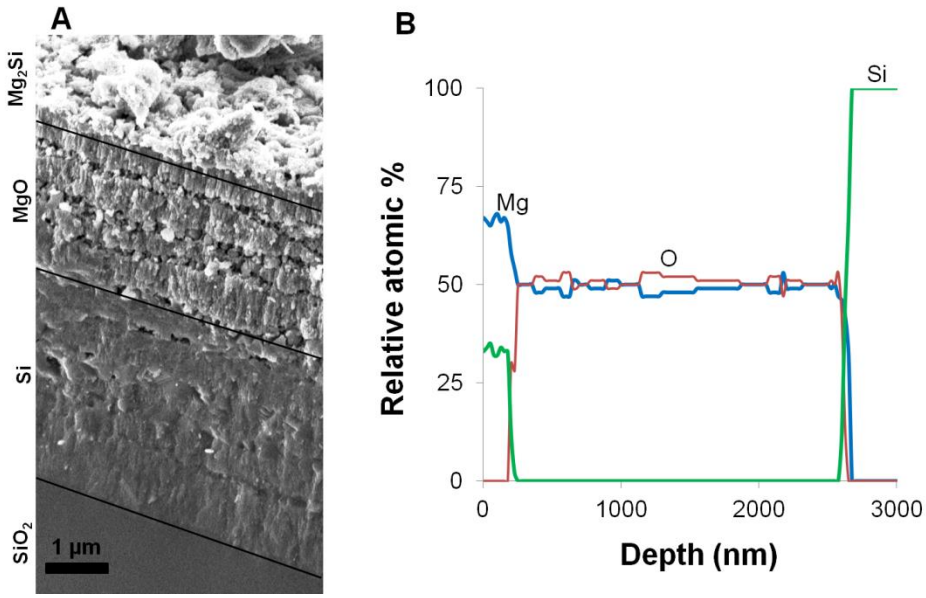

Figure 3-18. (**A**) SEM image of the cross-section of the borosilicate glass after heating it with 2.5 µm Mg on it. (**B**) Elemental composition at different depths for film shown in (**A**).

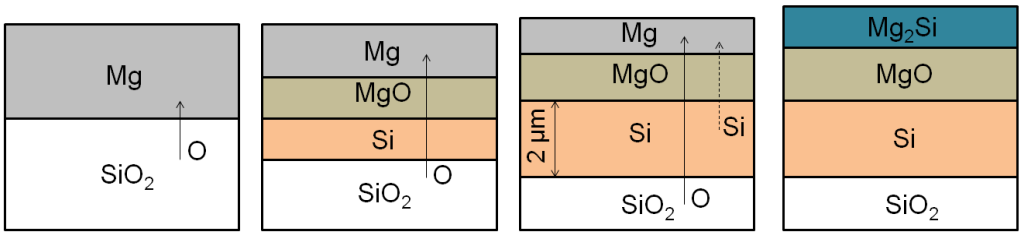

Scheme 3-1. Schematic representation of formation of various compounds during magnesiothermic reduction.

3.2.3.3 Influence of reaction temperature.

Magnesiothermic reduction of silica is an exothermic reaction and control of the reaction temperature is crucial if particle morphology is to be retained. Reduction of SiO_2 is qualitatively slower at 500 ^oC (measured) and the resulting Si particles are not sintered. Increasing the measured temperature to 600 ^oC and beyond increases the reaction rate, however under these conditions the heat evolved by the reaction between SiO_2 and Mg results in particle sintering and loss of the target morphology (**Figure 3-19**). Higher reaction temperature also favors formation of Mg_2Si.[13] Addition of salt (*e.g.*, NaCl or KCl) heat sinks to the reaction system helps prevent sintering of the Si nanomaterials.[50]

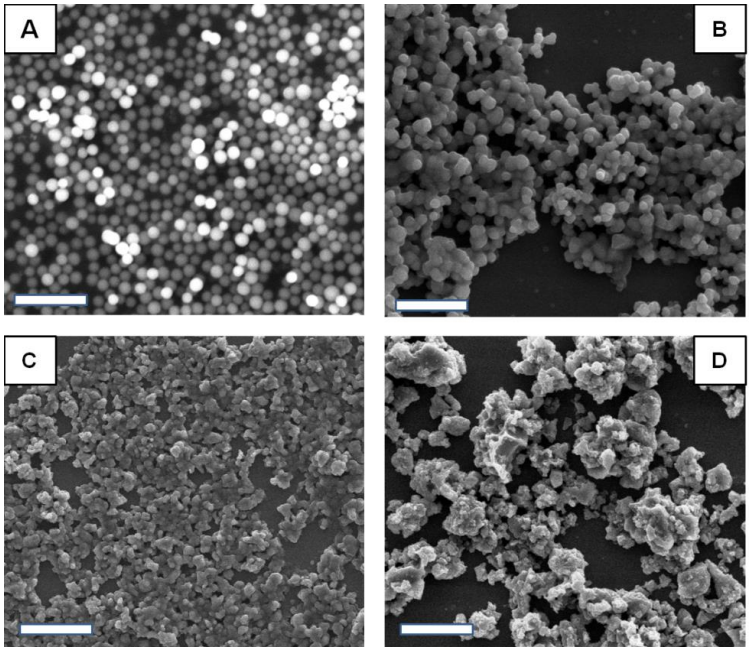

Figure 3-19. Secondary electron SEM images of Si-NCs formed at (**A**) 500 ^oC, (**B**) 600 ^oC, (**C**) 700 ^oC, and (**D**) 800 ^oC. The scale bar is 1 µm.

3.2.3.4 Influence of precursor porosity and HF etching.

Efforts were made to extend the Mg reduction protocol to fabricate mesoporous and aero-gel equivalents of elemental Si by reducing MCM-41 and silica aerogels, respectively. After the reduction and removal of MgO, the structural integrity of most of the samples was compromised (**Figure 3-20**) and the original structural order was lost.

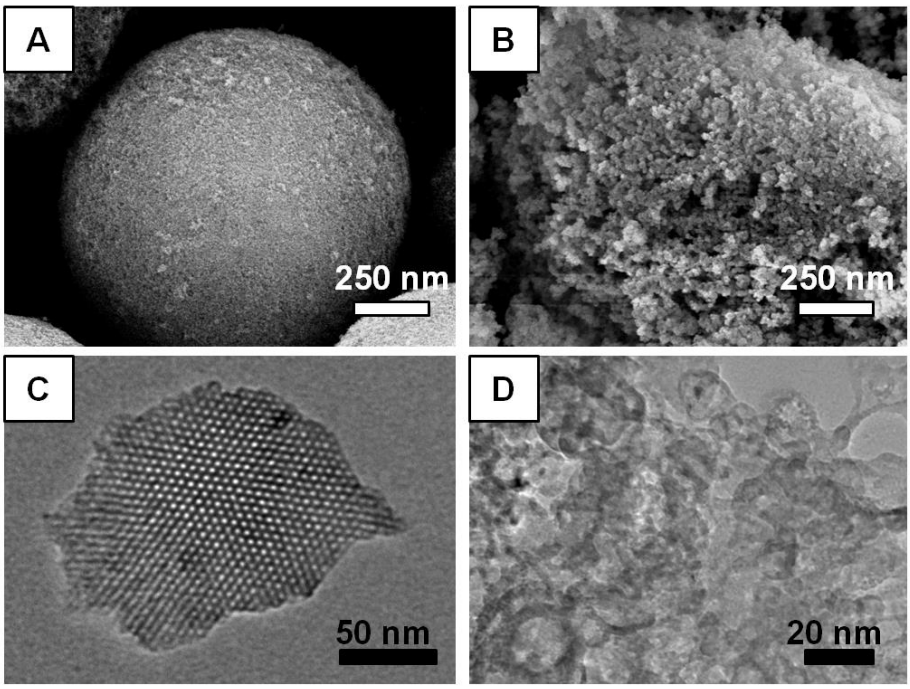

Figure 3-20. Secondary electron SEM images of silica aerogel (**A**) before reduction and (**B**) after reduction. Bright field TEM images of commercial MCM-41 (**C**) before reduction and (**D**) after reduction.

The silicon nanomaterials obtained from Mg reduction of the porous structures were treated with HF acid to remove any residual SiO_2 and provide a hydride surface termination suitable for further surface modification.[9] The Si products were treated with HF solution for 15 minutes and extracted using toluene. Smaller Si particles were formed after the etching process which are believed to originate from disintegration of the original structure (**Figure 3-21A**). Si obtained from MCM-41 and Stöber silica reduction, yielded freestanding Si-NCs with average particle size of 4.0 nm and 8.3 nm, respectively.

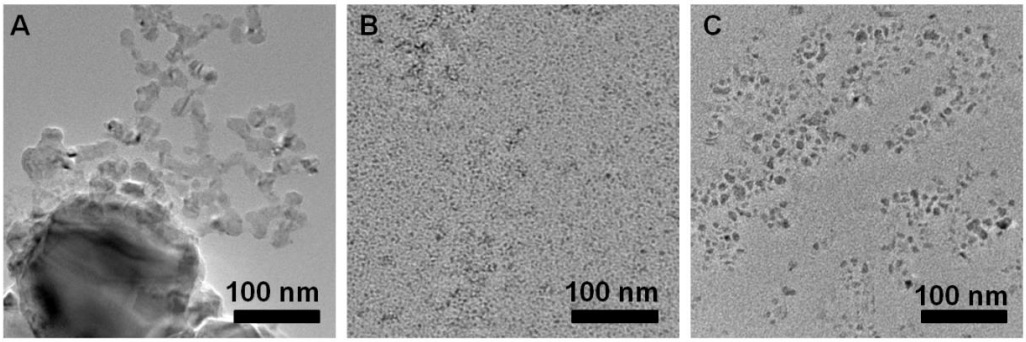

Figure 3-21. TEM images of Si products after etching and originally obtained by reducing (**A**) Stöber silica particles, (**B**) MCM-41, and (**C**) silica aerogel.

The Si-NCs obtained by reducing MCM-41 behave very similar to quantum confined Si-NCs. They can be further functionalized with various surface ligands such as akyl groups, amines and trioctylphosphine (TOPO) to yield luminescent Si-

NCs (**Figure 3-22**). The origin of the different photoluminescence colors is discussed in detail in Chapter 6.

Figure 3-22. Si-NCs (~ 4.0 nm) functionalized with dodecylamine (blue), TOPO (yellow) and dodecyl (red), under UV-illumination.

3.2.4 Conclusions

The present investigation into the mechanism of magnesiothermic reduction of silica indicates it proceeds *via* migration of oxygen ions from SiO_2 to Mg. After enough Si is formed, the reaction to make Mg_2Si is favoured, presumably arising from Si migration. Increasing the applied temperature, increases the reduction rate, however the exothermic nature of the reaction leads to sintering of the silicon particles and loss of the target morphology. Finally, the presented results suggest magnesiothermic reduction is not ideal for preparation of porous silicon nanomaterials *via* reduction of porous silica structures because the original structure is not retained. While the present study does not rule out such synthesis, significant further study is required if such structures are to be realized and it may be necessary

to explore the addition of heat sinks (*e.g.*, salts) to better control reaction temperature.

3.3 References.

1. S. Ossicini, L. Pavesi and F. Priolo, *Light Emitting Silicon for Microphotonics*, Springer, Berlin, 2003.
2. N. H. Alsharif, C. E. M. Berger, S. S. Varansai, Y. Chao, B. R. Horrocks and H. K. Dutta, *Small*, 2009, **5**, 221.
3. A. Meldrum, R. F. Haglund, L. A. Boatner and C. W. White, *Adv. Mater*., 2001, **13**, 1431.
4. U. Kahler and H. Hofmeister, *Opt. Mater*., 2001, **17**, 83.
5. F. Gorbilleau, X. Portier, C. Ternon, P. Voivenel, R. Madelon and R. Riszk, *Appl. Phys. Lett*., 2001, **78**, 3058.
6. D. Mayeri, B. L. Phillips, M. P. Augustine and S. M. Kauzlarich, *Chem. Mater*., 2001, **13**, 765.
7. A. Shiohara, S. Hanada, S. Prabhakar, K. Fujioka, T. H. Lim, K. Yamamoto, P. T. Northcote and R. D. Tilley, *J. Am. Chem. Soc*., 2010, **132**, 248.
8. J. D. Holmes, K. J. Ziegler, R. C. Doty, L. E. Pell, K. P. Johnston and B. A. Korgel, *J. Am. Chem. Soc*., 2001, **123**, 3743.
9. C. M. Hessel, E. J. Henderson and J. G. C. Veinot, *Chem. Mater*., 2006, **18**, 6139.
10. E. J. Henderson, J. A. Kelly and J. G. C. Veinot, *Chem. Mater*., 2009, **21**, 5426.
11. M. Pauthe, E. Bernstein, J. Dumas, L. Saviot, A. Pradel and M. Riber, *J. Mater. Chem*., 1999, **9**, 187.
12. C. M. Hessel, D. Reid, M. G. Panthani, M. R. Rasch, B. W. Goodfellow, J. Wei, H. Fuji, V. Akhavan and B. A. Korgel, *Chem. Mater*., 2012, **24**, 393.
13. Z. Bao, M. R. Weatherspoon, S. Shian, Y. Cai, P. D. Graham, S. M. Allan, G. Ahmad, M. B. Dickerson, B. C. Church, Z. Kang, H. W. Abernathy III, C. J. Summers, M. Liu and K. H. Sandhage, *Nature*, 2007, **446**, 172.
14. K. Nozawa, H. Gailhanou, L. Raison, P. Panizaa, H. Ushiki, E. Sellier, J. P. Delville and M. H. Delvilee, *Langmuir*, 2005, **21**, 1516.
15. L. P. Singh, S. K. Agarwal, S. K. Bhattacharya, U. Sharma and S. Ahalawat, *Nanomater. Nanotechnol*., 2011, **1**, 44.
16. www.roperld.com/science/minerals/indium.htm
17. Y. Yang, Q. Huang, A. W. Metz, J. Ni, S. Jin, T. J. Marks, M. E. Madsen, A. DiVenere and S. Ho, *Adv. Mater*., 2004, **16**, 321.
18. M. Abb, P. Albella, J. Aizpurua and O. L. Muskens, *Nano Lett*., 2011, **11**, 2457.
19. E. P. S. Arlindo, J. A. Lucindo, C. M. O. Bastos, P. D. Emmel and M. O. Orlandi, *J. Phys. Chem. C*, 2012, **116**, 12946.

20. J. Lee, S. Lee, G. Li, M. A. Petruska, D. C. Paine and S. Sun, *J. Am. Chem. Soc*., 2012, **134**, 13410.

21. J. G. Tait, B. J. Worfolk, S. A. Maloney, T. C. Hauger, A. L. Elias, J. M. Buriak, K. D. Harris, *Sol. Energ. Mat. Sol. C.*, **2013**, *110*, 98.

22. K. H. Sandhage, U. S. patent 7,067,104 (27 June 2006).

23. X. Liu, C. Giordano and M. Antonietti, *J. Chem. Mater*., 2012, **22**, 5454.

24. W. Luo, X. Wang, C. Meyers, N. Wannenmacher, W. Sirisaksoontorn, M. M. Lerner and X. Ji, *Scientific Reports*, 2013, **3**, 1.

25. J. R. Szczech, M. A. Lukowski and S. Jin, *J. Mater. Chem*., 2010, **20**, 8389.

26. M. Dasog and J. G. C. Veinot, *Chem. Commun*., 2012, **48**, 3760.

27. M. Dasog, L. F. Smith, T. K. Purkait and J. G. C. Veinot, *Chem. Commun*., 2013, **49**, 7004.

28. Y. Shi, F. Zhang, Y. Hu, X. Sun, Y. Zhang, H. I. Lee, L. Chen and G. D, Stucky, *J. Am. Chem. Soc*., 2010, **132**, 5552.

29. O. Takeda and T. H. Okabe, *Mater. Trans*., 2006, **47**, 1145.

30. E. K. Richman, C. B. Kang, T. Brezeninski and S. H. Tolbert, *Nano Lett*., 2008, **8**, 3075.

31. M. Ibisate, D. Golmayo and C. Lopez, *Adv. Mater*., 2009, **21**, 2899.

32. M. Barati, S. Sarder, A. McLean and R. Roy, *J. Non-Cryst. Sol*., 2011, **357**, 18.

33. M. Guo, X. Zou, H. Ren, F. Muhammad, C. Huang, S. Qiu and G. Zhu, *Micro. Meso. Mater*., 2011, **142**, 194.

34. Y. Zhang and J. Huang, *J. Mater. Chem*., 2011, **21**, 7161.

35. J. Zhu and C. G. Meng, *Mater. Sci. Forum*, 2011, **1069**, 675.

36. L. Pallavidino, M. Liscidini, A. Virga, A. Chiodoni, E. Descrovi, J. Cos, L. C. Andreani, C. F. Pirri, F. Geobaldo and F. Giogis, *Opt. Mater*., 2011, **33**, 563.

37. H. C. Tao, L. Z. Fan and X. Qu, *Electrochem. Acta*, 2012, **71**, 194.

38. K. Chen, Z. Bao, J. Shen, G. Wu, B. Zhou and K. H. Sandhage, *J. Mater. Chem*., 2012, **22**, 16196.

39. H. C. Tao, M. Huang, L. Z. Fan and X. Qu, *Solid State Ionics*, 2012, **220**, 1.

40. D. Chen, X. Mei, G. Ji, M. Lu, J. Xie, J. Lu and J. Y. Lee, *Angew. Chem. Int. E*d., 2012, **51**, 2409.

41. J. K. Yoo, J. Kim, Y. S. Jung and K. Kang, *Adv. Mater*., 2012, **24**, 5452.

42. M. Dasog, Z. Yang and J. G. C. Veinot, *CrystEngComm*., 2012, **14**, 7576.

43. L. Batchelor, A. Loni, L. T. Canham, M. Hasan and J. L. Coffer, *Silicon*, 2012, **4**, 259.

44. M. P. Liu, C. H. Li, H. B. Du and X. Z. You, *Chem. Commun*., 2012, **48**, 4950.

45. D. P. Wong, H. T. Lien, Y. T. Chen, K. H. Chen and L. C. Chen, *Green Chem*., 2012, **14**, 896.

46. S. Zhu, C. Zhu, J. Ma, Q. Meng, Z. Guo, Z. Yu, T. Lu, Y. Li, D. Zhang and W. M. Lau, *RSC Adv*., 2013, **3**, 6141.

47. S. Venkateswaran, R. Yuvakkumar and V. Rajendra, *Phosphorus, Sulfur, and Silicon*, 2013, **188**, 1178.

48. L. Shi, P. Shen, D. Zhang, E. Dong and Q. Jiang, *Appl. Surf. Sci*., 2013, **274**, 124.

49. Z. Wen, G. Lu, S. Mao, H. Kim, S. Cui, K. Yu, X. Hunag, P. T. Hurley, O. Mao and J. Chen, *Electrochem. Commun*., 2013, **29**, 67.

50. W. Luo, X. Wang, C. Meyers, N. Wannenmacher, W. Sirisaksoontorn, M. M. Lerner and X. Ji, *Scientific Reports*, 2013, **3**, 1.

51. A. Xing, J. Zhang, Z. Bao, Y. Mei, A. S. Gordin and K. H. Sandhage, *Chem. Commun*., 2013, **49**, 6743.

52. Y. Bao, D. Jiang and J. Gong, *Key Eng. Mater*., 2013, **544**, 29.

53. The literature search was done on 22 November 2013. SciFinder and Scopus search engines were used.

54. X. Qingquan, X. Quan, C. Qian, Z. Kejie, Y. Zhiqiang and S. Xiangqian, *J. Semiconduc*., 2011, **32**, 082002.

55. L. D. Gelb and K. E. Gubbins, *Langmuir*, 1999, **15**, 305.

56. A. Badalyan and P. Pendleton, *Langmuir*, 2003, **19**, 7919.

Chapter 4:

Low Temperature Synthesis of Silicon Nitride (Si_3N_4) and Silicon Carbide (SiC) Nanomaterials *via* Magnesiothermic Reduction Method*

* Portions of this chapter has been published

- M. Dasog and J. G. C. Veinot, *Chem. Commun*., 2012, **48**, 3760 - 3762. (Reproduced by permission of The Royal Society of Chemistry)

- M. Dasog, L. F. Smith, T. K. Purkait and J. G. C. Veinot, *Chem. Commun*., 2013, **49**, 7004 - 7006. (Reproduced by permission of The Royal Society of Chemistry)

4.1 Solid-State Synthesis of β-Silicon Nitride Nanocrystals.

4.1.1 Introduction

Optically active nanomaterials based upon silicon are attractive for applications such as bio-imaging,[1] electronics,[2,3] and photovoltaics,[4] in part because they are abundant and non-toxic.[1,5] Zero-dimensional silicon nitride (Si_3N_4) nanomaterials have been investigated because of their greater chemical and thermal stability compared to their elemental Si counterparts.[6-16] However, as a result of various synthetic challenges outlined below, very few reports have appeared.

Bulk Si_3N_4 is an insulator and hence, is not expected to be influenced by quantum size effects. It is often prepared by carbothermal reduction,[6,7] or direct nitridation[8-10] – both approaches are energy intensive and frequently require temperatures exceeding 1400 ^{o}C. Si_3N_4 nanostructures are also prepared *via* other chemical methods such as inorganic salt metathesis involving the reaction of silicon tetrachloride and sodium azide,[11,12] pyrolysis of polyaluminasilazane,[13,14] or direct reaction of $CaSi_2$ and $MgSi_2$ with ammonium salts.[15,16] These reagents not only react violently, but can also produce intermediate compounds that are difficult to separate from the desired product. More importantly, Si_3N_4 nanomaterials obtained from these reactions are typically size polydisperse and a mixture of the various known polymorphs (*i.e.*, α and β structures). In this section of the present chapter the synthesis of small (*i.e.*, d<10 nm) highly luminescent β -Si_3N_4 NCs obtained from the reaction of sol-gel derived silica with magnesium and ammonia formed

in-situ through the thermal decomposition of urea is reported (as shown in **Scheme 4-1**).

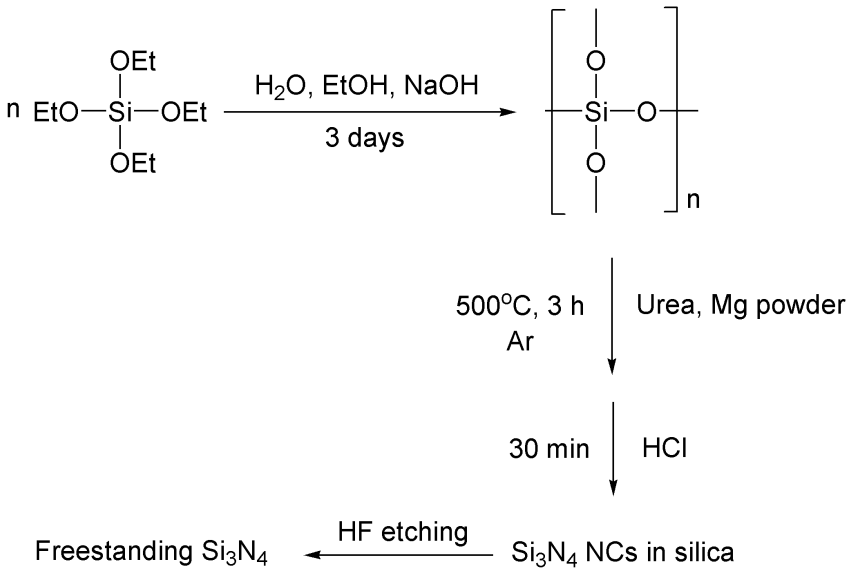

Scheme 4-1. Synthetic approach to freestanding β- Si_3N_4 NCs.

4.1.2 Experimental

4.1.2.1 Materials

Tetraethoxysilane (TEOS, 99%, Sigma-Aldrich), urea ($CO(NH_2)_2$, 98%, Fisher), sodium hydroxide (NaOH, 97%, Caledon), magnesium powder (Mg, 99%, BDH), toluene (ACS grade, BDH), ethanol (ACS grade, Sigma-Aldrich), hydrofluoric acid (HF, 49%, J. T. Baker) were used as received.

4.1.2.2 Synthesis of the $(SiO_2)_n$ sol-gel polymer.

The silica sol-gel was synthesized *via* a base catalyzed method. Briefly, TEOS (5 mL, 22.5 mmol) was stirred with ethanol (10 mL), deionized water (20 mL) and NaOH solution (10 M, 0.5 mL) for 3 days. The white precipitate was collected by vacuum filtration and washed with deionized water multiple times (4 × 25 mL). The solid was transferred to an oven and was kept there for 24 hours at 100 ^{o}C to drive off residual water and ethanol (yield 92%).

4.1.2.3 Synthesis, purification and isolation of freestanding Si_3N_4 NCs.

Silica sol-gel polymer (1.00 g, 17 mmol w.r.t. Si content), urea (0.90 g, 15 mmol) and magnesium powder (0.82 g, 34 mmol) were mixed manually with a mortar and pestle and thermally processed at 500°C for 3 hours in a tube furnace under 5% H_2/95% Ar atmosphere in a quartz boat. The resulting grey/black powder (1.62 g) was treated with concentrated hydrochloric acid (5 mL) for 30 min to remove reaction byproducts. The grey/white precipitate (0.65 g) was isolated by vacuum filtration. The solid was washed with deionized water until the washings showed a neutral pH (ca. 7) as evaluated by pH paper. The solid was subsequently washing with ethanol (20 mL) and acetone (3 × 20 mL) and was air dried to yield crude, silica contaminated Si_3N_4 nanocrystals.

The solid obtained from the HCl extraction was treated with hydrofluoric acid to remove SiO_2 impurities. In a typical etching procedure, 100 mg of the sample was transferred to a PET beaker and 1:1:1 solution of 49% $HF_{(aq)}$: H_2O : ethanol (10 mL) was added. The mixture was stirred for 60 min followed by extraction into 10

mL toluene. The freestanding nanocrystals were washed multiple times with toluene by centrifugation at 4000 rpm.

4.1.2.4 Fourier Transform Infrared Spectroscopy (FTIR)

FTIR spectroscopy was performed on powder samples using a Nicolet Magna 750 IR spectrometer.

4.1.2.5 X-ray Powder Diffraction (XRD)

XRD was performed using an INEL XRG 3000 X-ray diffractometer equipped with a Cu K_α radiation source (λ = 1.54 Å). Bulk crystallinity for all samples was evaluated on finely ground samples mounted on a low-intensity background silicon (100) sample holder.

4.1.2.6 Thermogravimetric Analysis (TGA)

TGA was performed on PerkinElmer Pyris 1 using a platinum sample pan at a heating rate of 18 ^{o}C/min in air.

4.1.2.7 X-Ray Photoelectron Spectroscopy (XPS)

XPS analysis was performed using a Kratos Axis Ultra instrument operating in energy spectrum mode at 210 W. The base pressure and operating chamber pressure were maintained at 10^{-7} Pa. A monochromatic Al K_α source (λ = 8.34 Å) was used to irradiate the samples, and the spectra were obtained with an electron take-off angle of 90°. To minimize sample charging, the charge neutralizer filament was used when required. Survey spectra were collected using an elliptical spot with major and minor axis lengths of 2 and 1 mm, respectively, and 160 eV pass energy with a step of 0.33 eV. CasaXPS software (Vamas) was used to interpret high-

resolution (HR) spectra. All of the spectra were internally calibrated to the C 1s emission (284.8 eV). After calibration, the background was subtracted using a Shirley-type background to remove most of the extrinsic loss structure.

4.1.2.8 Photoluminescence (PL) Spectroscopy

PL spectra for the solution phase samples were acquired using a Varian Cary Eclipse Fluorescence Spectrometer in a quartz cuvette.

4.1.2.9 Absorbance (UV-Vis) Spectroscopy

UV-Visible spectra were recorded on Cary 400 UV-Vis Spectrometer in a quartz cuvette.

4.1.2.10 Transmission Electron Microscopy (TEM)

TEM analyses were performed using a JOEL-2010 (LaB_6 filament) with an accelerating voltage of 200 kV. High resolution TEM analysis was performed on Hitachi H9500 TEM instrument with an accelerating voltage of 300 kV. The samples were prepared by drop coating solutions of composite or freestanding NCs dispersed in ethanol and toluene, respectively onto a carbon coated copper grid (400 mesh) and allowing the solvent to evaporate in air. The particle sizes were measured using Image J software.[17] The HRTEM images were processed using DigitalMicrograph software.[18]

4.1.2.11 Scanning Electron Microscopy (SEM)

SEM analysis was performed on JSM- 6010LA In TouchScope instrument with an accelerating voltage of 10 kV. The powder sample was mounted on carbon tape for imaging.

4.1.3 Results and Discussion

4.1.3.1 Synthesis of silica particles.

Stöber silica particles for the present investigation were obtained from a base catalyzed sol-gel reaction of tetraethoxysilane (TEOS), which yielded particles of sizes ranging from 10 – 250 nm (**Figure 4-1**).[19]

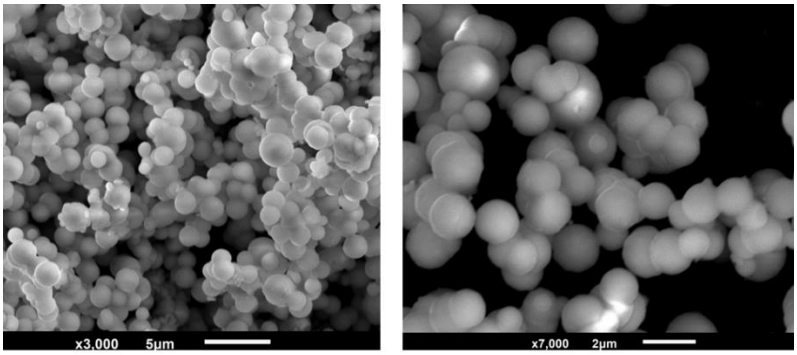

Figure 4-1. SEM images of TEOS derived Stöber silica particles.

4.1.3.2 Synthesis of Si_3N_4 nanocrystals.

The sol-gel product, urea, and Mg powder were mechanically mixed using a mortar and pestle and subsequently heated at 500 ^{o}C for 3 hours in a flowing Ar atmosphere. The resulting grey/black solid was treated with concentrated hydrochloric acid to remove any soluble by-products (*e.g.*, MgO, unreacted Mg, *etc.*). The grey powder remaining after HCl extraction contained Si_3N_4 NCs and unreacted SiO_2 particles as confirmed by broad reflections in the X-ray powder diffraction (XRD) pattern (**Figure 4-2A**). All reflections are characteristic of β-phase Si_3N_4; no reflections arising from other Si_3N_4 polymorphs (*i.e.*, α and γ

structures) were detected.[13,14] The broad reflection at ca. 20° is attributed to amorphous silica.[11,20] The powder also glowed blue under UV-illumination (λ = 365 nm) as demonstrated in **Figure 4-2B**.

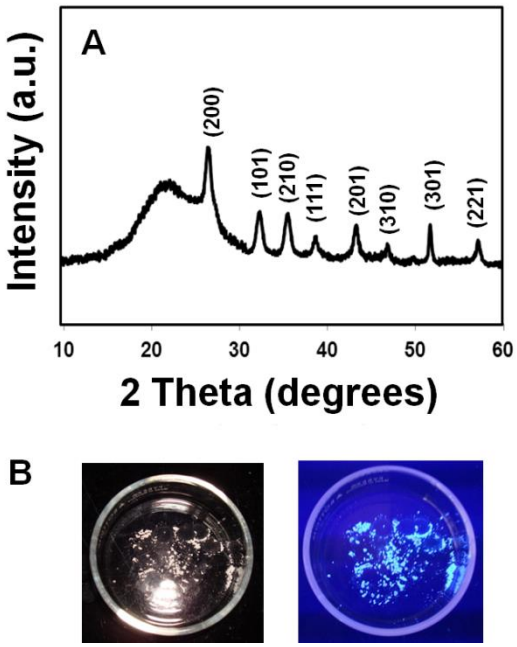

Figure 4-2. (**A**) XRD pattern and (**B**) appearance under ambient (left) and UV (right) illumination of the crude reaction product after HCl extraction.

To provide an understanding of the formation of Si_3N_4 NCs in the present system the reaction mixture was heated to different temperatures and the products formed were evaluated using XRD (**Figure 4-3**). Clearly, urea thermally decomposes forming ammonia which reacts with magnesium metal to form magnesium nitride (Mg_3N_2) at ca. 300°C as outlined in the following equations.[21,22]

$$NH_2(CO)NH_{2(s)} \rightarrow HNCO_{(g)} + NH_{3(g)}$$

$$3Mg_{(s)} + 2NH_{3(g)} \rightarrow Mg_3N_{2(s)} + 3H_{2(g)}$$

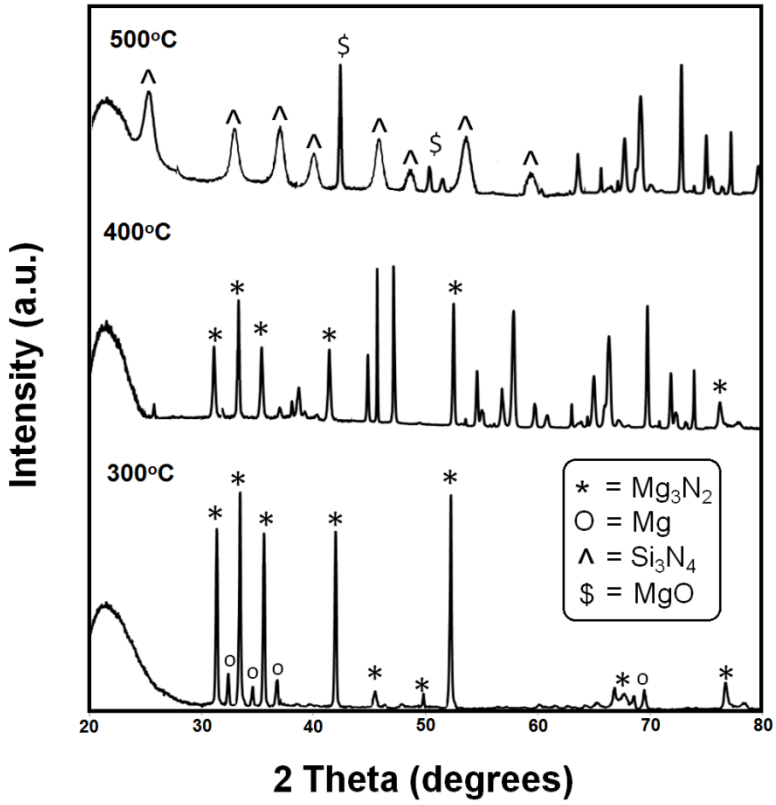

Figure 4-3. XRD patterns of reaction product mixtures obtained by thermally processing SiO_2, Mg and urea mixture at the indicated temperatures.

Once formed, the Mg_3N_2 undergoes solid-state metathesis with silica at temperatures above 300°C, to form Si_3N_4 and MgO. It is reasonable this process proceeds *via* formation of intermediates such as Si_2N_2O and $MgSiN_2$ which may account for the unidentified XRD reflections.[23] For the present system, the reaction proceeds to completion (*i.e.*, formation of Si_3N_4) for the smallest silica particles

whereas larger particles remain incompletely reacted. Thermogravimetric (TGA) analysis was performed in air between temperatures 25ºC – 900ºC to ascertain if carbon impurities remained in the crude reaction product (**Figure 4-4**). Slight weight loss (3%) was observed below 100ºC, which is believed to be loss of solvent molecules. No significant weight loss was observed above 100ºC, consistent with negligible carbon impurities being present at the sensitivity of the TGA method.

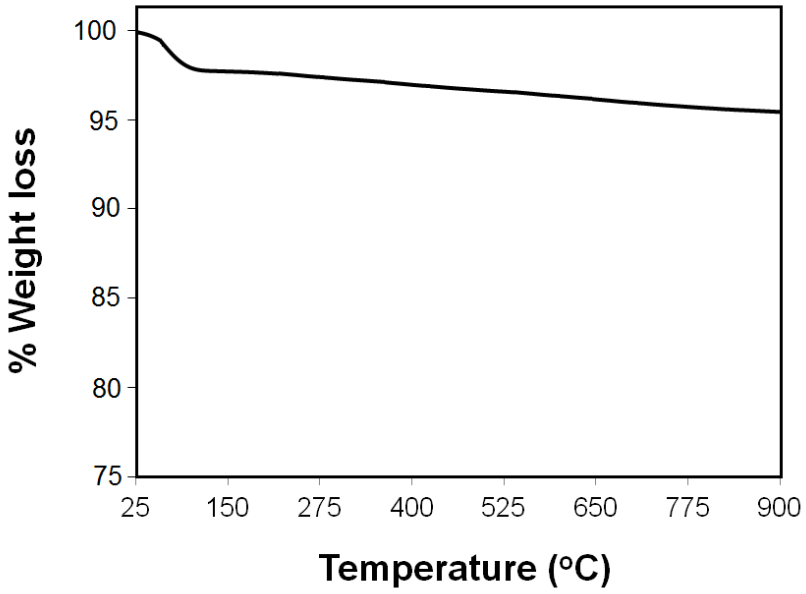

Figure 4-4. Thermogravimetric analysis (TGA) of crude Si_3N_4 NCs in air at a heating rate of 18 ºC/min.

4.1.3.3 Freestanding Si_3N_4 nanocrystals.

Freestanding β-Si_3N_4 NCs were obtained by etching the solid that remained after the HCl extraction with 1:1:1 mixture of HF:EtOH:H_2O followed by extraction into toluene.[24] HRTEM analysis (**Figure 4-5**) shows individual NCs with crystal lattice spacings corresponding to 0.33 and 0.26 nm for (200) and (210) planes of β-Si_3N_4, repectively.[25] The average particle size was determined to be 8.8 ± 1.0 nm.

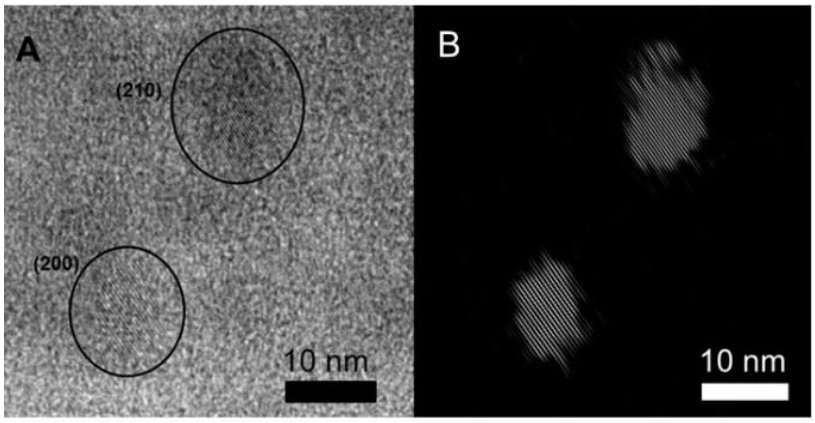

Figure 4-5. (**A**) HRTEM and (**B**) inverse Fourier transformed HRTEM image of freestanding β-Si_3N_4 NCs.

Spectroscopic analysis indicates the surface chemistry of the present β-Si_3N_4 NCs is complex. While some evidence of Si-H moieties is present at ca. 2100 cm^{-1}, the FTIR spectrum (**Figure 4-6**) suggests NC surfaces are populated primarily by nitrogen atoms as evidenced by strong N–H vibrations at ca. 3300 cm^{-1}. Other

spectral features characteristic of β-Si_3N_4 such as, Si–N asymmetric stretching at ca. 850 cm^{-1}, Si–N symmetric stretching at ca. 480 cm^{-1}.[26] The absorption at ca. 1150 cm^{-1} may be assigned to Si–O stretching, which likely results from surface oxidation of Si atoms.[12]

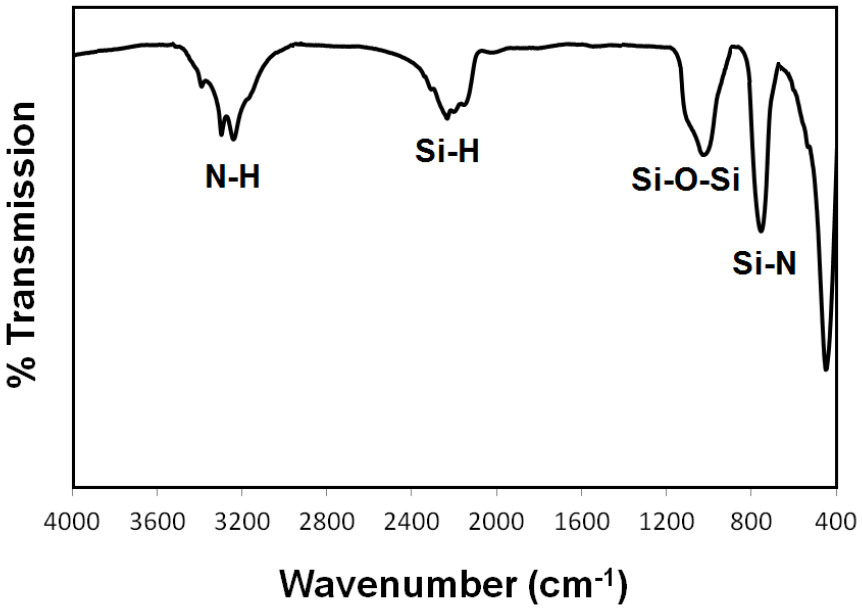

Figure 4-6. FTIR spectrum of freestanding β-Si_3N_4 NCs obtained by drop casting toluene suspension of the NCs on silicon wafer.

X-ray photoelectron spectroscopy (XPS) analysis of freestanding β-Si_3N_4 NCs (**Figure 4-7**) gives Si 2p and N 1s binding energies of 102 and 397.9 eV, respectively in agreement with literature values.[11] The low intensity Si 2p emission at ca. 103 eV is attributed to trace surface oxide consistent with FTIR analysis (*vide*

supra). The N 1s emission at 399 eV indicates the presence of surface N–H.[11] The quantification of silicon and nitrogen emissions afforded a Si:N ratio of 0.77:1, consistent with the expected ratio of 0.75:1 for β-Si_3N_4.

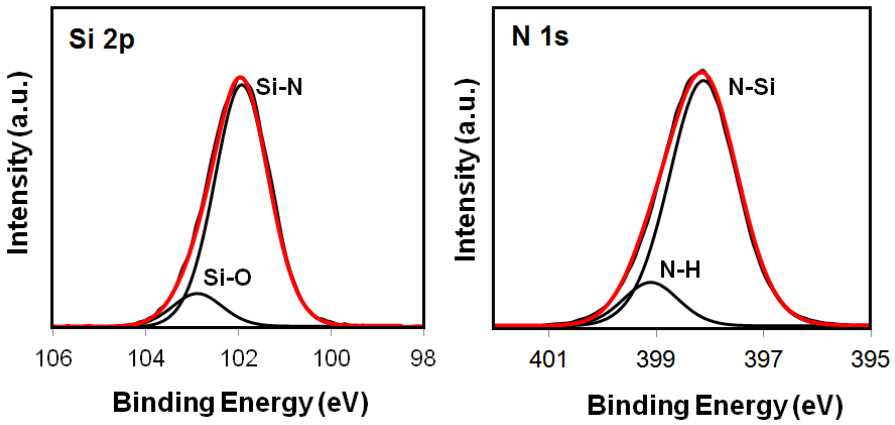

Figure 4-7. HR XP spectra of Si 2p and N 1s region of β-Si_3N_4 NCs. For clarity only $2p_{3/2}$ peaks are shown (Red - fitted line).

Photoluminescence (PL) and absorption spectra of toluene suspensions of freestanding β-Si_3N_4 NCs are shown in **Figure 4-8**. The NCs exhibit intense blue emission (**Figure 4-8B**) upon excitation at 325 nm and the emission maxima is at 425 nm. Because β-Si_3N_4 is not a semiconductor this PL is not the result of quantum confinement. While the exact origin of the PL is currently unclear,[27] it has been suggested it originates from a charge transfer process from silicon to nitrogen.[28]

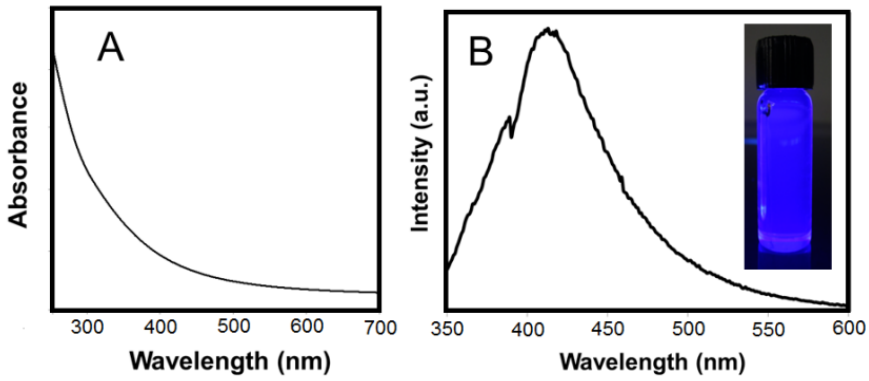

Figure 4-8 (**A**) Absorbance and (**B**) PL spectra of freestanding β-Si_3N_4 NCs.

4.1.4 Conclusions

In conclusion, the first synthesis of freestanding β-Si_3N_4 NCs *via* a straightforward solid-state reaction of a sol-gel derived precursor has been demonstrated. The resulting luminescent NCs were readily isolated *via* solution etching. With these well-defined β-Si_3N_4 NCs in hand, our ongoing investigations will comprehensive investigation of their luminescent properties using X-ray excited optical luminescence, expanding our study to controlling particle size and tailoring NC surface chemistry as well as exploring a variety of applications such as light-emitting diodes and photocatalysts.

4.2 Solid- State Synthesis of β-Silicon Carbide Nanomaterials

4.2.1 Introduction

Silicon carbide (SiC) is a wide band gap refractory material used for high power electronics,[29,30] photonic devices,[31,32] catalyst supports,[33] quantum computing,[34-36] among others. Many of these practical applications arise as a direct result of the excellent thermal, chemical and mechanical stability of SiC. Of late, there has been a push to make nanostructured SiC because the opportunities offered by size-dependent properties, increased surface area and the possibility to incorporate these materials into ever smaller electronic devices.[37] Some SiC nanocrystals (NCs) exhibit photoluminescence in near-UV to visible blue spectral region making them attractive candidates for light-emitting devices.[38-41] The benign nature of SiC has also enabled their use as biological labels.[41-44]

Conventionally, SiC NCs have been prepared by pyrolysis of carbon containing siloxane polymers at high temperatures (~1400°C).[45,24] Other methods explored include electrochemical etching of SiC wafers,[40,46,47] annealing of C_{60} loaded porous Si,[48] and ion implantation.[49,50] All these methods require high processing temperatures and/or costly infrastructure. Furthermore, none provide control over SiC particle morphology and always yield pseudospherical nanostructures. SiC nanostructures such as nano-rods, fibers, and ribbons have been prepared using metal-based catalysts which often incorporate themselves as impurities and compromise the purity of the material that is often required by the electronics industries.[51,52]

Magnesiothermic reduction has recently offered an attractive alternative for preparing a variety of Si-based nanomaterials at lower temperatures (~500°C). Recently, we reported formation of silicon and silicon nitride NCs using magnesiothermic reduction.[53,54] Shi *et al.* recently reported formation of SiC microstructures using a similar approach.[55] In absence of conclusive evidence, they proposed SiC formed *via* initial reduction of SiO_2 to Si by reaction with Mg followed by a catalysed reaction of Si with C to form SiC. In this section of the chapter, the synthesis of various β-SiC nanostructures of controlled morphologies (*e.g.*, particles, rods, fibers) at 600 ^{o}C using SiO_2, Mg, and C powders as the precursors is reported. In addition, a detailed mechanistic study that clearly demonstrates the reaction occurs *via* metathesis and not the catalyzed reaction proposed previously is described.

4.2.2 Experimental

4.2.2.1 Materials

Tetraethoxysilane (TEOS, 99%, Sigma-Aldrich), ammonium hydroxide (NH_4OH, 28%, Caledon), magnesium powder (Mg, 99%, BDH), glassy carbon powder (C, 98%, sigma-aldrich), polyvinylpyrrolidone (PVP, M_w = 55,000, Sigma-Aldrich), sodium citrate dihydrate (ACS grade, Sigma-Aldrich), *n*-butanol (ACS grade, Sigma-Aldrich), ethanol (ACS grade, Sigma-Aldrich) and hexanes (ACS grade, Sigma-Aldrich) were used as received.

4.2.2.2 Synthesis of Stöber silica particles.

Stöber silica particles were synthesized *via* base catalyzed sol-gel method. 10 mL (45 mmol) TEOS were stirred with ethanol (10 mL), deionized water (20 mL) and NH_4OH solution (28 %, 1 mL) for predetermined times to yield different size particles. The white precipitate was collected by vacuum filtration and washed with deionized water and ethanol multiple times (4 × 25 mL). The solid was transferred to an oven and was kept there for 24 hours at 100°C to drive off any residual water and ethanol.

4.2.2.3 Synthesis of silica nanorods.

Silica nanorods were prepared using a modified procedure reported by Kuijk *et al*. PVP (30 g, M_w = 55000) was dissolved in *n*-butanol (300 mL) by sonicating for 40 minutes. Absolute ethanol (30 mL), deionized water (8.4 mL) and sodium citrate dihydrate solution (0.18 M, 2 mL) were added to the butanol solution and the flask was manually shaken to mix the reagents. This was followed by addition of NH_4OH solution (6.5 mL, 28 %) and TEOS (3 mL, 13.5 mmol) to the reaction mixture. The mixture was manually shaken for 30 seconds and left undisturbed for 12 hours. The reaction mixture turns from a clear solution to cloudy suspension as the reaction proceeds. The white precipitate was collected by centrifuging at 4000 rpm for 15 minutes. The supernatant was discarded and the white solid washed with deionized water (50 mL) three times using centrifugation (4000 rpm). The solid was finally washed with ethanol (50 mL) and dried in oven overnight at 100°C. The resulting rods exhibited an average length of 1.5 ± 0.2 µm and diameter of 0.22 ± 0.04 µm.

4.2.2.4 Synthesis of silica nanofibers.

The nanofibers were prepared using the same procedure described above (for nanorods), however the reaction time was increased from 8 hours to 72 hours. The resulting fibers were longer than 10 µm and 0.20 ± 0.05 µm in diameter.

4.2.2.5 Synthesis of SiC nanomaterials.

0.25 g (4.2 mmol) of the silica precursor (*i.e.*, particles, nanorods or fibers) were manually mixed with 0.22 g (9.2 mmol) of magnesium powder and 0.05 g (4.2 mmol) of carbon powder and transferred to an alumina boat. The mixture was heated to 600 ^{o}C at a rate of 16 ^{o}C/min in a tube furnace under argon atmosphere and maintained at that temperature for 15 hours. The sample was cooled to room temperature and reheated to 500 ^{o}C for 30 minutes in air. The resulting grey solid was exposed to 5 M aqueous HCl (10 mL) for an hour to remove magnesium oxide. The solution was subsequently filtered and the grey solid was washed repeatedly with water. It was then dried in oven overnight at 100°C.

4.2.2.6 Scanning Electron Microscopy (SEM)

SEM images were recorded in a Field Emission Scanning Electron Microscope, JEOL 6301F. Ethanol dispersion samples were deposited on silicon wafer, which was attached with aluminum pin stubs using double sided carbon tape. Conductive coatings of chromium were applied on dry samples using Xenosput XE200 sputter coaters before loading them into SEM holder. All SEM images were recorded using secondary electron imaging with an accelerating voltage of 5.0 kV.

4.2.3 Results and Discussion

4.2.3.1 Stöber silica particles

Spherical SiO_2 particles were prepared using the Stöber method and tetraethoxysilane (TEOS).[56] Under basic conditions, TEOS hydrolyzes and condenses to form SiO_2 particles. Particle size was tailored by controlling reaction times. 8, 15 and 120 hours stirring time resulted in particle with average diameters of 30.6, 66.8, and 213.8 nm, respectively (**Figure 4-9**).

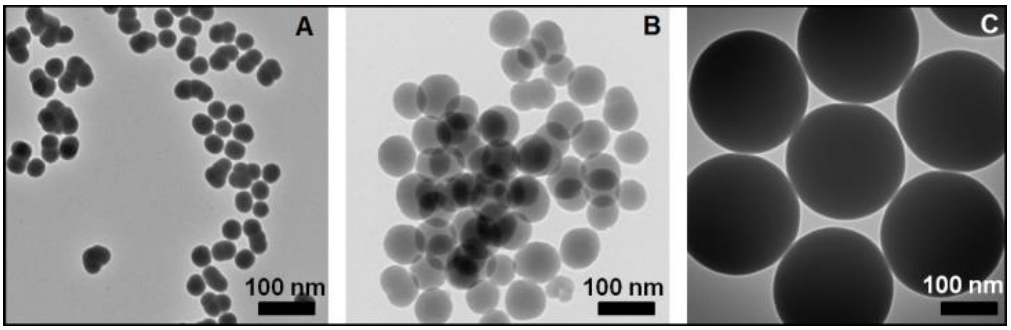

Figure 4-9. Bright-field transmission electron microscopy (TEM) images of (**A**) 30.6 ± 2.2 nm (**B**) 66.8 ± 5.7 nm and (**C**) 213.8 ± 5.4 nm silica nanoparticles.

4.2.3.2 Formation of SiC spherical nanocrystals.

Silica structures were converted to SiC by reacting stoichiometric quantities of SiO_2, Mg, and C at 600°C. Byproduct MgO was removed by treating the crude product mixture with hydrochloric acid. SEM images of resulting SiC particles show the original SiO_2 particle morphology was maintained during the conversion

process reaction, however an increase in the particle size is noted (**Figure 4-10, A-C**). SiO_2 particles with 30.6, 66.8, 213.8 nm diameters resulted in SiC particles of 51.3, 92.8 nm and 278.3 nm, respectively. It is reasonable this change in particle dimension arises as a result of differences in the Si-O (~1.6 Å) and Si-C (1.9 Å) bond lengths.[57] HRTEM analysis clearly shows characteristic lattice spacing of 2.5 Å for [111] plane of *β*-SiC (**Figure 4-10, D-E**) and the selected area electron diffraction (SAED) pattern confirms the product formed is crystalline (**Figure 4-10F**).[24]

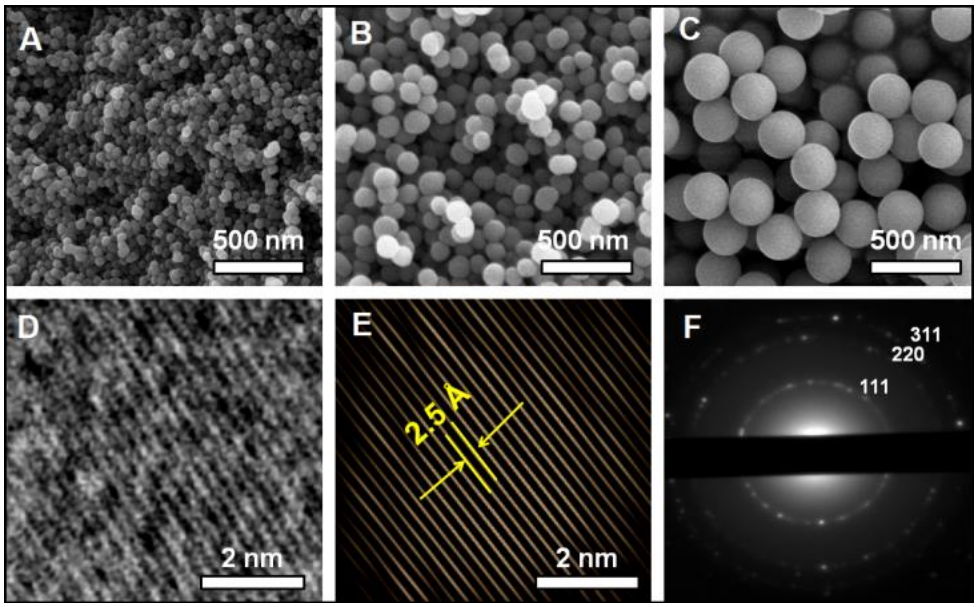

Figure 4-10. Scanning electron microscopy (SEM) images of *β*-SiC NCs with diameters of (**A**) 51.3 ± 5.5 nm, (**B**) 92.8 ± 6.6 nm, (**C**) 278.3 ± 8.2 nm, (**D**) High resolution transmission electron micrograph (HRTEM) image of *β*-SiC NC, (**E**) Fourier transformed image of (D) showing lattice spacing, and (**F**) Selected area electron diffraction (SAED) pattern of *β*-SiC NCs.

Bulk characterization of the resulting β-SiC NCs was performed using X-ray photoelectron spectroscopy (XPS), Fourier transform infrared spectroscopy (FTIR), and X-ray powder diffraction (XRD). High-resolution XP spectra of Si 2p and C 1s regions of the present NCs show peak maxima at 100.6 eV and 282.5 eV respectively which is characteristic of SiC **(Figure 4-11, A-B**).[45] FTIR spectra show Si-C stretching at ca. 830 cm^{-1} (**Figure 4-11C**).

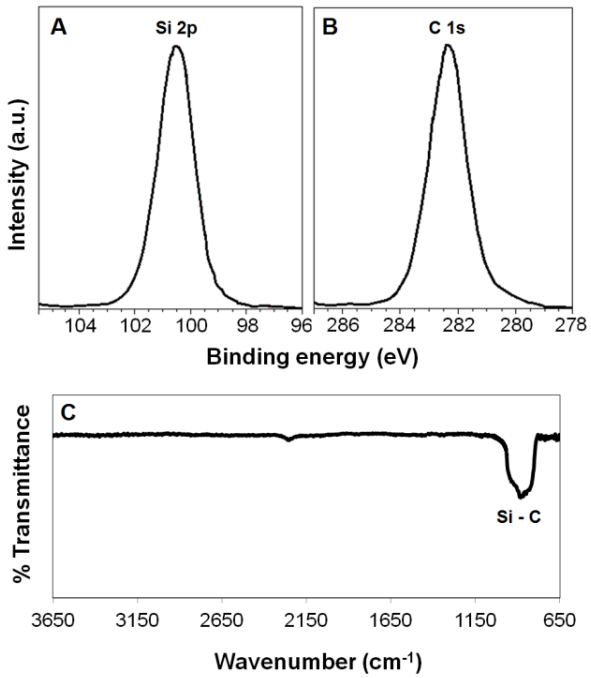

Figure 4-11. Representative high-resolution X-Ray photoelectron spectra of (**A**) Si 2p and (**B**) C 1s regions of β-SiC particles. (**C**) FTIR spectrum of β-SiC particles obtained from preparing KBr pellet.

The XRD pattern shows reflections at 36, 60 and 72° that are readily indexed to those of the (111), (220), and (311) reflections of β-SiC as shown later in **Figure 4-14**.[24]

4.2.3.3 Formation of one-dimensional SiC nanostructures.

To demonstrate the breadth of morphological control afforded of the present method, we synthesized numerous silica nanostructures including rods and fibers using a modified literature procedure (**Figure 4-12**).[58] Silica nanorods and fibers were prepared using a PVP template, base catalyzed sol-gel reaction with TEOS.

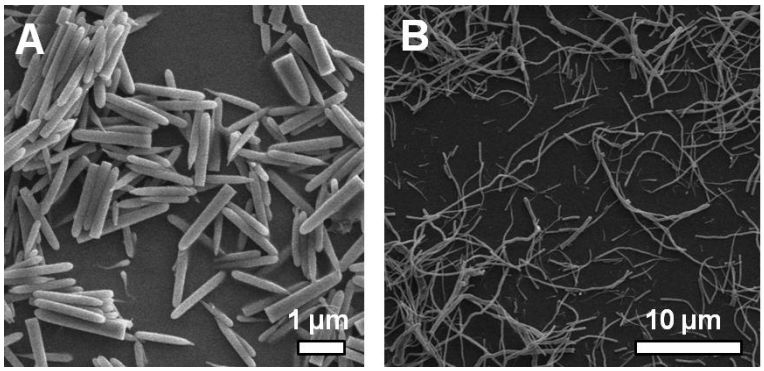

Figure 4-12. SEM images of silica (**A**) rods and (**B**) fibers.

The SiO_2 rods and fibers were similarly reacted with Mg and C powders to yield SiC rods and fibers (**Figure 4-13, A-B**). We further show that commercial glass wool can also be converted into long fibers of SiC (**Figure 4-13C**) using the present method.

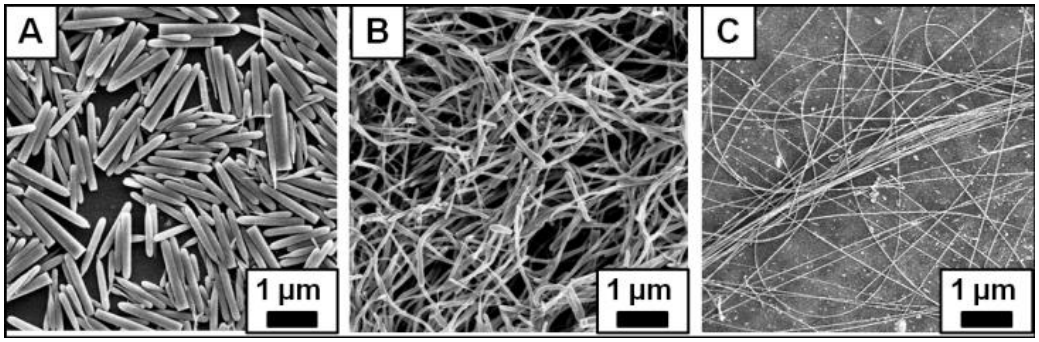

Figure 4-13. SEM images of SiC (**A**) Rods (length = 1.5 ± 0.2 µm, diameter = 0.20 ± 0.05 µm), (**B**) Fibers (length > 10 µm, diameter = 0.18 ± 0.04 µm) and (**C**) Fibers (length > 25 µm, diameter = 0.050 ± 0.001 µm).

XRD confirmed all the products were crystalline *β*-SiC (**Figure 4-14**).

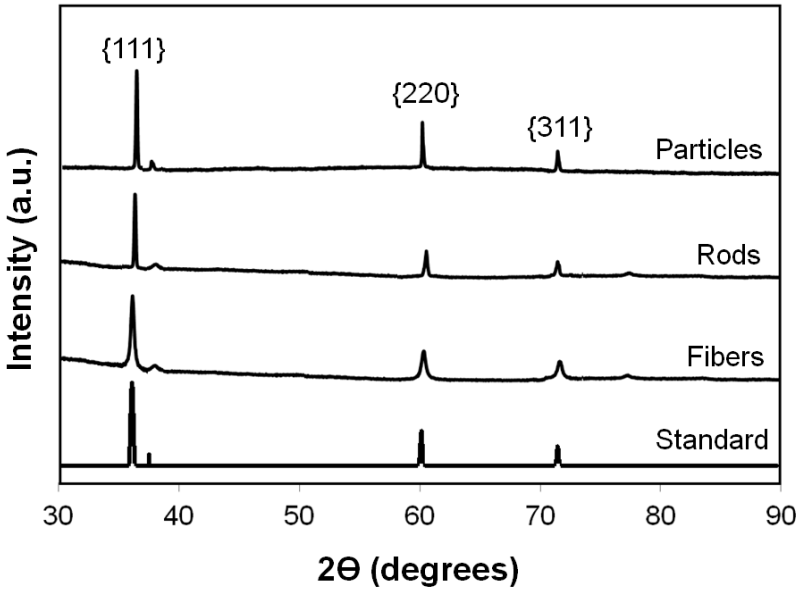

Figure 4-14. XRD pattern of various different *β*-SiC morphologies.

4.2.3.4 Reaction mechanism for the formation of SiC.

To date, the understanding of the mechanism of β-SiC formation from reaction of silica with C and Mg has been limited. If the utility of this method is to be fully exploited and controlled, it is paramount that the processes involved be identified. While Shi *et al*. proposed that Mg containing species catalyzed the Si + C $\rightarrow$ SiC reaction, we found control reactions of Si and C powder in presence of catalytic amounts of Mg or MgO at lower temperatures did not yield β-SiC. Therefore, we monitored the reaction products formed at different temperatures using XRD to obtain an understanding of the reaction (**Figure 4-15**).

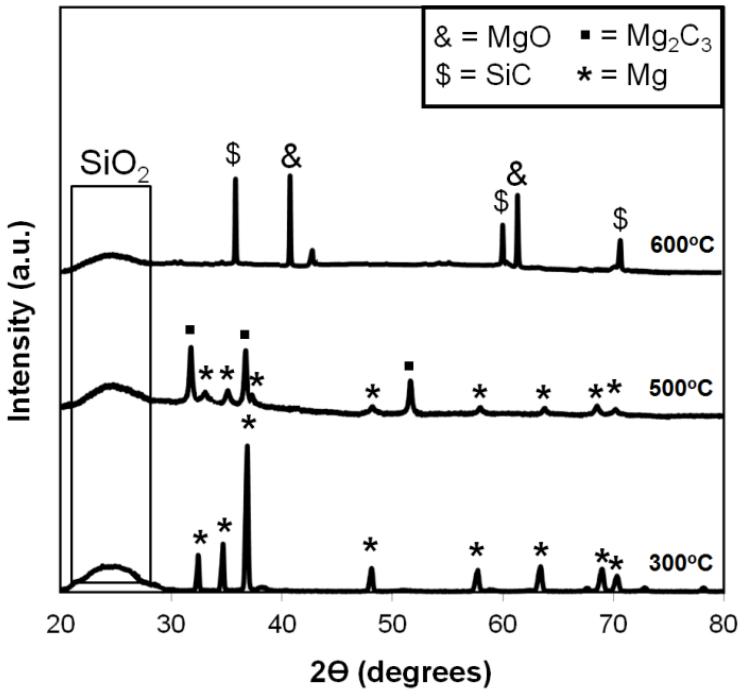

Figure 4-15. XRD pattern of the reaction product obtained from SiO_2, Mg and C mixture at various temperatures.

Using this approach it became clear that at temperatures below 500°C the Mg reacts with C to form Mg_2C_3. This magnesium sesquicarbide subsequently undergoes a metathesis reaction with SiO_2 to form SiC and MgO.

4.2.4 Conclusions

We have demonstrated the synthesis of *β*-SiC nanomaterials *via* a straightforward solid-state reaction of a sol-gel derived precursor. Using Mg not only reduces the reaction temperature but also allows preparation of materials with tailored morphologies thus eliminating the need for metal seeds. We have further provided conclusive evidence that SiC is formed from the metathesis of Mg_2C_3 and SiO_2 and is not catalytic as previously reported.

4.3 References.

1. F. Erogbogbo, K. T. Yong, I. Roy, G. X. Xu, P. N. Prasad and M. T. Swihart, *ACS Nano*, 2008**, 2**, 873.
2. L. Pavesi, L. Dal Negro, C. Mazzoleni, G. Franzò and F. Priolo, *Nature*, 2000**, 408**, 440.
3. S. Lombardo, B. De Salvo, C. Gerardi, and T. Baron, *Microelectron. Eng.*, 2004**, 72**, 388.
4. V. S. vrc ek, D. Mariotti, T. Nagai, Y. Shibata, I. Turkevych and M. Kondo, *J. Phys. Chem. C*, 2011, **115**, 5084.
5. M. Wang and W. Wang, *Environ. Sci. Technol*., 2008, **42**, 940.
6. K. Komeya and H. Inoue, *J. Mater. Sci*., 1975, **10**, 1243.
7. M. Ekelund and B. Forslund, *J. Am. Ceram. Soc*., 1992, **75**, 332.
8. L. W. Yin, Y. Bando, Y. –C. Zhu and Y. –B. Li, *Appl. Phys. Lett*., 2003, **83**, 3584.
9. J. Hu, Y. Bando, Z. Liu, F. Xu, T. Sekiguchi and J. Zhan, *Chem. Eur. J*., 2004, **10**, 554.
10. C. N. Kenneth, N. Y. Niagara Falls, *US Pat*., 2618565, 1952.
11. Y. –J. Bai, J. Bian, C. –G. Wang, B. Zhu, Y. –X. Qi, Y. –X. Wang, Y. –X. Liu and G. L. Geng, *J. Mater. Chem*., 2005, **15**, 4832.
12. H. –L. Zhu, F. –D. han, J. Q. Bi, Y. –J. Bai, Y. X. Qi, L. L. Pang, C. –G. Wang, S. –J. Li, *J. Am. Ceram. Soc*., 2009, **92**, 535.
13. S. T. Shwab and R. A. Page, *Mater. Sci. Eng*., 1995, 201.
14. F. Gao, W. Yang, Y. Fan and L. An, *J. Solid State Chem*., 2008, **181**, 211.
15. Y. Gu, L. Chen and Y. Qian, *J. Am. Ceram. Soc*., 2004, **87**, 1810.
16. F. Hofer, W. Veigl and E. Hengge, *Adv.Mater*., 1992, **4**, 501.
17. www.rsbweb.nih.gov/ij/
18. www.gatan.com/products/softwares/
19. A. M. Buckley and M. Greenblatt, *J. Chem. Educ.*, 1994, **71**, 599.
20. C. C. Yang and W. C. Chen, *J. Mater. Chem*., 2002, **12**, 1138.
21. S. D. Yim, S. J. Kim, J. H. Baik and I-. S. Nam, *Ind. Eng. Chem. Res*., 2004, **43**, 4856.
22. D. W. Kim, T. H. Kim, H. W. Park and D. W. Park, *Appl. Surf. Sci*., 2011, **257**, 5375.
23. A. Pawelec, B. Strojek, G. Weisbrod and S. Podsiadlo, *Ceram. Int.*, 2002, **28**, 495.

24. E. J. Henderson and J. G. C. Veinot, *J. Am. Chem. Soc*., 2009, **131**, 809.

25. A. Ziegler, C. Kisielowski and R. O. Ritchie, *Acta Mater*., 2002, **50**, 565.

26. M. Mikolajunas, J. Baltrusaitis, V. Kopustinskas, G. Vanagas, V. Grigaliunas and D. Virzonis, *Thin Solid Films*, 2009, **517**, 5769.

27. X. Zhang, D. Neiner, S, Wang, A. Y. Louie and S. M. Kauzlarich, *Nanotechnol.*, 2007, **18**, 095601.

28. A. N. Sorokin, A. A. Karpushin, V. A. Gritsenko and H. Wong, *J. of Non-Cryst. Sol.*, 2008, **354**, 1531.

29. N. G. Wright, A. B. Horsfall and K. Vassilevski, *Mater. Today*, 2008, **11**, 16.

30. C. R. Eddy Jr and D. K. Gaskill, *Science*, 2009, **324**, 1398.

31. D. M. Brown, E. T. Downey, M. Ghezzo, J. W. Kretchner, R. J. Saia, Y. S. Liu, J. A. Edmond, G. Gati, J. M. Pimbley and W. E. Schneider, *IEEE Trans. Electron Devices*, 1993, **40**, 325.

32. M. Mehregany, C. A. Zorman, N. Rajan and C. H. Wu, *Proc. IEEE*, 1998, **86**, 1594.

33. M. J. Ledoux and C. L. Pham-Huu, *Cattech*, 2001, **5**, 226.

34. W. F. Koehl, B. B. Buckley, F. J. Heremans, G. Calusine and D. D. Awschalom, *Nature*, 2011, **84**, 479.

35. Y. Liu, G. Wang, S. Wang, J. Yang, L. Chen, X. Qin, B. Song, B. Wang and X. Chen, *Phys. Rev. Lett*., 2011, **106**, 087205.

36. V. A. Soltamov, A. A. Soltamova, P. G. Baranov and I. I. Proskuryakov, *Phys. Rev. Lett*., 2012, **108**, 226402.

37. P. Mélinon, B. Masenelli, F. Tournus and A. Perez, *Nat. Mater*., 2007, **6**, 479.

38. J. Fan, H. Li, J. Wang and M. Xiao, *Appl. Phys. Lett*., 2012, **101**, 131906.

39. D. Dai, N. Zhang, W. Zhang and J. Fan, *Nanoscale*, 2012, **4**, 3044.

40. X. L. Wu, J. Y. Fan, T. Qiu, X. Yang, G. G. Siu and P. K. Chu, *Phys. Rev. Lett*., 2005, **94**, 026102.

41. J. Fan, H. Li, J. Jiang. K. Y. So, Y. W. Lam and P. K. Chu, *Small*, 2008, **4**, 1058.

42. J. Fan and P. K. Chu, *Small*, 2010, **6**, 2080.

43. T. Serdiuk, S. A. Alekseev, V. Lysenko, V. A. Skryshevsky and A. Géloën, *Nanotechnol.*, 2012, **23**, 315101.

44. J. Botsoa, V. Lysenko, A. Géloën, O. Marty, J. M. Bluet, G. Guillot, *Appl. Phys. Lett*., 2008, **92**, 173902.

45. M. Dasog, C. Rachinsky and J. G. C. Veinot, *J. Mater. Chem*., 2011, **21**, 12422.

46. M. Morales Rodriguez, A. Díaz Cano, T. V. Torchynska, T. V. G. Polupan and S. Ostapenko, *J. Non-Cryst. Solids*, 2008, **354**, 2272.

47. A. M. Rossi, T. E. Murphy and V. Reipa, *Appl. Phys. Lett*., 2008, **92**, 253112.

48. X. L. Wu, G. G. Siu, M. J. Stokes, D. L. Fan and X. M. Bao, *Appl. Phys. Lett*., 2000, **77**, 1292.

49. H. Weishart, V. Heera, F. Eichhorn, B. Pécz, A. Barna and W. Skorupa, *Diam. Relat. Mater*., 2003, **12**, 1241.

50. J. Khamsuwan, S. Intarasiri, K. Kirkby, P. K. Chu, S. Singkarat and L. D. Yu, *Nucl. Instrum. Meth. B*, 2012, **282**, 88.

51. W. Yang, H. Miao, Z. Xie, L. Zhang and L. An, *Chem. Phys. Lett*., 2004, **383**, 441.

52. J. Zhou, Z. Chen, M. Zhou, X. Gao and E. Xie, *Nanoscale Res. Lett*., 2009, **4**, 814.

53. M. Dasog, Z. Yang and J. G. C. Veinot, *CrystEngComm*., 2012, **14**, 7576.

54. M. Dasog and J. G. C. Veinot, *Chem. Commun*., 2012, **48**, 3760.

55. Y. Shi, F. Zhang, Y. Hu, X. Sun, Y. Zhang, H. Lee, L. Chen and G. D. Stucky, *J. Am. Chem. Soc*., 2010, **132**, 5552.

56. W. Stöber, A. Fink and E. Bohn, *J. Colloid. Interf. Sci*., 1968, **26**, 62.

57. U. Schubert and N. Husing, *Synthesis of Inorganic Materials*, Wiley-VCH, Weinheim, 2000.

58. A. Kuijk, A. Blaaderen and A. Imhof, *J. Am. Chem. Soc*., 2011, **133**, 2346.

Chapter 5:

Chemical Insight into the Origin of Red and Blue Photoluminescence Arising from Freestanding Silicon Nanocrystals*

* Portions of this chapter has been published

- M. Dasog, Z. Yang, S. Regli, T. M. Atkins, A. Faramus, M. P. Singh, E. Muthuswamy, S. M. Kauzlarich, R. D. Tilley, J. G. C. Veinot, *ACS Nano*, 2013, **7**, 2676 - 2685. (Copyright 2013 American Chemical Society)

- O. Wolf, M. Dasog, Z. Yang, I. Balberg, J. G. C. Veinot, O. Millo, *Nano Lett*., 2013, **13**, 2516 - 2521. (Copyright 2013 American Chemical Society)

5.1 Introduction

The wide-ranging impact of semiconductor nanoparticles, commonly referred to as quantum dots, is well established.[1,2] Extensive and far-reaching research focused on the synthesis of prototypical Cd-based quantum dots has yielded exquisite control of particle size, shape and surface chemistry, as well as a detailed fundamental understanding of their properties. As a result, there are many proof-of-concept applications of these materials in diverse areas including medical diagnostics, electronics, and solar energy conversion.[3-5] Despite the obvious benefits afforded by the tailorability of Cd-based quantum dots, Cd^{2+} cytotoxicity limits and potentially prevents their widespread use in biological and medical applications.[6] In addition, legislation exists or is pending that could further limit their use in many consumer products.[7] In response, there is a concerted push for "Cadmium-Free Quantum Dot" research programs.[8] One approach to addressing these issues is to supplant Cd-based semiconductors with a non-toxic alternative. Silicon is a particularly appealing candidate material because it is the second most abundant element in the earth's crust,[9] it is the workhorse material of the electronics industry and its chemistry is well developed, and perhaps most important it is biologically benign.[10-12]

While silicon appears to be the ideal replacement, its indirect band gap, and the associated disallowed band gap electronic transition has limited the application of bulk silicon in many photonic applications.[13] When visible photoluminescence (PL) was observed from porous-Si it brought the promise of linking silicon electronics and photonics.[14] Adding to its appeal, are proposals that the optical

response of porous-Si arose because of the influences of quantum confinement suggested the luminescence should be size-tunable.[15-17] Ever since, the optical properties of porous and nanocrystalline silicon have been extensively studied and remain the subject of curiosity and even controversy.

Freestanding Si NCs prepared from high purity reagents at high temperatures or using gas-phase methods exhibit quantum confined, size-dependent emission analogous to that observed for their CdSe counterparts.[18-21] This quantum confined band gap emission follows the predictions of the effective mass approximation (EMA) and exhibits comparatively long-lived excited state lifetimes (*i.e.*, ca. microseconds) - behavior that is consistent with the bulk-Si indirect bandgap.[22,23] Unfortunately, this is not the end of the story. There are numerous reports describing visible light emission from Si NCs whose emission maximum is incongruent with the EMA. For example, red-orange PL, frequently identified as the S-band, has been reported for surface oxidized Si NCs and has been attributed to quasi-direct transitions or surface states.[24-27] Under some circumstances, partially oxidized nanocrystalline silicon shows yellow emission suggested to arise either from surface Si=O species[28] or Si-O-C bonds.[29] Of all the visible luminescence arising from Si NCs, the origin of blue PL (frequently termed the F-band) from Si NCs remains one of the most controversial. Most often this blue PL with fast decay is attributed to a direct band gap transition in ultra small Si NCs.[30-36] Alternatively, it has been suggested the blue PL exhibited by some Si NCs originates from defect states in a surface sub-oxide and such luminescence from these NCs does not follow the EMA.[37-40] To date, no definitive explanation

explaining why certain oxide defects in Si NCs emit orange-red while others emit blue light has been provided. The origin of Si NC emission is clearly complex and involves many contributing factors. If the full potential of Si NCs is to be realized, it is essential that their luminescent properties be understood and effectively controlled.

Generally, Si NCs showing blue PL that does not follow the EMA are typically prepared using solution methods at comparatively low temperatures (*i.e.*, < 400 ^{o}C). The reactions leading to the formation of the Si NCs typically involve direct reduction of silicon halides[41-43] or reaction of Zintl salts.[44,45] After careful inspection of the reported conditions employed during these syntheses, it was identified that most employ reagents (*vide infra*) that could supply nitrogen impurities. The question then was posed: could it be nitrogen impurities supplied from these reagents that provide a species with a short-lived excited state that gives rise to the blue emission?

In this chapter, a systematic study designed to explore the influence of common nitrogen containing reagents on the optical behavior of Si NCs with the intent of bringing *chemical* insight to the red *vs*. blue debate is described. The present study involved titrating quantum confined red-emitting Si NCs obtained from the well-established thermolysis of hydrogen silsesquioxane (HSQ) with identified nitrogen sources induces blue PL. Detailed spectroscopic and electron microscopy characterization of the titrated red-emitting Si NCs and blue-emitting Si NCs obtained from traditional solution phase methods show trace nitrogen dopants at concentrations near detection limits of standard analytical methods. Most

importantly, this study definitively demonstrates that both nitrogen and oxygen are present in all Si NCs investigated here that show blue PL. Further studies demonstrate emission maxima of the blue emission exhibit solvatochromism consistent with it originating from a charge transfer state on the NC surfaces. Scanning tunneling microscopy (STM) studies were performed as part of a collaboration with the Millo group (Hebrew University) and the results from the STM study is briefly discussed.

5.2 Experimental

5.2.1 Materials.

All reagents were used as received unless noted otherwise. A methyl isobutyl ketone (MIBK) solution of hydrogen silsesquioxane (HSQ) (*i.e.*, FOx® 16) was obtained from Dow Corning. Electronic grade hydrofluoric acid (HF, 49%) was purchased from J.T. Baker. 1-dodecene was purchased from Sigma Aldrich and filtered through activated alumina to remove any peroxide impurities immediately before use. Tetraoctylammonium bromide (TOAB, 98%), allylamine (>99%), reagent grade toluene, chloroform, hydrochloric acid, ethanol, methanol and acetonitrile were obtained from Sigma Aldrich. Sodium silicide (Na_4Si_4) was purchased from SiGNa Chemistry, Inc. *N*, *N*-dimethylformamide (DMF), (Sigma-Aldrich, >99%) was degassed and distilled over sodium metal under reduced pressure.

5.2.2 Synthesis of oxide embedded silicon nanocrystals (Si NCs)

Si NCs embedded within a SiO_2-like matrix were prepared using a well-established literature procedure. MIBK was removed from the FOx-16® *in vacuo* leaving white HSQ powder. The solid was heated to 1100°C at 18°C/min for 1 hour under a reducing atmosphere of 5% H_2/ 95% Ar in a quartz boat within a standard Lindberg Blue tube furnace. After cooling to room temperature the resulting dark brown composite made up of Si NCs (diameter ca. 4 nm) embedded within a silica (SiO_2) matrix was obtained. This composite was ground to a fine powder using a mortar and pestle and subsequently etched with hydrofluoric acid to liberate hydride surface terminated Si NCs (*vide infra*).

5.2.3 Preparation of hydride terminated Si NCs.

Freestanding hydride terminated Si NCs liberated from the oxide matrix *via* hydrofluoric acid etching. Approximately 1 g of Si NC/SiO_2 composite was transferred to a Teflon® beaker and 30 mL of a 1:1:1: mixture of HF:H_2O:C_2H_5OH were added with stirring in subdued light. (Caution: Hydrofluoric acid is extremely dangerous and must be handled with great care.) The resulting dark brown, cloudy mixture was stirred for one hour. Hydrophobic hydride terminated Si NCs were extracted from the aqueous etching mixture using three 20 mL toluene extractions. The remaining aqueous solution was colourless and transparent. All remaining HF was neutralized using an excess of aqueous saturated solution of calcium chloride. The cloudy dark brown Si NC/toluene extracts were placed into glass test tubes and centrifuged using a low speed (7000 rpm) centrifuge for 5 minutes. After centrifugation, the toluene supernatant was decanted leaving a precipitate of

hydride terminated Si NCs. No effort was made to keep the particles under inert atmosphere during the extraction and centrifugation steps.

5.2.4 Surface functionalization of Si NCs with dodecene (Si NC-A)

Hydride terminated Si NCs were re-dispersed in 50 mL of 1-dodecene, and transferred into an oven dried Schenk flask. The cloudy brown suspension was degassed using three vacuum pump cycles and maintained under a dry argon atmosphere. The flask was placed in a silicone oil bath and heated to 190°C for 12 hours. After reaction, a transparent orange-brown solution was obtained consistent with effective functionalization. The reaction mixture was divided equally between four 50 mL PTFE centrifuge tubes. NCs were precipitated using a 3:1 mixture of C_2H_5OH:CH_3OH (20 mL). Particles were centrifuged at 14000 rpm for 20 min using a Beckman J2-21 high-speed centrifuge, followed by decanting of the supernatant. Three dissolution/precipitation/centrifugation cycles were performed using a chloroform/MeOH solvent/antisolvent pair. After the final precipitation the functionalized Si NCs were dispersed in toluene, filtered through a hydrophobic PTFE filter, and stored in a glass vial until further use.

5.2.5 Titration of hydride terminated Si NCs with nitrogen sources

Freshly prepared hydride terminated Si NCs (0.32 g) were suspended in toluene (20.00 mL) to yield 0.50 M solution based upon silicon. Freshly prepared toluene solutions of tetraoctylammonium bromide (0.50 M, 25.00 mL) and ethanol solutions of ammonium bromide (0.50 M, 25.00 mL) were used in all the following experiments. 200 μL of the 0.5 M hydride terminated Si-NC solution in toluene was exposed to predetermined amounts of the nitrogen containing compounds (as

tabulated below) and the volume increased to 300 μL using dry toluene (**Table 5-1**).

Table 5-1: A summary of the titration procedure used to monitor the influence of nitrogen containing reagent on Si NC photoluminescence.

Hydride terminated Si NCs in toluene (0.5 M)	Nitrogen containing compound (0.5 M)	Volume of toluene added	Total volume
200 μL	0 μL	100 μL	300 μL
200 μL	10 μL	90 μL	300 μL
200 μL	20 μL	80 μL	300 μL
200 μL	30 μL	70 μL	300 μL
200 μL	40 μL	60 μL	300 μL
200 μL	50 μL	50 μL	300 μL
200 μL	60 μL	40 μL	300 μL
200 μL	70 μL	30 μL	300 μL
200 μL	80 μL	20 μL	300 μL
200 μL	90 μL	10 μL	300 μL
200 μL	100 μL	0 μL	300 μL

The solution mixture was allowed to react for 3 hours. The characteristic orange luminescence of hydride terminated Si NCs upon exposure to a handheld UV-light (λ = 365 nm) was replaced by a faint blue emission. After 3 hours the reaction mixtures were centrifuged at 14000 rpm for 10 min. The supernatant contained Si NCs that reacted with nitrogen containing compounds, NH_4Br, or TOAB. TOAB was removed by selective precipitation upon cooling the mixture to ca. 0^oC

(ice/water bath) and adding 25 μL of acetonitrile as an antisolvent. The solution was centrifuged at 14000 rpm for 5 min. The supernatant was collected and was found to emit blue light upon exposure UV illumination.

5.2.6 Direct synthesis of dodecyl terminated Si NCs (Si NC-B). *Note*: *This synthesis was performed by the Kauzlarich group*.

Na_4Si_4 (0.20g) and NH_4Br (0.40g) were weighed and added to a Schlenk flask in a dry box which was then transferred to a Schlenk line. DMF (150 mL) was sparged with N_2 and added to the starting reagents *via* cannula. The solution was refluxed for 12 hours followed by the removal of the solvent *via* a short bridge distillation. Dodecene (40 mL) was sparged, added to the Schlenk flask *via* syringe and refluxed for 12 hours. The liquid was separated from the black/grey solid through centrifugation (8000 rpm for 10 minutes) and decanted. One quarter of the mixture was placed into a centrifuge tube and a 3:1 C_2H_5OH:CH_3OH mixture was added. The solution was centrifuged (8000 rpm for one hour) and a black precipitate was isolated. The precipitate was then dissolved into chloroform and precipitated with CH_3OH. The precipitate was dissolved into toluene and was filtered through a 0.45 μm filter and placed in vial.

5.2.7 Solution phase reductive synthesis of dodecyl surface terminated Si NCs (Si NC-C). *Note: This synthesis was performed by the Tilley group*.

All the reactions were performed under a nitrogen atmosphere. In a typical experiment, 0.0026 mole of $SiCl_4$ (0.3 mL) was dissolved in 1g of TOAB and 50 mL of anhydrous toluene. The solution was stirred for 20 minutes and hydrogen-terminated silicon quantum dots were formed by addition of a stoichiometric

amount of hydride reducing agent. Surface passivated quantum dots were formed by capping the hydrogen terminated quantum dots with dodecene. After transfer of the solution into a quartz reaction vessel, the passivation was carried out by irradiation with UV light (254 nm) for four hours.

Surface passivated quantum dots were purified by size exclusion column chromatography. The solution was filtered of using Millipore 0.45 μm filter paper. The solvent was removed under vacuum, and then the particles were dissolved into 10 mL of methanol. After 5 minutes sonication, the solution was concentrated down to 1 mL and filtered using a Millipore 0.22 μm syringe filter. The solution was put on the column (φ = 1 cm, 41.0 cm), containing Sephadex gel LH-20 (beads size 25-100 μm) as the stationary phase. Flow rate was set to one drop/4 s, and fractions were collected every 50 drops. Each fraction was checked for luminescence with a handheld UV lamp (365 nm). Luminescent fractions were collected and concentrated to 1 mL under vacuum. The concentrated solutions contain pure surface passivated silicon quantum dots.

5.2.8 Fourier Transform Infrared Spectroscopy (FTIR)

Fourier Transformation Infrared Spectroscopy (FT-IR) on the samples H-Si NCs and Si NC-A was performed using a Nicolet Magna 750 IR spectrometer. FT-IR on sample Si NC-C was collected on a Bruker optic GmbH alpha ATR-FTIR spectrometer.

5.2.9 X-ray Powder Diffraction (XRD)

XRD patterns were collected using an INEL XRG 3000 X-Ray diffractometer with CuK_{α} radiation (λ = 1.54 Å).

5.2.10 Thermogravimetric analysis (TGA)

TGA was performed on PerkinElmer Pyris 1 using a platinum sample pan and a heating rate of 18°C/min in air.

5.2.11 Nuclear Magnetic Resonance Spectroscopy

Proton nuclear magnetic resonance spectra (^{1}H NMR) were collected on 400 MHz Varian Inova instrument. The samples were dissolved in deuterated chloroform ($CDCl_3$).

5.2.12 X-ray Photoelectron Spectroscopy (XPS)

XPS analyses were performed using a Kratos Axis Ultra instrument operating in energy spectrum mode at 210 W. The base pressure and operating chamber pressure were maintained at 10^{-7} Pa. A monochromatic Al K_{α} source (λ = 8.34 Å) was used to irradiate the samples, and the spectra were obtained with an electron takeoff angle of 90°. To minimize sample charging, the charge neutralizer filament was used when required. Survey spectra were collected using an elliptical spot with major and minor axis lengths of 2 and 1 mm, respectively, and 160 eV pass energy with a step of 0.33 eV. CasaXPS software (VAMAS) was used to interpret high-resolution (HR) spectra. All of the spectra were internally calibrated to the C 1s emission (284.8 eV). After calibration, the background was subtracted using a

Shirley-type background to remove most of the extrinsic loss structure. The full width and half max (FWHM) for all the fitted peaks was maintained below 1.2 eV.

5.2.13 Photoluminescence Spectroscopy and Lifetime Measurements

Photoluminescence (PL) spectra of the solution phase samples were acquired using a Varian Cary Eclipse Fluorescence Spectrometer with a slit width of 5 nm. PL lifetime measurements were performed on samples drop-coated onto silicon wafers coated with 10 drops of the NC suspension (in toluene). Each sample was excited using the 349 nm line of a 25 mW Nd:YLF pulsed laser. Laser pulses (3 kHz) were controlled using a function generator connected to a PL-2001 Q-switched laser driver. Ultrafast lifetime measurements for the blue-emitting Si NCs were performed on a previously described system with temporal resolution of ~200 ps. In brief, the nanoparticles were dissolved in toluene to measure the lifetime decay. The sample was placed in a quartz cuvette and excited with a pulsed FP1060 laser (Fianium US Inc., Eugene, USA) which was frequency quadrupled to excite the samples at λ_{ex} = 355 nm using a fiber optic. The fluorescence decay signal was collected as a function of time as well as wavelength (every 5 nm) by the same fiber optic connected to a non-gated multichannel plate detector with an oscilloscope. The laser triggering, wavelength scanning, and data acquisition, storage, and processing were computer controlled using custom software written in LabVIEW and MATLAB. After each measurement sequence, the laser pulse temporal profile was measured at a wavelength slightly below the excitation laser line.

5.2.14 Transmission Electron Microscopy (TEM)

Transmission Electron Microscopy (TEM) images of samples H-Si NCs and H-Si NCs treated with allylamine, NH_4Br and TOAB were obtained using a JOEL-2012 (LaB_6 filament) electron microscope with an accelerating voltage of 200 kV. The TEM images of Si NC-A, Si NC-B and Si NC-C were obtained on a JEOL 2010 (LaB_6 filament) electron microscope operated at 200kV. High-resolution (HR) TEM images of H-Si NCs treated with NH_4Br and TOAB and Si NC-A were obtained from Hitachi-9500 electron microscope with an accelerating voltage of 300 kV. HRTEM images of Si NC-B were obtained on a JEOL 2500SE Schottky emitter microscope operating at 200kV and equipped with a Gatan multiscan camera and Si NC-C were obtained on a JEOL 2010 (LaB_6 filament) microscope.

TEM samples were prepared by drop coating freestanding Si NC suspension onto a carbon coated copper grid with a 400 µm diameter hole. The NC size was averaged over 200 particles, which were determined using Image J software (version 1.45).[46] The HRTEM images were processed using Gatan DigitalMicrograph software (version 2.02.800.0).[47]

5.2.15 Scanning Tunneling Microscopy (STM). *Note: These measurements were performed by the Millo group.*

For STM measurements, NCs were spin cast from a toluene solution onto atomically flat flame-annealed Au substrates. All measurements were performed at room temperature, using Pt-Ir tips. Tunneling current-voltage (I-V) characteristics were acquired after positioning the STM tip above individual NCs, realizing a double barrier tunnel junction (DBTJ) configuration[40] and momentarily disabling

the feedback loop. In general, care was taken to retract the tip as far as possible from the NC, so the applied tip-substrate voltage would fall mainly on the tip-NC junction rather than on the NC-substrate junction whose properties (capacitance and tunneling resistance) are determined by the layer of organic capping ligands that cannot be modified during the STM measurement. This protocol minimizes the voltage division induced broadening effects, and thus the measured gaps correspond well to the real SC gaps.[48-50] The dI/dV-V tunneling spectra, proportional to the local tunneling DOS, were numerically derived from the measured I-V curves. We have acquired the topographic images and tunneling spectra (on the NCs) with bias and current set-values of $V_s \cong 1.2$-1.5 V and $I_s \cong 0.1$-0.3 nA. The first is to ensure tunneling above the band edge and the other was the lowest value that still allowed acquisition of smooth tunneling spectra.

5.3 Results and Discussion

5.3.1 Hydride terminated Si NCs.

Oxide-embedded Si NCs were obtained from the thermally induced disproportionation of HSQ, a high purity electronics grade material containing sub-10 ppb concentrations of metal impurities. This product shows broad reflections in the X-ray powder diffraction (XRD) pattern that are characteristic of nanocrystalline Si domains that adopt the diamond crystal structure (**Figure 5-1**). In addition, a broad reflection arising from the amorphous silica matrix is observed at ca. 20°.

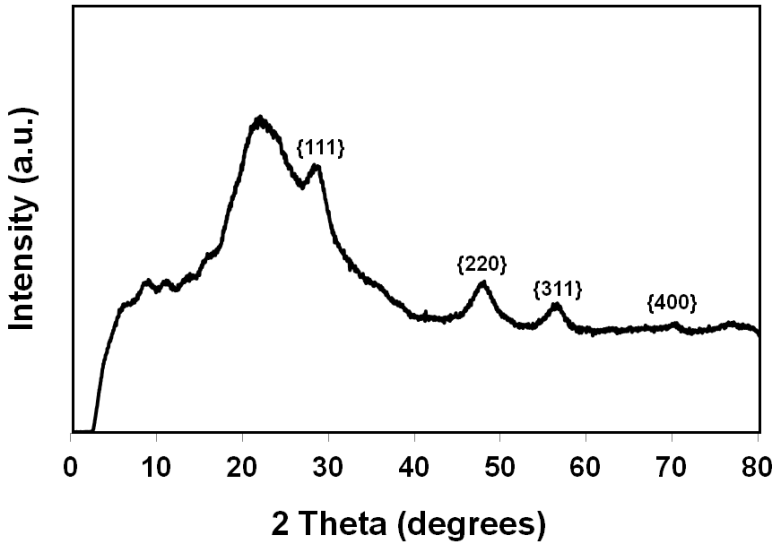

Figure 5-1. X-ray powder diffraction pattern of Si NCs embedded in silica.

This Si NC/SiO_2 composite was etched with 1:1:1 49% hydrofluoric acid:ethanol:water to liberate hydride surface terminated Si NCs (*i.e.*, H-Si NCs). The presence of the Si–H surface was confirmed using FT-IR spectroscopy (**Figure 5-2**), which showed characteristic stretching at ca. 2100 cm^{-1}. Weak Si–O–Si and Si–OH stretches are also noted at ca. $\leq$ 1200 cm^{-1} and $\geq$ 3000 cm^{-1}, respectively and result from trace oxidation of the NC surface occurring during sample preparation.[20]

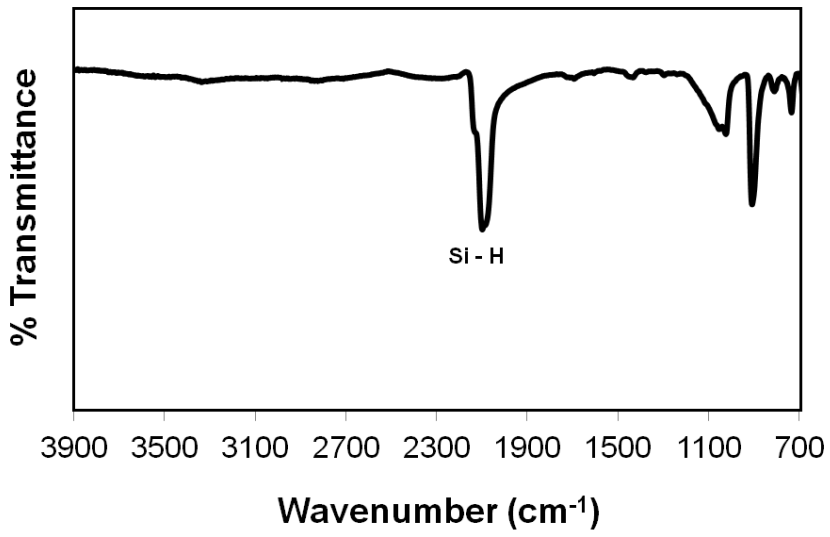

Figure 5-2. FT-IR spectrum of hydride terminated Si NCs obtained by drop coating on Si wafer from a toluene suspension.

The PL spectrum of a toluene solution of H-Si NCs shows a maximum at 630 nm upon excitation at 300 nm (**Figure 5-3A**). Excited state lifetime measurements provide a lifetime of $\tau = 1.6$ μs, in agreement with previous reports attributing the luminescence to an indirect band gap transition (**Figure 5-3B**).[23] A bright field transmission electron microscopy (TEM) image shows 3.5±0.4 nm average particle diameter consistent with the EMA (**Figure 5-4**). It is of significant importance to note the extreme air sensitivity and limited solubility of H-Si NCs preclude high accuracy direct TEM characterization; however, particle dimensions are consistent with those obtained for dodecyl surface functionalized (Si NC-A) obtained from post etching hydrosilylation (*vide infra*).

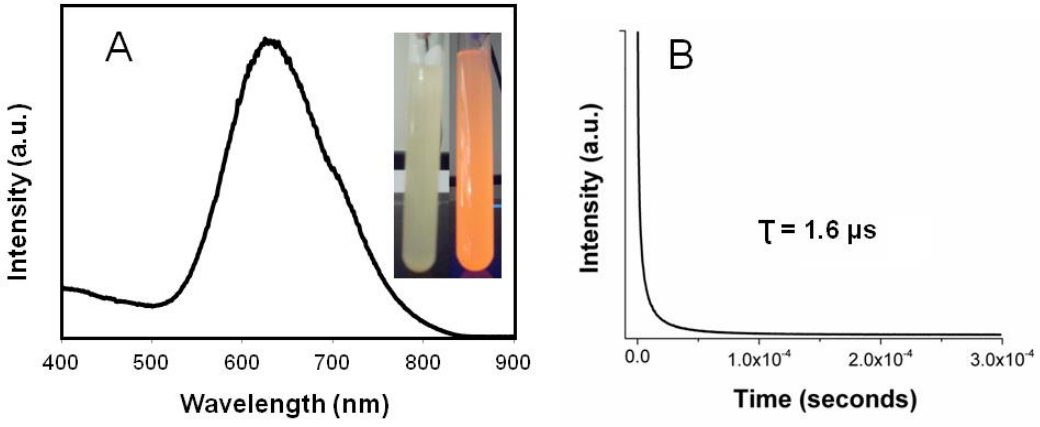

Figure 5-3. (A) PL spectrum of H-Si NCs (excitation λ = 300 nm). Inset: Photograph of toluene suspension of H-Si NCs. (B) Excited state lifetimes.

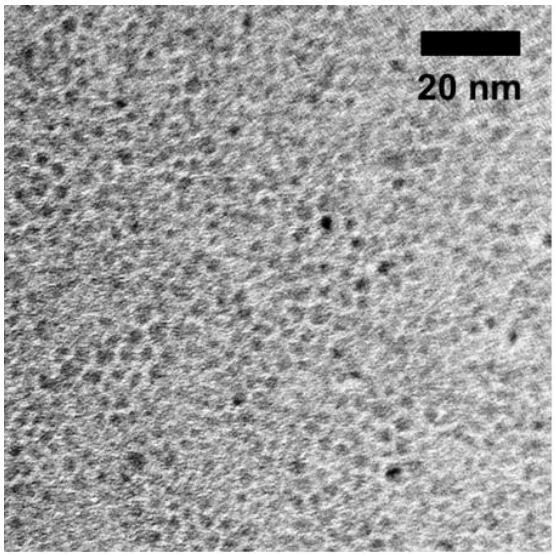

Figure 5-4. Bright field TEM image of H-Si NCs.

5.3.2 Dodecyl surface terminated Si-NCs obtained from HSQ, (Si NC-A).

Dodecyl surface functionalized Si NCs (Si NC-A) were prepared using established literature procedures.[51] The resulting Si NC-A were evaluated using a variety of techniques. The FT-IR spectrum (**Figure 5-5**) clearly shows the appearance of C–H stretching at ca. 2900 cm^{-1} and no evidence of Si–H stretching at 2100 cm^{-1}.

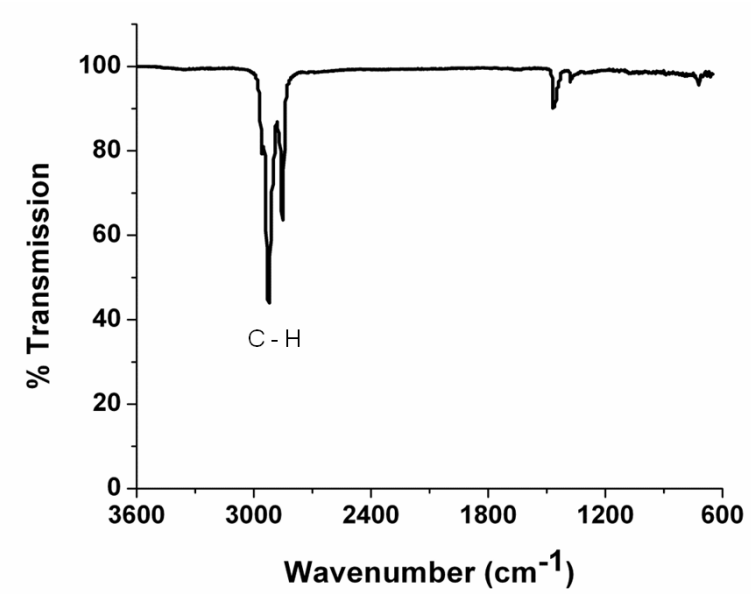

Figure 5-5. FT-IR spectrum of Si NC-A drop-coated from a toluene solution.

The X-ray photoelectron spectroscopy (XPS) of Si NC-A shows emissions arising only from silicon, carbon and oxygen (**Figure 5-6A**). The Si 2p spectral region has components characteristic of Si(0) and Si-C, and silicon suboxides (**Figure 5-6B**).

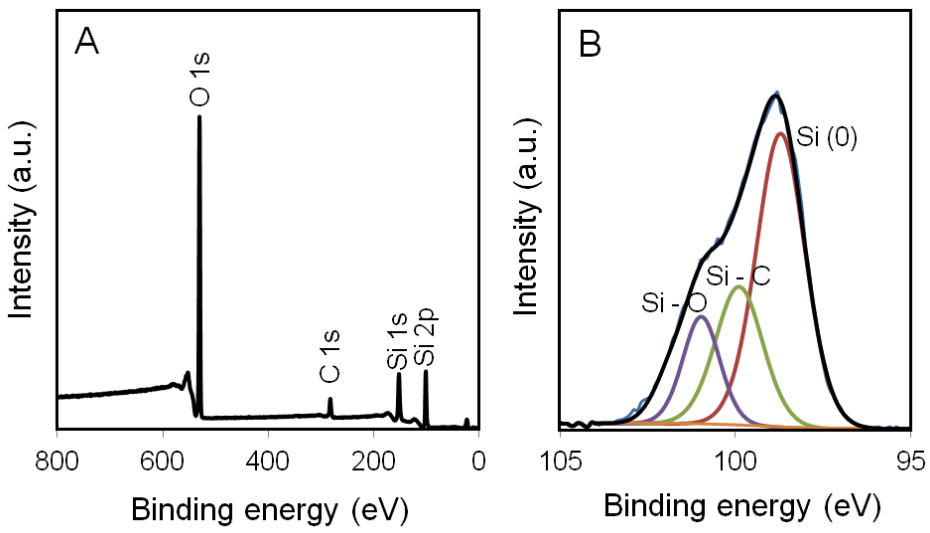

Figure 5-6. X-ray photoelectron spectra (XPS) of dodecyl surface functionalized Si NCs (Si NC-A). (**A**) Survey spectrum showing emissions arising from Si, C and O. (**B**) High resolution XP analysis of the silicon 2p spectral region. For clarity, only Si $2p_{3/2}$ emissions are shown.

The PL spectrum obtained from a non-opalescent toluene solution of Si NCs-A shows an emission maximum at ca. 720 nm (**Figure 5-7A**). PL lifetime measurements (**Figure 5-7B**) provide values in the microsecond regime (*i.e.*, τ = 19 μs) in agreement with emission lifetimes expected from indirect band gap semiconductors.[23] The red PL (**Figure 5-7C**) is consistent with an EMA estimate of particles size of 3.3 nm,[52] which is in agreement with TEM (3.5 ± 0.4 nm), high resolution (HR) TEM and XRD (3.6 nm) analysis (**Figure 5-8A-C**).

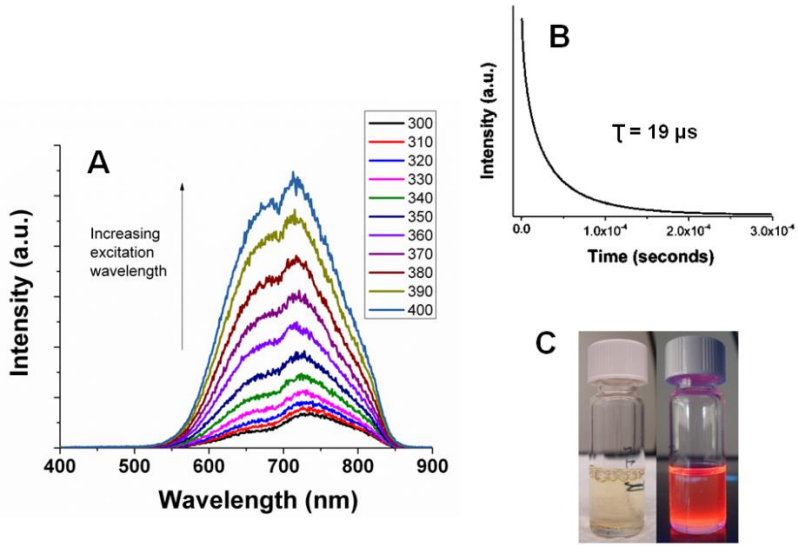

Figure 5-7. (**A**) PL spectra of Si NC-A excited at indicated wavelengths. (**B**) Excited state lifetimes. (**C**) Toluene dispersions of dodecyl terminated Si NCs under ambient (left) and UV irradiation (right).

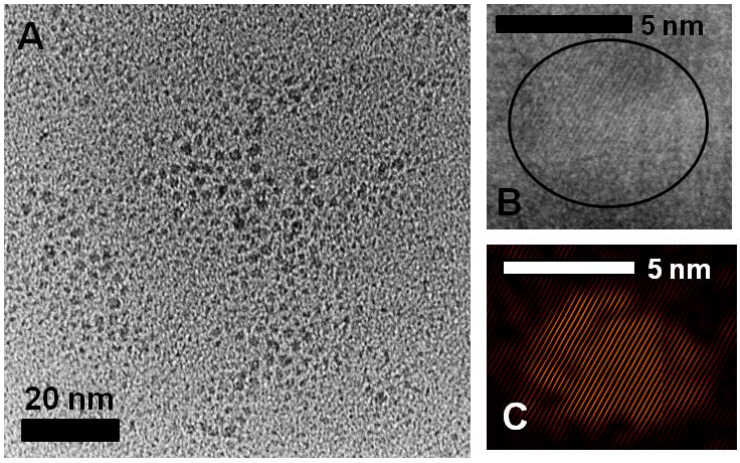

Figure 5-8. (**A**) Bright field TEM image of Si NC-A. (**B**) High-resolution transmission electron micrograph showing fringes of 0.33 nm characteristic of the Si{111} lattice spacing. (**C**) The inverse Fourier transform of the HRTEM image in **B.**

5.3.3 Dodecyl surface terminated Si NCs from the Na_4Si_4/NH_4Br reaction (Si NC-B)

Note: This study was performed by Kauzlarich group.

Si NCs were obtained by reacting sodium silicide with ammonium bromide salt. The intermediate H-Si NCs are never isolated in this reaction, but directly terminated with dodecyl surface groups *via* thermal hydrosilylation (Si NC-B). As is the case for all Si NCs presented here, the FT-IR spectrum shows expected absorption features (**Figure 5-9**), along with spectral features associated with silicon oxide at ca. 1100 - 1030 cm^{-1}.

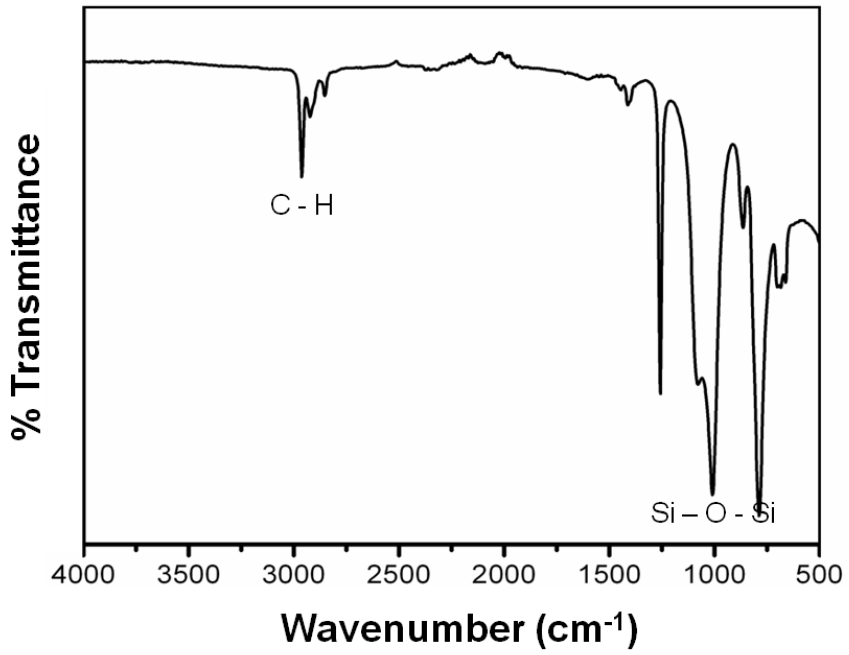

Figure 5-9. FTIR spectrum of Si NC-B.

This Zintl salt-based method produces comparatively polydispersed NCs with TEM analysis indicating Si core diameter of ca. 6 ± 2 nm for Si NC-B (**Figure 5-10**).

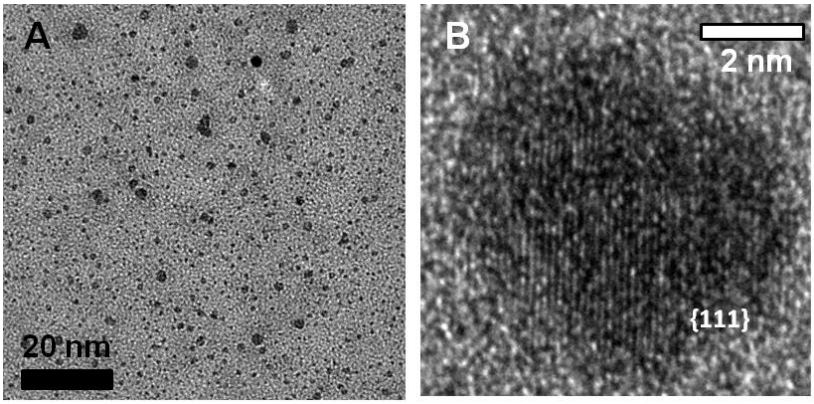

Figure 5-10. (**A**) Bright-field TEM image of Si NC-B. (**B**) HRTEM image showing lattice spacings of 0.32 nm characteristic of the {111} plane of Si.

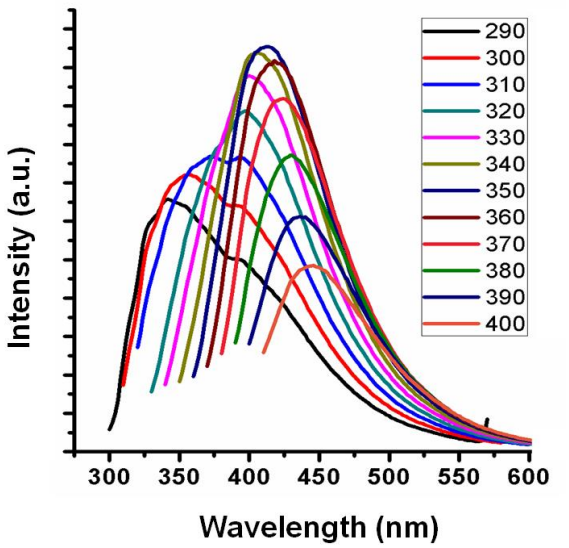

Figure 5-11. Excitation wavelength dependant PL spectra of Si NC-B in toluene.

Si NC-B exhibited an unstructured excitation wavelength dependent PL spectrum (**Figure 5-11**) in the blue spectral region that corresponds to EMA dimension of ca. 1.1 nm, which is incongruent with TEM data. In addition, short nanosecond excited state lifetimes (*i.e.*, τ < 10 ns) inconsistent with a band gap transition have been reported for these Si NCs.[53,54] XPS analysis of Si NC-B shows expected Si, O and C elemental signatures, as well as a low intensity emission in the N 1s spectral region (**Figure 5-12A**). The peak at 103.2 eV in Si 2p spectrum is consistent with a Si-N and Si-O species (**Figure 5-12B**). [55] The N 1s peak position is consistent with the nitrogen impurities being primarily located on the inside or sub-surface of the Si NC.[55]

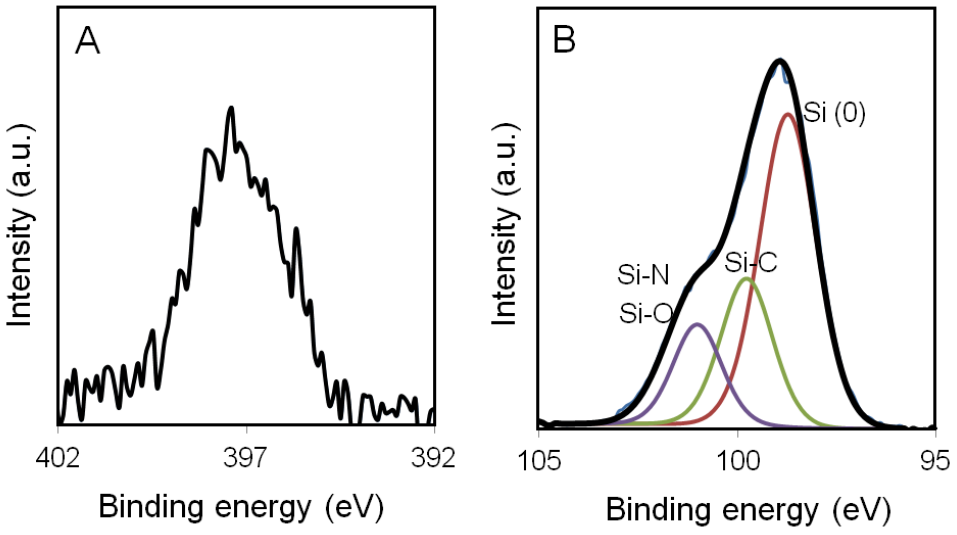

Figure 5-12. High-resolution X-ray photoelectron spectra (XPS) of the (**A**) N 1s and (**B**) Si 2p spectral regions of Si NC-B. Only Si $2p_{2/3}$ fitting peaks are shown. Si $2p_{1/2}$ components have been omitted for clarity.

5.3.4 Dodecyl surface terminated Si NCs from $SiCl_4$ reduction (Si NC-C).

Note: This study was performed by the Tilley group.

H-Si NCs are not isolated from the direct solution reduction of silicon tetrachloride. They are transient reaction species that are functionalized *in situ via* hydrosilylation in the presence of dodecene and surface functionalized Si NCs are obtained directly. The FT-IR spectrum of dodecyl (Si NC-C) terminated Si NCs (**Figure 5-13**) prepared using this procedure show spectral features arising from the expected functional groups as well as Si–O–Si absorptions.

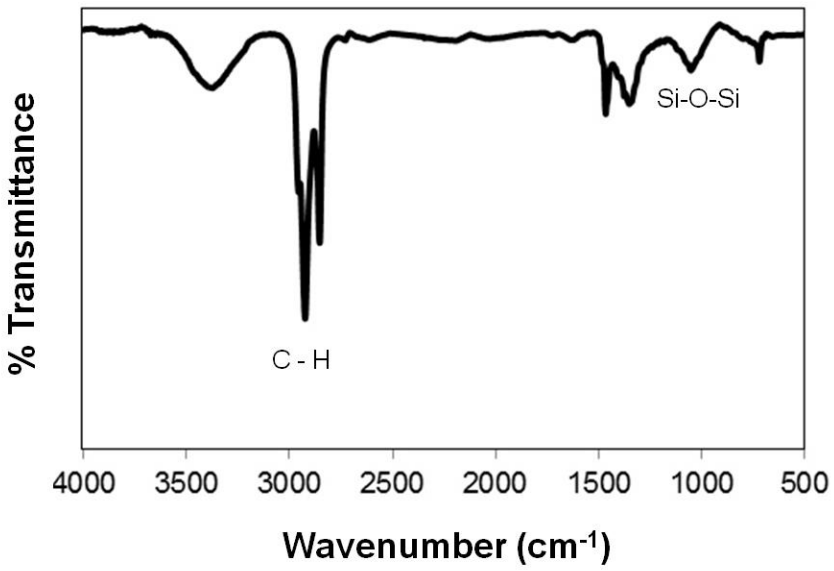

Figure 5-13. FT-IR spectrum of Si NC-C.

The PL spectra obtained for Si NC-C show excitation wavelength dependant emission maxima in the blue spectral region (**Figure 5-14**). In addition,

much shorter excited state lifetimes (*i.e.*, τ = 4 ns) have been reported, suggesting a band gap transition is not responsible.[42]

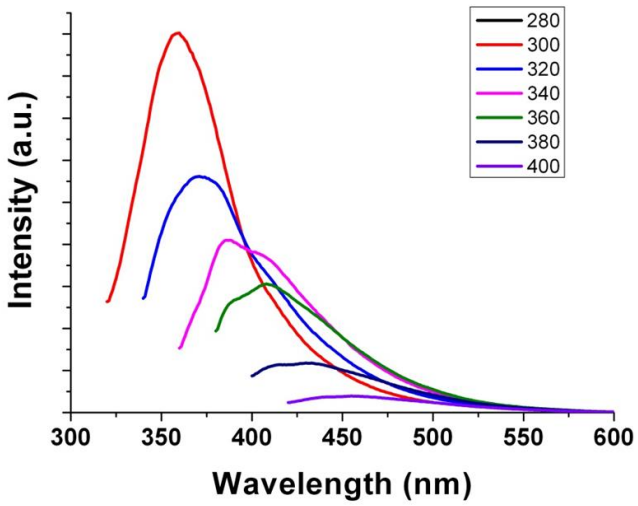

Figure 5-14. Excitation wavelength dependent PL spectra of Si NC-C obtained in toluene.

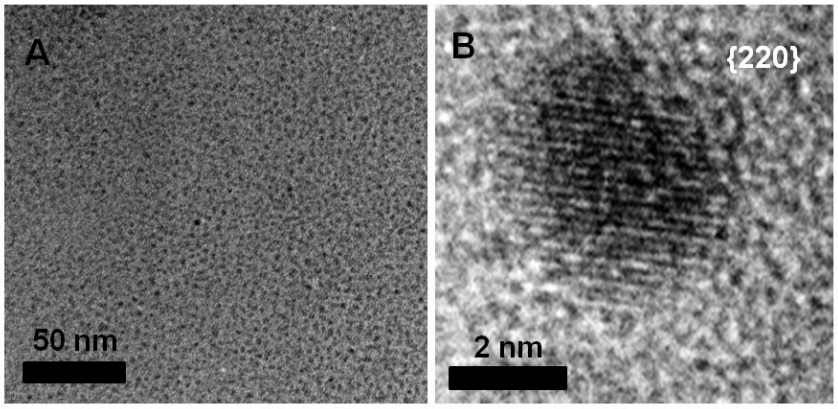

Figure 5-15. (**A**) Bright-field TEM image of Si NC-C. (**B**) HRTEM image showing fringes of 0.192 nm characteristic of the Si{220} lattice spacing.

TEM/HRTEM analysis indicates Si core dimensions of 2.7 ± 0.6 nm for Si NC-C (**Figure 5-15**). The X-ray photoelectron spectra (XPS) of Si NC-C showed the expected elemental signatures; however, surprisingly also showed a low-intensity emission in the N 1s spectral region (**Figure 5-16**). The higher binding energy of N 1s spectrum of the Si NC-C compared to that observed for Si NC-B suggests the N atoms are primarily at the surface of NCs obtained from $SiCl_4$ reduction.[56]

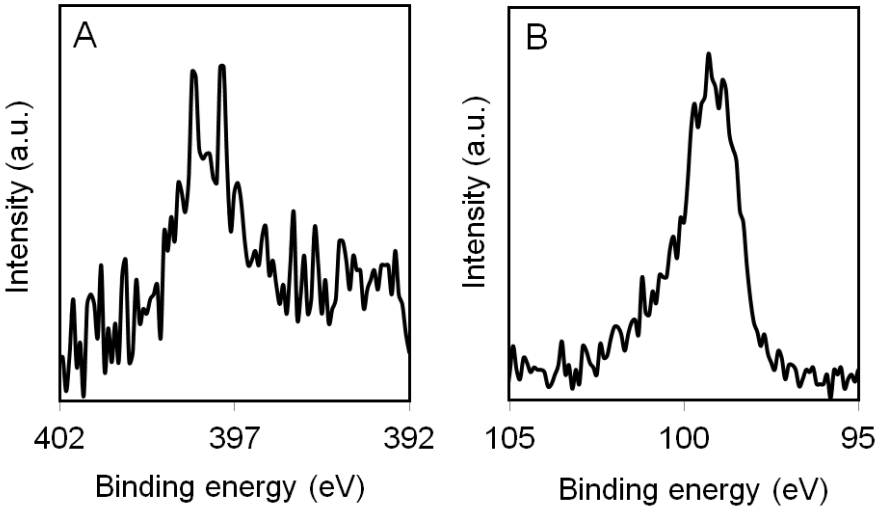

Figure 5-16. High resolution XP spectra of the (**A**) N 1s and (**B**) Si 2p spectral regions of Si NC-C.

A straightforward comparison of the Si NCs studied here indicates those exhibiting blue emission (*i.e.*, Si NC-B and Si NC-C) contain nitrogen impurities that could give rise to radiative centers that provide an alternative relaxation pathway to an indirect band gap transition. In this context, an experimental

demonstration showing that the PL maximum and excited state lifetimes of well-defined Si NCs would add clarity to the broader discussion regarding the origin of blue luminescence and be an invaluable advance in Si NC research and applications. For the blue-emitting Si NCs described here the experimental nitrogen sources are not necessarily obvious because the nitrogen containing reagents are frequently used in nanoparticle synthesis and are often considered spectators to the reaction.

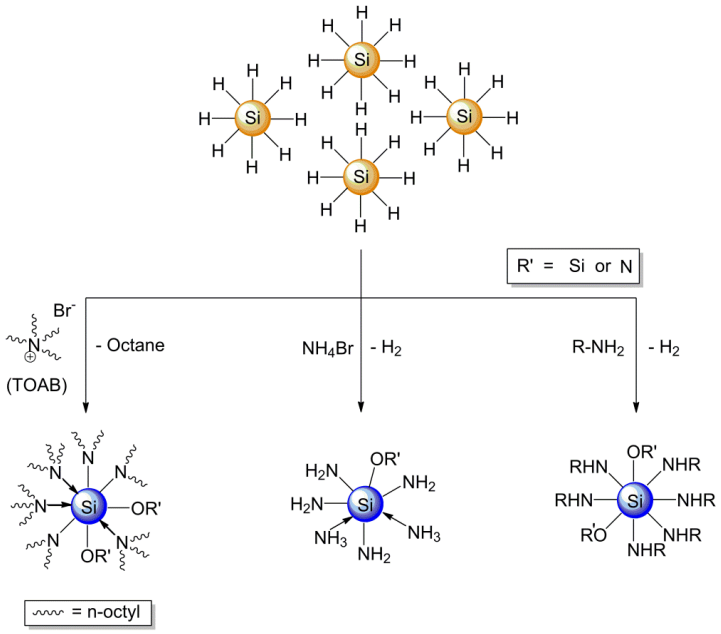

Scheme 5-1. Schematic representation of the experimental approach to forming blue-emitting Si NCs from exposure of H-Si NCs to common nitrogen sources (RNH_2, NH_4Br and tetraoctylammonium bromide (TOAB)).

In this regard, we have systematically evaluated potential nitrogen sources present in the syntheses of Si NC-B and Si NC-C, (*i.e.*, tetraoctylammonium bromide (TOAB) and ammonium bromide (NH_4Br)) in efforts to shift the luminescent response of H-Si NCs from EMA consistent red to the characteristic blue emission. To investigate the influence of these nitrogen-containing compounds we titrated these reagents into solutions of H-Si NCs (**Scheme 5-1**).

5.3.5 Influence of TOAB and NH_4Br on H-Si NC Photoluminescence.

The Si-H moiety is a very reactive species that may be converted into Si - X (X = C, N, O, S, halide, *etc*.) under relatively mild conditions.[57] TOAB reacts with H-Si NCs to initially form trioctylamine, which is suggested by XPS (N 1s peak at 399.7 eV (**Figure 5-17A**)).[58] The resulting trioctylamine binds coordinatively to the Si surface (N 1s peak at 398.8 eV, Si $2p_{3/2}$ peak at 101.1 eV (**Figure 5-17B**)) and undergoes further reduction to yield octane and dioctylamine (confirmed using ^{1}H NMR), that bonds covalently to the Si surface (N 1s peak at 398.0 eV and Si $2p_{3/2}$ peak at 103 eV). Various bonding environments are expected to complicate detailed interpretation of the XPS data, however a significant quantity of oxygen containing silicon species is present that is evident from the Si 2p XP spectrum.

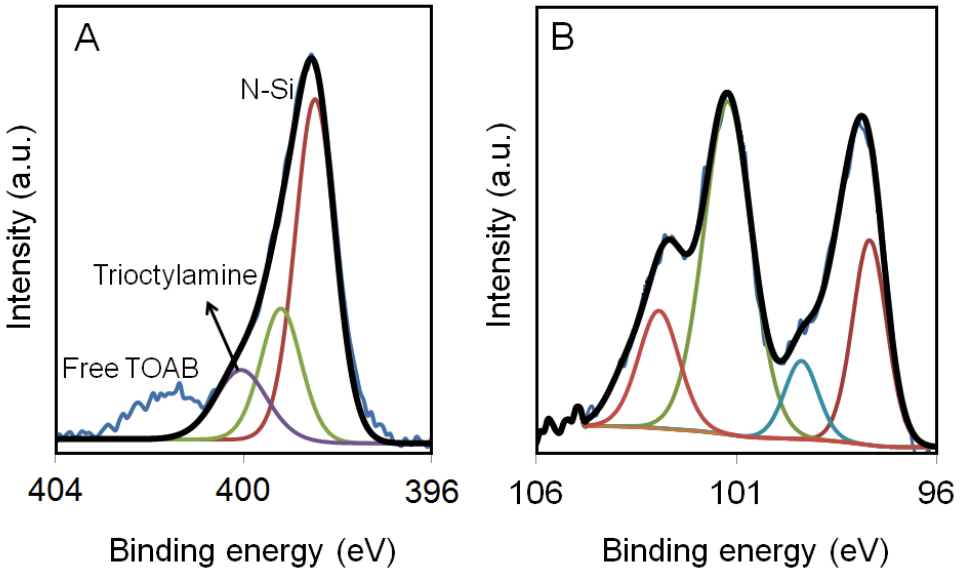

Figure 5-17. HR XP spectrum of (**A**) N 1s region and (**B**) Si 2p region of H-Si NCs reacted with TOAB. For clarity only Si $2p_{3/2}$ peaks are shown.

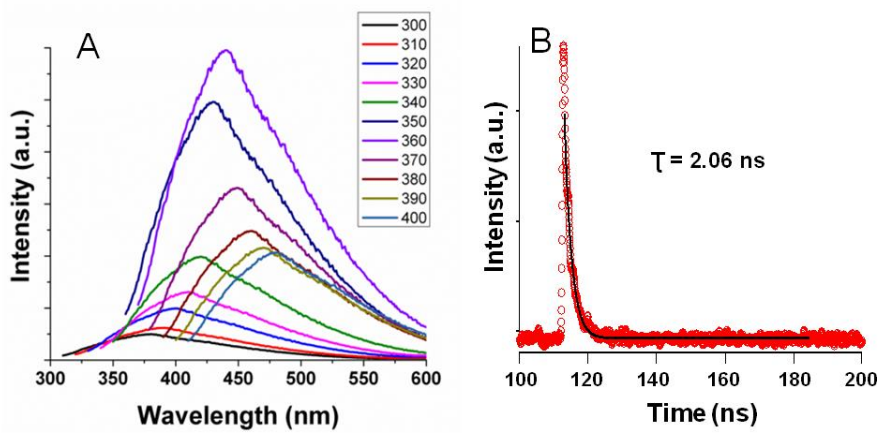

Figure 5-18. (**A**) Excitation wavelength dependent PL spectra, (**B**) Excited state lifetimes of H-Si NCs reacted with TOAB.

H-Si NCs reacted with TOAB exhibited excitation wavelength dependent blue PL (**Figure 5-18A**) and short excited state lifetimes (*i.e.*, ca. τ = 2.06 ns**,** **Figure 5-18B**).

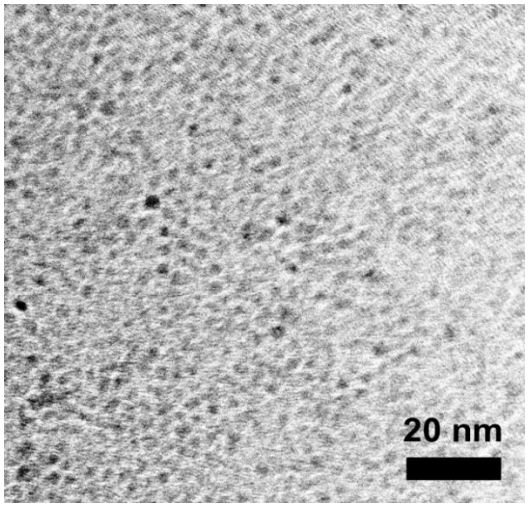

Figure 5-19. Bright field TEM image of H-Si NCs reacted with TOAB. The average particle size = 3.6 ± 0.8 nm.

TEM analyses confirm that these changes in PL do not arise from changes in NC size **(Figure 5-19)**. The evolution of the blue PL with increasing concentration of TOAB is shown in **Figure 5-20**.

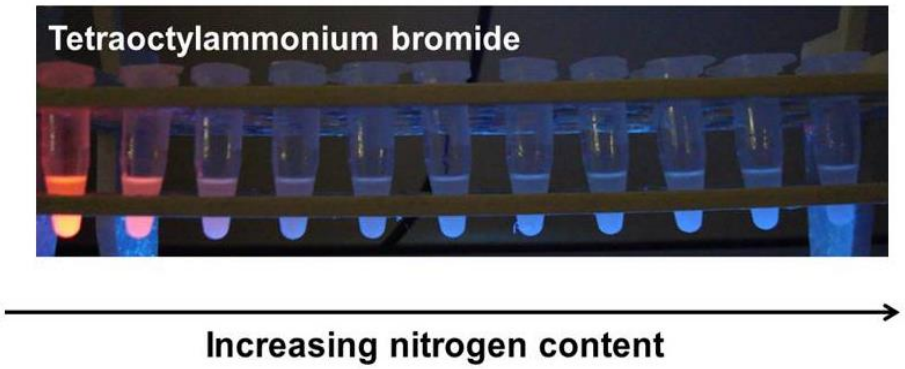

Figure 5-20. Photograph of H-Si NCs under UV illumination that have been reacted with increasing amount of TOAB.

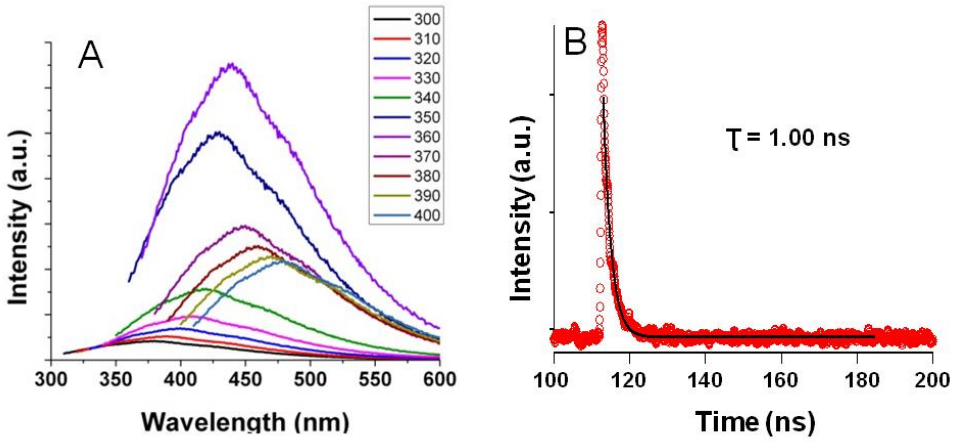

Figure 5-21. (**A**) Excitation wavelength dependent PL spectra, (**B**) Excited state lifetimes of H-Si NCs reacted with NH_4Br.

H-Si NCs also react with NH_4Br and change their emission color from red to blue. The excited state lifetime was found to be τ = 1.00 ns and excitation

wavelength dependent emission was noted (**Figure 5-21**). Si NC size was found to be 3.8 ± 0.7 nm by TEM (**Figure 5-22**).

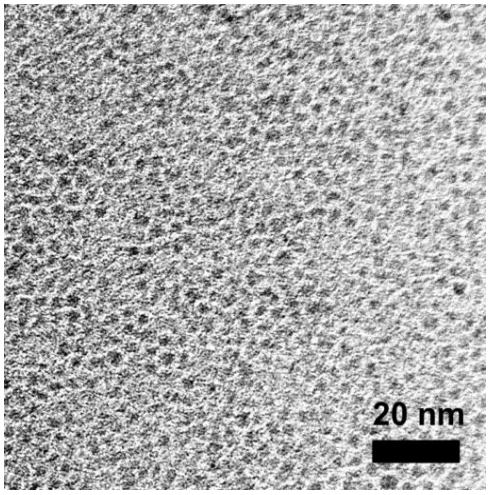

Figure 5-22. Bright field TEM image of H-Si NCs reacted with NH_4Br.

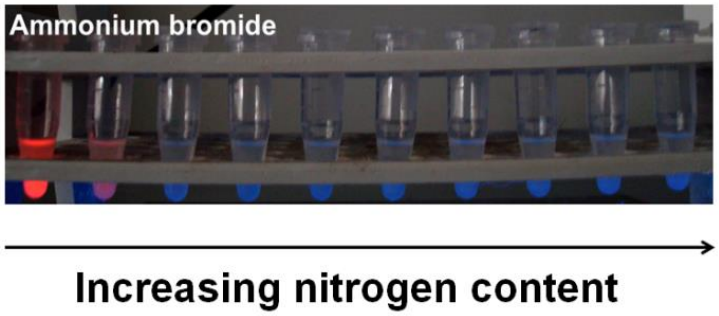

Figure 5-23. Photograph of H-Si NCs under UV illumination that have been reacted with increasing amount of NH_4Br.

Qualitatively, the relative PL intensity of the Si NCs treated with NH_4Br is lower than that of other blue-emitting Si NCs (**Figure 5-23**). This lower intensity PL could result from the limited solubility of $–NH_2$ functionalized Si NCs in the solvent medium.

The formation of a covalent Si–N and Si-O bond is confirmed by XPS (**Figure 5-24**). Both in the case of TOAB and NH_4Br very low concentrations of nitrogen compounds (< 0.2 nitrogen atomic %) are required to induce blue PL (**Figure 5-25**).

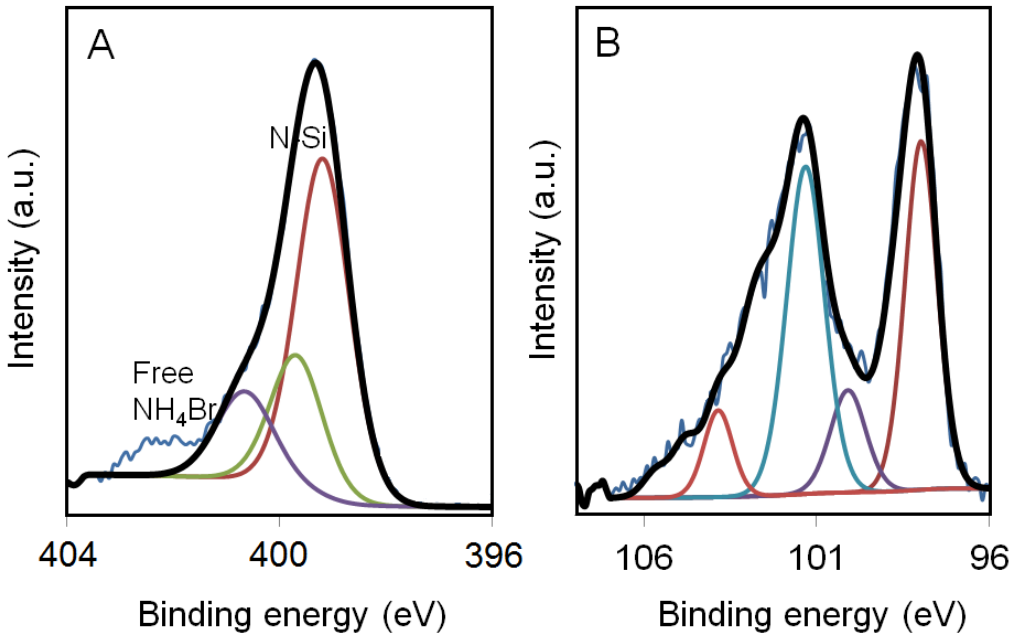

Figure 5-24. HR XP spectrum of (A) N1s region and (B) Si 2p region of H-Si NCs reacted with NH_4Br. Only Si $2p_{3/2}$ peaks are shown for clarity.

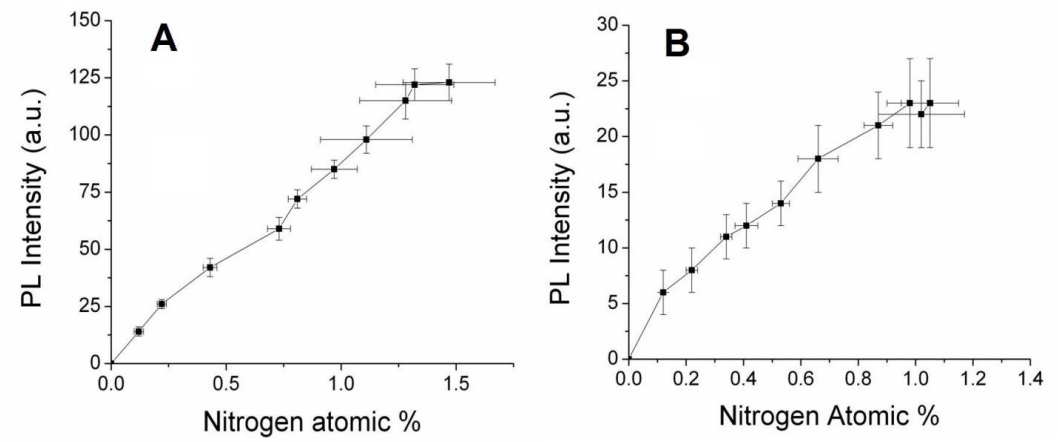

Figure 5-25. PL intensity at 420 nm vs. nitrogen concentration for H-Si NCs reacted with (A) TOAB and (B) NH_4Br.

Control experiments in which H-Si NCs were exposed to TOAB and NH_4Br in absence of air resulted in no blue PL and the red luminescence was quenched. Similarly, when H-Si NCs were exposed to air in absence of nitrogen compounds to oxidize the surface and no blue PL was observed. These observations are consistent with both nitrogen and oxygen being crucial for the appearance of blue PL in the present Si NCs.

5.3.6 Solvatochromism studies.

Blue PL has been reported for SiO_xN_y materials,[59-61] however the exact mechanism remains unknown. Nekrashevich *et al*. have calculated the electronic structure of silicon oxynitride and proposed a possible charge transfer mechanism from silicon to nitrogen or oxygen centers as its origin.[62] Similarly, Green *et al*. reported blue PL from silicon carboxylate structures that originated from charge

transfer mechanism.[63] Charge transfer based PL bands usually lie in the UV-Vis region, have short-lived excited states and exhibit solvatochromic response.[64] To explore the possible role of charge transfer mechanism in the origin of blue PL in the present systems we obtained PL spectra in a series of solvents of known polarities. PL spectra were collected for Si NC-C as well as H-Si NC reacted with TOAB and NH_4Br. In all cases, the PL maximum red-shifted with increasing solvent polarity consistent with a charge transfer excited state (**Figure 5-26**).[65] We observed a shift of ~ 50 nm in PL emission maximum by changing the solvent from pentane to chloroform. Red luminescent from Si NC-A and blue luminescent Si NC-B did not exhibit solvatochromic response. The lack of Si NC-B solvatochroism response is believed to be the result of the nitrogen impurities being localized within the particle and inaccessible to the solvent medium, consistent with XPS data presented here.

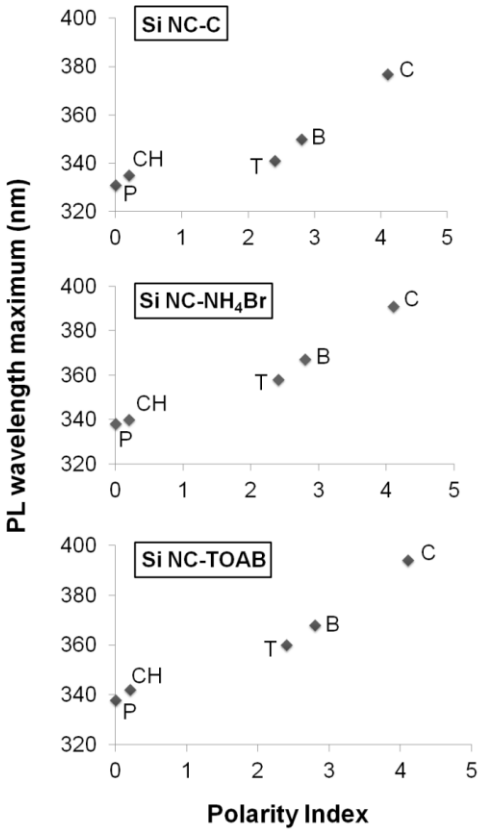

Figure 5-26. PL maximum vs. solvent polarity for different Si NCs. P = pentane, CH = cyclohexane, T = toluene, B = benzene and C = chloroform. The Si NC concentration was 1 mg/mL and the excitation wavelength was 300 nm.

5.3.6 STM studies.

STM studies were performed to investigate possible surface doping effects induced by the surface bounded ligands. A fundamental outcome of doping in bulk semiconductors is a shift of the Fermi level toward the conduction band for *n*-type doping and, conversely, toward the valence band for *p*-type doping. Remarkably, and quite surprisingly (for reasons that will be discussed below), a shift of the Fermi

level toward the *valence* band, consistent with *p*-type doping, is clearly identified in the *dI/dV-V* tunneling spectra measured on Si-NCs with NH_4Br- and allylamine-derived surface capping (**Figure 5-27 A,B**). A reasonable ligand-bonding configuration that explains the observed "*p*-doping" effect can be proposed when considering the protocol used to functionalize the NCs. As discussed earlier in this chapter, upon exposure to air or water a Si-O-N species forms on the NC surface. These surface groups are usually viewed as being electron withdrawing,[66] thus giving rise to a *p*-doped NC. In the case of NCs exposed to allylamine, an even stronger *p*-type like doping effect can be expected, since in addition to the above charge transfer associated with the Si-O-N surface group, the molecule has a dipole moment directed outward from the NC surface, which should give rise to further upwards shift of the Si-NC energy levels, akin to the reminiscent band-bending effect in semiconductor surfaces.[67]

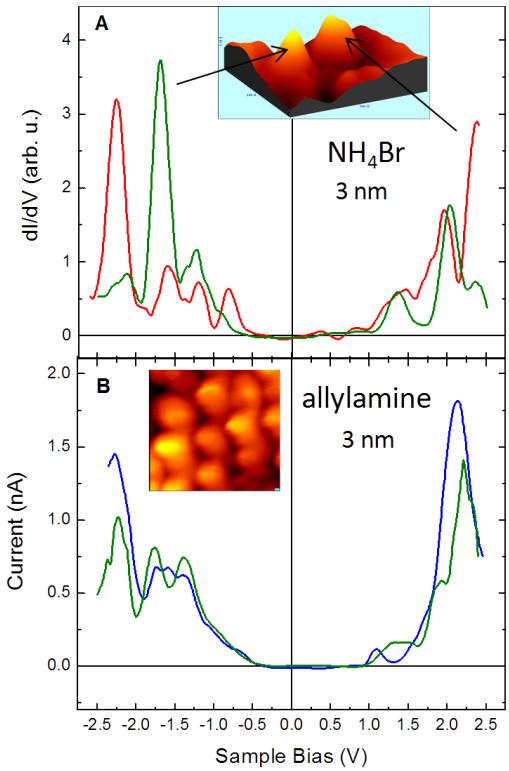

Figure 5-27. Effect of ligand-induced surface doping on Si-NCs. Two tunneling spectra measured on (A) NH_4Br capped 3 nm Si NCs presented in the inset and (B) allylamine functionalized Si NCs shown in the inset.

5.4 Conclusions.

Trace nitrogen and oxygen contamination of the presented Si NCs samples was confirmed by the XPS analysis and provides a reasonable explanation for the fast blue emission. The present study definitively shows the Si NCs prepared by two of the low temperature solution methods contain nitrogen/oxygen and that exposure of H-Si NCs to nitrogen containing reagents in the presence of oxygen effectively induces blue PL. Both of these findings support the hypothesis that a

nitrogen defect or impurity site provides a mechanism of the blue emission. While the exact identity of the nitrogen containing surface species remains unknown, it is clear the reactivity of Si-H surfaces must be considered when preparing luminescent Si NCs. Ongoing studies are aimed at identifying the emissive center and exploring methods to tailor its optical response. A *p*-type doping-like effect, manifested by a shift of the band-edge toward lower energies, is found to take place upon surface functionalization with allylamine and NH_4Br. These behaviors may be attributed to the combined effects of the electrical dipole of the ligands and charge transfer between them and the NC.

5.5 References.

1. A. P. Alivisatos, *Science*, 1996, **271**, 933.
2. A. Rogach, *Semiconductor Nanocrystal Quantum Dots*, Springer, 2008.
3. X. Michalet, F. F. Pinuad, L .A. Bentolila, J. M. Tsay, S. Doose, J. J. Li, G. Sundaresan, A. M. Wu, S. S. Gambhir and S. Weiss, *Science*, 2005, **307**, 538.
4. E. Biolatti, I. D'Amico, P. Zanardi and F. Rossi, *Phys. Rev. B*, 2002, **65**, 075306.
5. I. Gur, N. A. Fromer, M. L. Geier and A. P. Alivisatos, *Science*, 2005, **310**, 462.
6. G. F. Nordberg, *Environ. Health Perspect*., 1984, **54**, 213.
7. www.rohs.gov.uk.
8. www.psivida.com
9. www.rsc.org/periodic-table/element/14
10. K. Fujoka, S. Hanada, F. Kanaya, A. Hoshino, K. Sato, S. Tokosuka, Y. Takigami, K. Hirakuri, A. Shiohara, R. D. Tilley, N. Manabe, K. Yamamoto and Y. Manome, *J. Phys. Conf. Ser*., 2011, **304**, 12042.
11. F. Erogbogbo, K. T. Yong, R. Hu, W. C. Law, H. Ding, C. W. Chang, P. N. Prasad and M. T. Swihart, *ACS Nano*, 2010, **4**, 5131.
12. S. C. Bayliss, R. Heald, D. I. Fletcher and L. D. Buckberry, *Adv. Mater*., 1999, **11**, 318.
13. V. Kocevski, O. Eriksson and J. Rusz, *Phys. Rev. B*, 2013, **87**, 245401.
14. A. G. Cullis and L. T. Canham, *Nature*, 1991, **353**, 335.
15. T. K. Sham, D. T. Jiang, I. Couithard, J. W. Lorimer, X. H. Feng, K. H. Tan, S. P. Frigo, R. A. Rosenberg, D. C. Houghton, B. Bryskiewicz, *Nature*, 1993, **363**, 331.
16. A. G. Cullis, L. T. Canham and P. D. J. Calcott, *J. Appl. Phys*., 1007, **82**, 909.
17. G. Polisski, H. Heckler, D. Kovalev, M. Schwartzkopff and F. Koch, *Appl. Phys. Lett*., 1998, **73**, 1107.
18. X. Li, Y. He, S. S. Talukdar and M. T. Swihart, *Langmuir*, 2003, **19**, 8490.
19. X. D. Pi, R. W. Liptak, J. D. Nowak, N. P. Wells, C. B. Carter, S. A. Campbell and U. Kortshagen, *Nanotechol*., 2008, **19**, 245603.
20. C. M. Hessel, E. J. Henderson and J. G. C. Veinot, *Chem. Mater*., 2006, **18**, 6139.
21. D. S. English, L. E. Pell, Z. Yu, P. F. Barbara and B. A. Korgel, *Nano Lett*., 2002, **2**, 681.
22. M. S. Hybertsen, *Phys. Rev. Lett*., 1994, **72**, 1514.
23. V. A. Belyakov, V. A. Burdov, R. Lockwood and A. Meldrum, *Adv. Opt. Technol*., 2008, **2008**, 279502.

24. L. Pavesi, L. Dal Negro, L. Mazzoleni, G. Franzo and F. Priolo, *Nature*, 2000, **408**, 440.

25. L. Khriachtchev, M. Rasanen, S. Novikov and J. Sinkkonen, *Appl. Phys. Lett*., 2001, **79**, 1249.

26. J. Ruan, P. M. Fauchet, L. Dal Negro, M. Cazzanelli and L. Pavesi, *Appl. Phys. Lett*., 2003, **83**, 5479.

27. L. Dal Negro, M. Cazzanelli, L. Pavesi, S. Ossicini, D. Pacifici, G. Franzo, F. Priolo and F. Iacona, *Appl. Phys. Lett*., 2003, **82**, 4636.

28. M. V. Wolkin, J. Jorne, P. M. Fauchet, G. Allan and C. Delerue, *Phys. Rev. Let*t., 1999, **82**, 197.

29. K. Kusova, O. Cibulka, K. Dohnalova, I. Pelant, J. Valenta, A. Fucikova, K. Zidek, J. Lang, J. Englich, P. Matejka, P. Stepanek and S. Bakardjieva, *ACS Nano*, 2010, **4**, 4495.

30. G. Belomoin, J. Therrien and M. Nayfeh, *Appl. Phys. Lett*., 2000, **77**, 779.

31. J. Valenta, A. Fucikova, I. Pelant, K. Kusova, K. Dohnalova, A. Aleknevicius, O. Cibulka, A. Fojtik and G. Kada, *New J. Phys*., 2008, **10**, 073022.

32. V. Svrcek, T. Sasaki, Y. Shimizu and N. Koshizaki, *Appl. Phys. Lett*., 2006, **89**, 213113.

33. R. M. Sankaran, D. Holunga, R. C. Flagan and K. P. Giapis, *Nano Lett*., 2005, **5**, 537.

34. J. D. Holmes, K. J. Ziegler, R. C. Doty, L. E. Pell, K. P. Johnston and B. A. Korgel, *J. Am. Chem. Soc*., 2001, **123**, 3743.

35. K. Dohnalova, A. Fucikova, C. P. Umesh, J. Humpolickova, J. M. J. Paulusse, J. Valenta, H. Zuilhof and M. Hof, *Small*, 2012, **8**, 3185.

36. K. Zidek, I. Pelant, F. Trojanek, P. Maly, P. Gilliot, B. Honerlage, J. Oberle, L. Siller, R. Little and B. R. Horrocks, *Phys. Rev. B*, 2011, **84**, 085321.

37. K. Dohnalova, K. Zidek, L. Ondic, K. Kusova, O. Cibulka and I. Pelant, *J. Phys. D: Appl. Phys*., 2009, **42**, 135102.

38. E. Lioudakis, A. Othonos and A. G. Nassiopoulou, *Appl. Phys. Lett*., 2007, **90**, 171103.

39. M. Luppi and S. Ossicini, *Phys, Rev. B*, 2005, **71**, 035340.

40. A. Brewer and K. von Haeften, *Appl. Phys. Lett*., 2009, **94**, 261102.

41. J. H. Warner, A. Hoshino, K. Yamamoto and R. D. Tilley, *Angew. Chem. Int. Ed*., 2005, **44**, 4550.

42. A. Shiohara, S. Hanada, S. Prabakar, K. Fujioka, T. H. Lim, K. Yamamoto, P. T. Northcote and R. D. Tilley, *J. Am. Chem. Soc*., 2010, **132**, 248.

43. J. Zou, R. K. Baldwin, K. A. Pettigrew and S. M. Kauzlarich, *Nano Lett*., 2004, **4**, 1181.

44. K. A. Pettigrew, Q. Liu, P. P. Power and S. M. Kauzlarich, *Chem. Mater*., 2003, **15**, 4005.

45. C. S. Yang, R. A. Bley, S. M. Kauzlarich, H. W. H. Lee and G. R. Delgado, *J. Am. Chem. Soc*., 1999, **121**, 5191.

46. www.rsbweb.nih.gov/ij/

47. www.gatan.com/products/software/

48. U. Banin and O. Millo, *Ann. Rev. Phys. Chem*., 2003, **54**, 465.

49. E. P. A. M. Bakkers, Z. Hens, A. Zunger, A. Franceschetti, L. P. Kouwenhoven, L. Gurevich and D. Vanmaekelbergh, *Nano Lett*., 2001, **1**, 551.

50. E. P. A. M. Bakkers and D. Vanmaekelbergh, *Phys. Rev. B*, 2000, **62**, 7743.

51. J. A. Kelly, A. M. Shukaliak, M. D. Fleischauer and J. G. C. Veinot, *J. Am. Chem. Soc*., 2011, **133**, 9564.

52. L. E. Brus, *J. Phys. Chem*., 1986, **90**, 2555.

53. T. M. Atkins, A. Thibert, D. S. Larsen, S. Dey, N. D. Browning and S. M. Kauzlarich, *J. Am. Chem. Soc*., 2011, **133**, 20664.

54. X. Zhang, M. Brynda, R. D. Britt, E. C. Carroll, D. S. Larsen, A. Y. Louie and S. M. Kauzlarich, *J. Am. Chem. Soc*., 2007, **129**, 10668.

55. H. L. Zhu, F. D. Han, J. Q. Bi, Y. J. Bai, Y. X. Qi, L. L. Pang, C. G. Wang and S. J. Li, *J. Am. Ceram. Soc*., 2009, **92**, 535.

56. M. R. Alexander and F. R. Jones, *Surf. Interface Anal*., 1994, **22**, 230.

57. E. Keinan, *Pure & Appl. Chem*., 1989, **61**, 1737.

58. M. Dasog and J. G. C. Veinot, *Chem. Commun*., 2012, **48**, 3760.

59. X. Liu, J. N. Calata, H. Liang, W. Shi, X. Lin, K. Lin and G. G. Qin, *Mat. Res. Soc. Symp. Proc*., 1999, **588**, 141.

60. T. Noma, K. S. Seol, H. Kato, M. Fujimaki and Y. Ohki, *Appl. Phys. Lett*., 2001, **79**, 1995.

61. L. Zhang, T. Shi, Z. Tang, D. Liu, S. Xi, X. Li and W. Lai, *Nanoscale Res. Lett*., 2011, **6**, 469.

62. S. S. Nekrashevich and V. A. Gritsenko, *J. Appl. Phys*., 2011, **110**, 114103.

63. W. H. Green, K. P. Le, J. Grey, T. T. Au and M. J. Sailor, *Science*, 1997, **276**, 1826.

64. C. E. Housecraft and A. G. Sharpe, *Inorganic Chemistry*, Pearson, 1st. Ed., 2005.

65. T. He, D. A. Corley, M. Lu, N. H. Di Spinga, J. He, D. P. Nackashi, P. D. Franzon and J. M. Tour, *J. Am. Chem. Soc*., 2009, **131**, 10023.

66. P. V. Kamat, *J. Phys. Chem. C*, 2008, **112**, 18737.

67. A. M. Smith and S. Nie, *Acc. Chem. Res*., 2010, **43**, 190.

Chapter 6:

Tunable Photoluminescence from Silicon Nanocrystals

6.1 Introduction

Silicon (Si) is a material that has dominated the field of microelectronics[1-5] for quite some time, but when it comes to photonic devices it has had little impact due to its poor light emitting properties.[6] However, nano-structured Si has shown some promise in the development of light-emitting devices due to its surprising luminescence properties; these characteristics were initially observed in porous Si,[7-13] and more recently in Si nanocrystals (NCs).[14-17] Nano-crystalline Si (with particle size above 1.3 nm) has an indirect band gap, rendering the emission of light from the material relatively inefficient as significant amount of energy is often lost in the form of phonons in order to conserve the momentum.[8] The indirect nature of the band gap also leads to longer excited state lifetimes (ms - μs) and lowers the probability of radiative recombination.[18-20] This decreases the quantum yield of the photoluminescence (PL) arising from the band gap transition in Si-NCs, compared to the direct gap III-V[21-23] and II-VI[24-26] semiconductors.

Over the last decade, doping of Si-NCs with shallow impurities has been explored as a potential route to enhance the PL properties. Si-NCs have been doped or co-doped with phosphorus, boron, nitrogen, and hydrogen atoms.[27-39] While, researchers initially observed improvement in PL properties of phosphorus and boron doped Si-NCs, it quickly became evident that the enhancement was sensitive to dopant concentrations, fabrication methods, and location of the dopant atoms.[40-42] These factors are not easily controlled, hence doping does not offer a straightforward method to improve the optical properties of Si-NCs.

It is becoming increasingly evident that surface states and interfacial defects play crucial roles in determining the optical properties of Si-NCs.[6] As discussed in the previous Chapter, high energy blue PL can originate from nitrogen- and oxygen-based surface states.[43,44] Emissions of this type exhibit short-lived excited states and often exhibit higher photoluminescent quantum yields. Surface engineering can offer a means of creating brighter Si-NCs with tunable PL and faster lifetimes. While some reports of plasmonic enhancement of Si-NC PL have appeared,[45,46] no reports have described a systematic effort to alter the surface groups to tune the PL maximum have appeared.

In this Chapter, the Si-NCs with an average diameter of ~ 3 nm passivated with various different functional groups have been synthesized. The PL has been tuned across the visible spectrum through the incorporation of various functional groups without altering the particle size. The excited state lifetimes of all surface emitting Si-NCs are short lived (nanosecond) and the emission is brighter than those reported for Si-NCs emitting from a quantum confined band gap state.

6.2 Experimental

6.2.1 Materials.

Hydrogen silsesquioxane (HSQ) was purchased from Dow Corning Corporation (Midland, MI) as FOx-17. 1-Dodecene (97%, Sigma-Aldrich), trioctylphosphine oxide (TOPO, 97%, Sigma-Aldrich), phosphorus pentachloride (PCl_5, 98%, Sigma-Aldrich), dodecylamine (98%, Sigma-Aldrich), diphenylamine (99%, Sigma-

Aldrich), hydrofluoric acid (HF, 49%, J. T. Baker), toluene (ACS grade, BDH), anhydrous toluene (Sigma-Aldrich), methanol (MeOH, ACS grade, Sigma-Aldrich), and ethanol (EtOH, ACS grade, Sigma-Aldrich) were used without further purification.

6.2.2 Syntheses of oxide embedded Si-NCs.

Established literature procedures were used to prepare oxide-embedded silicon nanocrystals (Si-NC/SiO_2).[47] Briefly, solid HSQ (ca. 3 g) was placed in a quartz boat and transferred to a Lindberg Blue tube furnace and heated from ambient to a peak processing temperature of 1100 °C at 18 °C min^{-1} in a slightly reducing atmosphere (5% H_2/95% Ar). The sample was maintained at the peak processing temperature for 1 hour. Upon cooling to room temperature, the resulting amber solid was ground into a fine brown powder using an agate mortar and pestle. This yields oxide embedded Si-NCs with an average diameter of ca. 3 nm (composite [**1**]). To make larger particles, 0.5 g of composite [**1**] was transfered to a high temperature furnace (Sentro Tech Corp.) for further thermal processing under argon atmosphere. The composite was heated to 1200 °C at 10 °C/min and maintained at that temparature for an hour and cooled to room temperature. This yielded composite [**2**] with average Si-NC diameter of ca. 5nm embedded in silica matrix.

6.2.3 Synthesis of hydride terminated Si-NCs.

Freestanding hydride terminated Si-NCs liberated from the oxide matrix *via* hydrofluoric acid etching. Approximately 0.25 g of Si-NC/SiO_2 composite was transferred to a Teflon® beaker and 3 mL of DI water, EtOH, and 49% HF acid were added to the beaker with stirring in subdued light. (Caution: Hydrofluoric

acid can be extremely dangerous and must be handled with great care.) The resulting dark brown, cloudy mixture was stirred for one hour. Hydrophobic hydride terminated Si NCs were extracted from the aqueous etching mixture using three 20 mL toluene extractions. The remaining aqueous solution was colourless and transparent. All remaining HF was neutralized using an excess of aqueous saturated solution of calcium chloride. The cloudy dark brown Si NC/toluene extracts were placed into glass test tubes and centrifuged using a low speed (7000 rpm) centrifuge for 5 minutes. After centrifugation, the toluene supernatant was decanted leaving a precipitate of hydride terminated Si-NCs. No effort was made to keep the particles under inert atmosphere during the extraction and centrifuging steps.

6.2.4 Synthesis of dodecyl functionalized Si-NCs under inert atmosphere.

Hydride terminated Si-NCs (obtained from composite [**1**]) were re-dispersed in 50 mL of 1-dodecene, and transferred into an oven dried Schenk flask. The cloudy brown suspension was degassed using three vacuum pump cycles and maintained under a dry argon atmosphere. The flask was placed in a silicone oil bath and heated to 190 °C for 15 hours. After reaction, a transparent orange-brown solution was obtained consistent with effective functionalization. The reaction mixture was divided equally between four 50 mL PTFE centrifuge tubes. NCs were precipitated using a 3:1 mixture of EtOH:MeOH (20 mL). Particles were centrifuged at 14000 rpm for 20 min using a Beckman J2-21 high-speed centrifuge, followed by decanting of the supernatant. Three dissolution/precipitation/centrifugation cycles were performed using a toluene/MeOH/EtOH mixture (1:3:1). After the final

precipitation, the functionalized Si NCs were dispersed in toluene, filtered through a hydrophobic PTFE filter, and stored in a glass vial until further use.

6.2.5 Synthesis of dodecyl functionalized Si-NCs in air.

Hydride terminated Si-NCs (obtained from composite [**1**]) were re-dispersed in 5 mL of 1-dodecene and 25 mL toluene. The reaction mixture was refluxed at 110 ^{o}C for 12 hours. After reaction, a transparent orange-brown solution was obtained consistent with effective functionalization. The reaction mixture was divided equally between four 50 mL PTFE centrifuge tubes. NCs were precipitated using a 3:1 mixture of EtOH:MeOH (20 mL). Particles were centrifuged at 14000 rpm for 20 min using a Beckman J2-21 high-speed centrifuge, followed by decanting of the supernatant. Three dissolution/precipitation/centrifugation cycles were performed using a toluene/MeOH/EtOH mixture (1:3:1). After the final precipitation the functionalized Si NCs were dispersed in toluene, filtered through a hydrophobic PTFE filter, and stored in a glass vial until further use.

6.2.6 Synthesis of trioctylphosphine oxide (TOPO) Si-NCs.

Hydride terminated Si-NCs were redispersed in 50 mL toluene containing 2.0 g of TOPO. The reaction mixture was stirred for 8 hours under ambient conditions. A clear orange solution was obtained after completion of the reaction and was stored in a glass vial until further use.

6.2.7 Reaction of carbon dioxide (CO_2) with Si-NCs.

Hydride terminated Si-NCs (obtained from composite [**1**]) were dispersed in 10 mL dry toluene and transferred to a 100 mL Bergoh high pressure steel reactor

maintained under Ar atmosphere. The reaction flask was evacuated and filled with 10 bar CO_2. This was followed by heating at 150 ^oC for 3 hours. The reaction flask was cooled to room temperature and the pressure was released. The reaction mixture consisted of yellow solution containing soluble particles and an orange precipitate. The precipitate was removed *via* centrifugation at 8000 rpm. The supernatant was collected and filtered through a hydrophobic PTFE filter, and stored in a glass vial until further use.

6.2.8 Synthesis of dodecylamine functionalized Si-NCs.

Hydride terminated Si-NCs (obtained from composite [**2**]) were dispersed in 5 mL anhydrous toluene and transferred to a Schlenk flask containing 15 mL anhydrous toluene. 0.35 g of PCl_5 was added to the hydride Si-NCs and stirred together for an hour at 40 ^oC under Ar atmosphere. Toluene and byproduct PCl_3 were removed *in vacuo* and an orange precipitate was left behind. 15 mL of anhydrous toluene was added to the reaction flask, followed by 0.25 g of dodecylamine. The reaction mixture was heated at 40 ^oC for 8 hours under an Ar atmosphere. The flask was cooled to room temperature and the clear light yellow solution was transferred to a separatory funnel and washed with distilled water thrice to remove excess dodecylamine and hydrochloride salt. The toluene layer was filtered through a hydrophobic PTFE filter, and the particles were stored in a glass vial until further use.

6.2.9 Synthesis of diphenylamine functionalized Si-NCs.

Hydride terminated Si-NCs (obtained from composite [**2**]) were dispersed in 5 mL anhydrous toluene and transferred to a Schlenk flask containing 15 mL anhydrous

toluene. 0.35 g of PCl_5 were added to the hydride Si-NCs and the mixture was stirred for an hour at 40 ^oC under Ar atmosphere. Toluene and byproduct PCl_3 were removed *in vacuo* and an orange precipitate was left behind. 15 mL of anhydrous toluene was added to the reaction flask, followed by 0.30 g of diphenylamine. The reaction mixture was heated at 40 ^oC for 8 hours under Ar atmosphere. The flask was cooled to room temperature and the clear light brown solution was transferred to a separatory funnel and washed with distilled water thrice to remove the hydrochloride salt. Excess diphenylamine was removed *via* crystallization at -20 ^oC and the crystals were removed by vacuum filtration. The particles were filtered through a hydrophobic PTFE filter, and stored in a glass vial until further use.

6.2.10 Fourier Transform Infrared Spectroscopy (FTIR)

Fourier Transformation Infrared Spectroscopy (FT-IR) were performed using a Nicolet Magna 750 IR spectrometer. The samples were drop-coated on a Si wafer from the respective solutions.

6.2.11 Transmission Electron Microscopy (TEM)

Transmission Electron Microscopy (TEM) images were obtained using a JOEL-2012 (LaB_6 filament) electron microscope with an accelerating voltage of 200 kV. TEM samples were prepared by drop coating freestanding Si NC suspension onto a carbon coated copper grid with a 400 µm diameter hole. The NC size was averaged over 200 particles, which were determined using Image J software (version 1.45).[48]

6.2.12 Photoluminescence Spectroscopy

Photoluminescence (PL) spectra of the solution phase samples were acquired using a Varian Cary Eclipse Fluorescence Spectrometer with a slit width of 5 nm.

6.2.13 Photoluminescence Lifetime measurements. *Note: These measurements were performed by the Hegmann Group, University of Alberta.*

Nanosecond (ns) lifetime measurements were performed using an excitation pulse of a 400-nm second harmonic signal from a BBO crystal pumped by 800-nm pulses from Ti:Sapphire laser (RegA900 with 65 fs pulse width and 250 kHz repetition rate) with average excitation power of 1.83 mW. For microsecond carrier recombination lifetime measurements, a 1 kHz frequency-doubled 400nm pulses from another Ti:Sapphire laser (Legend Elite, 45 fs pulse width) were used to excite the PL at an average excitation power of 4.5 mW. A fast silicon photodiode (Thorlabs, PDA36A rise time 20.6 ns) coupled to a 300 MHz oscilloscope (Tektronix) was used to measure the microsecond carrier recombination lifetime. The photodiode was placed perpendicular to the excitation pulses and a bandpass filter (Edmund Optics) was used to select a particular emission wavelength. The fittings were performed using OriginPro 9.1 software.[49]

6.2.14 X-ray Photoelectron Spectroscopy (XPS)

XPS analyses were performed using a Kratos Axis Ultra instrument operating in energy spectrum mode at 210 W. The base pressure and operating chamber pressure were maintained at 10^{-7} Pa. A monochromatic Al K_α source (λ = 8.34 Å) was used to irradiate the samples, and the spectra were obtained with an electron takeoff angle of 90°. To minimize sample charging, the charge neutralizer filament was

used when required. Survey spectra were collected using an elliptical spot with major and minor axis lengths of 2 and 1 mm, respectively, and 160 eV pass energy with a step of 0.33 eV. CasaXPS software (VAMAS) was used to interpret high-resolution (HR) spectra. All of the spectra were internally calibrated to the C 1s emission (284.8 eV). After calibration, the background was subtracted using a Shirley-type background to remove most of the extrinsic loss structure. The full width at half maximum (FWHM) for all the fitted peaks was maintained below 1.2 eV.

6.2.15 Scanning Tunneling Microscopy (STM). *Note: These measurements were performed by the Millo group, Hebrew University*.

For STM measurements, NCs were spin cast from a toluene solution onto atomically flat flame-annealed Au substrates. All measurements were performed at room temperature, using Pt-Ir tips. Tunneling current-voltage (I-V) characteristics were acquired after positioning the STM tip above individual NCs, realizing a double barrier tunnel junction (DBTJ) configuration[50] and momentarily disabling the feedback loop. In general, care was taken to retract the tip as far as possible from the NC, so the applied tip-substrate voltage would fall mainly on the tip-NC junction rather than on the NC-substrate junction whose properties (capacitance and tunneling resistance) are determined by the layer of organic capping ligands that cannot be modified during the STM measurement. This protocol minimizes the voltage division induced broadening effects, and thus the measured gaps correspond well to the real SC gaps.[51-53] The dI/dV-V tunneling spectra, proportional to the local tunneling DOS, were numerically derived from the

measured I-V curves. We have acquired the topographic images and tunneling spectra (on the NCs) with bias and current set-values of $V_s \cong 1.2$-1.5 V and $I_s \cong 0.1$-0.3 nA. The first is to ensure tunneling above the band edge and the other was the lowest value that still allowed acquisition of smooth tunneling spectra.

6.3 Results and Discussion

6.3.1 Dodecyl functionalized Si-NCs under inert atmosphere.

As discussed in detail in Chapter 5, oxide-embedded Si-NCs were obtained *via* disproportionation of HSQ at high temperature (1100 ^{o}C). Hydride terminated Si-NCs were obtained by the removal of the oxide matrix upon treating it with HF acid solution. Since the hydride terminated Si-NCs are prone to oxidation, they were protected with alkyl groups *via* thermally induced hydrosilylation using established literature procedures (**Scheme 6-1**).[54] The FT-IR spectrum (**Figure 6-1**) shows C - H stretch at ca. 2900 cm^{-1} and no evidence of Si - H (ca. 2100 cm^{-1}) or Si - O - Si (ca. 1100 cm^{-1}) was observed.

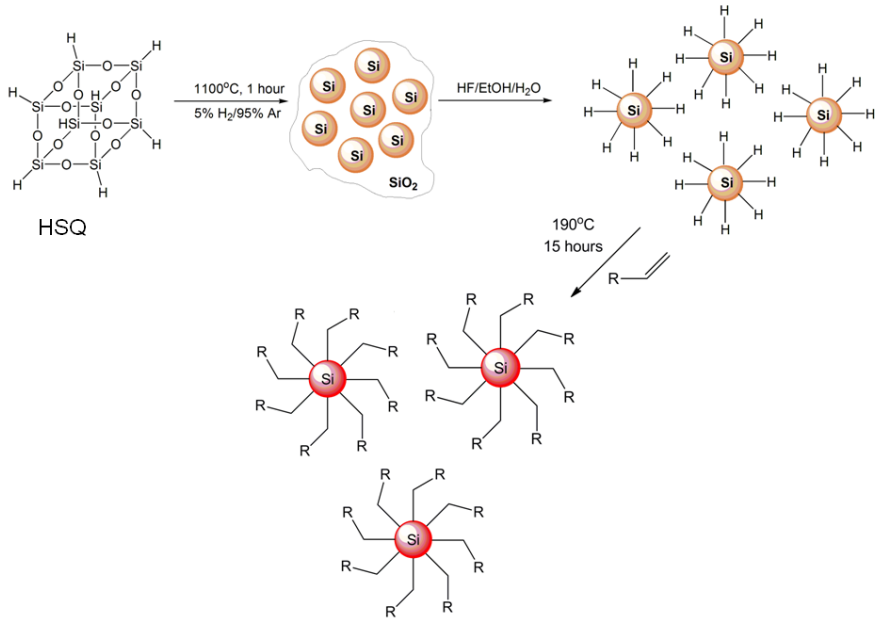

Scheme 6-1. Schematic representation of synthesis of alkyl functionalized Si-NCs in inert atmosphere.

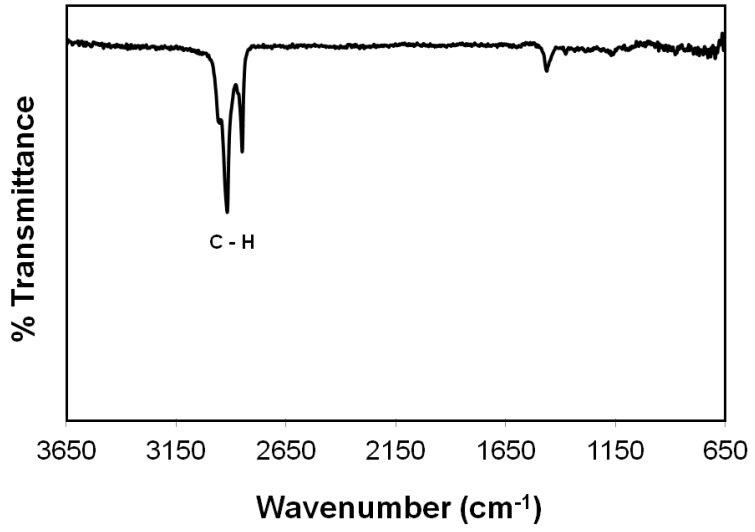

Figure 6-1. FT-IR spectrum of dodecyl functionalized Si-NCs under inert atmosphere.

Figure 6-2 shows the bright field TEM image of the dodecyl functionalized Si-NCs. The average diameter of the NCs was found to be 3.6 ± 0.6 nm.

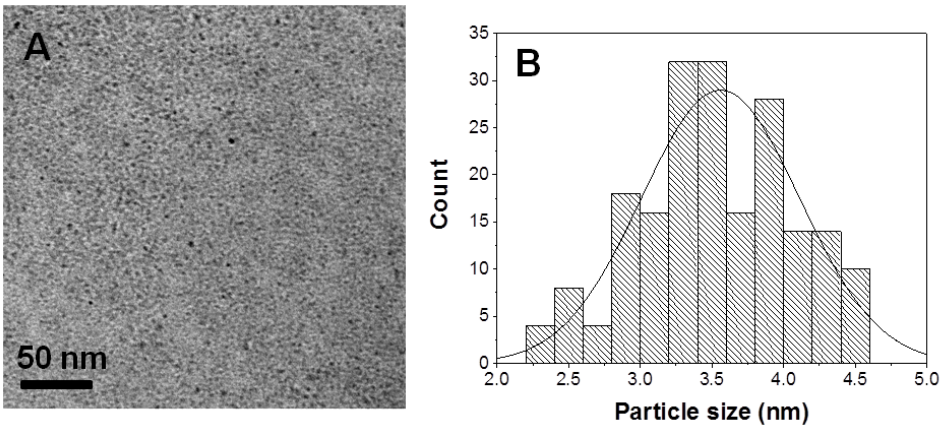

Figure 6-2. (**A**) Bright field TEM image of dodecyl Si-NCs functionalized under inert atmosphere. (**B**) Particle size distribution.

The PL response of these Si-NCs shows a red emission centered at ca. 750 nm (**Figure 6-3**) with an excited state lifetime in microsecond range (*i.e.*, 19 µs), consistent with a band gap emission.[19] These alkyl terminated NCs will be used as a baseline band gap emission standard for comparison with NCs emitting from surface states.

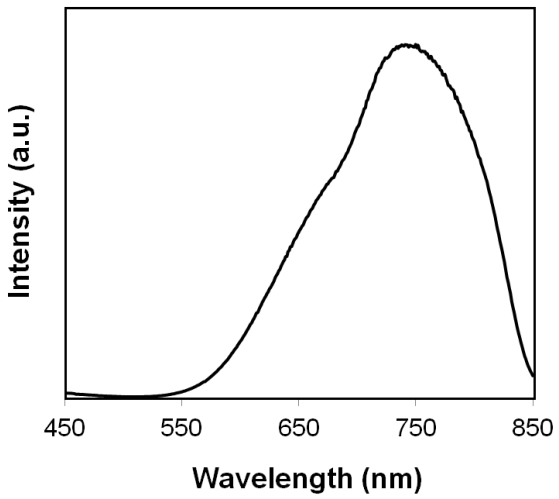

Figure 6-3. PL spectrum of dodecyl Si-NCs functionalized under inert atmosphere (λ_{ex} = 350 nm).

6.3.2 Dodecyl functionalized Si-NCs in air.

In this method of functionalization, hydrosilylation was carried out in air at 110 ^{o}C. Under these conditions, oxygen acts as a radical initiator thus allowing the reaction to occur at temperatures lower than 190 ^{o}C.[55] Oxygen also reacts with the Si-NC surface leading to partial oxidation (**Scheme 6-2**).

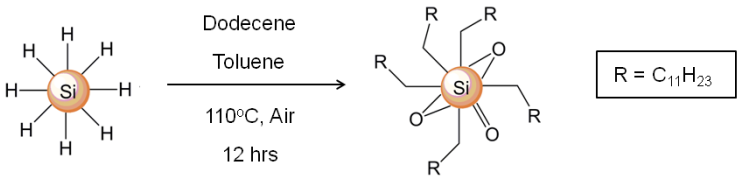

Scheme 6-2. Schematic representation of alkyl functionalization of Si-NC surface in air.

The oxidation is evident from the FT-IR spectrum (**Figure 6-4**) where a significant Si-O-Si stretch is observed at ca. 1100 cm^{-1}. The alkane C-H stretch is observed at ca. 2870 cm^{-1}, however the alkene peaks, =C-H at ~ 3050 cm^{-1} and C=C at ~1600 cm^{-1} are not observed after functionalization.[56] Complete reaction of all silicon hydride surface groups with either dodecene or oxygen is confirmed by the absence of Si - H stretch at ~ 2100 cm^{-1}.

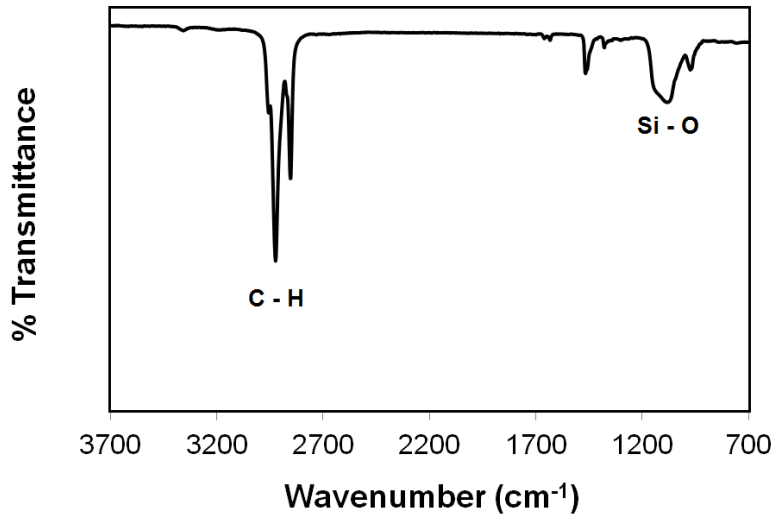

Figure 6-4. FT-IR spectrum of dodecyl Si-NCs functionalized in air.

Oxidation of the Si surface is further confirmed from XPS analysis (**Figure 6-5**). The high resolution Si 2p spectrum shows peaks at 100.1, 101 and 101.8 eV corresponding to Si(I), Si(II) and Si(III) oxidation states, respectively.[46] The presence of Si(0) is confirmed by the presence of peak at 99.2 eV.

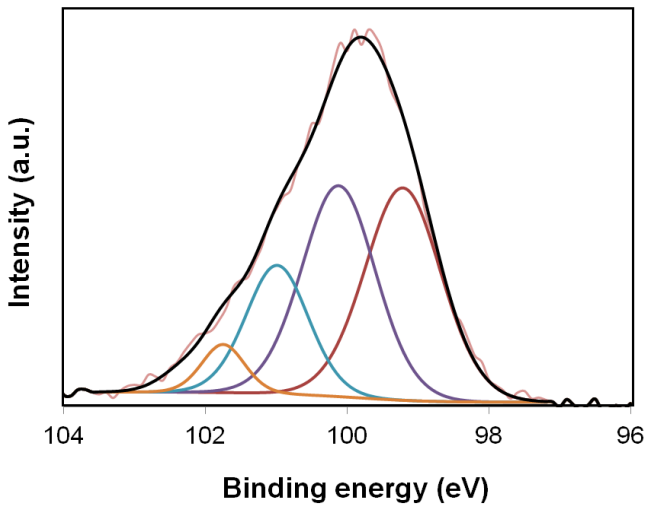

Figure 6-5. High resolution XP spectrum of Si 2p region for dodecyl Si-NCs functionalized in air. For clarity only Si $2p_{3/2}$ peaks are shown.

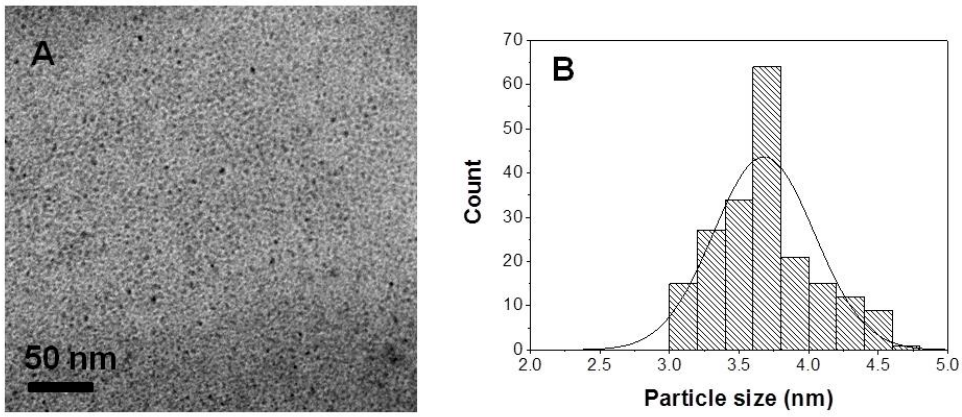

Figure 6-6. (**A**) Bright field TEM image of dodecyl Si-NCs functionalized in air. (**B**) Particle size distribution.

The TEM analysis of the Si-NCs yielded an average diameter of 3.7 ± 0.4 nm (**Figure 6-6**).

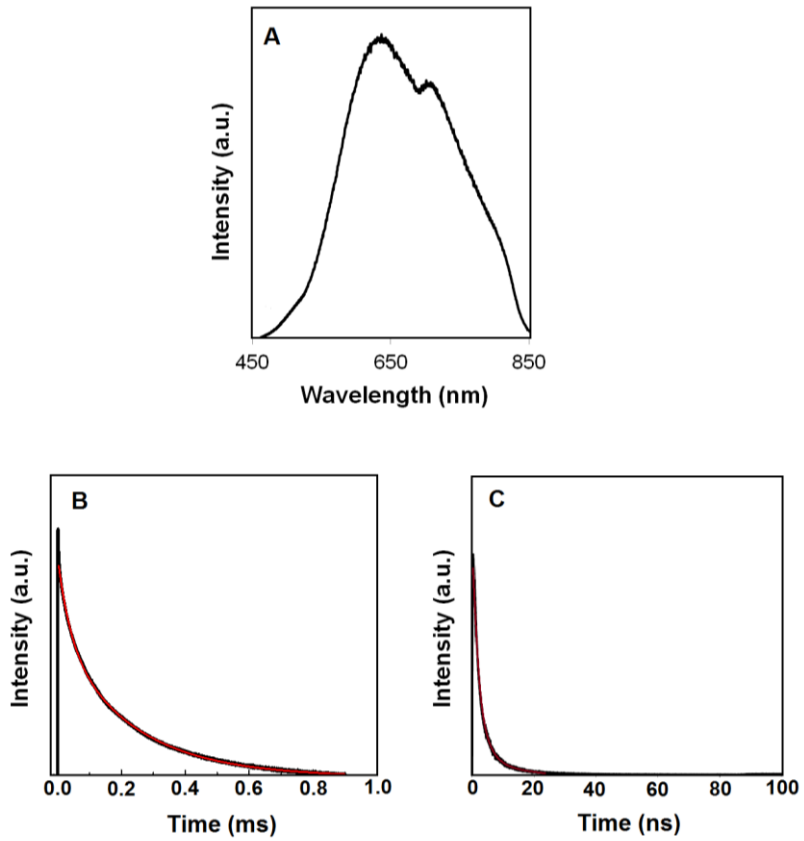

Figure 6-7. (**A**) PL spectrum of dodecyl Si-NCs functionalized in air (λ_{ex} = 350 nm). (**B**) Long-lived excited state lifetime of dodecyl Si-NCs with τ = 40 µs. (**C**) Short-lived excited state lifetimes of dodecyl Si-NCs with τ = 5 ns. Red line corresponds to the fitted data.

The PL spectrum showed significant blue-shift with the maximum centered at ca. 630 nm (**Figure 6-7A**) compared to the dodecyl Si-NCs synthesized under inert atmosphere. A shoulder peak is observed at ca. 720 nm. It is possible this peak corresponds to the emission from the band gap transition. The photoluminescent lifetime measurements afford both a long (40 µs) and short (5 ns) lived excited state

(**Figure 6-7B**). The short lived excited state and blue-shifted PL can be attributed to the presence of Si=O defect state.[57]

6.3.2 TOPO Si-NCs.

Hydride terminated Si-NCs were reacted with TOPO to yield oxidized Si-NCs. The particles are further coordinated to TOPO molecules which renders them soluble in organic solvents (**Scheme 6-3**).

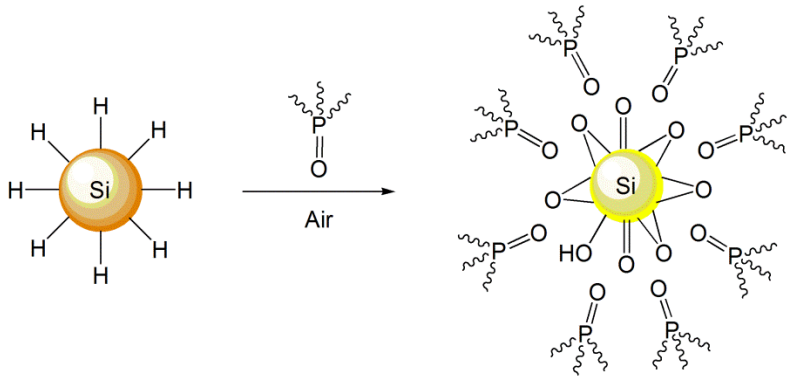

Scheme 6-3. Reactivity of hydride terminated Si-NCs with excess TOPO.

Molecular silanes are known to reduce phosphine oxides to their parent tri-substituted phosphine.[58,59] Similarly, it is believed the hydride on Si-NC surface reduces TOPO to trioctylphosphine (TOP). However, the reaction is carried out in air and this leads to the oxidation of the freshly formed TOP back to TOPO (**Scheme 6-4**).[60] In this redox reaction, the Si hydride surface is oxidized but the

exact nature of Si-O bonding environment remains unclear. It is possible that combination of bridging Si-O-Si, silanol Si-O-H, and Si=O species are present.

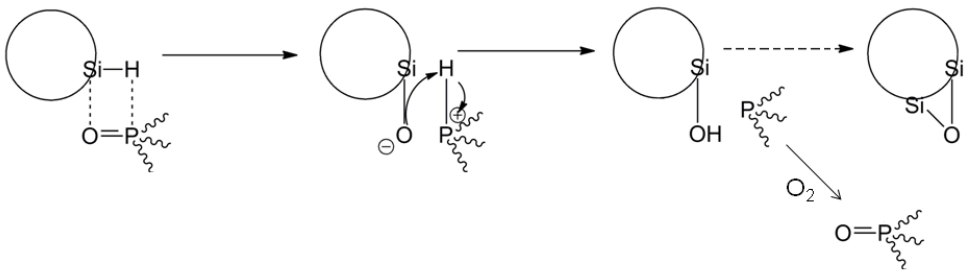

Scheme 6-4. Schematic representation of reactivity of Si hydride surface with TOPO.

Figure 6-8 shows the FT-IR spectra of neat TOPO and TOPO Si-NCs. In both spectra, P=O stretching at ca. 1120 cm^{-1}, C-H stretches ca. 2870, 1470, and 1370 cm^{-1} are observed. A weak Si-O stretch is observed in TOPO Si-NC sample at 1080 - 1040 cm^{-1} consistent with the presence of oxide.[56] The oxidation of the particles is more evident from XPS analysis. The high resolution XP spectrum of Si 2p region shows Si(I) and Si(II) peaks ca. 100 and 100.8 eV, respectively (**Figure 6-9**).[46] The Si(0) peak is at 99 eV confirming the particles are not completely oxidized when freshly prepared. However, the TOPO Si-NCs oxidize over time and is discussed later.

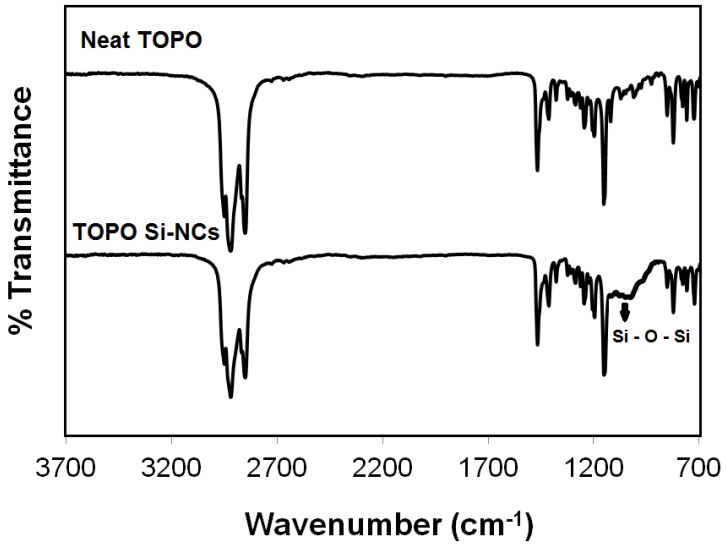

Figure 6-8. FT-IR spectra of neat TOPO and hydride terminated Si-NCs reacted with TOPO.

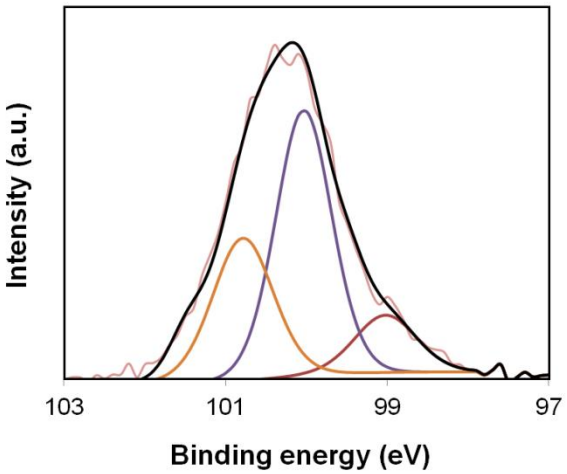

Figure 6-9. High resolution XP spectrum of Si 2p region of TOPO Si-NCs. For clarity only Si $2p_{3/2}$ peaks are shown.

The bright field TEM image shows Si-NCs with average diameter of 3.1 ± 0.5 nm, however the quality of the image is poor due to the presence of large excess of organic ligand (**Figure 6-10**). Attempts to remove the excess TOPO *via* selective precipitation and low temperature crystallization were unsuccessful leading to agglomeration and precipitation of the Si-NCs.

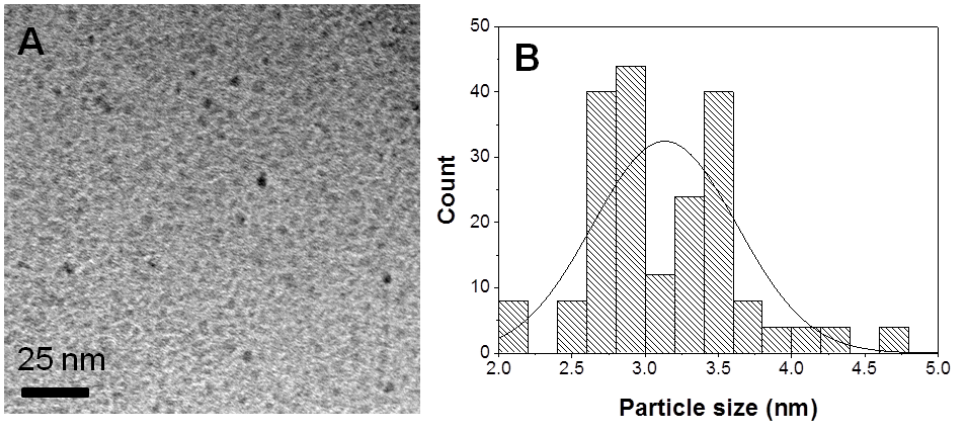

Figure 6-10. (**A**) Bright field TEM image of TOPO Si-NCs. (**B**) Particle size distribution.

Upon excitation at 350 nm, TOPO Si-NCs emit yellow with a PL maximum centered at 590 nm. A shoulder peak is observed at 700 nm, however its origin remains unclear. In light of the obvious complexities, caution must be exercised when interpreting structure in Si-NC PL spectra. It is possible that the emission peak shape is manifestation of the particle size distribution or emission from different surface states. The excited state lifetime consisted of two components with

τ = 0.68 ns and τ = 5.20 ns (**Figure 6-11**). The origin of ultra fast lifetime (*i.e.*, 0.68 ns) is unclear but the 5.20 ns lifetime is consistent with the Si=O defect state.[57] No microsecond components were observed in the lifetime measurements consistent with the PL originating solely from the defect states.

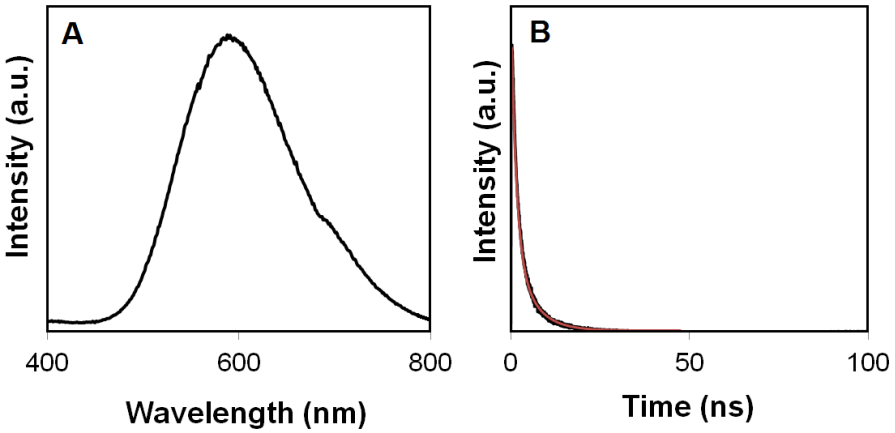

Figure 6-11. (**A**) PL spectrum of TOPO Si-NCs (λ_{ex} = 350 nm). (**B**) Excited state lifetime of TOPO Si-NCs.

Single particle STM studies were performed on ca. 3 nm diameter dodecyl and TOPO Si-NCs.[44] The STM determined band gaps are shown in **Figure 6-12.** Dodecyl and TOPO Si-NCs exhibit similar density-of-states (DOS). The effect of quantum confinement was observed for TOPO Si-NCs (**Figure 6-13**) with increasing particle size yielding a decrease in the band gap. This suggests that the measured energy-gaps are independent of the oxygen related defects.

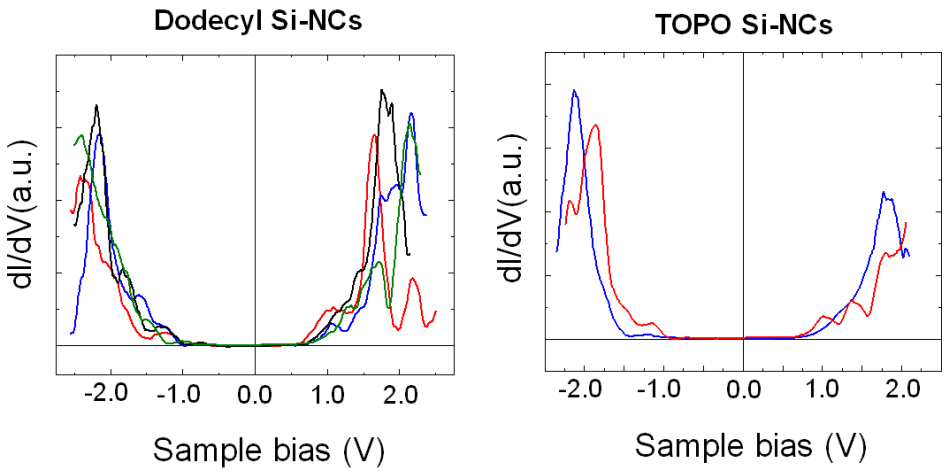

Figure 6-12. Tunneling spectra measured for ~ 3 nm dodecyl and TOPO Si-NCs.

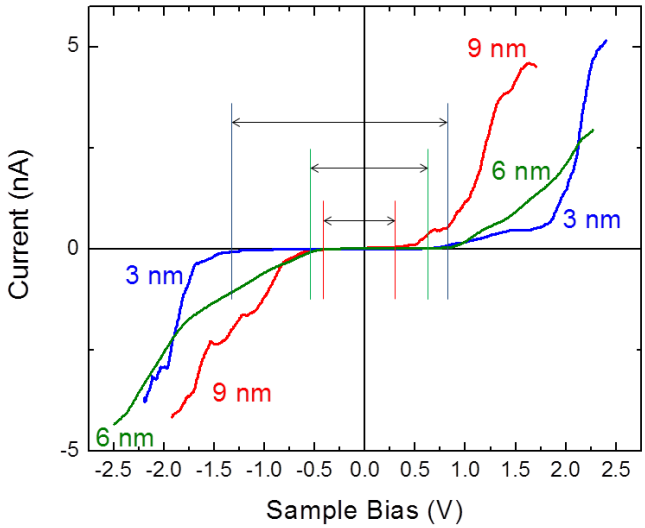

Figure 6-13. Tunneling spectra for 3 nm, 6 nm, and 9 nm TOPO Si-NCs.

The oxidation process is dynamic and slowly continues in the TOPO Si-NCs. Its effect on the PL was monitored over a year. Initially a slight blue-shift in the PL maximum is observed, followed by quenching of the PL (**Figure 6-14**). This observation can be attributed to a decrease in the Si-NC core size followed by complete conversion to SiO_2 and removal of Si=O defect sites. Supporting this interpretation of the PL data, X-ray photoelectron spectroscopy (XPS) analysis of these samples show a general increase in oxidation as the Si 2p peak shifts toward higher binding energies with increasing time (**Figure 6-15**).

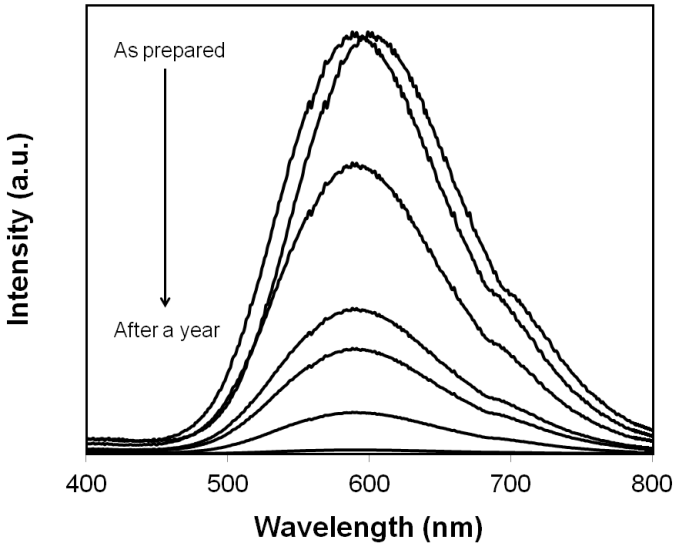

Figure 6-14. Evolution of the PL spectra of 3 nm TOPO Si-NCs over one year (λ_{ex} = 350 nm). The spectra were collected for a freshly prepared sample, and then after 2, 4, 6, 8, 10 and 12 months.

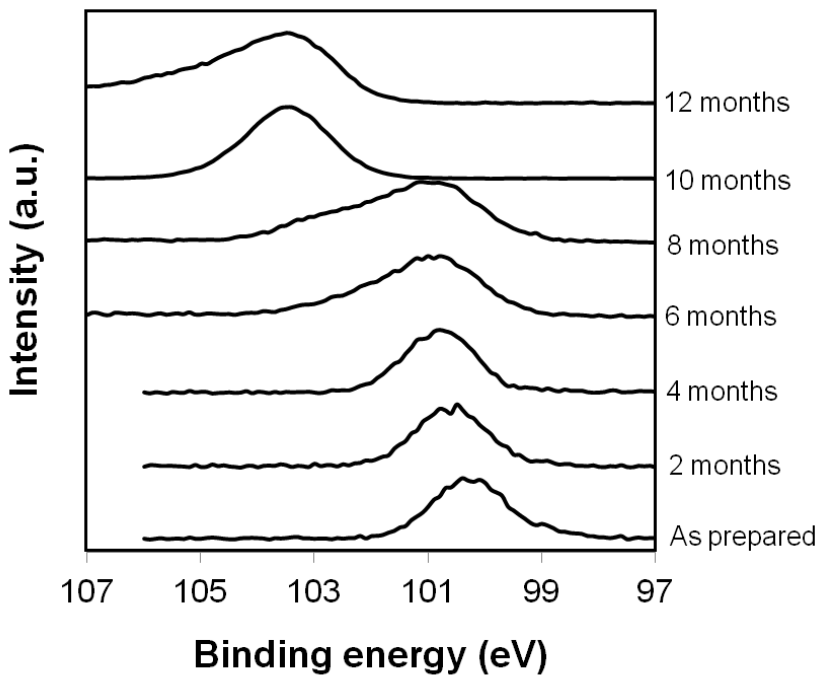

Figure 6-15. High resolution XP spectra of Si 2p region for TOPO Si-NCs at various intervals over a year.

6.3.4 Dodecylamine Si-NCs.

Amine functionalized Si-NCs were prepared by reacting chloride terminated Si-NCs with dodecylamine under mild heating (40 ^{o}C) as summarized in **Scheme 6-5**. The chloride particles were synthesized by reacting hydride terminated Si-NCs with PCl_5.[62] Relatively larger (~ 5 - 6 nm) hydride terminated Si-NCs were used for this reaction as PCl_5 is known to etch away the Si surface.[63] After the chlorination of Si surface, no effort was made to isolate the particles and the reaction with dodecylamine was carried out *in situ*.

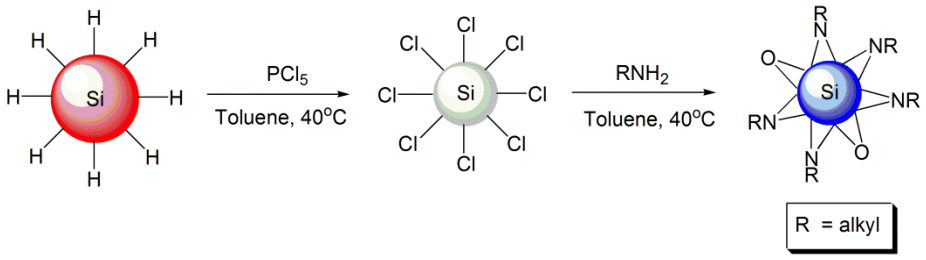

Scheme 6-5. Schematic representation of synthesis of dodecylamine functionalized Si-NCs.

The FT-IR spectra of neat dodecylamine and Si-NCs functionalized with dodecylamine are shown in **Figure 6-16**. Characteristic N-H stretches (ca. 3300 - 3100 cm^{-1} and 1600 cm^{-1}) are observed in neat dodecylamine but are absent from the Si-NC spectrum consistent with amine group reacting with silicon chloride. The C-H stretches from the alkyl chain are observed at ca. 2900 and 1470 cm^{-1} in neat dodecylamine and functionalized Si-NCs. Partial oxidation of Si-NCs is evidenced by the presence of Si-O-Si stretch ca. 1120 cm^{-1}.[56] The high resolution XP spectrum of Si 2p region shows two distinctive peaks corresponding to Si(0) core atoms with peak at 98.8 eV and surface Si atoms attached to either N or O with peak at 102 eV. The N 1s region can be fit to two peaks. The peak at 397.8 eV is characteristic of bridging nitrogen atoms (Si-N-Si). The chemical species responsible for the emission at 399.5 eV is unclear, but can be tentatively assigned to Si-N-O type of species (**Figure 6-17**).[43]

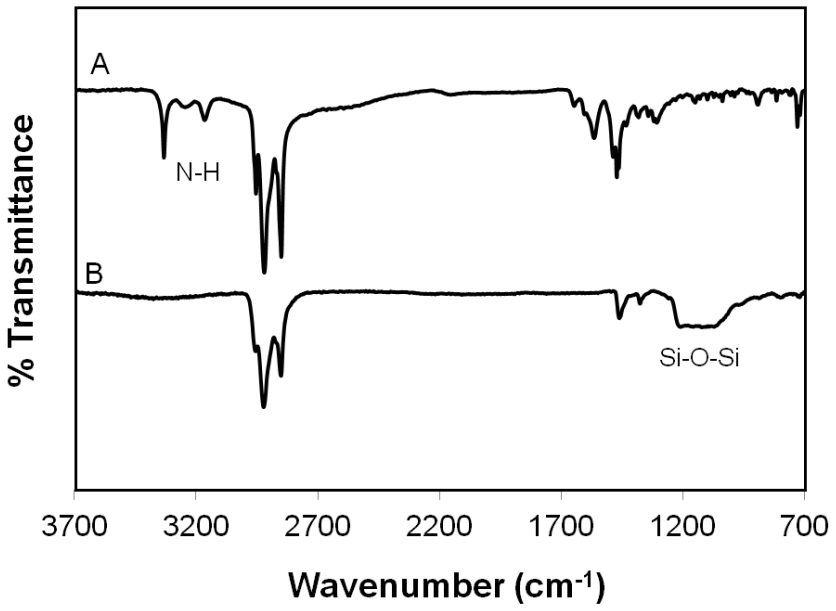

Figure 6-16. FT-IR spectra of (**A**) neat dodecylamine and (**B**) dodecylamine functionalized Si-NCs.

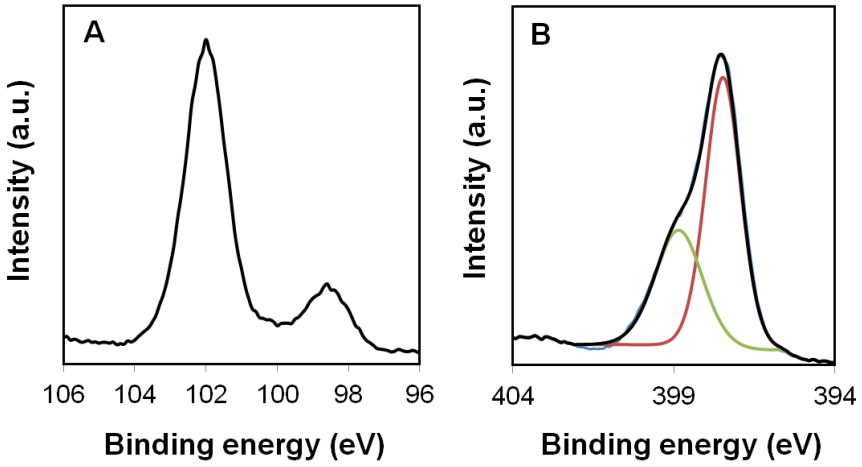

Figure 6-17. High resolution XP spectrum of (**A**) Si 2p region and (**B**) N 1s region for dodecylamine functionalized Si-NCs.

The average particle size for dodecylamine functionalized Si-NCs was found to be 4.1 ± 0.5 nm from TEM analysis (**Figure 6-18**).

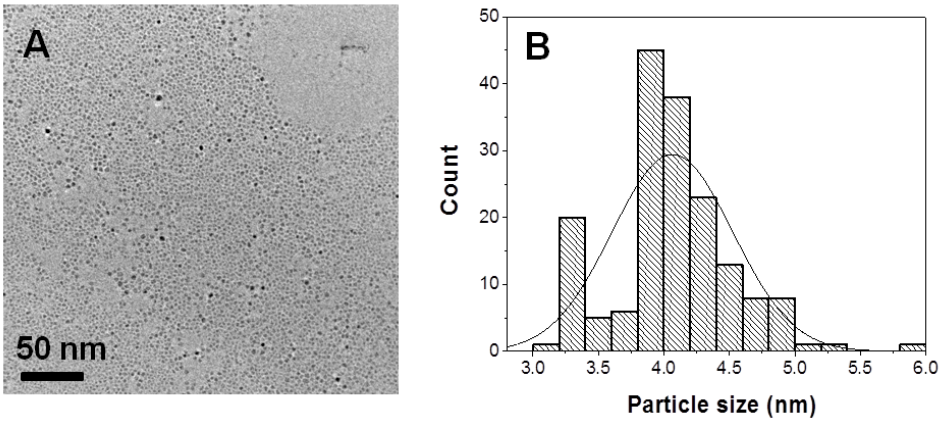

Figure 6-18. (**A**) Bright field TEM image of dodecylamine Si-NCs. (**B**) Particle size distribution.

Optical properties of dodecylamine functionalized Si-NCs were investigated and they exhibit properties very similar to the amine NCs discussed in Chapter 5. The NCs emit blue color and the excited state lifetimes were found to be on the order of 6.46 ns (**Figure 6-19**). Solvatochromic studies were performed to determine if a charge transfer process was responsible for blue emission similar to previous observations. There was a slight red-shift in the PL maximum with increasing polarity of the solvent (**Figure 6-20**) consistent with the blue PL originating from a charge transfer state involving nitrogen, oxygen and silicon atoms.[43,64]

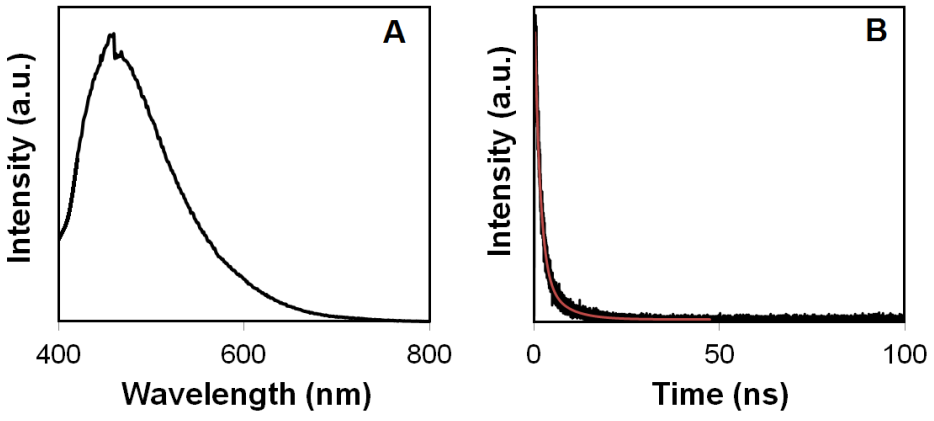

Figure 6-19. (**A**) PL spectrum of dodecylamine Si-NCs (λ_{ex} = 350 nm). (**B**) Excited state lifetimes of dodecylamine Si-NCs with τ = 6.46 ns.

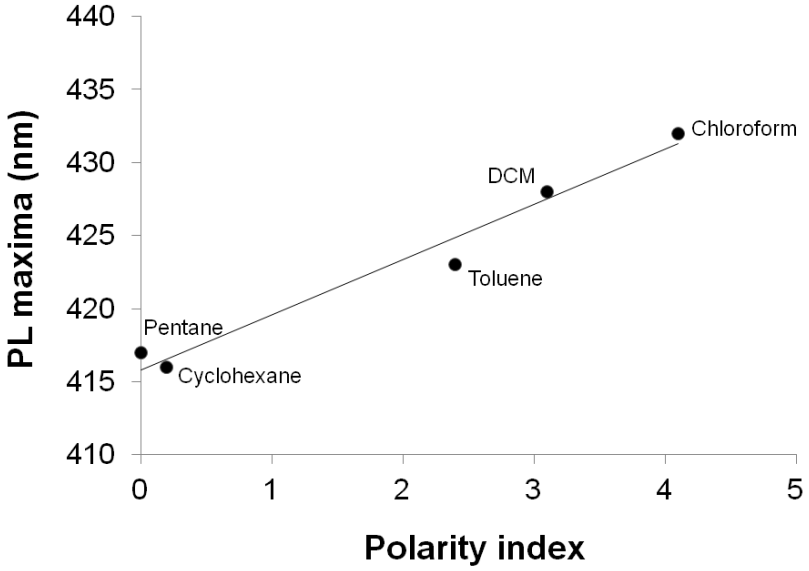

Figure 6-20. PL maxima of dodecylamine Si-NCs *vs.* solvent polarity index. The Si-NC concentration was 0.5 mg/mL and the excitation wavelength was 350 nm.

6.3.5 Diphenylamine Si-NCs.

Recently, Li *et al*. reported green luminescent diphenylamine functionalized Si-NCs.[65] These NCs were prepared *via* reduction of $SiCl_4$ to yield chloride terminated Si-NCs. They further reacted with diphenylamine *in situ* to give the desired product. The authors reported oxygen was crucial to observing the green PL with nanosecond (5 ns) lifetimes. A similar reaction was explored for the chloride terminated Si-NCs obtained from PCl_5 reaction. The chlorination of Si surface was performed by reacting 5 - 6 nm hydride Si-NCs with PCl_5 followed by reaction with diphenylamine (**Scheme 6-6**).

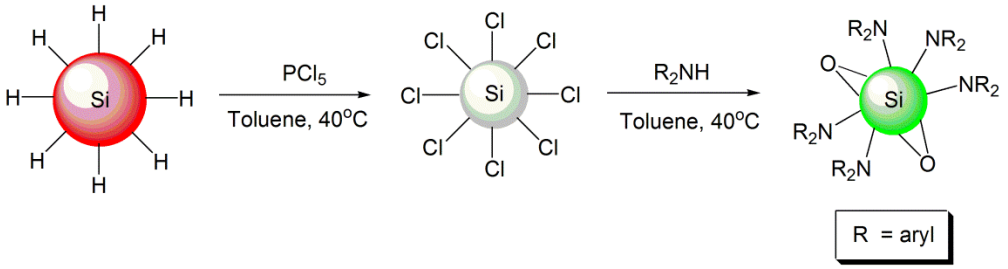

Scheme 6-6. Schematic representation of synthesis of diphenylamine functionalized Si-NCs.

The FT-IR spectra of neat diphenylamine and diphenylamine functionalized Si-NCs are shown in **Figure 6-21**. The N-H stretch ca. 3400 cm^{-1} disappears after functionalization. The aromatic C-H stretches are observed at ca. 3050 and 1000 -

700 cm^{-1} and C=C stretches at ca. 1600 - 1400 cm^{-1} in both spectra. A weak broad stretch is observed at ca. 1040 cm^{-1} that can be assigned to Si-O-Si stretch.[56]

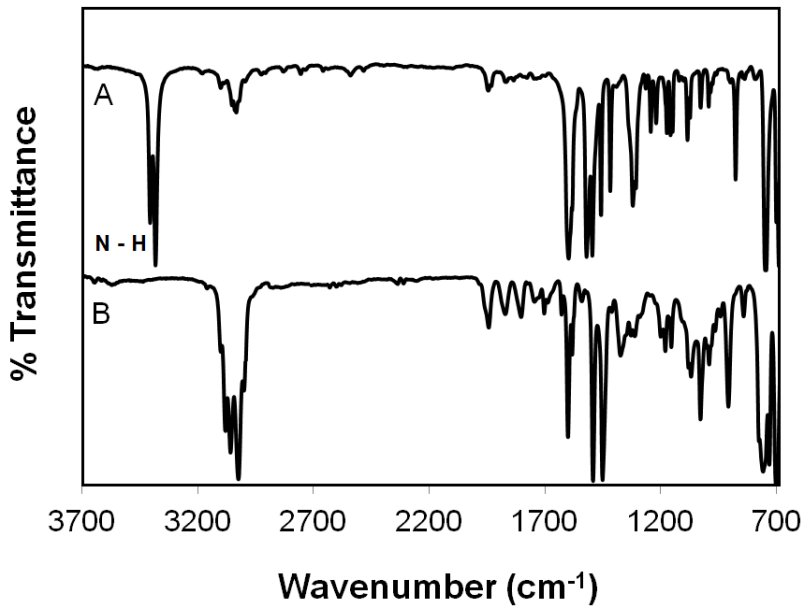

Figure 6-21. FT-IR spectra of (**A**) neat diphenylamine and (**B**) diphenylamine functionalized Si-NCs.

The high resolution XP spectrum of Si 2p region shows two peaks corresponding to Si(0) core at 98.9 eV and surface Si attached to N and O atoms with a peak centered at 101.4 eV (**Figure 6-22**). The N 1s region can be fitted to three peaks corresponding to Si-N-Si (398 eV), Si-N-O (399.6 eV), and free diphenylamine (400.8 eV).[43] The average Si-NC size was found to be 3.9 ± 0.5 nm (**Figure 6-23**) from TEM analysis.

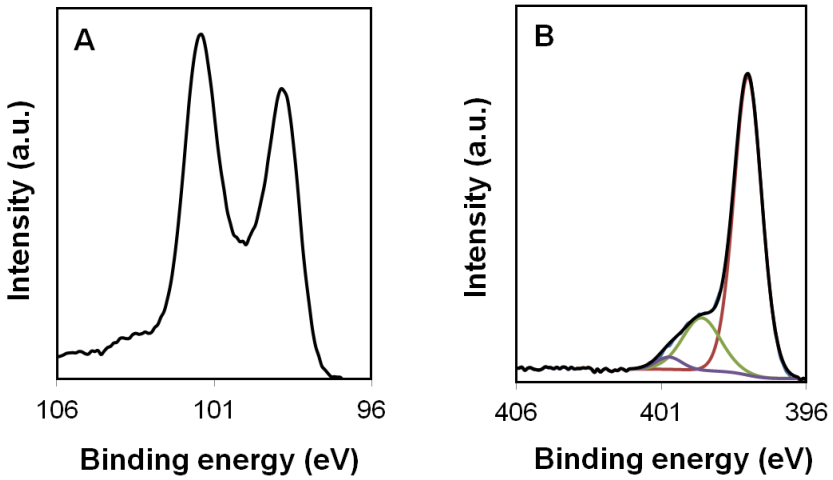

Figure 6-22. High resolution XP spectra of (A) Si 2p and (B) N 1s region of diphenylamine functionalized Si-NCs.

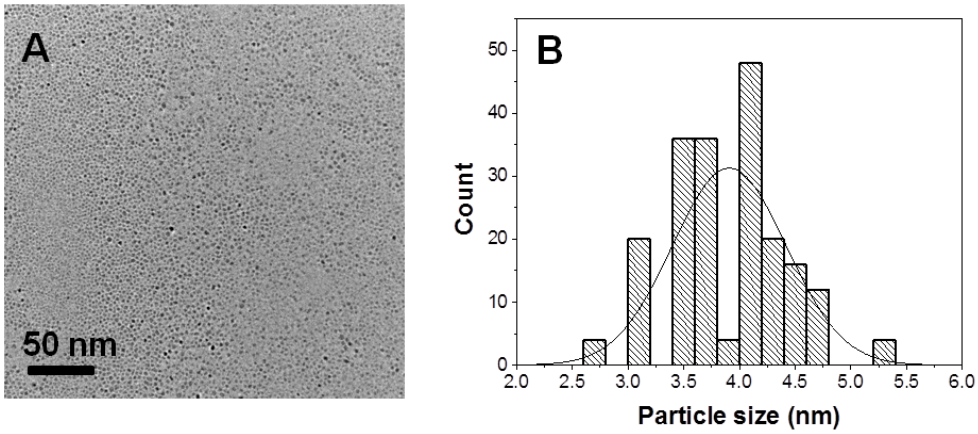

Figure 6-23. (**A**) Bright field TEM image of diphenylamine Si-NCs. (**B**) Particle size distribution.

Diphenylamine functionalized Si-NCs emit green light (**Figure 6-24**), which is red-shifted compared to the emission from alkyl-amine stabilized Si-NCs.

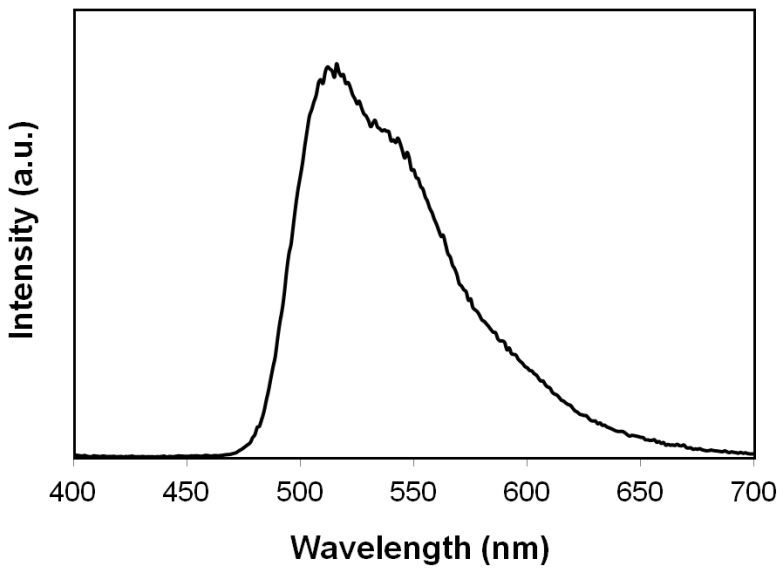

Figure 6-24. PL spectrum of diphenylamine Si-NCs (λ_{ex} = 350 nm).

6.3.6 CO_2 reactions with Si-NCs.

Hydride terminated Si-NCs were reacted with CO_2 at high pressure (10 bar) and 150 ^{o}C for 3 hours to yield acetal stabilized particles as shown in **Scheme 6-7**. At longer times (> 12 hours), the reaction continues further to yield formaldehyde and oxide coated Si-NCs. Previously, CO_2 has been converted to methanol using silanes as the reducing agents.[66,67] However these reactions were catalyzed by carbenes or ammonia-borane complexes. In the current study, the reduction of CO_2

occurs in the absence of an external catalyst, however a minimum temperature of 150 ^{o}C and 10 bar pressure are required.

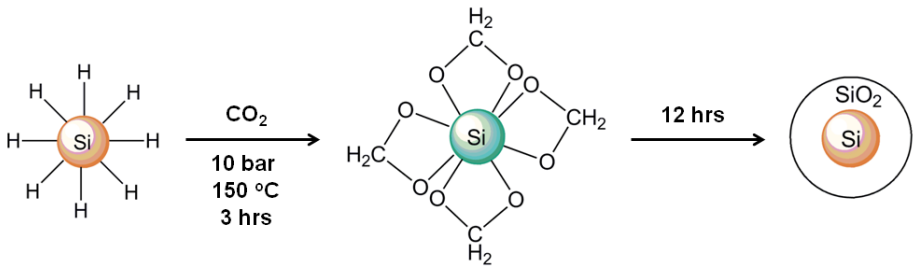

Scheme 6-7. Reaction of hydride terminated Si-NCs with CO_2.

Figure 6-25 shows the FT-IR spectra of Si-NCs at various stages of the reaction. The Si-H stretches ca. 2100 and 920 cm^{-1} can be seen in freshly prepared hydride terminated Si-NCs. After 3 hours, C-H stretch ca. 2920 cm^{-1} and C-O, Si-O-C, Si-O-Si stretches between 1300 - 1080 cm^{-1} appear. After 12 hours the Si-NCs precipitate from the reaction mixture due to complete surface oxidation and the IR of this solid a predominate spectral feature corresponding to Si-O-Si stretching at ca. 1100 cm^{-1}. A weak C-H stretch is also observed at 2900 cm^{-1}.[56] The acetal stabilized Si-NCs have an average diameter of 3.4 ± 0.5 nm as determined from TEM analysis (**Figure 6-26**).

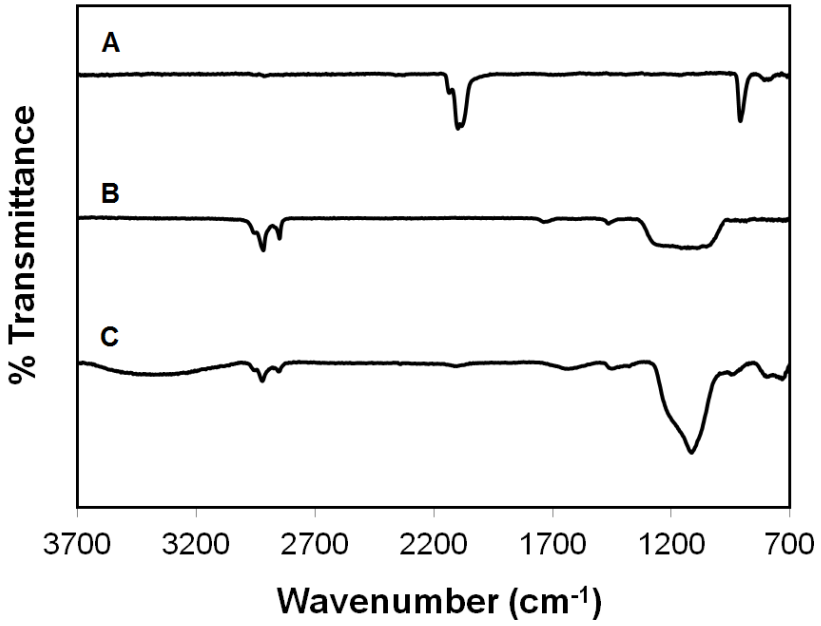

Figure 6-25. FT-IR spectra of (**A**) hydride terminated Si-NCs, (**B**) hydride Si-NCs after reacting with CO_2 for 3 hours, and (**C**) hydride Si-NCs after reacting with CO_2 for 12 hours.

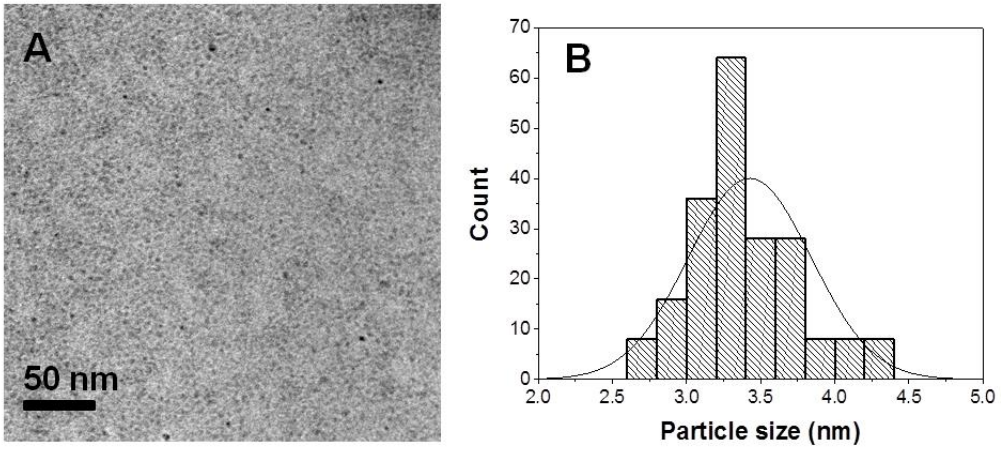

Figure 6-26. (**A**) Bright field TEM image of acetal Si-NCs. (**B**) Particle size distribution.

The high resolution XP spectrum of Si 2p region for acetal Si-NCs show, Si(0), Si(I), Si (II), and Si(IV) oxidation states with peaks at 98.8, 100.3, 101.4, and 103.5 eV, respectively (**Figure 6-27**).[46]

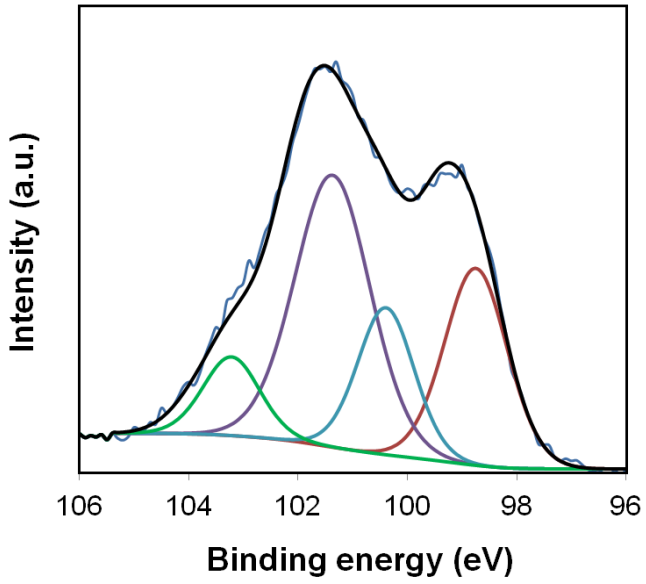

Figure 6-27. High resolution XP spectrum of Si 2p region for acetal Si-NCs. For clarity only $2p_{3/2}$ peaks are shown.

The acetal Si-NCs emit in the blue-green visible spectral region with a PL maximum at 480 nm (**Figure 6-28A**). The excited state lifetime analysis showed a double exponential decay, with values of 1.42 and 5.40 ns (**Figure 6-28B**).

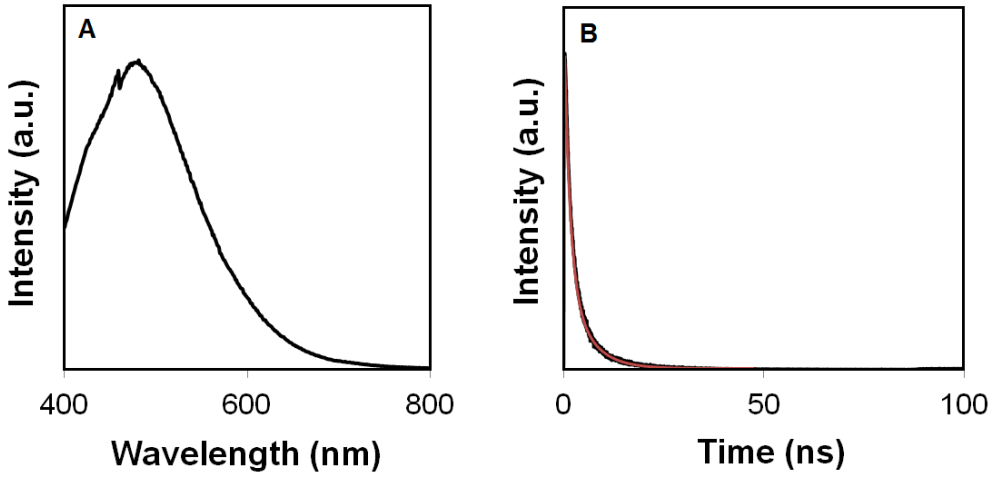

Figure 6-28. (**A**) PL spectrum of acetal Si-NCs (λ_{ex} = 350 nm). (**B**) Excited state lifetimes of acetal Si-NCs.

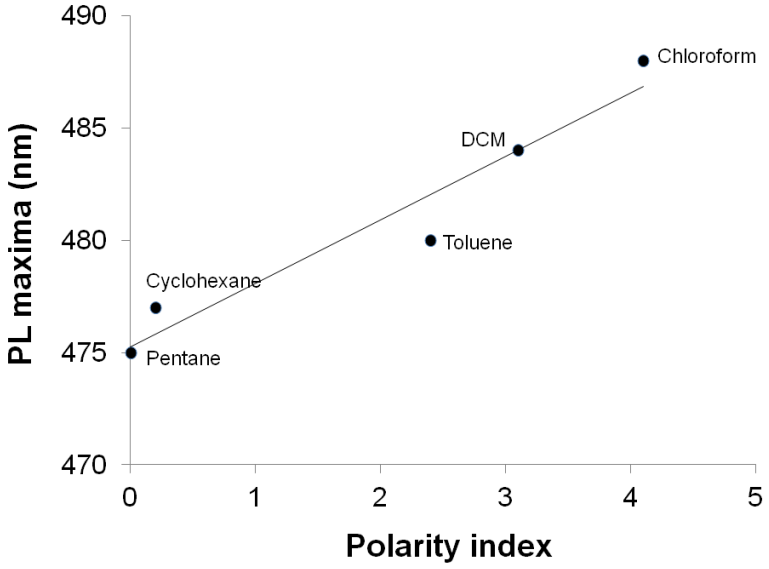

Figure 6-29. PL maxima of acetal Si-NCs *vs.* solvent polarity index. The Si-NC concentration was 0.4 mg/mL and the excitation wavelength was 350 nm.

Similar emission has been reported by Green *et al*.[68] and Manhat *et al*.[69] from carboxylate functional groups on Si surfaces. These emissions are believed to originate from a charge transfer process. Solvatochromism studies were performed to confirm this and the PL maximum red shifts with increasing polarity of the solvent (**Figure 6-29**) as expected.

After 12 hours of reaction, a brown precipitate was obtained from reaction mixture that emits orange color (**Figure 6-30**). The emission likely originates from oxide defect states.[70] SEM imaging shows agglomerated NCs consistent with oxide cross-linking (**Figure 6-31**) of the NCs.

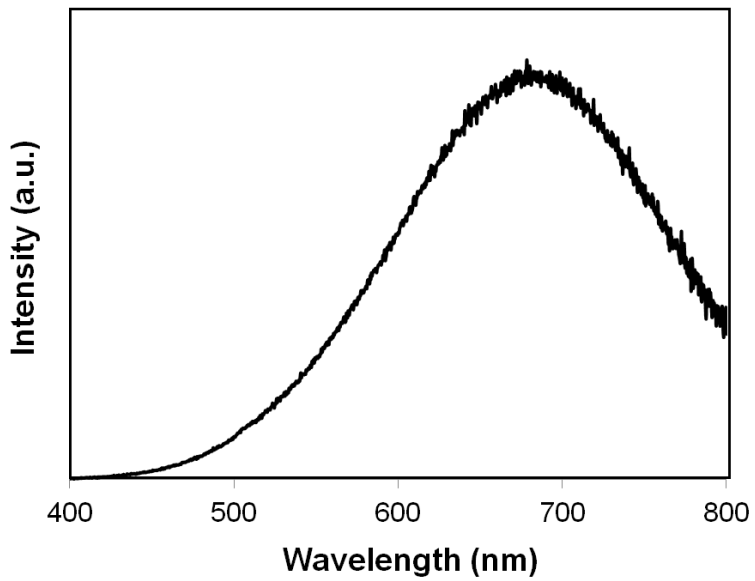

Figure 6-30. PL spectrum of oxide coated Si-NCs obtained from reacting hydride terminated Si-NCs with CO_2 for 12 hours.

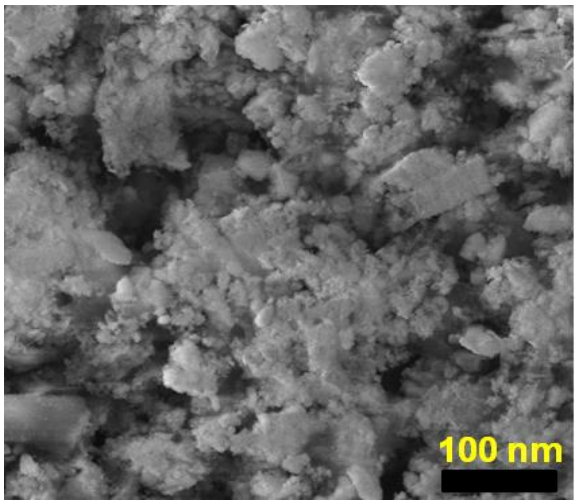

Figure 6-31. SEM image of the precipitate obtained from reacting hydride terminated Si-NCs with CO_2 for 12 hours.

6.3.7 Summary of the PL from surface modified Si-NCs.

All the Si-NCs prepared for this study had an average particle diameter between 3 - 4 nm. According to the effective mass approximation (EMA) theory, these particles should emit between 750 and 900 nm and have a microsecond lifetime, given the emission results from band gap transition.[71] However, only dodecyl Si-NCs functionalized under inert conditions behave according to EMA predictions. The Si-NCs proposed to contain Si=O defect states (i.e., TOPO Si-NCs and dodecyl Si-NCs functionalized in air) exhibit nanosecond PL lifetimes and a PL maximum that is blue-shifted when compared to the size dependent EMA prediction. These NCs do not exhibit a solvatochromic response and the DOS within their band structure remains unaltered despite the defect-based emission. For these samples, defect emissions are influenced by the particle size. Alternatively,

Si-NCs functionalized with alkyl and aryl amines and acetal groups exhibit photoluminescent response that is independent of the particle size. Emission from these particles is believed to originate from a surface charge transfer process and the PL maximum is dependent on solvent polarity (i.e., solvatochromic). These transitions are also rapid and have nanosecond lifetimes. **Figure 6-32** shows the photograph of 3 - 4 nm Si-NCs with various surface groups under UV-illuminations. The NCs of similar sizes emit across the visible spectrum and defect emissions appear brighter compared to the EMA based PL.

Figure 6-32. Photograph of ~ 3 nm Si-NCs functionalized with various surface groups, under UV illumination.

6.4 Conclusions

In this Chapter, Si-NCs with various surface protecting groups were synthesized. The resulting materials exhibited PL across the visible spectrum and have short-lived excited state lifetimes. This study shows that surface engineering

can provide a better alternative to tune the optical properties of Si-NCs and introduces addition degrees of freedom (*e.g.*, excited state lifetime, PL maximum, *etc*.) to the tailoring of Si-NC optical response. Throughout these studies it was also determined that chloride termination on Si-NC surface offers a convenient platform off of which functional groups may be tethered. Finally, this is the first report showing reactivity of hydride terminated Si-NCs with CO_2 and TOPO.

6.5 References

1. P. Ball, *Nat. Mater*., 2005, **4**, 119.
2. R. J. Cava, *Nature*, 2006, **444**, 427.
3. J. T. Yates Jr., *Science*, 1998, **279**, 335.
4. D. P. Kern, T. F. Kuech, M. M. Oprysko, A. Wagner and D. E. Eastman, *Science*, 1988, **241**, 936.
5. S. E. Thompson and S. Parthasarathy, *Materialtoday*, 2006, **9**, 20.
6. L. Pavesi and R. Turan, Silicon Nanocrystals, Wiley-VCH, Weinheim, 1 ed., 2010.
7. T. K. Sham, D. T. Jiang, I. Coulthard, J. W. Lorimer, X. H. Feng, K. H. Tan, S. P. Frigo, R. A. Rosenberg, D. C. Houghton and B. Bryskiewicz, *Nature*, 1993, **363**, 331.
8. A. G. Cullis and L. T. Canham, *Nature*, 1991, **353**, 335.
9. L. T. Canham, *Nature*, 2000, **408**, 411.
10. F. Cunin, T. A. Schmedake, J. R. Link, Y. Y. Li, J. Koh, S. N. Bhatia and M. J. Sailor, *Nat. Mater*., 2002, **1**, 39.
11. K. D. Hirschman, L. Tsybeskov, S. P. Duttagupta and P. M. Fauchet, *Nature*, 1996, **384**, 338.
12. J. Linnros, *Appl. Phys. Lett*., 1995, **66**, 3048.
13. L. Pavesi, L. Dal Negro, C. Mazzoleni, G. Franzo and F. Priolo, *Nature*, 2000, **408**, 440.
14. M. L. Mastronardi, E. J. Henderson, D. P. Puzzo, Y. L. Chang, Z. B. Wang, M. G. Helander, J. H. Jeong, N. P. Kherani, Z. H. Lu and G. A. Ozin, *Small*, 2012, **8**, 3647.
15. M. L. Mastronardi, E. J. Henderson, D. P. Puzzo and G. A. Ozin, *Adv. Mater*., 2012, **24**, 5890.
16. K. Y. Cheng, R. Anthony, U. R. Kortshagen and R. J. Holmes, *Nano Lett*., 2010, **10**, 1154.
17. T. Creazzo, B. Redding, E. Marchena, J. Murakowski and D. W. Prather, *Opt. Exp*., 2010, **18**, 10924.
18. C. Garcia, B. Garrido, P. Pellegrino, R. Ferre, J. A. Moreno, L. Pavesi, M. Cazzanelli and J. R. Morante, *Physica E*, 2003, **16**, 429.
19. C. Garcia, B. Garrido, P. Pellegrino, R. Ferre, J. A. Moreno, J. R. Morante, L. Pavesi and M. Cazzanelli, *Appl. Phys. Lett*., 2003, **82**, 1595.
20. M. L. Mastronardi, F. Maier-Flaig, D. Faulkner, E. J. Henderson, C. Kubel, U. Lemmer and G. A. Ozin, *Nano Lett*., 2012, **12**, 337.
21. R. Outlon, J. J. Finley, A. D. Ashmore, I. S. Gregory, D. J. Mowbray, M. S. Skolnick, M. J. Steer, S. L. Liew, M. A. Migliorato and A. J. Cullis, *Phys. Rev. B*, 2002, **66**, 5313.

22. J. J. Finley, A. Lemaitre, A. D. Ashmore, D. J. Mowbray, M. S. Skolnick, M. Hopkinson, T. F. Krauss, *Phys. Stat. Sol. B*, 2001, **224**, 373.
23. P. W. Fry, L. Harris, S. R. Parnell, J. J. Finley, A. D. Ashmore, D. J. Mowbray, M. S. Skolnick, M. Hopkinson, G. Hill and J. C. Clark, *J. Appl. Phys*., 2000, **87**, 615.
24. S. A. Empedocles and M. G. Bawendi, *Science*, 1997, **278**, 2114.
25. A. P. Alivisatos, *Science*, 1996, **271**, 933.
26. B. S. Mashford, M. Stevenson, Z. Popovic, C. Hamilton, Z. Zhou, C. Breen, J. Steckel, V. Bulovic, M. Bawendi, S. Coe-Sullivan and P. T. Kazlas, *Nat. Photonics*, 2013, **7**, 407.
27. A. B. Filonov, S. Ossicini, F. Bassani and F. Arnaud d'Avitaya, *Phys. Rev. B*, 2002, **65**, 195317.
28. M. Fujii, A. Mimura, S. Hayashi and K. Yamamoto, *Appl. Phys. Lett*., 1999, **75**, 184.
29. A. Miura, M. Fujii, S. Hayashi, D. Kovalev and F. Koch, *Phys. Rev. B*, 2000, **62**, 12625.
30. M. Fujii, A. Mimura, S. Hayashi, Y. Yamamoto and K. Murakami, *Phys. Rev. Lett*., 2002, **89**, 206805.
31. M. Fujii, K. Toshikiyo, Y. Takase, Y. Yamaguchi and S. Hayashi, *J. Appl. Phys*., 2003, **94**, 1990.
32. M. Fujii, Y. Yamaguchi, Y. Takase, K. Ninomiya and S. Hayashi, *Appl. Phys. Lett*., 2004, **85**, 1158.
33. G. A. Kachurin, S. G. Cherkova and V. A. Volodin, *Nucl. Inst. Meth. Phys. Res. B*, 2004, **222**, 497.
34. M. Fujii, Y. Yamagachi, Y. Takase, K. Ninomiya and S. Hayashi, *Appl. Phys. Lett*., 2005, **87**, 211919.
35. G. A. Kachurin, S. G. Cherkova, V. A. Volodin, D. M. Marin, D. I. Tetelbaum and H. Becker, *Semiconduc.*, 2006, **40**, 72.
36. D. I. Tetelbaum, O. N. Gorshkov, S. A. Trushun, D. G. Revin, D. M. Gaponova and W. Eckstein, *Nanotechol*., 2000, **11**, 295.
37. D. I. Tetelbaum, S. A. Trushin, V. A. Burdov, A. I. Golovanov, D. G. Revin and D. M. Gaponova, *Nucl. Inst. Meth. Phys. Res. B*, 2001, **174**, 123.
38. D. I. Tetelbaum, O. N. Gorshkov and V. A. Burdov, *Phys. Sol. Stat*., 2004, **46**, 17.
39. A. N.. Mikhaylov, D. I. Tetelbaum and V. A. Burdov, *J. Nanosci. Nanotech*., 2008, **8**, 780.
40. V. A. Belyakov, V. A. Burdov, R. Lockwood and A. Meldrum, *Adv. Opt. Tech*., 2008, **2008**, 279502.
41. D. J. Norris, A. L. Efros and S. C. Erwin, *Science*, 2008, **319**, 1776.
42. V. Chikan, *J. Phys. Chem. Lett*., 2011, **2**, 2783.

43. M. Dasog, Z. Yang, S. Regli, T. M. Atkins, A. Faramus, M. P. Singh, E. Muthuswamy, S. M. Kauzlarich, R. D. Tilley and J. G. C. Veinot, *ACS Nano*, 2013, **7**, 2676.
44. O. Wolf, M. Dasog, Z. Yang, I. Balberg, J. G. C. Veinot and O. Millo, *Nano Lett*., 2013, **13**, 2516.
45. K. Dohnalova, A. N. Poddubny, A. A. Prokofiev, W. Dam de Boer, C. P. Umesh, J. M. J. Paulusse, H. Zuihof and T. Gregorkiewicz, *Light*, 2013, **2**, 47.
46. X. Tang, Y. Huang, Y. Wang, W. Zhang and J. Peng, *Appl. Phys. Lett*., 2008, **92**, 251116.
47. C. M. Hessel, E. J. Henderson and J. G. C. Veinot, *Chem. Mater*., 2006, **18**, 6139.
48. www.rsbweb.nih.gov/ij/
49. www.originlab.com
50. A. Brewer and K. von Haeften, *Appl. Phys. Lett*., 2009, **94**, 261102
51. U. Banin and O. Millo, *Ann. Rev. Phys. Chem*., 2003, **54**, 465.
52. E. P. A. M. Bakkers, Z. Hens, A. Zunger, A. Franceschetti, L. P. Kouwenhoven, L. Gurevich and D. Vanmaekelbergh, *Nano Lett*., 2001, **1**, 551.
53. E. P. A. M. Bakkers and D. Vanmaekelbergh, *Phys. Rev. B*, 2000, **62**, 7743.
54. J. A. Kelly, A. M. Shukaliak, M. D. Fleischauer and J. G. C. Veinot, *J. Am. Chem. Soc*., 2011, **133**, 9564.
55. Z. Yang, M. Iqbal, A. R. Dobbie and J. G. C. Veinot, *J. Am. Chem. Soc*., 2013, **135**, 17595.
56. R. M. Silverstein, F. X. Webster and D. J. Kiemle, Spectroscopic Identification of Organic Compounds, John Wiley and Sons, New Jersey, 7th ed., 2005.
57. M. V. Wolkin, J. Jorne, P. M. Fauchet, G. Allan and C. Delerue, *Phys. Rev. Lett*., 1999, **82**, 197.
58. Y. Li, L. Q. Lu, S. Das, S. Pisiewicz, K. Junge and M. Beller, *J. Am. Chem. Soc*., 2012, **134**, 18325.
59. H. C. Wu, J. Q. Yu and J. B. Spencer, *Org. Lett*., 2004, **6**, 4675.
60. C. R. Hilliard, N. Bhuvanesh, J. A. Gladysz and J. Blumel, *Dalton Trans*., 2012, **41**, 1742.
61. T. H. Chan and A. Melnyk, *J. Am. Chem. Soc*., 1970, **92**, 3718.
62. M. Dasog and J. G. C. Veinot, *Phys. Stat. Solidi A*, 2012, **209**, 1844.
63. M. Y. Bashouti, K. Sardashti, S. W. Schmitt, M. Pietsch, J. Ristein, H. Haick and S. H. Christiansen, *Prog. Surf. Sci*., 2013, **88**, 39.
64. T. He, D. A. Corley, M. Lu, N. H. Di Spinga, J. He, D. P. Nackashi, P. D. Franzon and J. M. Tour, *J. Am. Chem. Soc*., 2009, **131**, 10023.
65. Q. Li, Y. He, J. Chang, L. Wang, H. Chen, Y. Tan, H. Wang and Z. Shao, *J. Am. Chem. Soc*., 2013, **135**, 14924.

66. G. Menard and D. W. Stephan, *J. Am. Chem. Soc*., 2010, **132**, 1796.
67. S. N. Riduan, Y. Zhang and J. Y. Ying, *Angew. Chem. Int. Ed*., 2009, **48**, 3322.
68. W. H. Green, K. P. Le, J. Grey, T. T. Au and M. J. Sailor, *Science*, 1997, **276**, 1826.
69. B. A. Manhat, A. L. Brown, L. A. Black, J. B. A. Ross, K. Fichter, T. Vu, E. Richman and A. M. Goforth, *Chem. Mater*., 2011, **23**, 2407.
70. N. Korunska, M. Baran, L. Khomenkova, V. Yukhymchuk, Y. Goldstein, E. Savir and J. Jedrzejewski, *Mater. Sci. Eng. C*, 2003, **23**, 691.
71. C. M. Hessel, D. Reid, M. G. Panthani, M. R. Rasch, B. W. Goodfellow, J. Wei, J. Wei, H. Fujii, V. Akhavan and B. A Korgel, *Chem. Mater*., 2011, **24**, 392.

Chapter 7:

Conclusions and Future Directions

7.1 Conclusions.

Inorganic quantum dots have paved the way for numerous advances in both fundamental and applied sciences.[1] While Group II-VI and III-V based quantum dots have been well studied and their application has been demonstrated across various disciplines, there is a nascent need for an alternative that is inexpensive, non-toxic, and abundant. Silicon-based quantum dots have been proposed as a viable alternative, however their optical properties are not well described by models typically applied. Solution methods reported to afford silicon nanocrystals (Si-NCs) do not provide precise control over the NC size or the PL properties. Gas-phase and solid-state methods provide near monodisperse Si-NCs with size-tunable PL response, but they require substantial energy input and costly infrastructure.[2] The work presented in this thesis was aimed toward addressing some of these issues. Chapters 2, 3, and 4 of this thesis detail efforts aimed at mitigating the temperature requirements necessary for preparing Si-based nanomaterials while Chapters 5 and 6 describe detailed investigations into the roles of various factors contributing to the optical properties of Si-NCs.

In Chapter 2, various sol-gel copolymers $(HSiO_{1.5})_n(RSiO_{1.5})_m$ (R = C_2H_5, C_4H_9, C_6H_{13}, C_8H_{17} and $C_{10}H_{21}$) were synthesized. The steric bulk of the 'R' group was increased with the aim of creating a more open oxide network that was expected to facilitate Si atom diffusion during thermal treatment at lower temperatures (i.e., < 1100 ^{o}C). Unfortunately, incorporating bulkier 'R' groups led to substantial concentrations of carbon impurities and inhibits formation of Si-NCs. In fact, at the highest C content processing these precursors yielded carbon

encapsulated SiO_2 clusters and SiC NCs were formed. Another approach to lowering the processing temperature involved addition of salts to the sol-gel polymer that were intended to lower the softening temperature of the silica matrix. It was determined that $AlCl_3$ hydrolyses and copolymerizes with $HSiCl_3$ to form a sol-gel copolymer. Upon thermal treatment this copolymer yields Si-NCs embedded within an aluminosilicate matrix. This process allowed for formation of Si-NCs at lower temperature (ca. 700 ^{o}C) presumably due to softening of the aluminosilicate matrix; however, freestanding NCs could not be isolated using standard etching procedures.

Chapter 3 examines the magnesiothermic reduction process and its application to the synthesis of Si nano- and microparticles starting from Stöber silica. The reaction was carried out at temperatures as low as 500 ^{o}C. The resulting particles were porous because of localized shrinking of the structure as a result of loss of oxygen atoms from the silica matrix. Mechanistic studies also suggest that the reduction occurs *via* migration of O atoms to Mg. Magnesiothermic reduction was further extended to reduce silica fibers, cubes, rods, films, aerogels, and commercial MCM-41. The morphology was retained for precursors except aerogels and MCM-41 which experienced significant structural damage. The generality of the Mg reduction approach also allows preparation of Si thin films that were tested as transparent conducting layer in organic light-emitting diodes (OLEDs). While initial results were promising, further optimization is required to obtain devices exhibiting better performance metrics.

The vast utility of the magnesiothermic reduction method was extended and high purity Si_3N_4 as well as SiC nanostructures were prepared at temperatures significantly below what is typically required (Chapter 4).

Phase pure β-Si_3N_4 particles were prepared by the reaction of silica, urea, and magnesium at 500 ^oC. Mechanistic studies revealed that the reaction proceeds *via* decomposition of urea to form ammonia that reacts *in situ* with magnesium to form Mg_3N_2. The Mg_3N_2 then undergoes metathesis with silica to form Si_3N_4 and MgO. The resulting particles were highly photoluminescent. SiC particles, rods, and fibers were prepared by reacting silica, Mg, and C at 600 ^oC. Mechanistic studies revealed the reaction proceeds through Mg_2C_3 which undergoes metathesis with silica to form SiC and MgO. Both Si_3N_4 and SiC are attractive materials owing to their thermal and chemical stability and biocompatibility. This method offers a convenient route to make phase pure Si_3N_4 and SiC of any shape at low temperature.

The origin of blue luminescence in Si-NCs prepared *via* solution phase methods was investigated and the results are summarized in Chapter 5. It was established that the presence of trace nitrogen and oxygen impurities leads to blue luminescence with short-lived excited states. Solvatochromic studies indicate the PL originates from a charge transfer process involving Si, N, and O centers and that the optical response is independent of particle size.

Building on the discovery (outlined in Chapter 5) that N-based surface groups dramatically impact the photoluminescent response of Si-NC, Chapter 6 outlines the functionalization of Si-NCs with various surface groups to yield short-

lived excited states and PL that spans the visible spectrum. It was discovered that alkyl amine, acetal, aryl amine, trioctylphosphine oxide, dodecyl (functionalized in air), and dodecyl (functionalized in Ar) protected Si-NCs emit blue, blue-green, green, yellow, orange, and red photoluminescence, respectively. This is the first example where the PL from Si-NCs has been systematically altered across the visible spectrum *via* surface groups.

7.2 Future directions.

7.2.1 Synthesis of novel materials.

The Mg reduction approach clearly offers tailoring of Si particle size, shape, and porosity while also providing a convenient method to prepare large quantities of material. The scope of the general magnesiothermic and other related reduction reactions are limited only by the creativity of the researcher. Countless materials with varied compositions, properties, and morphologies can be achieved through rational design and synthesis of the oxide precursor. Preliminary experiments indicate that it is possible to prepare Ge, Sn, and Si_xGe_y alloys as well as heretofore unknown Ge-Si core-shell structures. It can also be used to make various carbides such as ZrC, TiC, WC, Al_4C_3 *etc*. which are typically synthesized *via* carbothermal reduction at temperatures between 1500 - 2000 ^oC.[3] These materials are of great interest as they exhibit exceptional chemical stability and are highly sought out abrasive materials. To summarize, it is possible to create a library of nanomaterials in their elemental form, as well as nitrides and carbides of varying size and shape

using this magnesiothermic reduction process. The materials can be further used for a variety of applications such as Li-ion batteries, greenhouse gas sequestration, catalyst supports, templates, nano-reactors, *etc*.

7.2.2 Biological applications.

Quantum dots have quickly replaced organic dyes in biological analysis owing to their increased photostability, brightness, and ability to integrate multiple properties (such as magnetic, optical, therapeutic, *etc*.) into a single particle.[4] While Si has been proven to be non-toxic, it requires surface functionalization to be applied in biological systems. Addition of biomolecules such as polysaccharides, peptides, DNA, RNA, antibodies, *etc*. enhances the probability of the NC uptake by the cells and can target specific biological moieties (*e.g*. tumor cells).[5] To date no straightforward methods have been reported to covalently attach such biomolecules to Si-NC surface. The chloride surface termination offers a convenient route to tailoring Si-NC surface chemistry and introduce various surface groups that add to the NC utility and scope of application. For example, preliminary investigations involving the attachment of mannose and alanine (**Scheme 7-1**) indicate these functionalities render Si-NCs water-soluble while maintaining their PL response. The mannose functionalized Si-NCs were taken up by mammalian cancer cells and remain fluorescent, making cell imaging possible (**Figure 7-1**). ^{29}Si has been explored as an MRI contrast agent for over half a century.[6] By enhancing the concentration of the ^{29}Si isotope in Si-NCs, coupled with its biocompatibility, optical, and photothermal properties, one can create a perfect nanocarrier with multiple functions.

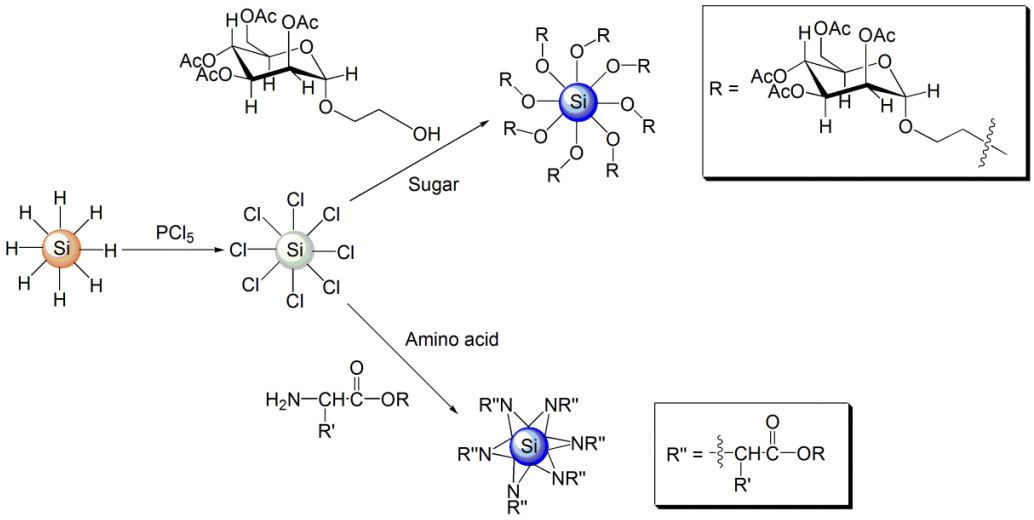

Scheme 7-1. Schematic representation of surface functionalization of Si-NC with mannose and amino acid groups.

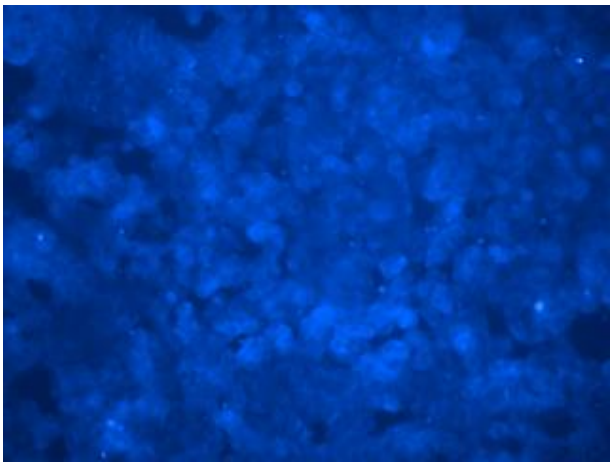

Figure 7-1. Fluorescent microscopy image of MCF-7 cells incubated with mannose functionalized Si-NCs.

7.2.3 Sensor applications.

The optical response of Si-NCs can be quenched or altered by exposing them to specific compounds (*e.g*. nitro-, amine-, ketone- functional groups). This observation was used to our advantage to develop Si-NC based disposable sensors to detect nitroaromatic explosives (**Figure 7-2**).[7]

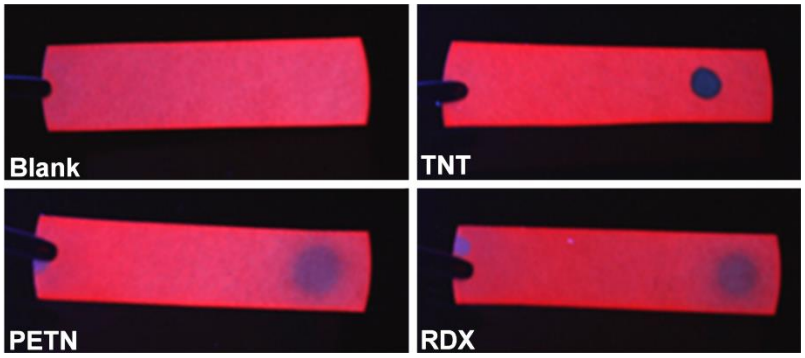

Figure 7-2. Images of dodecyl functionalized Si-NC coated filter paper under a handheld UV-lamp without the presence of nitrocompound and in the presence of solutions of TNT, PETN, and RDX, respectively.

While currently this procedure is non-selective, by careful modification of the NC surface one can develop size or functional group specific and ratio-metric sensors. Addition of surface groups with co-ordination sites would allow the chelation of metal ions that would trigger a change in optical response of the Si-NCs. Such systems can be used for detecting heavy metal ion impurities in contaminated water, soil, *etc*.

7.2.4 Photovoltaic devices.

Quantum dot based light emitting diodes (LEDs) have a very promising future.[8] However, Si quantum dots are not the most attractive candidates given their long lived excited states, which slows down the switching times in devices.[9] The defect based emissions reported here have short lived excited lifetimes. This discovery is a major step towards creating environmentally friendly lighting sources. Also, Si-NC based solar-cells can be fabricated by synthesizing NC/polymer hetero-structures.[10] The surface modification procedures can be extended to attach interesting polymers to the NC surface. Such structures would also allow the use of inexpensive fabrication techniques such as inkjet printing or spray coating. By tuning the NC size one can tune the absorption across the solar spectrum, generate multiple excitons owing to quantum confinement effect, and thus effectively increase the device efficiency.[11]

7.2.5 The blues - completing the story.

While the role of N in blue emission has been established, it does not address all the reports of blue emitting Si-NCs. Ongoing studies in the Veinot group include investigation of blue PL originating from chlorine/oxygen-based impurities in Si-NCs. Si-NCs with various functional groups derived from chloride-terminated surfaces (**Scheme 7-2**) unexpectedly exhibit blue luminescence. Solvatochromic studies are underway to determine if a charge transfer process is responsible for these properties. In addition, detailed material analysis is being performed to determine the nature and concentration of chlorine-based impurities.

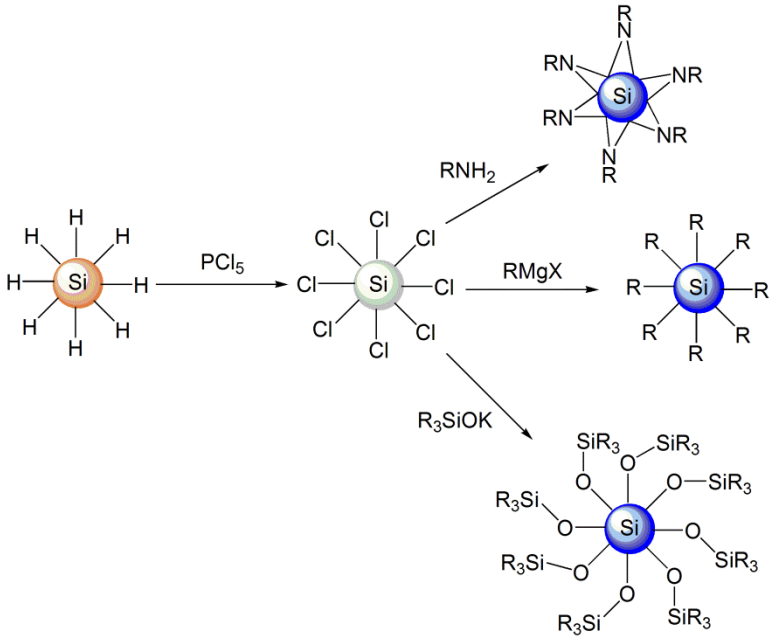

Scheme 7-2. Various blue-emitting Si-NCs derived from chloride terminated Si-NCs.

It was also determined that PCl_5 effectively etches the Si-NC surface. Studies are also being done to analyze etching rates under different reaction conditions. PCl_5 reactions may provide a way to perform face-selective etching to yield interesting morphologies.

7.3 References.

1. D. Bera, L. Qian, T. K. Tseng and P. H. Holloway, *Materials*, 2010, **3**, 2260.
2. S. Godefroo, M. Hayne, M. Jivanescu, A. Stesmans, M. Zacharias, O. I. Lebedev, G. Van Tendeloo and V. V. Moshchalkov, *Nat. Nanotechol*., 2008, **3**, 174.
3. M. D. Sacks, C. A. Wang, Z. Yang and A. Jain, *J. Mater. Sci*., 2004, **39**, 6057.
4. T. Jamieson, R. Bakhshi, D. Petrova, R. Pocock, M. Imani and A. M. Seifalian, *Biomaterials*, 2007, **28**, 4717.
5. S. Jin, Y. Hu, Z. Gu, L. Liu and H. C. Wu, *J. Nanomater*., 2011, **2011**, 834139.
6. R. G. Shulman and B. J. Wyluda, *Phys. Rev*., 1956, **103**, 1127.
7. C. M. Gonzales, M. Iqbal, M. Dasog, D. Piercey, R. Lockwood, T. M. Klapotke, A. Meldrum and J. G. C. Veinot, *Nanoscale*, 2014, Accepted.
8. A. J. Shields, *Nat. Photonics*, 2007, **1**, 215.
9. W. D. A. M. de Boer, D. Timmerman, K. Dohnlova, I. N. Yassievich, H. Zhang, W. J. Buma and T. Gregorkiewicz, *Nat. Nanotechol*., 2010, **5**, 878.
10. Z. Yang, M. Dasog, A. R. Dobbie, R. Lockwood, Y. Zhi, A. Meldrum and J. G. C. Veinot, *Adv. Func. Mater*., 2013, DOI: 10.1002/adfm.201302091.
11. I. J. Kramer and E. H. Sargent, *Chem. Rev*., 2013, DOI: 10.1021/cr400299t.

Appendices

Appendix A: Quantum Yield Measurements.

Quantum yields were determined using methods adapted from the work of Williams *et al*.[1] 9,10-biphenylanthracene in cyclohexane, coumarin 1 in absolute ethanol, and naphthalene in cyclohexane were used as the reference organic dyes. The etched silicon based samples were dissolved in toluene. All the organic solvents were passed through a column of anhydrous magnesium sulfate to remove any adhering moisture prior to making the solutions. The stock solutions were made by dissolving 10 mg of the organic dye in the solvent mentioned above and stirred until the entire solid dissolved. The solutions were then filtered through a membrane filter (2 µm) to remove suspended impurities and a series of diluted solutions were made with absorbances ranging between 0.1 and 0.01. PL spectra were acquired for the exact same solutions and the slit width was maintained at 5 – 10 nm depending on the species. The slopes of integrated fluorescence intensity versus UV-Vis absorbance were plotted and compared to confirm the quality of the reference curves. In all cases, the experimentally determined quantum yields were in good agreement with literature values: 9, 10-biphenylanthracene, 0.9; coumarin 1, 0.73; and naphthalene, 0.23. The etched samples and the reference samples were excited at the same wavelength and PL was recorded with the same slit width. The slopes of the integrated PL intensity versus absorbance were found for the etched samples and the quantum yields were calculated using the following equation:

$$\varphi_{x=}\ \varphi_{st}\ \left(\frac{m_x}{m_{st}}\right)\left(\frac{\eta_x^2}{\eta_{st}^2}\right)$$

where ‘ϕ’ is the quantum yield, ‘m’ is the slope of the integrated PL versus absorbance curve and ‘η’ is the refractive index of the solvent. The subscript ‘st’ refers to the standard organic dye while ‘x’ indicates the unknown species to be calculated.

References

1. A. T. R. Williams, S. A. Winfield, and J. N. Miller, *Analyst*, 1983, **108**, 1067.

Appendix B: Scherrer Equation for Particle Size Determination.

In 1918, Paul Scherrer proposed a method to estimate crystallite sizes from monochromatic incident radiation, using the equation:[1]

$$B(2\theta) = \frac{K\lambda}{L\ cos\theta}$$

where *B* is the value of full width at half maximum (FWHM) of the peak in radians, *K* is a shape factor constant with a value of 0.9, λ is the wavelength of the X-ray, *L* is the size of the crystallite, and θ is the Bragg angle. The peak width (*B*) is inversely proportional to the crystallite size (*L*).

The peaks chosen for the Scherrer analysis are typically between 30 and 60°.[2] The peaks below 30° compromise the analysis due to peak asymmetry, while peaks above 60° are typically too broad and close to the baseline to obtain quality FWHM measurements. If possible multiple peaks are analyzed and the final value is obtained by averaging the '*L*' value obtained from each peak. An example is provided below, where Si-NC (obtained from heating HSQ at 1200 °C) size is estimated using Scherrer analysis. In this example, the (220) and (331) peaks are used.

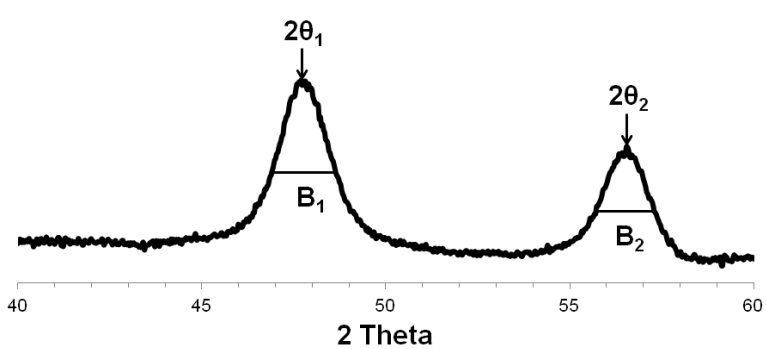

$\lambda = 0.154$ nm

$B_1 = 0.02618$ radians $B_2 = 0.02670$ radians

$\theta_1 = 23.875^o$ $\theta_2 = 28.269^o$

$L_1 = 5.82$ nm $L_2 = 5.99$ nm

$L = (L_1 + L_2)/2 = 5.90$ nm

References.

1. A. L. Patterson, *Phys. Rev*., 1939, **56**, 978.
2. J. I. Langford and A. J. C. Wilson, *J. Appl. Cryst*., 1978, **11**, 102.